The impact of environment on the evolution of protoplanetary discs

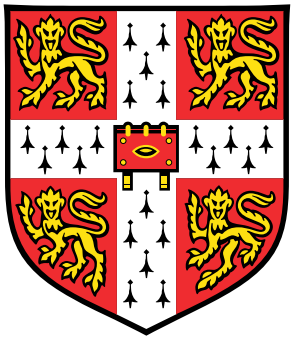

Stefano Facchini

Institute of Astronomy

University of Cambridge

This dissertation is submitted for the degree of

Doctor of Philosophy

Fitzwilliam College January 2016

Dedicated to my parents, Mario and Mirella, and to Irene

Declaration

I hereby declare that except where specific reference is made to the work of others, the contents of this dissertation are original and have not been submitted in whole or in part for consideration for any other degree or qualification in this, or any other university. This dissertation is my own work and contains nothing which is the outcome of work done in collaboration with others, except as specified in the text and Acknowledgements. This dissertation contains fewer than 60,000 words including appendices, bibliography, footnotes, tables and equations and has fewer than 150 figures.

Stefano Facchini
January 2016

Abstract

Protoplanetary discs represent the mass reservoir for planet formation, and the chemico-physical mechanisms occurring during their lifetime sculpt the fundamental properties of the planets born within them. Historically, protoplanetary discs have been initially considered as idealised isolated systems orbiting around a single star. However, recent surveys are showing that both multiplicity and the natal environment can significantly affect disc evolution, since most of stars are born in intermediate-large groups and clusters. Sub-mm surveys of Class 0 objects is compatible with all stars being born in multiple systems. Close binaries (with orbital separation $< 40\,\mathrm{AU}$) are likely associated to a circumbinary disc, which can be misaligned to the binary plane. Such misalignment leads to a warped structure of the disc. In this thesis, I show that warp evolution in circumbinary protoplanetary discs is well described by simple 1D wave equations, by testing such 1D model with 3D SPH simulations. I also apply the 1D model to transition discs, and show that a massive planet orbiting within the central cavity can be inferred by a small warp in the outer disc, which can be probed by spatially resolved ^{12}CO line profiles. The two most relevant environmental mechanisms affecting protoplanetary discs are star-disc encounters, and external photoevaporation. In this thesis, I show that sub-mm observations of the RW Aur system are well described by an ongoing tidal encounter between the circumprimary disc and the secondary star. This makes RW Aur the only system known to date to be undergoing this kind of interaction. I also present new X-Shooter spectral observations of the primary star, which shed a new light in constraining the physical mechanism responsible for the peculiar light curve of the system. Finally, in this thesis I construct a new model of FUV dominated external photoevaporation, extending the parameter space explored in previous literature, and investigating how grain growth affects the mass loss rates.

Table of contents

Chapter 1

Introduction

The last years have witnessed an outstanding improvement in our knowledge of the properties of planets in the Solar Neighbourhood. The advent of the Kepler mission, together with radial velocity measurements, has brought the number of known extrasolar planets (exoplanets) up to ~ 2000. This sample is large enough to let us start using statistical tools to study the properties of exoplanets. The picture that is emerging from these initial studies has significantly revolutionised our understanding. As an example, completely new classes of planets have been found to be orbiting Main Sequence stars, such as the so-called Hot Jupiters and Super Earths. Recent observations have shown both worlds that are drastically different from the ones present in our Solar System, such as 'diamond' planets (such as 55 Cancri e; Madhusudhan, Lee & Mousis, 2012), and potential Earth-twins thousands of light years from us (such as Kepler 452b; Jenkins et al., 2015). In future years, with the advent of new space missions, and the construction of new observational facilities on the ground, we will be able to advance the knowledge of the spectrum of exoplanets properties in our Galaxy to astonishing levels.

In the mean time, parallel observations and advanced theoretical models have focused on the environments where planets are very likely to be born and grow: the so-called protoplanetary discs. These objects are dust laden gaseous structures orbiting around new born stars. They represent the mass reservoir for planet formation, and their chemico-physical mechanisms sculpt the fundamental properties of the planets born within them. Studying their birth, evolution and final dispersal is of fundamental importance if we want to try answering the compelling questions: how was the Earth formed, such as to have the properties we see today? How do planets form in general? How fast is this process? How are their properties connected to the initial environment in which they are born?

These very days are probably the most exciting ones in addressing these questions. In recent years observations in the protoplanetary discs field have significantly accelerated this

process of understanding, even though we are still far from a conclusive and comprehensive answer. In particular, the Infrared (IR) space missions Herschel and Spitzer have permitted us to detect a large number of these sources. Even more importantly, we have now access to spatially resolved observations of a large number of discs, thanks to the advent of (sub-)mm interferometers, such as the Submillimeter Array (SMA), the Combined Array for Research in Millimeter-wave Astronomy (CARMA), the Plateau de Bure Interferometer (PdBI), and the Acatama Large Millimeter Array (ALMA). Such resolved maps are a unique opportunity to study the interplay between planets and their birth environments, as we will see in due course.

However, the majority of stars are not born in isolation, and environmental effects can dramatically affect the evolution of protoplanetary discs (and consequently of exoplanets). Even our own Solar System shows evidence of the impact of environment in shaping its structure, such as its outer radius (e.g. Adams, 2010). Thus understanding the relevance of environmental effects is of fundamental importance, since most of the protoplanetary discs are likely to be affected by the ambient conditions.

In this thesis, I address three different aspects of the interplay between disc evolution and birth environment, in particular dealing with binarity, star-disc encounters, and external photoevaporation.

In this introductory chapter, I briefly review the evidence we have today of the impact of the birth environment on the properties of protoplanetary discs. I then describe the arguably most important mechanisms affecting their evolution, and finally summarise the goals of the thesis in Section 1.5.

1.1 Protoplanetary disc evolution

Protoplanetary discs form around almost all new born stars. They represent the simple consequence of angular momentum conservation of the gaseous material gravitationally collapsing towards the protostar. General reviews on their observational properties can be found in Williams & Cieza (2011) and Dutrey et al. (2014). *Protostars and Planets VI* includes other reviews on specific aspects of their evolution, and we will mention them in due course when appropriate.

Observationally, there are at least two classifications of protoplanetary discs. Firstly, Lada (1987) categorised young stellar objects (YSOs) in three Classes (I-II-III) based on the slope of the Spectral Energy Distribution (SED) in the mid-IR between 2 and 25 μm. These

three classes indicate an SED that rises, declines with significant IR excess, and declines with negligible IR excess, respectively. In particular, if we define

$$\alpha_{\rm IR} = \frac{d\log \nu F_\nu}{d\log \nu}, \tag{1.1}$$

we can associate Class I, II and III objects with $\alpha_{\rm IR} > 0$, $-1.5 < \alpha_{\rm IR} < 0$, and $\alpha_{\rm IR} < -1.5$, respectively (Andre & Montmerle, 1994). Andre, Ward-Thompson & Barsony (1993) introduced an even redder Class (Class 0). Both Class 0 and I individuate YSOs still embedded in their primordial envelope, whereas class III objects are usually PMS stars with little or no evidence of dust around them. They are often considered as YSOs due to their position in the HR diagram. The second classification is based on accretion properties. YSOs showing bright emission lines (mostly Hα) and strong ultraviolet (UV) excess are referred to as classical T Tauri stars (CTTs), whereas YSOs with negligible or no accretion signatures are referred to as weak line T Tauri stars (WTTs). Generally CTTs have Class II SEDs, and WTTs Class III SEDs.

IR and (sub-)mm observations have allowed statistical studies of disc occurrence in star forming regions since the late 80's (Strom et al., 1989; Beckwith et al., 1990). More recent studies, which have reached a much higher level of sample completeness, have led to good estimates of disc lifetimes, by comparing disc occurrence in different star forming regions (Mamajek, 2009; Fedele et al., 2010; Kraus et al., 2012). Different discs tracers, in particular IR excess and spectral accretion signatures, agree with an average lifetime of ~ 3 Myr (see Fig. 1.1). Planet formation models such as the core accretion scenario, show that the time needed to assemble the core of a gas giant planet is within one or few Myr (e.g. Movshovitz et al., 2010), and planetary seeds do have the time to grow to observed masses on similar timescales (see Helled et al., 2014, for a recent review), in agreement with the estimated disc lifetime.

The evolution of an isolated disc around a single star has initially been described as a succession of quasi-steady states of an infinitely thin disc (Lynden-Bell & Pringle, 1974), within which mass and angular momentum are transported radially by shearing torques. These very successful models (namely, thin accretion models; Pringle, 1981) usually assume that in every quasi steady-state the gas rotates in centrifugal equilibrium with Keplerian velocity $v_K = \sqrt{GM_*/R}$, where M_* is the mass of the central star and R is the cylindrical radius of the gas particle. Disc evolution is thus set by angular momentum transfer within (or from) the disc. Angular momentum is usually described to be transported by shearing (viscous) forces, where the physical mechanism responsible for the angular momentum transfer is usually neglected. In these cases, disc evolution is modelled with a Navier-Stokes equation, where the effective dynamical viscosity ν is parametrised with $\nu = \alpha c_{\rm s}^2 \Omega^{-1}$ (Shakura &

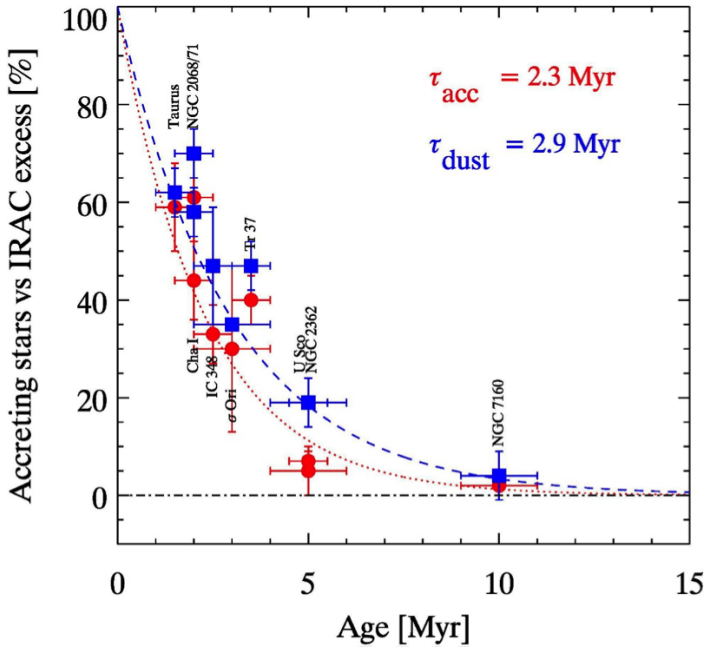

Fig. 1.1 Disc occurrence versus time in different stars forming regions, as probed by IR excess (blue squares) and accretion traces by Hα (red dots). The two datasets are exponentially fitted by the blue dashed and red dotted lines, respectively. Figure from Fedele et al. (2010).

Sunyaev, 1973), where c_s is the sound speed in the gaseous flow and Ω is the angular velocity. The dimensionless parameter α is usually considered to be constant within the disc (the so-called α-discs, e.g. D'Alessio et al., 1998). In this thesis I will always use this simplified model, which is a very useful approximation to study disc evolution without very expensive numerical calculations. Note that the accretion rates observed in Class II objects indicate that the physical mechanism at the origin of angular momentum transport in discs cannot be fluid viscosity. If this was the case, discs would evolve on a timescale of ~ 10 Gyr, whereas they are observed to evolve on faster timescales, as explained above. A large progress has been attained in the construction of theoretical models of the physical mechanisms at the origin of angular momentum transport. Interested readers can look at the comprehensive reviews by Armitage (2011) and Turner et al. (2014), which summarise the most promising candidates (magneto-rotation instability, gravitational instability, magnetically launched winds, baroclinic instability).

1.1.1 Transition discs

α-discs models fail to reproduce the dispersal of protoplanetary discs, since they predict a slow homologous depletion of the mass surface density, with $M_d \propto t^{-3/2}$ (Hartmann et al.,

1998), where $M_{\rm d}$ is the mass of the disc and t the time variable. However, statistical studies show that the final phase of disc evolution occurs on short timescales (~ 10 times shorter than the typical disc lifetime, e.g. Andrews & Williams, 2005; Koepferl et al., 2013). The efficiency of the disc clearing mechanism(s) is supported by non-detections of gas around WTTs (Pascucci et al., 2006; Ingleby et al., 2009; Hardy et al., 2015). Current observations indicate that discs are likely to evolve going through a transitional phase (see the observational review by Espaillat et al., 2014), where a hole is carved in the inner disc, just prior to the final disc dispersal. These central cavities, which are not predicted by simple viscous evolution, are either indirectly observed by looking at the SED, showing a characteristic IR deficit at short wavelengths indicating the lack of hot thermal emission in the proximity of the central star, or directly probed by spatially resolved submm observations.

Transition discs are now generally considered as the evolutionary stage prior to the disc final dispersal. Different models have been invoked to explain these observations (see Clarke, 2011; Alexander et al., 2014, for recent reviews). The most successful certainly are photoevaporation caused by the energetic (EUV, FUV or X-ray) radiation from the central star (e.g. Alexander, Clarke & Pringle, 2006; Gorti & Hollenbach, 2009; Owen, Clarke & Ercolano, 2012, respectively), or planet carving (e.g. Zhu et al., 2011; Owen, 2014). Owen & Clarke (2012) have shown that transition discs can be divided in roughly two classes, based on their mm flux and cavity radius. In particular, mm bright discs with large cavities are incompatible with X-rays photoevaporative models, whereas mm faint discs with small inner hole radii can be explained by photoevaporation. The former class is more likely to be associated with inner planets, acting as dams to the large grains (e.g. Pinilla, Benisty & Birnstiel, 2012; Owen, 2014), and where gas is depleted but still present in the inner cavity (van der Marel et al., 2015).

There is still no clear evidence of what causes the fast dispersal of the gas from the outer regions of the disc outside the central hole, where most of the mass lies, even though thermodynamical instabilities have been invoked as possible dispersal mechanisms (e.g. Owen et al., 2013). Independently of the physical cause, the final outcome of this rapid phenomenon is probably a debris disc, which still bears low amount of gas, but likely released by energetic impacts among the debris (recent reviews are by Matthews et al., 2014; Wyatt et al., 2015).

1.1.2 Grain growth

Another important element of disc evolution is grain settling and growth, a fundamental step of the process leading to the formation of planetary embryos (e.g. Beckwith, Henning &

Nakagawa, 2000). A comprehensive review of observations, laboratory experiments and theoretical models on this subject can be found in Testi et al. (2014).

The interstellar medium (ISM) is formed by both gas and dust. The dust component is formed by small grains ($s_{\rm max} \sim 0.25 - 1\,\mu$m, where $s_{\rm max}$ is the maximum grain size, see e.g. Draine, 2011), and is characterised by a size distribution. This grain size distribution is usually assumed to be described by a power law, where $dn/ds \propto s^{-q}$. In the ISM, $q \approx 3.5$, as observationally derived by Mathis, Rumpl & Nordsieck (1977). Growth of these dust grains to larger sizes is expected to start in pre-stellar dense cores (e.g. Keto & Caselli, 2008). Furthermore, recent observations indicate potential evidence of large grains in collapsing envelopes of class 0/I objects (e.g. Tobin et al., 2013; Miotello et al., 2014). However, protoplanetary discs are still considered as the most favourable environment where dust grains can coagulate up to planetesimal sizes.

One observational evidence of this hypothesis comes from our own Solar System, where chondrites are found to be formed by mm-sized chondrules and by smaller calcium aluminium inclusions (CAI), which are probably heated agglomerates of primitive micron-sized particles. Absolute ages of chondrules are found to lie in a range of few Myr (Connelly et al., 2012, see Fig. 1.2), starting from the CAIs formation stage (which is assumed to be the time zero point of the astronomical age of the Sun). This result indicates that the assembling of CAIs and chondrules occurred throughout the disc lifetime. The second evidence comes from interferometric observations of protoplanetary discs, as we show below.

In principle, probes of grain growth in protoplanetary discs can be obtained at different wavelengths. IR observations can probe the dust content in discs upper layers, via scattered light imaging (in both intensity and polarisation), and by characterisation of dust emission features at 10 and 20 μm. However, these observations probe the optically thin layers of discs, which can be as high as 4-5 H above the disc midplane (where H is the scaleheight of the disc), where turbulent mixing is not effective enough to drag the largest grains to these heights. Effective grain growth is expected to occur significantly in the disc midplane, where the largest grain are vertically settled. These regions can be observed by longer (sub-)mm wavelengths, since continuum emission is usually optically thin in the outer regions for not-extremely massive discs. For a grain size distribution with minimum and maximum grain sizes $s_{\rm min}$ and $s_{\rm max}$, the dust thermal emission is controlled by the dust opacity κ_ν, which can be well approximated by $\kappa_\nu \propto \nu^\beta$, when $\lambda \gtrsim s_{\rm max}$. The spectral index β at (sub-)mm wavelengths does not depend on $s_{\rm min}$ when $s_{\rm min} < 1\,\mu$m (e.g. Draine, 2006), since the contribution of small dust at such long wavelengths in negligible. In the optically thin regime, and in the Rayleigh-Jeans limit, $\beta = \alpha_{\rm mm} - 2$, where $\alpha_{\rm mm}$ is the slop of the sub-mm SED ($F_\nu \propto \nu^{\alpha_{\rm mm}}$). Note the $\alpha_{\rm mm} \approx 3.7$ in the ISM. With these two simple assumptions, determining β can

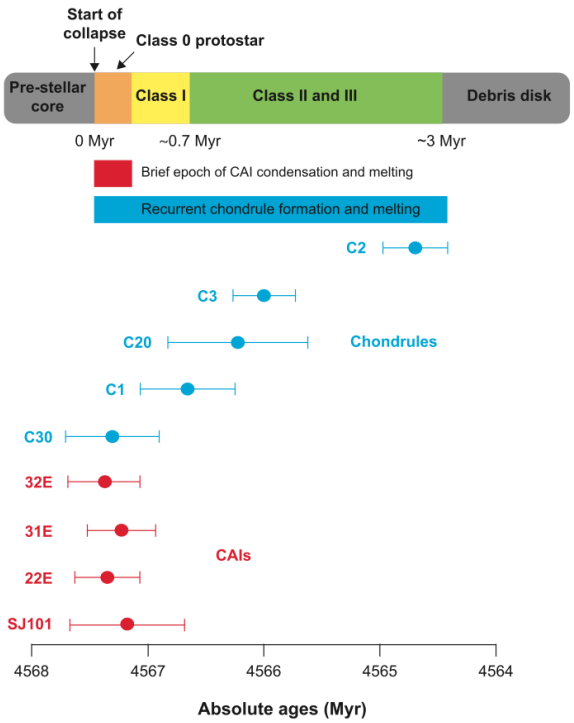

Fig. 1.2 Ages of CAIs and chondrules in our Solar System. Figure from Connelly et al. (2012).

probe effective grain growth, since β is related to both the maximum grain size $s_{\max}$ and to the slope of the grain size distribution q (e.g. see Draine, 2006, and the left panel of Fig. 1.3). Initial surveys of a few star forming regions indicate that dust has grown up to at least mm-sizes in almost all sources (see the right panel of Fig. 1.3 and papers by Andrews & Williams, 2005, 2007; Ricci et al., 2010b,a). These results indicate that grain growth effectively occurs in protoplanetary discs. The permanence of such large grains within the disc is still a challenging result, since theoretical models predict that grains larger than a specific size would quickly be removed by efficient radial drift (e.g. Weidenschilling, 1977; Takeuchi & Lin, 2002; Birnstiel, Dullemond & Brauer, 2010; Birnstiel, Klahr & Ercolano, 2012). Pressure bumps (i.e. radial inhomogeneities in the disc) are able to trap large grains locally (e.g. Pinilla et al., 2012) and possibly lead to the formation of planetary embryos in these overdense regions via some instability (as the streaming instability, see Johansen et al., 2007). Other proposed mechanisms are summarised in the recent review by Johansen et al. (2014).

In this Section we have very briefly addressed some key aspects of the evolution of protoplanetary discs. However, we have considered the very ideal case where the central

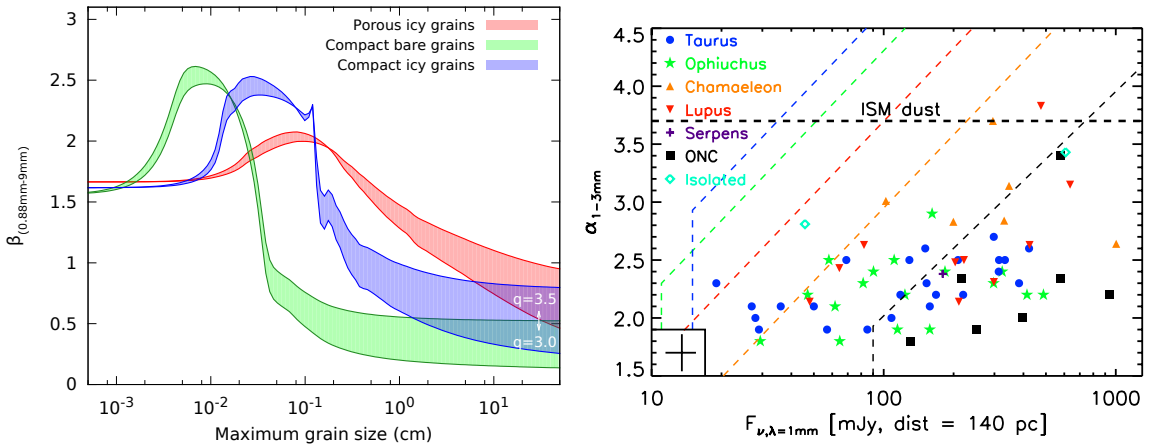

Fig. 1.3 Left panel: expected spectral index β between 0.88 and 9 mm vs maximum grain size of the dust distribution. Right panel: observed $\alpha_{\rm mm}$ index between 1 and 3 mm vs flux at 1 mm for objects in a sample of star forming region. Coloured dashed lines indicate the sensitivity limit of the surveys. Figures from Testi et al. (2014).

star is single (i.e. is not part of a multiple system), and where environmental effects can be neglected. In the next Sections, we address more systematically how multiplicity and environment can play a relevant role in determining disc evolution.

1.2 Binarity

It is now well known that the majority of stars in star forming regions are in binary or higher order multiple systems (see e.g. the reviews by McKee & Ostriker, 2007; Reipurth et al., 2014). IR observations have been used in large surveys of Class I protostars to determine their multiplicity frequency (e.g. Duchêne et al., 2007; Connelley, Reipurth & Tokunaga, 2008a,b). Longer wavelengths are needed for Class 0 protostars; using SMA observations, Chen et al. (2013) found that multiplicity frequency of Class 0 YSOs are compatible with all stars being born in multiple systems (see Fig. 1.4), if we take into account that close protobinaries are systematically unresolved. Such frequency then decays with evolutionary class, due to dynamical instabilities of the primordial multiple systems. On the theoretical side, hydrodynamical models of gravitationally unstable molecular clouds succeed in reproducing the observed multiplicity of new born stars (e.g. Bate, 2009). Some of these models still lack important physics, as radiative feedback, and use simple barotropic assumptions. More recent simulations indicate that radiative feedback does indeed have an important effect in reducing the number of close binaries (Offner et al., 2009). However,

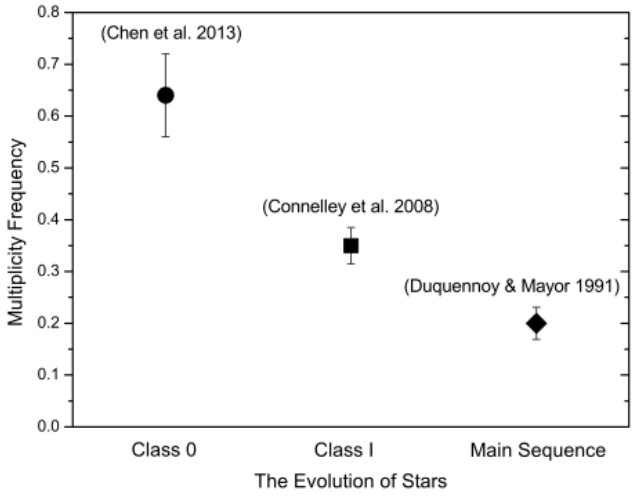

Fig. 1.4 Figure from Chen et al. (2013).

simulations by Bate (2012) do reproduce the observed multiplicity with simulations including radiative feedback, due to wide binaries spiralling in to smaller separations.

In the last decade the possibility of detecting discs around multiple systems (and both stellar components in close binaries) has dramatically improved, thanks to the high angular resolution of interferometers. These observations have shown that Class II stars in multiple system do have circumstellar discs and evidence of accretion (e.g. Mathieu et al., 1997). If we focus on the circumbinary case, only a few discs have been imaged directly (e.g. Dutrey, Guilloteau & Simon, 1994; Beust & Dutrey, 2005), since massive circumbinary discs seem rare for separations $\lesssim 100$ AU (Jensen, Mathieu & Fuller, 1996). However, the bulk of the population of circumbinary discs occurs for close binaries: occurrence studies of debris discs around MS stars have highlighted that close binaries (with separations smaller than ~ 3 AU) are more likely to have a circumbinary debris disc than wider pairs (with separations between ~ 3 and 40 AU; Trilling et al., 2007). Finally, indirect evidence of former protoplanetary circumbinary discs is the recent detection of circumbinary planets (Deeg et al., 2008; Lee et al., 2009; Beuermann et al., 2010), some of which have been probed by Kepler (e.g. Kepler-16, 34, 35, 47; Doyle et al., 2011; Welsh et al., 2012; Orosz et al., 2012).

1.2.1 Evolution of (circum)binary discs

Multiplicity has an impact on the global evolution of circumstellar discs. Cieza et al. (2009) used Spitzer surveys of 4 star forming regions (Ophiuchus, Taurus, Chameleon I and Corona Australis) to present the first statistical evidence that circumstellar discs in close binary

systems ($a < 40$ AU, where a is the binary separation, and thus in agreement with the findings by Trilling et al., 2007) are short-lived with respect to single star systems (see Fig. 1.5). For circumprimary and circumsecondary discs, this is probably due to a combined effect of disc tidal truncation (which reduces the viscous timescale) and photoevaporation. For circumbinary discs, Alexander (2012) suggested that discs around close binaries ($a \lesssim 1$ AU) should be long-lived, since the tidal torque will inhibit viscous accretion (Pringle, 1991), and the potential well is deep enough to prevent an efficient photoevaporation. Accretion onto the central stars occurs via tidal streams, where the accretion rate can be approximated with 10% of the accretion rate of a steady-state accretion disc (e.g. MacFadyen & Milosavljević, 2008). However, a proper numerical treatment of the accretion process in circumbinary discs has been longly debated. Recent converged SPH simulations (Young, Baird & Clarke, 2015; Young & Clarke, 2015) have shown that the amount of accreted material onto the primary or the secondary star depends strongly on the local temperature of the gas. Thus, the thermodynamics of the inner regions of the disc has a deep impact in determining the final mass ratio of the binary. Finally, the surface density profile of a circumbinary disc is affected by the torques of central binaries. The disc is roughly truncated at a tidal radius which depends on the binary mass ratio (Artymowicz & Lubow, 1994), and the gas surface density profile smoothly grows with radius, until it starts decreasing with a typical power law profile. As mentioned in Section 1.1.2, large dust grains will remain confined outside the pressure bump, and this mechanism could explain why continuum emission at submm wavelengths in circumbinary discs is located at a larger radius than the expected tidal radius (Cazzoletti et al., in prep.). This mechanism can explain the observations of the most famous circumbinary disc, GG Tau (Dutrey, Guilloteau & Simon, 1994; Andrews et al., 2014, and references therein).

1.2.2 Warps in (circum)binary discs

A significant discrepancy between discs around single stars and in binary systems is that the orbital plane of the binary and the plane of the outer disc are likely to be misaligned (e.g. Bonnell et al., 1992; Bate, Lodato & Pringle, 2010). In the latter case, the disc is likely to gain a warp, which strongly affects the global evolution of the disc. This fact has been invoked as a possible explanation of the misalignment between the stellar rotation axis and planets' orbits (Bate, Lodato & Pringle, 2010), measurable via the Rossiter McLaughlin effect (e.g. Triaud et al., 2010; Albrecht et al., 2012). A detailed overview of theoretical models of disc warping in protoplanetary binary systems will be presented in Section 2.3.

Until a few years ago, we lacked observational evidence of warped protoplanetary discs. In binary systems, tilted discs had been inferred only around X-ray binaries showing a

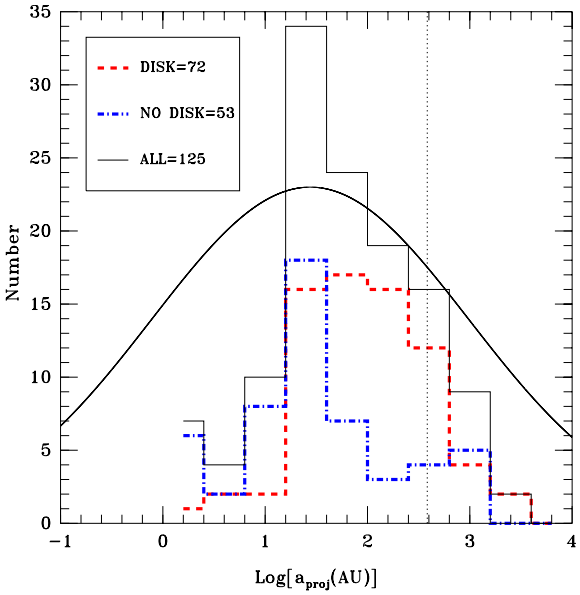

Fig. 1.5 Figure from Cieza et al. (2009). From their caption: "Histogram of projected separations for targets with and without Spitzer excesses indicating the presence of a disk. Systems without an excess clearly tend to have smaller separations. The solid curve represents the distribution of binaries in solar-type stars (Duquennoy & Mayor, 1991). The census of companions is still highly incomplete for separations < 20 AU."

long term modulation of the periodic light curve (see Kotze & Charles, 2012, and references therein), and some cataclysmic variables (summarised by Olech, Rutkowski & Schwarzenberg-Czerny, 2009). However, very recently, observational features in a few protoplanetary discs have been interpreted as signatures of disc warping. In particular, the advent of interferometric observations with the ALMA has allowed to start measuring precise gas kinematics via molecular line profiles, which is one of the most powerful tools to detect disc warping. For example, Rosenfeld et al. (2012) has observed an excess in the emission at high velocity in the inner disc of TW Hya, which they interpreted as a possible inner warp. Another case is HD 100546, where a warp has been invoked to interpret the twisted first moment map of CO (3-2) (Pineda et al., 2014), and even earlier as a possible explanation of the spiral structure observed in scattered light (Quillen, 2006) and of the asymmetric line profiles from single-dish observations (Panić et al., 2010). The most recent case is HD 142527. Marino, Perez & Casassus (2015) have modelled the strongly asymmetric scattered light image of this protoplanetary disc with a highly misaligned inner disc, casting a shadow onto the outer regions. The misaligned inner disc could be tracing the inclination of the stellar companion (Biller et al., 2012; Close et al., 2014) observed within the huge mm cavity of the transition disc. Furthermore, CO (6-5) ALMA observations of the system have shown a twisted velocity centroid map (Casassus et al., 2015), which can be modelled by extreme

disc warping, probably caused by a dynamical interaction with the low mass companion. Non-Keplerian flows have also been detected with lower angular resolution in CO (3-2) (Casassus et al., 2013; Rosenfeld, Chiang & Andrews, 2014). Finally, the KH 15D binary system has been modelled as a compact precessing misaligned circumbinary disc, which causes the long-term modulation of the light curve of the system (Chiang & Murray-Clay, 2004; Herbst, LeDuc & et al., 2010; Lodato & Facchini, 2013; Windemuth & Herbst, 2014). All these observations go together with complementary recent findings, where disc warping has not been detected yet, but where circumprimary (and sometimes circumsecondary) discs are clearly misaligned with the orbital plane of the binary (e.g. Roccatagliata et al., 2011; Jensen & Akeson, 2014; Williams et al., 2014). Some of these discs are very likely to show kinematic signatures of disc warping, when higher angular resolution observations will be available. Finally, circumbinary planets do not offer much constraints on the evolution of misaligned discs, since the observations are heavily biased towards aligned (and thus eclipsing) systems. Only small misalignments are observed, as in the case of Kepler-413b, where the relative inclination is $\sim 2.5^\circ$ (Kostov et al., 2014).

1.3 Environmental effects

Star formation occurs in regions of local gas and stellar over densities in our galaxy. Lada & Lada (2003), Porras et al. (2003) and others have shown that the probability density function for cluster membership number N for clusters in the Solar Neighbourhood scales with $1/N^2$. This relation seems to hold in the whole galaxy, up to extremely massive clusters. Thus the cumulative probability for a star to be born in a cluster of size $\leq N$ is inversely proportional to N (e.g. Adams, 2010). Within 2 kpc of the Sun, the median value of this distribution (also taking into account isolated stars) is ~ 300 (Adams et al., 2006; Allen et al., 2007), but in the whole galaxy the median value is much higher, since the upper limit of the probability density function is higher than in the Solar Neighbourhood. The cluster environment is expected to affect the evolution of new born stars via radiation and momentum feedback (e.g. Dale, Ercolano & Bonnell, 2013), e.g. triggering star formation, limiting the radial extent of protoplanetary discs, etc... These phenomena will impact the frequency of planet-bearing systems: for example, Longmore et al. (2014) estimated that $\sim 10\%$ of all stars may have the formation of planets in the habitable zone affected by their natal environment.

There is observational evidence that the environment of star forming regions can significantly affect the evolution of protoplanetary discs. Until recent years the only evidence of such interplay has come from single objects showing clear signatures of an on-going interaction between their disc and the ambient environment (e.g. O'Dell, Wen & Hu, 1993;

Bally, O'Dell & McCaughrean, 2000; Vicente & Alves, 2005). With the advent of sub-millimeter surveys, we can now start accessing statistical samples of relevant properties of protoplanetary discs (mostly their mass and outer radius) and infer whether they do show imprints of being affected by the environment. Such studies have shown that this is indeed the case in the most extreme star forming region within 500 pc from us, the Orion Nebula Cluster (ONC). In this cluster, de Juan Ovelar et al. (2012) have suggested that typical disc sizes decrease as a function of the stellar surface density of the environment in which they are embedded. Even more interestingly, Mann et al. (2014) (see also Mann & Williams, 2010) have shown that discs tend to be less massive in the immediate vicinity of the dominant O star in the ONC, θ^1C. Note however that Mann et al. (2015) and Richert et al. (2015) have not observed such a trend in other O-stars bearing clusters. Finally, Stolte et al. (2010) have shown that in the Arches cluster (which is more massive and more compact than the ONC) disc frequency is an increasing function of distance from the centre of the cluster. For milder star forming regions, we still lack observational evidence of how important the environment can be in shaping the structure and the evolution of discs. Spatially resolved surveys of discs might be able to clarify this.

The two main mechanisms that can affect protoplanetary discs are star - disc gravitational interactions, and photoevaporation. We describe them in more detail in the next two Sections. Another very interesting interaction between circumstellar discs and the environment is chemical enrichment of the central star and the potential planetary system. In particular, discs may sweep up ambient material ejected by supernova explosions, rapidly rotating stars or stellar binaries and accrete it onto the star and onto the (proto)planets. We do not describe this mechanism in this thesis. Interested readers can have a look at the review by Adams (2010) and the paper by Bastian et al. (2013) to explore this phenomenon in the natal environment of our own Solar System and in massive stellar clusters, respectively.

1.3.1 Star-disc encounters

In an α-disc framework, the disc outer radius viscously spreads outwards (Lynden-Bell & Pringle, 1974). Initial results seem to confirm this result in low density star forming regions (Isella, Carpenter & Sargent, 2009; Guilloteau et al., 2011). In denser clusters, during the lifetime of a disc (see Section 1.1), gravitational encounters with other stars may perturb the disc, truncating it to a defined outer radius, and steepening the surface density profile (see Hall, 1997; Breslau et al., 2014; Rosotti et al., 2014; Vincke, Breslau & Pfalzner, 2015, and references therein). Very few objects that might be undergoing such encounters have been detected (Cabrit et al., 2006; Salyk et al., 2014), since the timescale of observability is very

short. However, in recent years numerical simulations have set important steps forward in estimating the importance of this kind of interaction.

In the literature, the effect of a stellar fly-by on a disc bearing star is usually studied in isolation, for a few dynamical timescales (e.g. Clarke & Pringle, 1993; Breslau et al., 2014; Muñoz et al., 2015). In particular, Breslau et al. (2014) derived an analytical prescription for the outer radius of the truncated discs by exploring a parameter space of different stellar masses and impact parameters with discs described by test particles (hydro effects are neglected). They modelled the encounters via prograde coplanar parabolic orbits, obtaining the following prescription for the disc outer radius: $R_{\rm out} = 0.28 R_{\rm peri} m_{12}^{-0.32}$, where $m_{12} = M_2/M_1$ is the mass ratio of the two stars, and $R_{\rm peri}$ is the impact parameter for a coplanar encounter. They did not explore the effects of the misalignment between the disc and the plane of the parabola. Recent results by Lubow, Martin & Nixon (2014) analysed how the tidal truncation radius estimates are affected by the misalignment between a disc and an external binary. Their results indicate that the external torque decreases quite rapidly with inclination, leading to a larger circumstellar disc. Similarly, we expect the same kind of behaviour for a fly-by interaction, even though in this case resonances do not come into play. Finally, the analytic prescription by Breslau et al. (2014) strongly depends on the definition of the outer radius. They define it as the point where the surface density profile presents a maximum in its radial gradient. However nothing prevents an observer from detecting regions of the disc outside this radius, where the material will be less bound and in more elliptical orbits. Muñoz et al. (2015) analysed the resulting morphology of a disc-disc interaction with hydrodynamical simulations (using the code AREPO; Springel, 2010), and the eventuality of the formation of a bound binary system when the energy injected to disrupt the discs is large enough (i.e. the discs are highly massive). They explored how the results are affected by changing the impact parameter, the mass of the discs, and the relative inclination angles. In particular, they noticed that the characteristic large spirals trailing the discs in disc-disc encounters (Clarke & Pringle, 1993) are almost absent for retrograde encounters.

In order to test how significant are these encounters in dispersing discs in both small and large clusters, there have been at least two different approaches. The first one consists in modelling the stellar dynamics within the cluster with N-body simulations, and determining *a posteriori* the impact of the tidal interactions on circumstellar discs by using the results of the simulations of the star-disc encounters modelled in isolation. Similar studies are e.g. by Scally & Clarke (2001), Olczak, Pfalzner & Spurzem (2006), Pfalzner (2008) and Olczak et al. (2012). All the listed works concentrated in modelling the ONC and the Arches clusters. As an example, Olczak, Pfalzner & Spurzem (2006) estimated that over 12.5 Myr about 5% of discs in the ONC (and $\sim 10\%$ in the core) would be destroyed outright. A set of more

general N-body simulations performed by Malmberg et al. (2007) and Malmberg, Davies & Heggie (2011), where they explored different N values and half-mass radii, showed that in some cases more than 80% of the stars were non-singleton, i.e. they did have a stellar fly-by closer than 1000 AU. Finally, Vincke, Breslau & Pfalzner (2015) simulated star clusters using a N-body code ranging over stellar densities, clusters masses and IMF realisations. They concluded that $\sim 15\%$ of all discs are reduced to sizes smaller than 100 AU for ONC-like clusters. The same number can be as high as $\sim 39\%$ for denser clusters, such as IC 348.

The second approach consists in hybrid N-body - hydrodynamical simulations, where the stellar dynamics is coupled to the hydrodynamical evolution of circumstellar discs. In this way, the effect of the stellar encounters onto the disc evolution is not evaluated *a posteriori*, but is directly computed in the numerical simulations. A first attempt in this direction has been performed by Rosotti et al. (2014). They modelled a cluster of 100 disc-bearing stars, with equal masses and initially spatially distributed as a Plummer sphere. The results are very sensitive to disc viscosity. When this is high, disc spreading is fast enough to wash out any disturbance caused by distant encounters. They also found that disc radii are more significantly affected than disc masses by stellar star-disc encounters: when viscosity is low, distant encounters harden the mass surface density of the disc, shrinking it to smaller radii, but preserving most of the mass. Tidal truncation can therefore accelerate disc evolution, by decreasing the viscous timescale of the disc, and also accelerate grain growth in the inner regions, where gas density is increased. Note that this work is a first attempt, since many assumptions are not realistic: all stars have equal masses, and the resolution of the hydrodynamics is so low that viscosity is often boosted to unphysical values. Both the approaches briefly reported here confirm that disc in stellar clusters gravitational interactions affect disc radii more significantly than disc masses (Rosotti et al., 2014; Vincke, Breslau & Pfalzner, 2015).

1.4 External photoevaporation

An arguably more important mechanism is the photoevaporation caused by the energetic radiation permeating the young associations. When stars form in groups, EUV (Extreme Ultraviolet, $h\nu > 13.6$ eV) and FUV (Far Ultraviolet, $6 < h\nu < 13.6$ eV) radiation of the most massive stars heats the outer regions of protoplanetary discs, and can drive a gaseous flow from the disc surface (Hollenbach et al., 1994; Adams et al., 2004). Such a scenario has been very successful in explaining the so-called 'proplyds' (Johnstone, Hollenbach & Bally, 1998; Störzer & Hollenbach, 1999; Richling & Yorke, 2000), i.e. dark silhouette discs or cocoon-like structures observed in star forming regions. Such objects have been

observed for example in the ONC (O'Dell, Wen & Hu, 1993; Bally, O'Dell & McCaughrean, 2000), in Cyg OB2 (Wright et al., 2012), in Carina (Smith, Bally & Morse, 2003), and in other star forming regions showing massive OB associations (i.e. luminous sources of high energy radiation). When the UV flux impinging onto the discs is less severe than in these star forming regions, the effect of such mass loss on the evolution of protoplanetary discs, and the impact on their planet formation potential, is however rarely considered (see Section 3.1).

To be more quantitative, external photoevaporation can be summarised in three different regimes. When the EUV component is dominant, due to the proximity of a massive O star (e.g. θ^1C in the ONC), the EUV flux reaches the surface of the disc, heating it up to $\sim 10^4$ K. A completely ionised flow is formed, driving gas outwards in a spherical fashion and photoevaporating the disc (Hollenbach et al., 1994). The mass loss rate can be expressed by the approximated relation (Johnstone, Hollenbach & Bally, 1998; Adams, 2010):

$$\dot{M} \approx (9\times10^{-8} M_\odot/\mathrm{yr}) \left(\frac{\Phi}{10^{49}\,\mathrm{s}^{-1}}\right)^{1/2} \left(\frac{d}{10^{17}\,\mathrm{cm}}\right)^{-1} \left(\frac{R_\mathrm{d}}{30\,\mathrm{AU}}\right)^{3/2}, \tag{1.2}$$

where Φ is the EUV photon luminosity and d is the distance from the ionising source.

When the EUV flux is less severe, the FUV field can generate a neutral wind that is optically thick to the EUV radiation, since the FUV component has a larger penetrating depth than the EUV one. When this is the case, two different regimes may occur, depending on the disc size R_d. We define the gravitational radius R_g of the disc as the radius at which the thermal energy is equal to the gravitational binding energy (equivalently, as the radius at which the sound speed is equal to the escape velocity):

$$R_\mathrm{g} = \frac{GM_*\mu m_\mathrm{H}}{k_\mathrm{B}T} \approx 100\,\mathrm{AU} \left(\frac{T}{1000\,\mathrm{K}}\right)^{-1} \left(\frac{M_*}{M_\odot}\right), \tag{1.3}$$

where T is the temperature, M_* is the mass of the central star, and μ the mean molecular weight. When $R_\mathrm{d} > R_\mathrm{g}$, the wind is launched from both the surface and the outer radius of the disc (e.g. Johnstone, Hollenbach & Bally, 1998), and it reaches supersonic velocities in proximity of the disc surface. Such discs are defined to be supercritical. The mass loss rates can be computed by requiring that the wind velocity is roughly uniform (and equal to the sound speed), and that the column density of the wind to the FUV radiation is such that the optical depth is ~ 1 (Johnstone, Hollenbach & Bally, 1998; Adams et al., 2004). As derived in these two works, we can express the mass loss rate due to the impinging FUV radiation:

$$\dot{M} \approx (1.2\times10^{-7} M_\odot/\mathrm{yr}) \left(\frac{T}{600\,\mathrm{K}}\right)^{1/2} \left(\frac{R_\mathrm{d}}{100\,\mathrm{AU}}\right), \tag{1.4}$$

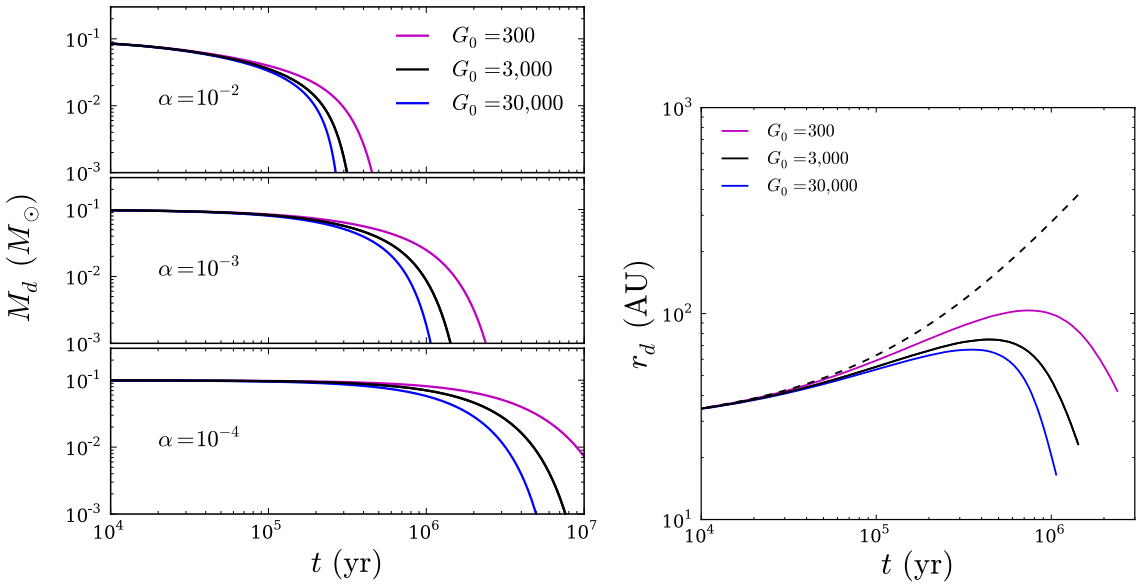

Fig. 1.6 Left panel: mass of discs embedded in different FUV ambient fields as a function of time for different values of disc viscosities. These solutions are obtained combining the mass loss rates by Adams et al. (2004) with an α-disc model. Right panel: disc outer radius in the same simulations, when $\alpha = 10^{-3}$. The dashed line represents the disc outer radius when no external photoevaporation is considered. Comparing the two plots, it is apparent that the disc is dispersed when photoevaporation dominates over viscous spreading and the disc shrinks, thus leading to shorter viscous timescales. Figures from Anderson, Adams & Calvet (2013).

where we have assumed a cross section at FUV wavelengths of $8 \times 10^{-22}\,\mathrm{cm}^2$ (Störzer & Hollenbach, 1999, see Chapter 6 for a detailed discussion on the cross section dependency on the dust properties within the flow).

However, moderate FUV fields are not able to heat up the outer regions of discs to high enough temperatures, such that $R_\mathrm{d} < R_\mathrm{g}$. Adams et al. (2004) have shown that when this is the case, the flow structure can be described by a non isothermal Parker wind, with the addition of a centrifugal term. This model uses the reasonable assumption that the mass loss rate from the outer rim of the disc dominates the mass loss rate from the surface of the disc (see the Appendix in Adams et al., 2004), where the gas is more embedded in the gravitational potential well of the central star. This regime will be thoroughly considered in Chapter 6. Since the outer regions of discs contain the bulk of the mass and since the rate of disc evolution is determined by the outer disc radius, such external winds have important implications for disc lifetimes and surface density profiles. Indeed, as noted by Clarke (2007) and confirmed by Anderson, Adams & Calvet (2013), such winds accelerate disc clearing not on account of the mass lost in the wind (which is a fraction of that accreted onto the star over the disc lifetime) but instead because they modify the disc's outer boundary, preventing disc spreading and keeping the viscous timescale relatively short (see Fig. 1.6). Anderson, Adams & Calvet (2013) have shown that even mild environments (with $N \sim 300 - 500$) can have a significant impact on the global evolution of protoplanetary discs, reducing their lifetime to $\sim 1 - 2\,\mathrm{Myr}$.

1.5 Structure of the thesis

In this thesis, I address different aspects of the impact of environment on the evolution of protoplanetary discs. The approach will very heterogeneous, and the covered topics will range over a wide spectrum of physical phenomena. In chapters 2 and 3 I focus on the 3D structure of a circumbinary disc misaligned to the binary plane. In particular, in chapter 2 I show that warp evolution in circumbinary protoplanetary discs is well described by simple 1D wave equations, by testing such a 1D model with 3D SPH simulations. In chapter 3 I apply the 1D model to transition discs, and show that a massive planet orbiting within the central cavity can be probed by a small warp in the outer disc.

Chapters 4 and 5 focus on the RW Aurigae binary system. In the first chapter I show that the morphology and gas kinematics of the system is due to a star-disc encounter, by comparing detailed observations with synthetic observations derived by post-processing SPH hydrodynamical simulations of the system. The second chapter contains new spectral

observations of the primary star RW Aur A, which I obtained in March, 2015. These observations shed a new light on the origin of the peculiar light curve of the system.

In chapter 6 I deal with the external photoevaporation mechanism. I construct a new model of FUV dominated photoevaporation in the subcritical regime, extending the parameter space explored in previous literature, and investigating how grain growth affects the mass loss rates. Finally, in chapter 7 I summarise the main results of the whole thesis, and present future prospects for the topics covered in the different chapters.

Chapter 2

Wave-like warp propagation in circumbinary discs: numerical simulations

This chapter is mostly based on the paper by Facchini, Lodato & Price (2013).

2.1 Introduction

Observational evidence of warped protoplanetary discs has grown in the last few years, as reported in Section 1.2.2. Analytic and semi-analytic theories of warp propagation have been developed in two different regimes (see Section 2.3): one where the warp evolves diffusively in a thin accretion disc with a diffusive coefficient inversely proportional to disc viscosity (Papaloizou & Pringle, 1983; Pringle, 1992; Ogilvie, 1999), and one where the warp propagates via bending waves in thick or inviscid discs (Papaloizou & Lin, 1995; Lubow & Ogilvie, 2000).

The diffusive case has been explored both analytically (Scheuer & Feiler, 1996; Pringle, 1996; Lubow, Ogilvie & Pringle, 2002) and numerically (Lodato & Pringle, 2007; Nixon & King, 2012). In particular, high resolution numerical simulations have been performed, obtaining a good agreement with the analytic theory in the linear and mildly non-linear regime (Lodato & Price, 2010).

The bending–wave regime has been less analysed. Analytic studies have given a description of the wave propagation in the linear regime (Lubow & Ogilvie, 2000, 2001; Lubow, Ogilvie & Pringle, 2002), and other studies have been accomplished on the non-linear case (Gammie, Goodman & Ogilvie, 2000; Ogilvie, 2006). Only a few poorly resolved numerical

simulations have been performed to date via SPH codes (Larwood & Papaloizou, 1997; Nelson & Papaloizou, 1999, 2000). More recently, Fragner & Nelson (2010) performed 3D simulations using a 3D grid code.

In this work we focus on warp propagation via bending waves in protostellar circumbinary discs. We test the linear regime with numerical simulations. In order to address this issue, we use a 1D ring code (as in Lubow, Ogilvie & Pringle, 2002) and full 3D SPH simulations. We find that the agreement between the linear theory and the simulations is good, even at very low viscosities. Finally, 3D simulations allow us to explore the non-linear regime, which has been poorly addressed so far.

The chapter is organised as follows. In Section 2.2 we derive a time independent approximation of the gravitational potential generated by the central binary and we extrapolate the torques to which the disc is subjected. In Section 2.3 we describe warp propagation in the linear regime. In Section 2.5 we describe the numerical setup used to perform the 3D SPH simulations and we report our main results both in linear and in non-linear regime. Finally, in Section 2.6 we draw our conclusions.

2.2 The binary - disc torque

In this Section we determine the gravitational potential generated by the binary. A similar analysis, restricted to binaries with extreme mass ratios, has been done by Nixon, King & Pringle (2011). Here, we generalise their results to arbitrary mass ratios. Similar derivations are present in a few other papers, such as Ivanov, Papaloizou & Polnarev (1999) and Nayakshin (2005).

We consider two stars with masses M_1 and M_2, that rotate in two circular orbits, on a plane described by the cylindrical polar coordinates (R,ϕ) and perpendicular to the $z-$axis. We place the origin of our coordinate system in the centre of mass. The geometry of the system, as well as the definition of various quantities of interest, is shown in Fig. 2.1. We denote with r_1 the distance between M_1 and the centre of mass, and similarly for r_2 and M_2. The distance between the two stars is $a = r_1 + r_2$. We finally place a test particle m in a generic position with coordinates (R,ϕ,z). We call s_1 and s_2 the distance between m and M_1 and m and M_2. We are focusing on a restricted three body problem in 3D space.

We now consider a reference frame S corotating with the two stars. In this particular system they are both at rest at $(r_1,\pi,0)$ and $(r_2,0,0)$, respectively. The potential in this reference frame is:

$$\Phi(R,\phi,z) = -G\left(\frac{M_1}{s_1} + \frac{M_2}{s_2}\right) - \frac{1}{2}\Omega_{\rm b}^2 R^2, \tag{2.1}$$

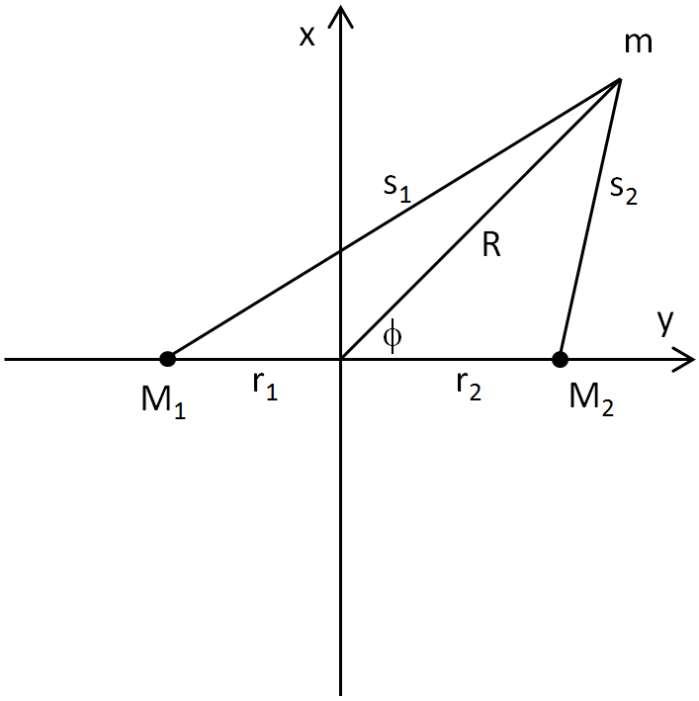

Fig. 2.1 The binary system in the corotating frame of reference centred in the centre of mass. M_1 and M_2 are the two stars, and m is the test particle. For simplicity in this figure we locate m in the (R,ϕ) plane. The quantity r_1 indicates the distance between M_1 and the centre of mass, and analogously for r_2 and M_2. The distances between $m-M_1$ and $m-M_2$ are called s_1 and s_2, respectively.

where Ω_b is the angular velocity of the binary, given by

$$\Omega_b^2 = \frac{G(M_1+M_2)}{a^3}. \tag{2.2}$$

In equation 2.1 the second term is due to the non-inertial nature of the reference frame, and it represents the centrifugal potential. The orbital frequency Ω_b is simply calculated from Kepler's third law. Finally it can be easily shown that:

$$\begin{aligned} s_1^2 &= r_1^2 + R^2 + 2r_1 R\cos\phi + z^2; \\ s_2^2 &= r_2^2 + R^2 - 2r_2 R\cos\phi + z^2. \end{aligned} \tag{2.3}$$

We now move to an inertial reference frame S', with the origin coincident with that of S. we do not have the centrifugal term anymore, and the ϕ angle undergoes the simple transformation $\phi \to \phi' = \Omega_b t$. In this frame we obtain the following gravitational potential:

$$\begin{aligned} \Phi(R,\phi'=\Omega_b t,z) = \quad & -G\frac{M_1}{(R^2+r_1^2+2r_1R\cos\Omega_b t+z^2)^{1/2}} \\ & -G\frac{M_2}{(R^2+r_2^2-2r_2R\cos\Omega_b t+z^2)^{1/2}}. \end{aligned} \tag{2.4}$$

This is the most general form of the gravitational potential of a circular binary. We could now expand the above relation in a Fourier series with azimuthal wavenumber σ to distinguish the various contributions to the potential. In order to avoid it, we make the assumption, as it has been made by Nixon, King & Pringle (2011) and earlier by e.g. Lubow & Ogilvie (2001), that the perturbations to the potential of the $\sigma \geq 1$ modes are oscillatory, and if we are far enough from resonances, they will have no long-term secular effect. Long-term effects on the orbit of the test particle, and hence eventually on the disc, come from the only zero-frequency term. Since we are interested in the secular dynamics of the disc, we can just consider this $\sigma = 0$ mode (Bate et al., 2000).

In order to calculate this time-independent term we use the fact that physically this $\sigma = 0$ term is given by replacing the two masses M_1 and M_2 with the same masses spread uniformly over their orbit, i.e. two rings of mass M_1 and M_2 and radius r_1 and r_2 in the (R,ϕ) plane (see Nixon, King & Pringle, 2011). The gravitational potential for the generic test particle is then:

$$\Phi(R,z) = -\frac{GM_1}{2\pi}\int_0^{2\pi}\frac{d\phi}{\tilde{s}_1} - \frac{GM_2}{2\pi}\int_0^{2\pi}\frac{d\phi}{\tilde{s}_2}, \tag{2.5}$$

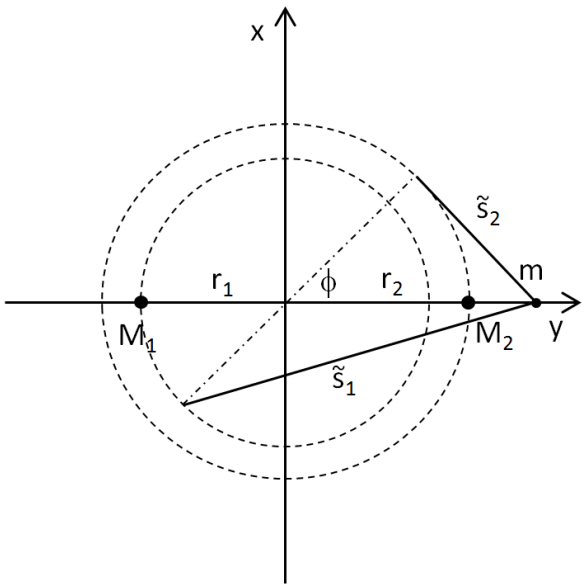

Fig. 2.2 The binary system in an inertial frame of reference centred in the centre of mass. M_1 and M_2 are now spread in two massive annuli with radii r_1 and r_2, respectively, and m is the test particle, positioned at $(R,0,z)$ (we place it at $\phi = 0$ because of the rotational symmetry about the z-axis of the problem). The new $\tilde{s}_1$ and $\tilde{s}_2$ define the distances between a generic point of the two massive annuli and the test particle.

where

$$\tilde{s}_1^2 = R^2 + r_1^2 + z^2 + 2Rr_1\cos\phi,$$
$$\tilde{s}_2^2 = R^2 + r_2^2 + z^2 - 2Rr_2\cos\phi. \tag{2.6}$$

The new $\tilde{s}_1$ and $\tilde{s}_2$ define the distances between a generic point of the two massive annuli and the test particle positioned at $(R,0,z)$ (we place it at $\phi = 0$ because of the rotational symmetry about the z-axis of the problem, see Fig. 2.2), while s_1 and s_2 indicate the distances between the two stars at rest in the corotating reference frame and a generic particle.

We introduce the factor $\eta = M_1M_2/M^2$ and the total mass $M = M_1 + M_2$. We recall that $a = r_1 + r_2$. If we now expand equation 2.5 in powers of r_1/R, r_2/R and z/R, keeping terms only up to second order we find:

$$\Phi(R,z) = -\frac{GM}{R} - \frac{GM\eta a^2}{4R^3} + \frac{GMz^2}{2R^3} + \frac{9}{8}\frac{GM\eta a^2 z^2}{R^5}.$$

We notice that by taking the limits $\eta \to M_2/M_1$ and $M \to M_1$ we obtain the equivalent of equation 4 of Nixon, King & Pringle (2011), in which they calculated the same gravitational potential but in the simplified case where $M_2 \ll M_1$.

The perturbations affecting the disc particles can be expressed in terms of the orbital frequency Ω, the vertical oscillation frequency Ω_z, and the epicyclic frequency κ (see Section 2.3). Their definition follows below:

$$\Omega^2 = \frac{1}{R}\frac{\partial \Phi}{\partial R}\bigg|_{z=0}, \tag{2.7}$$

$$\Omega_z^2 = \frac{\partial^2 \Phi}{\partial z^2}\bigg|_{z=0}, \tag{2.8}$$

$$\kappa^2 = 4\Omega^2 + 2R\Omega\frac{d\Omega}{dR} = 4\Omega^2\left[1 + \frac{1}{2}\frac{d\ln\Omega}{d\ln R}\right]. \tag{2.9}$$

For the binary potential of equation 2.7 we obtain:

$$\Omega^2 = \frac{GM}{R^3} + \frac{3}{4}\frac{GM\eta a^2}{R^5}, \tag{2.10}$$

$$\Omega_z^2 = \frac{GM}{R^3} + \frac{9}{4}\frac{GM\eta a^2}{R^5}, \tag{2.11}$$

$$\kappa^2 = \frac{GM}{R^3} - \frac{3}{4}\frac{GM\eta a^2}{R^5}. \tag{2.12}$$

To first order, thus,

$$\frac{\Omega_z^2 - \Omega^2}{\Omega^2} = \frac{3}{2}\frac{\eta a^2}{R^2}, \tag{2.13}$$

$$\frac{\kappa^2 - \Omega^2}{\Omega^2} = -\frac{3}{2}\frac{\eta a^2}{R^2}. \tag{2.14}$$

We will use this approximation throughout the whole chapter.

In summary, in this Section we have deduced the time independent term of the gravitational potential of a generic binary system, formed by two different stars of mass M_1 and M_2, in the hypothesis that the disc particles rotate at a large radius ($R \gg r_1,\ r_2$) and low height ($z \ll R$).

2.3 Theory of wave-like warp propagation

We consider here the propagation of warps in thin, almost Keplerian accretion discs. The quantities that define their dynamics are the angular velocity $\Omega(R)$, the surface density $\Sigma(R)$ and the angular momentum per unit area $\mathbf{L}(R)$. H describes the scale height of the disc, and

it is related to the sound speed c_s via $H = c_s/\Omega$. We assume here that the disc is composed of a series of flat, infinitesimally thin rings, each of which can be oriented arbitrarily in space. A single ring at radius R is thus described by two angles: the tilt angle β with respect to the z axis, and the azimuthal angle γ that defines the orientation of the tilt with respect to an arbitrary axis, perpendicular to z. If β varies with R, we will have a warped disc. If γ varies with radius the disc is additionally twisted. Here, R should be intended as a spherical coordinate, even though at each radius the disc is thin in the direction perpendicular to the local rotation plane. Therefore we define in complex notation the tilt of the disc $W(R,t)$ at each radius as $W(R,t) = \beta(R,t)\exp[i\gamma(R,t)]$ (Pringle, 1996). These quantities are related to the specific angular momentum through $\mathbf{l}(R) = \mathbf{L}(R)/L(R) = (\cos\gamma\sin\beta, \sin\gamma\sin\beta, \cos\beta)$.

We consider a standard α-prescription for the viscosity: $\nu = \alpha c_s H$ (Shakura & Sunyaev, 1973).

Warp propagation can be described in two different regimes. Papaloizou & Pringle (1983) had already suggested that whenever $\alpha < H/R < 1$ warps would probably propagate via bending waves, whereas when $H/R < \alpha < 1$ the equations describing the evolution would be diffusive (Pringle, 1992). These results have been confirmed analytically; Papaloizou & Lin (1995) derived the equations describing the evolution in the case $\alpha < H/R < 1$, and they confirmed that they evolve via wave equations. Equivalent formulations have been derived later by Demianski & Ivanov (1997) and Lubow & Ogilvie (2000) (hereafter, Lubow & Ogilvie (2000)). Throughout this work we use the formulation by Lubow & Ogilvie (2000).

Lubow & Ogilvie (2000) have shown that when the disc is nearly Keplerian and non self-gravitating, the linearised equations for bending waves (with azimuthal wavenumber $m = 1$) may be written as:

$$\Sigma R^2 \Omega \frac{\partial \mathbf{l}}{\partial t} = \frac{1}{R}\frac{\partial \mathbf{G}}{\partial R} + \mathbf{T}, \tag{2.15}$$

and

$$\frac{\partial \mathbf{G}}{\partial t} + \left(\frac{\kappa^2 - \Omega^2}{\Omega^2}\right)\frac{\Omega}{2}\mathbf{e}_z \times \mathbf{G} + \alpha\Omega\mathbf{G} = \Sigma R^3 \Omega \frac{c_s^2}{4}\frac{\partial \mathbf{l}}{\partial R}, \tag{2.16}$$

where

$$\mathbf{T} = -\Sigma R^2 \Omega \left(\frac{\Omega_z^2 - \Omega^2}{\Omega^2}\right)\frac{\Omega}{2}\mathbf{e}_z \times \mathbf{l}, \tag{2.17}$$

where $\mathbf{e}_z$ is the unit vector perpendicular to the binary orbit.

In our assumptions the warp is small, therefore $l_x, l_y \ll 1$ and $l_z \approx 1$. Thus, by considering $l_z = 1$, we can consider the equations on the xy-plane only. The term $2\pi\mathbf{G}$ is the internal torque and $\mathbf{T}$ the external torque density. The external torque is due to the lack of spherical symmetry in the potential, and is proportional to the term $\Omega_z^2 - \Omega^2$ (equation 2.17). Instead, equation 2.16 shows that the internal torque is mediated by horizontal epicyclic motions. The

term proportional to α tends to dissipate the waves through an exponential factor. Finally, note that the external torque is related to the precession frequency of the ring $\Omega_{\rm p}$, as we know it should be from simple mechanics (Lodato & Pringle, 2006). By knowing that $\mathbf{L} = \Sigma R^2 \Omega \mathbf{l}$ we can rewrite equation 2.17 as:

$$\mathbf{T} = \frac{-(\Omega_z - \Omega)(\Omega_z + \Omega)}{\Omega^2} \frac{\Omega}{2} \mathbf{e}_z \times \mathbf{L} \approx \Omega_{\rm p} \times \mathbf{L}. \tag{2.18}$$

If $\Omega_z \approx \Omega$, then $\Omega_{\rm p} = (\Omega - \Omega_z)\mathbf{e}_z$ (Nixon, King & Pringle, 2011).

A different but equivalent set of equations can be used by defining the dimensionless complex variable $W(R,t) = l_x + i l_y$ and the complex variable $G(R,t) = G_x + i G_y$. We can thus rewrite equation 2.15 and 2.16 as:

$$\Sigma R^2 \Omega \left[\frac{\partial W}{\partial t} + \left(\frac{\Omega_z^2 - \Omega^2}{\Omega^2} \right) \frac{i\Omega}{2} W \right] = \frac{1}{R} \frac{\partial G}{\partial R}, \tag{2.19}$$

and

$$\frac{\partial G}{\partial t} + \left(\frac{\kappa^2 - \Omega^2}{\Omega^2} \right) \frac{i\Omega}{2} G + \alpha \Omega G = \Sigma R^3 \Omega \frac{c_{\rm s}^2}{4} \frac{\partial W}{\partial R}. \tag{2.20}$$

Let us consider the propagation velocity of the waves. By neglecting the external torque and the non-Keplerian term we can obtain a first order approximated dispersion relation (Nelson & Papaloizou, 1999):

$$\omega = \frac{1}{2} [i\alpha\Omega \pm (c_{\rm s}^2 k^2 - \alpha^2 \Omega^2)^{\frac{1}{2}}], \tag{2.21}$$

where k is the radial wavenumber and ω is the wave frequency. Therefore if the disc is inviscid ($\alpha = 0$) the warp propagates as a non-dispersive wave with wave speed $c_{\rm s}/2$. Moreover, propagation becomes purely diffusive in the limit $|\omega| \ll \alpha\Omega$. Note that in the Keplerian limit ($\Omega = \Omega_z = \kappa$) equations 2.15 and 2.16 explicitly tend to a diffusive equation when this condition is verified (i.e. when the third term of the l.h.s. of equation 2.16 dominates over the first two).

Finally, Lubow, Ogilvie & Pringle (2002) have shown that in the inviscid case the dispersion relation associated to equation 2.15 and 2.16 is given by:

$$\left[\omega - \left(\frac{\Omega^2 - \Omega_z^2}{2\Omega} \right) \right] \left[\omega - \left(\frac{\Omega^2 - \kappa^2}{2\Omega} \right) \right] = \frac{c_{\rm s}^2}{4} k^2. \tag{2.22}$$

In the case of $\omega = 0$, whenever $\kappa^2 - 2\Omega^2 + \Omega_z^2 = 0$, which is the case for our binary potential, the spatial configuration that the disc will reach is an evanescent wave. We shall see that this theoretical prediction made by Lubow, Ogilvie & Pringle (2002) is verified by our results.

Finally, note that in this Section we have considered the linear case only. Some efforts have been spent in the last decade to cover the non-linear case in Keplerian and nearly Keplerian discs, both in the diffusive regime (Ogilvie, 1999; Lodato & Price, 2010) and in the wave-like one (Ogilvie, 2006).

2.4 Time-dependent evolution: a 1D model

In this Section we describe and use a 1D model for warp propagation via bending waves in a disc subject to a binary torque. We consider R as the only spatial variable of the system. The disc is discretised into a set of thin annuli that can be tilted and interact with one another via pressure and viscous forces. In this dynamical evolution, we neglect the dependence of Σ on time. In fact, from the dispersion relation of the wave equations we know that for low viscosity discs, bending waves propagate on a timescale $t_{\rm dyn} = 2R/c_{\rm s}$, whereas the viscous evolution of Σ occurs on a timescale $t_\nu = R^2/\nu$. Therefore:

$$\frac{t_{\rm dyn}}{t_\nu} = \frac{2R\nu}{c_{\rm s}R^2} = 2\alpha\frac{H}{R}. \tag{2.23}$$

Since we know that $\alpha < H/R \ll 1$ we can neglect the evolution of Σ.

Moreover, we neglect the angular momentum variations of the binary, which is affected by the gravitational potential of the disc. We do not consider the back-reaction of the disc onto the binary angular momentum because we focus on low mass discs, where their angular momentum is negligible compared to the binary one (this back-reaction is considered in Foucart & Lai 2013).

In order to compute the evolution we move to four dimensionless differential equations from equations 2.15 and 2.16. We use the following parametrisation: $R = R_{\rm in}x$, $\Omega = \Omega_{\rm in}x^{-3/2}$, $\Sigma = \Sigma_{\rm in}x^{-p}$, $t = \Omega_{\rm in}^{-1}(H_{\rm in}/R_{\rm in})^{-1}\tau$, $\mathbf{l} = W_\infty\lambda$ and $\mathbf{G} = G_{\rm in}\Gamma$. Then, we set $G_{\rm in} = \Sigma_{\rm in}R_{\rm in}^4\Omega_{\rm in}^2(H_{\rm in}/R_{\rm in})W_\infty$. With these definitions, we obtain the following set of 4 equations:

$$\frac{\partial\lambda_x}{\partial\tau} = x^{p-3/2}\frac{\partial\Gamma_x}{\partial x} + \chi x^{-7/2}\lambda_y, \tag{2.24}$$

$$\frac{\partial\lambda_y}{\partial\tau} = x^{p-3/2}\frac{\partial\Gamma_y}{\partial x} - \chi x^{-7/2}\lambda_y, \tag{2.25}$$

$$\frac{\partial \Gamma_x}{\partial \tau} + \alpha \frac{R_{\rm in}}{H_{\rm in}} x^{-3/2} \Gamma_x + \chi x^{-7/2} \Gamma_y = x^{3/2-p} \left(\frac{c}{2}\right)^2 \frac{\partial \lambda_x}{\partial x}, \tag{2.26}$$

$$\frac{\partial \Gamma_y}{\partial \tau} + \alpha \frac{R_{\rm in}}{H_{\rm in}} x^{-3/2} \Gamma_y - \chi x^{-7/2} \Gamma_x = x^{3/2-p} \left(\frac{c}{2}\right)^2 \frac{\partial \lambda_y}{\partial x}, \tag{2.27}$$

where c is the dimensionless sound speed ($c = x^{-3/4}$ in this chapter), and

$$\chi = \frac{3}{4} \eta \frac{(a/R_{\rm in})^2}{H_{\rm in}/R_{\rm in}}. \tag{2.28}$$

All the physics is included in two parameters: $\alpha/(H_{\rm in}/R_{\rm in})$ and χ. The first one is the measure of the importance of viscous and pressure effects, the second one determines the magnitude of the external torque due to the binary potential with respect to pressure forces. The parameter $H_{\rm in}/R_{\rm in}$ is a scale parameter determining the speed of the temporal evolution.

Lubow, Ogilvie & Pringle (2002) solved the same problem for the Lense-Thirring case with a different but equivalent set of equations in the complex domain. We prefer to use our equations, because they show the dependence of the evolution on the physical parameters more transparently. However, we use their result as an important comparison. By implementing the Lense-Thirring torque, and by setting the exact same set of parameters as they did, we obtain their same result for the disc tilt shape. This confirms the equivalence of the two sets of equations.

2.4.1 Code and boundary conditions

The numerical code we use to solve equations 2.24-2.27 implements the same numerical algorithm used by Lubow, Ogilvie & Pringle (2002). We consider Γ to be defined at N logarithmically distributed grid points (typically $N = 1001$, for the inviscid simulations we used $N = 4001$), and λ to be defined at the half grid points. We opt for a logarithmically distributed spatial grid because the torque is much stronger at the inner edge. In this way we can proceed with a leapfrog algorithm. The tracking of the evolution can be read in Section 4.1 of Lubow, Ogilvie & Pringle (2002).

2.4.2 Results

Henceforth in the whole chapter we use $p = 1/2$, since for this surface density profile we can compare our numerical results with the analytical solution of the inviscid case reported in Facchini, Lodato & Price (2013). We perform a first generic simulation with the following set of parameters: $(H_{\rm in}/R_{\rm in}) = 0.1$, $\alpha = 0.05$, $\eta = 0.25$ and $(a/R_{\rm in}) = 0.5$. We recall that

$\eta = 0.25$ corresponds to the case $M_1 = M_2$. We make these choices because $H_{\rm in}/R_{\rm in} = 0.1$ is the typical value for protostellar discs, when $\alpha = 0.05$ we expect a low-viscosity behaviour, $M_1 = M_2$ gives a sizable torque, and finally $a/R_{\rm in} = 0.5$ makes the approximation of a time independent gravitational potential reasonable. In the whole Section we will then use: $x_{\rm in} = 1$, $x_{\rm out} = 90$ and $W_\infty = 1$. The time unit will naturally be $\Omega_{\rm in}^{-1}$.

We consider a disc initially aligned with the binary plane in the inner parts, and misaligned in the outer parts. Thus as an initial condition we take $\lambda_x = 0$ for $x \leq 18$, $\lambda_x = \frac{1}{2}\{1 + \sin[\pi(x-20)/4]\}$ for $18 \leq x \leq 22$, and $\lambda_x = 1$ for $x \geq 22$ (Lubow, Ogilvie & Pringle, 2002). λ_y is initially set to 0. In this way at $t = 0$ we just have a tilt, with no twist. In other terms, $\gamma(x, t = 0) = 0$ at each radius.

The evolution of the warp in this case is shown in Fig. 2.3. It is apparent that the discontinuity does propagate inwards and outwards as a bending wave. As the inwardly propagating wave reaches the inner edge, it bounces back and reacts to the strong external torque due to the binary, until it forms a stationary wave reaching a steady state on a sound crossing timescale. The outwardly travelling discontinuity keeps on propagating throughout the whole simulation. In the top panel of Fig. 2.3 we report the tilt evolution, where the tilt is defined as $\sqrt{\lambda_x^2 + \lambda_y^2}$ (normalised at 1 at infinity) up to a computational time $t = 4000$. The bottom panel of Fig. 2.3 shows the same simulation up to $t = 20000$. These figures do not show the information about the twist, but we will analyse it later in this Section. Finally, note that the waves propagate with a velocity $\approx c_{\rm s}/2$, as predicted by the dispersion relation in the low-viscosity case. From the figures we can observe small ripples propagating behind the outwardly travelling wave front. These are given by small numerical instabilities and are damped away by viscous interactions in almost a simulation time. We have verified that they can be reduced by increasing the spatial resolution. We have performed simulations with a set of initial conditions (e.g. an initially tilted untwisted disc), and the final state of the disc shape we obtain does not depend on them.

We have then explored the parameters space by modifying the two parameters governing the physics of the system: χ and $\alpha/(H_{\rm in}/R_{\rm in})$. By modifying χ, we change the physical parameters of the binary system, either the distance between the two stars or the ratio between the two masses. Fig. 2.4 shows the tilt evolution when $a/R_{\rm in} = 0.1$, $\eta = 0.25$, $H_{\rm in}/R_{\rm in} = 0.1$ and $\alpha = 0.05$. The disc edge lies further away from the binary (the inner radius is larger than the tidal truncation radius). This choice is equivalent to reducing the binary mass ratio and keeping the inner radius fixed. In this case, the external torque due to the non spherical symmetry of the potential is reduced, and therefore the disc tends to stay misaligned with respect to the binary plane. In Fig. 2.5 we portray two simulations with different values of viscosity. The top panel has $\alpha = 0.01$, the bottom one $\alpha = 0.6$, while the other

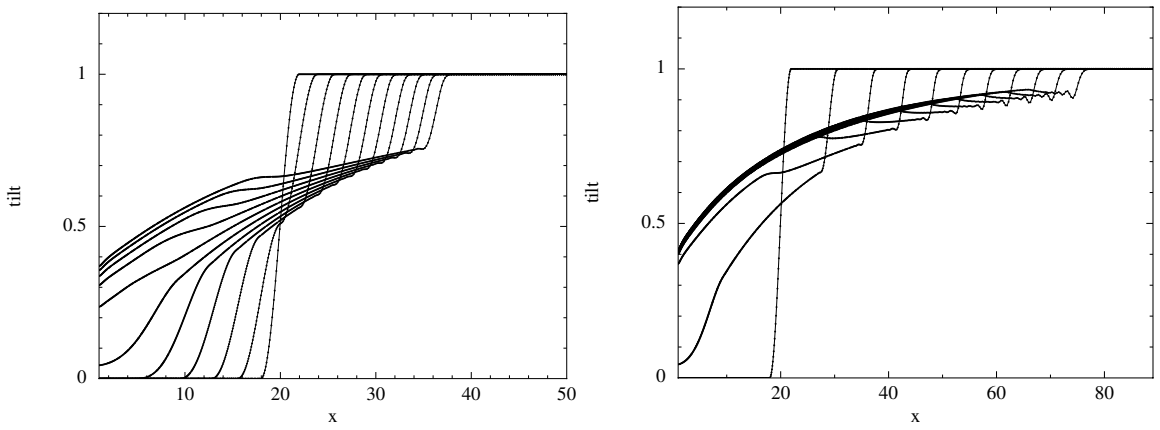

Fig. 2.3 Tilt evolution as a function of radius of an initially warped protostellar circumbinary disc in the linear low-viscosity regime, given the following set of parameters: $(H_{\rm in}/R_{\rm in}) = 0.1$, $\alpha = 0.05$, $\eta = 0.25$ and $(a/R_{\rm in}) = 0.5$. We recall that $\eta = 0.25$ corresponds to $M_1 = M_2$. Left panel: early evolution of the tilt, shown at 11 equally spaced times $t = 0$, 400, 800,...,4000. Right panel: late evolution of the the tilt at 11 equally spaced times $t = 0$, 2000, 4000,...,20000.

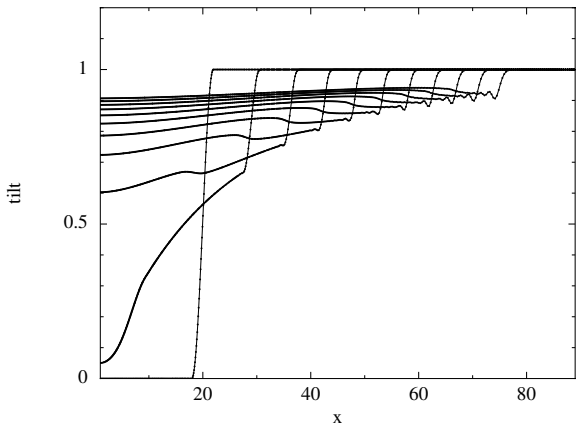

Fig. 2.4 Tilt evolution as a function of radius at 11 equally spaced times $t = 0$, 2000, 4000,...,20000 with $(H_{\rm in}/R_{\rm in}) = 0.1$, $\alpha = 0.05$, $\eta = 0.25$ and $(a/R_{\rm in}) = 0.1$.

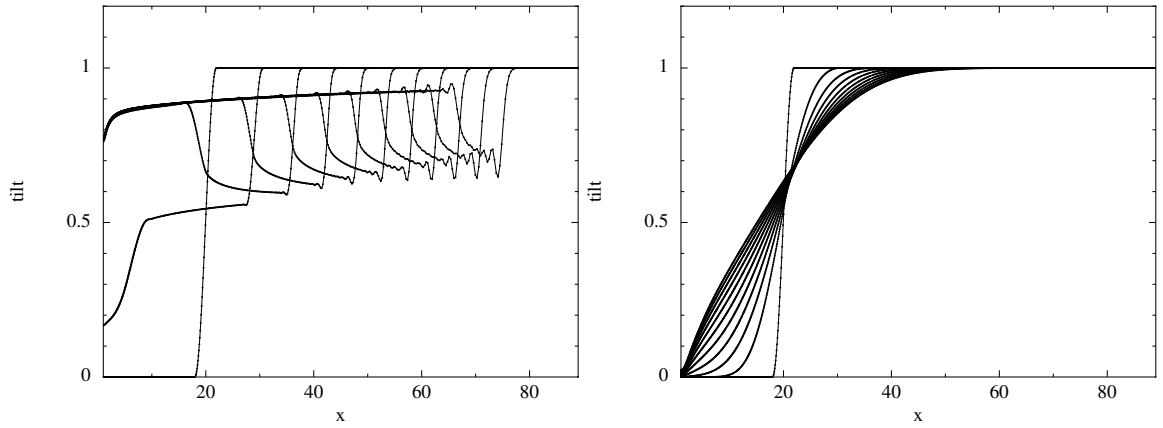

Fig. 2.5 Left panel: tilt evolution for an initially warped disc with $(H_{\rm in}/R_{\rm in}) = 0.1$, $\alpha = 0.01$, $\eta = 0.25$ and $(a/R_{\rm in}) = 0.5$ at 11 equally spaced times $t = 0$, 2000, 4000,...,20000. Right panel: tilt evolution for the same disc with $\alpha = 0.6$.

parameters are $a/R_{\rm in} = 0.5$, $\eta = 0.25$ and $H_{\rm in}/R_{\rm in} = 0.1$. The second one lies in the diffusive regime ($H/R < \alpha < 1$), and it shows its characteristic behaviour. We can note two relevant differences between the two panels. First, in the diffusive simulation the disc tends to align with the binary plane in the inner parts, as already illustrated in previous works (Lodato & Pringle, 2006, 2007). Secondly, in this case the evolution of the shape of the disc slows down significantly, since the dispersion relation does strongly depend on α.

So far we have not specified how the final solutions differ from one another with respect to the phase. In Fig. 2.6 we illustrate the phase (as a function of radius) for the two cases reported in Fig. 2.5. We can observe that both discs are twisted in the inner regions. Moreover, the magnitude of the twist increases as the viscosity increases. The twisting of the disc is therefore strongly correlated to viscosity (in fact viscosity is the only physical quantity that can induce shear forces in this case). The limit case is $\alpha = 0$; inviscid discs present no twist at all for $t \to \infty$, independently of the initial condition.

2.5 Full 3D simulations

Hitherto in order to describe warp propagation in protostellar circumbinary discs, we have made many approximations. We recall them here. First of all, we have considered the gravitational potential generated by the two central stars as time independent. In order to do so, we assumed that the inner edge of the disc was quite far from the binary, $r_1/R_{\rm in} < 1$ and $r_2/R_{\rm in} < 1$. Secondly, in the thin-disc approximation, we have considered $\partial_t \Sigma = 0$, because the viscous time scale is much longer than the sound crossing time, which is the

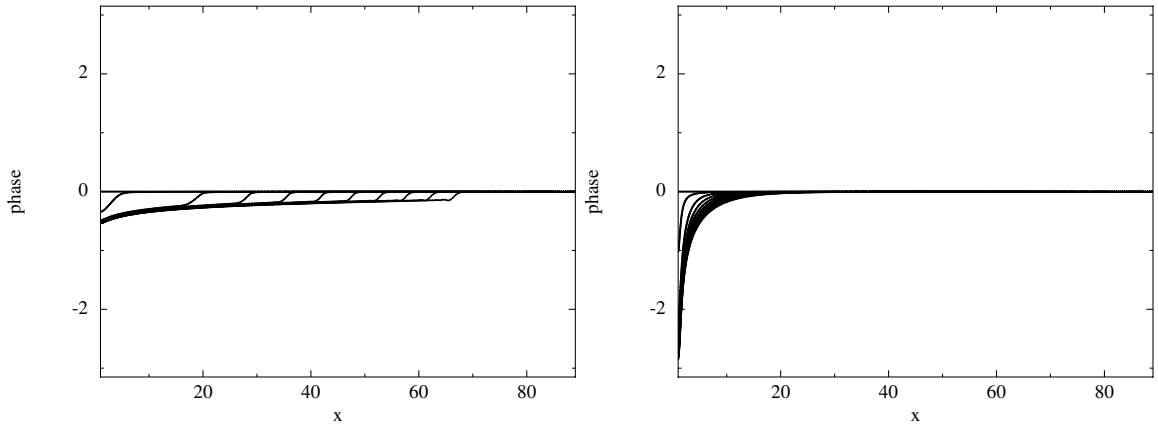

Fig. 2.6 Phase evolution of the same discs portrayed in Fig. 2.5 (top panel: $\alpha = 0.01$; bottom panel: $\alpha = 0.6$). The twist of the disc correlates with the viscosity: the more viscous the disc is, the more twisted it gets.

warp evolution time in the wave-like regime. Then, we have considered the linear (small amplitude) waves propagating with the single $m = 1$ mode.

3D hydrodynamical simulations allow us to model our physical systems without making any of the assumptions listed above. First of all, we can implement the rotation of the two central stars directly without estimating the time-independent contribution of their gravitational potential. The particles describing the disc flow will be subject to the full potential generated by the binary. Secondly, we do not have to make any assumption about the warp dynamics, and especially the assumption of linear perturbations. By comparing the results of the 3D simulations with the results obtained by the 1D code, we will be able to check whether our assumptions were reasonable, and in which parameters range we can consider them valid.

2.5.1 SPH and viscosity

We perform our 3D simulations by using a smoothed particle hydrodynamics (SPH) code (see Price, 2012, for a recent review). We have used the PHANTOM code by Daniel Price (see e.g. Lodato & Price, 2010; Price & Federrath, 2010), which has been shown to perform well in dealing with warp propagation in the diffusive (non self-gravitating) regime (see Lodato & Price, 2010; Nixon, King & et al., 2012, for two recent applications). As already mentioned in the introduction, SPH codes have already been used to simulate warp propagation in the bending-wave (thick disc) regime, but with very low resolution (Nelson & Papaloizou, 1999, 2000).

In this Section we shall not go through SPH theory. We will just describe how we implemented an isotropic viscosity in the code. We know that SPH codes implement an artificial viscosity in order to spread discontinuities over a few smoothing lengths. It has been known for some time (Murray, 1996) that the artificial terms in SPH can be understood straightforwardly as numerical representations of second derivatives of the velocity, and this makes viscosity act also when there is a purely shear flow, as in an accretion disc. The α parameter for the shear viscosity is related to the artificial one ($\alpha_{\rm art}$) by:

$$\alpha_{\rm SS} = \frac{1}{10}\alpha_{\rm art}\frac{\bar{h}}{H}, \tag{2.29}$$

where $\bar{h}$ is the averaged smoothing length at radius R and H the scale-height of the disc at the same radius[1]. Lodato & Price (2010) showed excellent agreement between this relation and the outcome of their simulations. The notation $\alpha_{\rm SS}$ is used to discriminate between the directly implemented physical viscosity (see below) and the physical viscosity due to the artificial one. Thus, we could simulate the physical viscosity of our discs by using the artificial one. However, in order to keep a uniform value for $\alpha_{\rm SS}$, we would need a constant ratio $\bar{h}/H$ in the disc. In the case of power-law density and sound speed profiles, this requires the two exponents to be related by $p+2q=3$ (e.g. $p=1.5$, $q=0.75$). My choice for these two parameters is different though, since we preferred to use $p=0.5$ in order to compare our 1D code with Lubow, Ogilvie & Pringle (2002). To mimic viscosity, in this work we used an alternative formulation proposed by Flebbe, Muenzel & et al. (1994), where we evaluate directly the stress tensor in the Navier-Stokes equation. We preferred this formulation to the similar one by Español & Revenga (2003) because the former has been well tested by Lodato & Price (2010), and the latter does not conserve angular momentum. By this method, we have direct control of the viscous terms, since we set the shear viscosity by hand:

$$\nu = \alpha c_{\rm s}^2(R)/\Omega(R), \tag{2.30}$$

where α is the chosen value of the viscosity parameter, and the profiles of the sound speed $c_{\rm s}$ and of the (Keplerian) angular velocity Ω are prescribed functions of R. Moreover, we can set the bulk viscosity to 0. In this work, however, we still keep a small amount of artificial viscosity in order to correctly dissipate shocks if they are present and prevent particle interpenetration using the Morris & Monaghan (1997) switch. Moreover, when the physical α is set to 0 in order to simulate an inviscid motion, we will need an artificial viscosity in order to prevent chaotic motions of SPH particles (Price & Federrath, 2010) that

[1] In all the simulation presented in this chapter, $\bar{h}/H < 0.5$ for $R > 6a$ (see Section 2.5.2 for the setup of the simulations), thus the disc is partially resolved in the vertical direction.

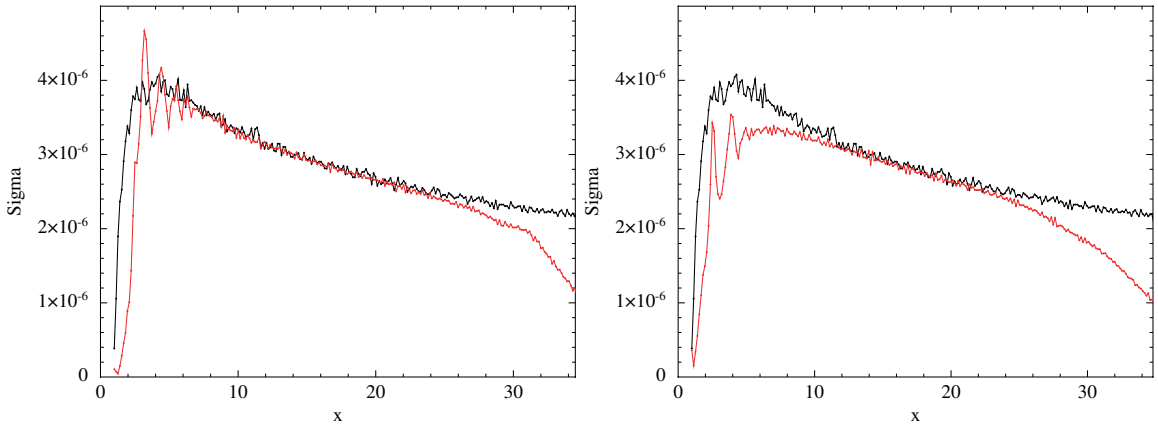

Fig. 2.7 Left panel: evolution of Σ for an initially untwisted tilted disc with $\alpha = 0.05$, $H_{\rm in}/R_{\rm in} = 0.1$, $\eta = 0.25$, $R_{\rm in} = a$ and $\beta_\infty = 5^\circ$. Right panel: evolution of Σ for the same setup but with $\alpha = 0.2$. The black lines refer to $t = 0$, while the red lines to $t = 4000$, which is the end of both simulations.

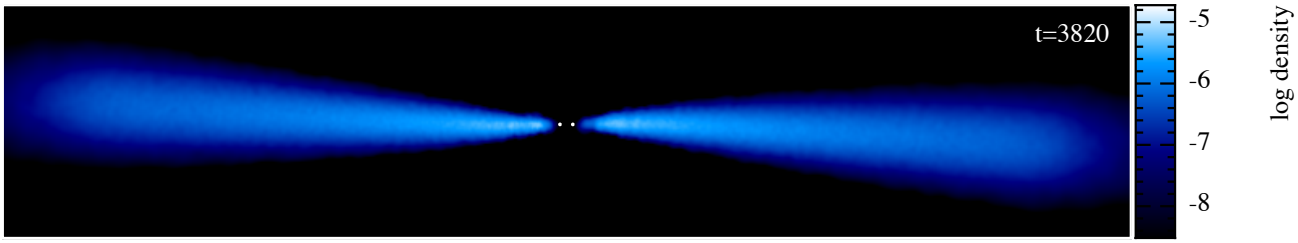

Fig. 2.8 Cross Section of the inner regions of the disc in the SPH calculations at a resolution of 1 million particles with $\alpha = 0.05$, $H_{\rm in}/R_{\rm in} = 0.1$, $\eta = 0.25$ and $\beta_\infty = 5^\circ$ at $t = 3820$. The two white points represent the two central stars. The colour scale indicates density in code units.

would increase the effective viscosity instead of reducing it. In the simulations presented in this Section, we have used $\alpha_{\rm art,max} = 0.5$ and $\alpha_{\rm art,min} = 0.01$ (unless specified otherwise), where the value of $\alpha_{\rm art}$ between this two values is estimated via the Morris and Monaghan switch. The Vonneumann & Richtmyer (1950) $\beta_{\rm art}$ parameter has been set equal to 2.

Finally, note that in our simulations we did not compute the energy equation. We adopted a locally isothermal equation of state (set by the q parameter assigned to the local sound-speed).

2.5.2 Numerical setup and initial conditions

We model the two central stars as sink particles. i.e. non-gaseous particles with appropriate boundary conditions (Bate, Bonnell & Price, 1995). We assign an accretion radius to each of

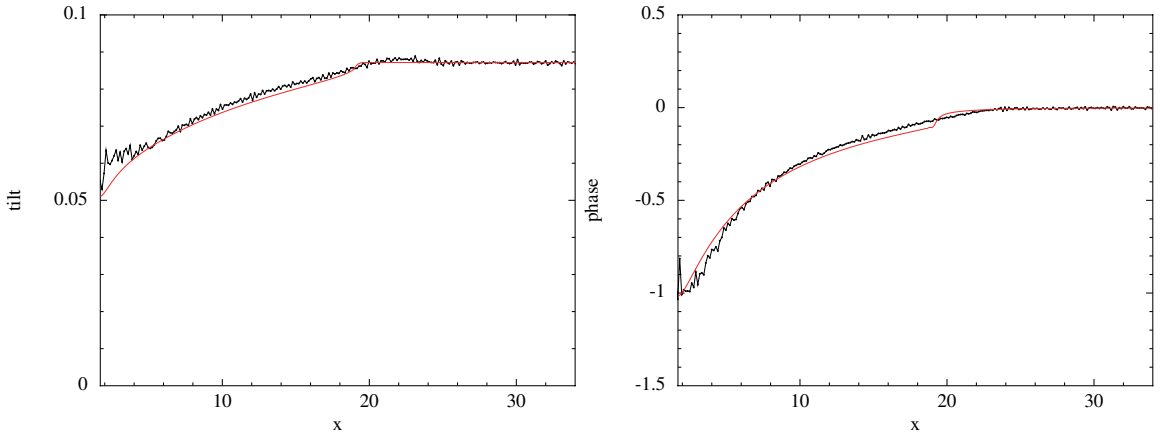

Fig. 2.9 Tilt and phase evolution of an initially untwisted tilted disc, with $\eta = 0.25$, $(H_{\rm in}/R_{\rm in}) = 0.1$, $\alpha = 0.05$, $\beta_\infty = 5^\circ$ and $N = 1$ million at $t = 2000$. The red line depicts the corresponding 1D simulation, where the inner edge of the disc has been set equal to $R_{\rm t} = 1.7a$.

the two sink particles, i.e. the radius within which we can consider the fluid as accreted onto the star. This feature allows us not to follow the dynamics of gas particles too close to the binary system, since it would be computationally expensive. We assign an accretion radius of $0.05R_{\rm in}$ to each star.

We have run simulations with different resolutions. We go from $N = 10^5$ to $N = 2 \cdot 10^6$, where N is the number of particles used. Once we have assigned the values of the physical parameters of the system (see below), we distribute the particles so that the disc attains a prescribed initial density profile. We assign each particle a radius dependent sound-speed $c_{\rm s}$, where $c_{\rm s} \propto R^{-q}$ as usual. We then distribute the particles in the vertical direction, in order for the density to have a Gaussian profile in the z-direction. The scale-height is set to $H = c_{\rm s}/\Omega$. Finally, the initial angular velocity is assigned by taking into account pressure contributions:

$$v_\phi = v_{\rm K} \left[1 - (p+2q) \left(\frac{c_{\rm s}}{v_{\rm K}} \right)^2 \right]^{1/2}, \tag{2.31}$$

where $v_{\rm K} = \sqrt{GM/R}$ is the usual Keplerian velocity.

As initial condition, we implement a surface density equal to:

$$\Sigma(R) = \Sigma_0 R^{-p} \left(1 - \sqrt{\frac{R_{\rm in}}{R}} \right), \tag{2.32}$$

where p is the usual coefficient introduced in Section 2.4.2. Note that this is slightly different from the pure power law used above in Section 2.4.2. We use the above relation because

otherwise the inner gas would be pushed inwardly by the strong pressure gradient at the inner edge. Moreover, with this setup it is reasonable to consider the x and y components of the torque equal to 0. Note that Σ_0 does not play a key role in our simulations, as long as $M_d \ll M_1 + M_2$, where M_d is the mass of the disc. In fact, self-gravity is not implemented in the SPH code. However, sink particles do feel the gravitational force generated by the gas particles. Since $M_d \ll M_1 + M_2$, the back-reaction of the disc on the angular momentum of the binary is negligible ($M_d = 0.01M$ in all the simulations). We do not impose any condition at the outer edge. We just consider wide discs, in such a way that $t_\nu = R_{\rm out}^2/\nu \gg t_{\rm sound}$, where $t_{\rm sound}$ is the sound crossing time, so that the external boundary condition does not affect the evolution in the inner regions, which are the ones we are interested in. However, we do not simulate too wide discs because most of the mass lies in the outer regions ($M(R) \propto R^{2-q}$), but we need a high resolution at the very inner edge where the external torque is stronger. The dynamic range of our simulations is $R_{\rm out}/R_{\rm in} = 35$.

The other parameters have been set to: $p = 0.5$, $q = 0.75$, $H_{\rm in}/R_{\rm in} = 0.1$, $\eta = 0.25$ and $R_{\rm in} = a$. This set of parameters is slightly different from our standard runs of Section 2.4. In particular, here we consider a disc that is initially closer to the central binary. We made this choice in order to have a more prominent warp. Otherwise, since the resolution at small radii is relatively poor (because $\Sigma \to 0$), the features of the warp would be masked by the low signal to noise ratio. Note however that the inner radius of the disc will be pushed further from the central binary due to tidal forcing. We will discuss this issue in detail in Section 2.5.3. The time variable t is expressed in terms of $\Omega_{\rm in}^{-1}$ in the whole Section.

As initial condition we used an untwisted disc uniformly tilted with respect to the binary plane. Therefore, at $t = 0$, $\beta(R) = {\rm const}$ and $\gamma(R) = 0$. The initial inclination angle and the physical viscosity will be specified later while presenting the results.

2.5.3 Results

In this Section we compare the results of the 3D SPH simulations with the ones obtained by the 1D code. New 1D simulations are reported here, with a surface density profile equal to the one reported in equation 2.32. In order to compare the results we had to compute azimuthally averaged disc quantities of the the SPH simulations in a number of thin shells. The procedure is the one described in Section 3.2.6 of Lodato & Price (2010). The number of shells has been set to 300.

Before comparing the results, we have verified that $\partial_t \Sigma \approx 0$ in the SPH simulations. We looked at the evolution of Σ in a simulation time ($t_{\rm stop} = 4000$) for two cases: $\alpha = 0.05$ and $\alpha = 0.2$. Note that with our setup $t_\nu \approx 10^5 (0.2/\alpha) \gg t_{\rm stop}$. For these two simulations $N = 1$ million. In Fig. 2.7 we show Σ at the beginning of the two simulations and at their very

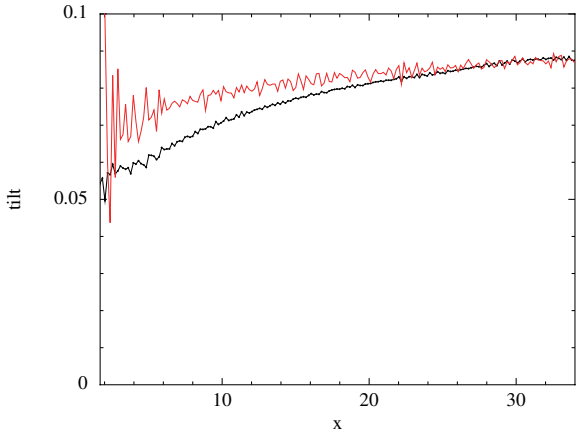

Fig. 2.10 Tilt of two differently resolved discs, with $\alpha = 0.05$ and $\beta_\infty = 5°$, at $t = 4000$. The black line portrays a disc with $N = 1$ million particles, and the red line a disc with $N = 100000$ particles. For less well resolved discs, the tidal torques at the inner disc edge are less effective, leading to a smaller warp.

end. From the results illustrated in the figure we can conclude that the assumption $\partial_t \Sigma \approx 0$ is satisfied at least in the bulk of the disc, even in the diffusive regime ($\alpha = 0.2$). However, we can make the following observations.

Firstly, at the outer edge the surface density profile smooths towards a continuous configuration. The initial condition presents a discontinuity at the outer radius, which is damped out quite quickly by pressure forces. Secondly, and more importantly, in both cases we observe an evolution at the inner edge: the inner radius is pushed further from the binary by tidal forcing, as we expect since the initial inner radius is smaller than the tidal truncation one. From Artymowicz & Lubow (1994) we expect it to be at a radius $R_\mathrm{t} \approx 1.7a$ when $\eta = 0.25$. Note that the location of the inner disc edge has a strong effect on the warp, given the strong radial dependence of the binary torques. In the two cases shown in Fig. 2.7 R_t lies around $1.5 - 1.9a$, in good agreement with the predicted $1.7a$.

Finally, we have verified that the binary angular momentum variations are negligible over the simulation time.

Linear regime

We analyse the warp dynamics in three cases: $\alpha = 0.05$, $\alpha = 0.2$ and $\alpha \approx 0$. In the first case the disc falls in the wave-like regime, in the second one it is in the diffusive regime, and the third one is the closest possible value to the inviscid case. Initially, at $t = 0$, the disc is tilted with respect to the binary plane by an angle $\beta_\infty = 5°$. Both Nelson & Papaloizou (1999) and Ogilvie (2006) have shown that in absence of an external torque (which does not modify the

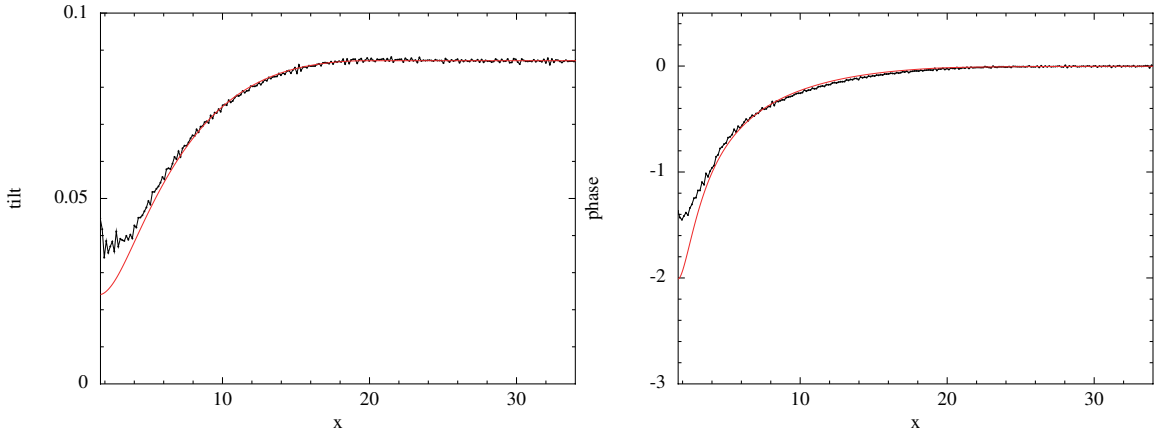

Fig. 2.11 Tilt and phase evolution of an initially untwisted tilted disc, with $\eta = 0.25$, $(H_{\rm in}/R_{\rm in}) = 0.1$, $\alpha = 0.2$, $\beta_\infty = 5^\circ$ and $N = 1$ million at $t = 2000$. Black lines show the SPH results, while red lines indicate the 1D model.

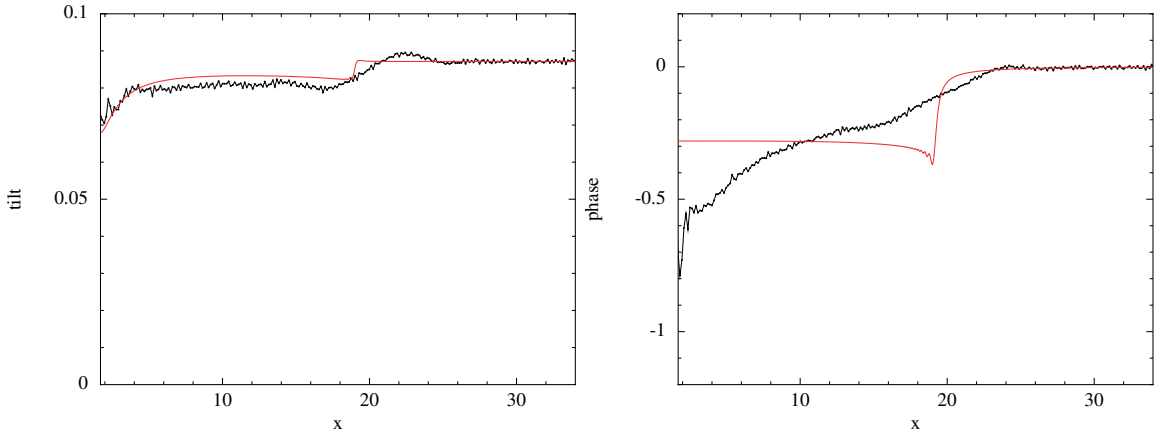

Fig. 2.12 Tilt and phase evolution of an initially untwisted tilted disc, with $\eta = 0.25$, $(H_{\rm in}/R_{\rm in}) = 0.1$, $\alpha = 0$, $\beta_\infty = 5^\circ$ and $N = 1$ million at $t = 2000$. Black lines show the SPH results, while red lines indicate the 1D model. Also here, the inner edge of the disc is set at $1.7a$ for the 1D runs. SPH succeeds in reproducing the tilt evolution, even for almost inviscid discs. The phase shows an apparent disagreement due to the contribution of the artificial viscosity to the effective one.

regime the waves propagate with, anyway) such a small inclination ensures a linear regime for the wave propagation. We have run other simulations with lower values of the initial β_∞, but since we are dealing with full 3D simulations, we have to take the finite thickness into account. When β_∞ is too small (i.e. $\tan\beta_\infty \lesssim H/R$), we obtain a very noisy measure of the tilt. By increasing β_∞ up to 5°, we reduce the noise-to-signal ratio. Therefore we report the results of the 5° simulations only.

Let us start with the case of $\alpha = 0.05$. In Fig. 2.9 we report the evolution of the tilt and the phase at $t = 2000$. The number of particles used in this simulation is $N = 1$ million. We illustrate the results of the 3D simulation with the black lines, and the ones of the corresponding 1D simulation with the red lines. In the 1D simulations the inner edge of the disc has been set equal to $R_\mathrm{t} = 1.7a$. The general trend of the 3D simulations is in very good agreement with the 1D ones. Both the tilt and the twist tend to a steady state. Moreover, the tilt tends to a steady state that has a shape described by an evanescent wave. There is a good agreement also in the propagation velocity. Overall, the evolution of both the tilt and the phase throughout the simulation is in very good agreement with that obtained by solving the linearised warp equations in 1D.

An additional effect (not apparent in these plots) is that the evolution shows a small periodic oscillation with time. This is due to the imperfect rotational symmetry about the z-axis of the gravitational potential, which enforces wobbling modes into the disc (Bate et al., 2000), especially with $\sigma = 2$.

We have also tested the effects of limited resolution in SPH by running a simulation with the same parameters as above but with 10 times fewer particles. The tilt evolution in this case is shown in Fig. 2.10. We see that in this case the disc develops a smaller warp (i.e., the inner disc tends to stay more aligned with the outer disc). This is due to the fact that decreasing the resolution, we do not resolve equally well the inner disc edge. The disc thus appears truncated by tidal torques at a slightly larger radius ($\sim 2a$ in this case), thus decreasing the warp amplitude. We find a very good agreement in the evolution of the tilt by comparing this poorly resolved simulation with a 1D simulation with an inner radius equal to $2a$.

We have just described a disc in which the wave-like regime is expected in the whole disc. Now we use the same setup (simulations with $N = 1$ million particles) as above, but we set $\alpha = 0.2$. By knowing that $H/R = 0.1\, x^{-1/4}$, the condition $\alpha \gtrsim H/R$ is verified in the whole disc. Therefore with $\alpha = 0.2$ the warp evolves diffusively. We compare the 3D results with the ones obtained in Section 2.4 for the same value of α. In Fig. 2.11 we report the results for the tilt and the phase evolution, respectively. The inner edge of the disc has been set to $R_\mathrm{t} = 1.7a$ for the 1D simulations. We observe a good agreement. This confirms that the equations do describe the evolution even in a diffusive regime (see Section 2.3). A small

discrepancy is still present at the very inner edge because of the low resolution when Σ tends to 0 (and the associated error in the estimate of R_t), but this does not affect the shape in the outer regions of the disc.

Finally, we try to simulate the dynamics of an inviscid disc. In order to do it, we consider a disc with physical viscosity equal to 0. However, as we have already mentioned in Section 2.5.1, we cannot remove the artificial viscosity from the simulations completely. In this Section we use the following viscosity parameters: $\alpha_{\rm art,max} = 0.5$, $\alpha_{\rm art,min} = 10^{-5}$ and $\alpha = 0$. We used such a low value for $\alpha_{\rm art,min}$ because when $\nabla \cdot \mathbf{v} < 0$ the Morris and Monaghan switch ensures that discontinuities are smoothed by a higher value of $\alpha_{\rm art}$. The artificial viscosity grows to its maximum value when $|h\nabla \cdot \mathbf{v}| > c_s$. We tried to use lower values of $\alpha_{\rm art,max}$, but, as predicted, the simulations become noisy. In Fig. 2.12 we report the tilt and the phase evolution of such a disc.

In the tilt we see a good agreement between the 3D simulation and the 1D solution (where, as usual, the inner radius of the disc has been set equal to $R_t = 1.7a$). In the 3D tilt we note a bump on the wavefront. This is due to the fact that in the 3D simulation N is not large enough to resolve the tilt discontinuity at the wavefront of the 1D code: such a discontinuity is smoothed over some smoothing lengths.

The phase evolution is very different. As described in Section 2.4.2, in the 1D case when $\alpha = 0$ the disc rotates and reaches a steady state that is untwisted. Instead, in the 3D case the disc does present a twist. This fact emphasises that our simulations are not completely inviscid, since the artificial viscosity is acting as a small effective viscosity in the disc (see equation 2.29). The small amount of this effective viscosity produces the twist observable in the figure. Moreover, the resolution is not high enough to resolve the strong phase discontinuity of the 1D simulation. SPH is smoothing the discontinuity over some smoothing lengths.

Still, we note that the agreement between theory and simulations is remarkable, even for almost inviscid discs.

Non-linear regime

If we enhance the initial inclination angle, the linear theory fails. As reported above, some efforts have been made in order to describe the non-linear regime, both numerically (Nelson & Papaloizou, 1999) and analytically (Ogilvie, 2006), the latter in the absence of external torques. In this Section we simulate the non-linear regime of wave-like warp propagation via SPH simulations with a much higher resolution than in previous works. Moreover, we focus on the case where the disc is subject to external torques, due to the central misaligned binary. We use 2 million particles, and the following set of parameters: $\alpha_{\rm art,max} = 0.5$, $\alpha_{\rm art,min} = 0.01$,

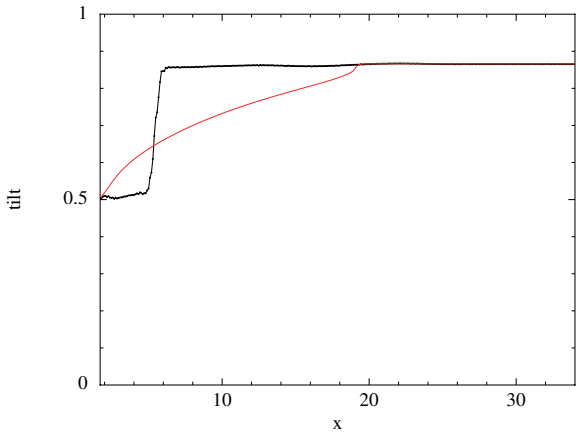

Fig. 2.13 Tilt and phase evolution of an initially untwisted tilted disc, with $\beta_\infty = 60^\circ$, $\eta = 0.25$, $(H_{\rm in}/R_{\rm in}) = 0.1$ and $N = 2$ million at $t = 2000$. A sharp break occurs in the 3D simulations (black line). The linear theory (red line) fails to describe the warp evolution for such high inclinations.

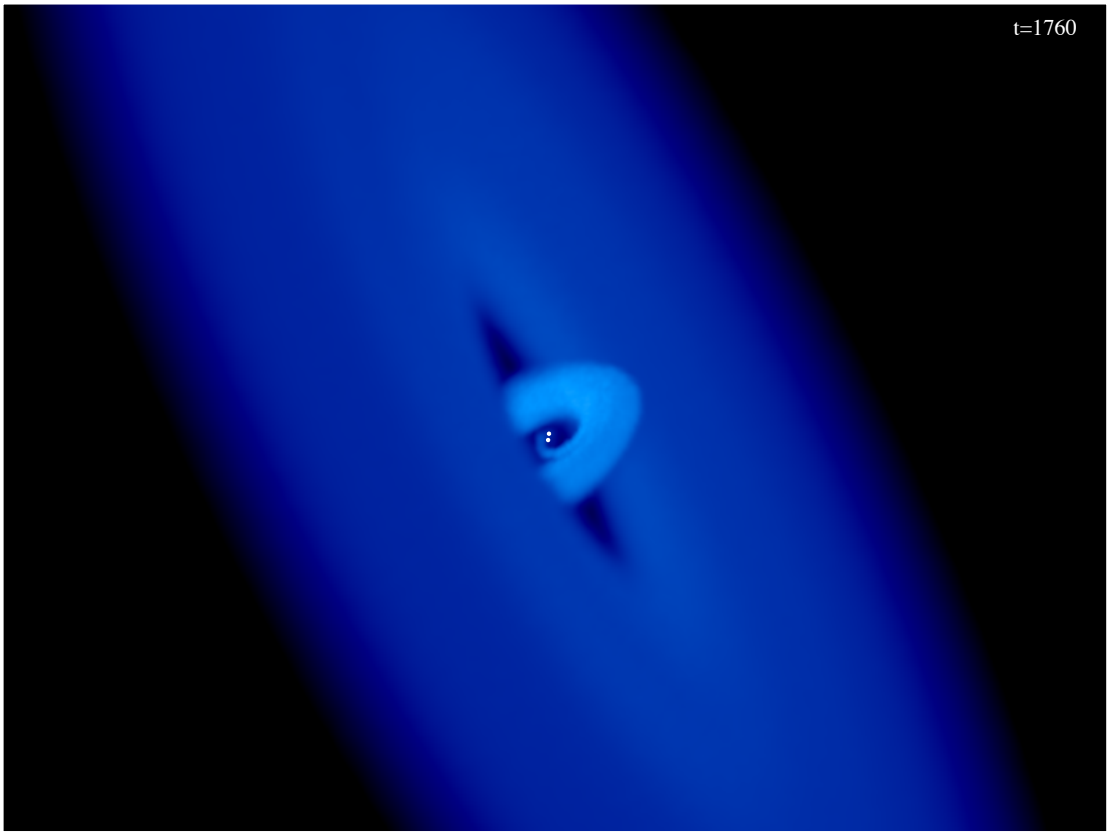

Fig. 2.14 3D structure of the disc shown in Fig. 2.13 at $t = 1760$. The disc breaks in two almost separated discs. The inner one starts precessing, since its width is very narrow.

$\alpha = 0.05$, $H_{\rm in}/R_{\rm in} = 0.1$, $M_1 = M_2 = 0.5$ and $r_1/R_{\rm in} = r_2/R_{\rm in} = 0.5$. This is the same set used for the simulation portrayed in Fig. 2.9. we have used the usual formulation for the viscosity, since we know that in non-linear cases shocks are much more likely to occur.

We have performed simulations with three different initial inclinations of the disc plane with respect to the binary plane: $\beta_\infty = 20$, 40 and 60°. The 20° inclined disc starts showing relevant discrepancies from the linear regime, but it is in the 40° and even more in the 60° inclined disc that the evolution is completely different from the one predicted by the linear theory. In this Section we report the results of the most inclined disc only as an example. Further studies on this issue are required.

Let us analyse the case with $\beta_\infty = 60°$. In Fig. 2.13 we show the evolution of the tilt at $t = 2000$. As above, we illustrate the results of the 3D simulation with the black line, and the ones corresponding to the linear 1D simulation with the red line. For the 1D simulation the inner edge has been set equal to $R_{\rm t} = 1.7a$ we can immediately observe that the discrepancy is very remarkable, and that the linear theory fails to describe the warp propagation in such an extreme case. From Fig. 2.14 we note that the disc breaks sharply. Moreover, the 3D simulation shows that the inner ring starts precessing.

This kind of behaviour has already been observed by Lodato & Price (2010) and Nixon, King & et al. (2012), the latter focusing on discs subject to Lense-Thirring precession. Their simulations focus on the diffusive regime ($\alpha > H/R$), but they both obtain the breaking of the disc with low values of α. Moreover, Fragner & Nelson (2010) have seen the same result via a grid code, and Larwood & Papaloizou (1997) via SPH simulations, but with a much lower resolution than ours. Note that we have performed the same kind of simulation, but with a lower viscosity ($\alpha = 0.01$), and the general result is equivalent to the more viscous case. After the publication of the paper by Facchini, Lodato & Price (2013), a set of new simulations reproduced such disc breaking in the bending-wave regime. Interested readers can look for example at Nealon, Price & Nixon (2015), and at Nixon & King (2015) for a review of the topic.

2.6 Conclusions

In this chapter we have performed 3D SPH simulations of misaligned circumbinary discs, and we have compared these results with the ones obtained with the 1D ring code. By focusing on the linear case, we have firstly verified the validity of the assumptions made in the 1D model. Secondly, we have tested that the agreement is good, both in the tilt and in the twist, in the wave-like regime. Small discrepancies are due to the low resolution in the inner regions of the disc. By increasing the value of viscosity, we have verified that the wave equations do

succeed in simulating the viscous regime (the agreement between 3D and 1D simulation is remarkable), with the *caveat* that this is valid for short enough timescales. Finally, we have performed simulations at very low viscosities, close to the inviscid case. By comparing the SPH results to the 1D inviscid ones, we have obtained a good agreement, at least in the tilt evolution. This fact emphasises how well SPH is able to reproduce the warp evolution of discs, even for the case of extremely low viscosities. We have shown that standard tools, such as the Morris & Monaghan switch, are indeed effective at reducing artificial viscosity and ensure the possibility of running almost inviscid warped disc SPH simulations.

In the non-linear regime, we have shown that for high inclination angles of the disc plane with respect to the binary one the disc breaks, and the inner ring precesses almost completely disconnected from the outer regions of the disc. Additional studies are required to further explore this last issue.

Chapter 3

Probing the presence of planets in transition discs' cavities via warps: the case of TW Hya

In this chapter we exploit the theoretical framework of warp propagation in binary systems used in chapter 2 to verify whether warped structures can be used as tracers of protoplanets embedded in protostellar discs. This chapter is based on the paper by Facchini, Ricci & Lodato (2014). This project was born after a discussion with Luca Ricci. I have led the whole project, running all the simulations, performing the whole analysis and writing most of the paper.

3.1 Introduction

It is still observationally challenging to observe planets in the act of formation, i.e. when they are still embedded or surrounded by a protoplanetary disc. For example, Reggiani et al. (2014) managed to detect a point-like IR excess in L' and J bands around HD169142 (see also Biller et al., 2014). Since massive protoplanets are expected to accrete quite vigorously, accretion tracers as Hα emission lines are used to detect low mass companions and possibly massive planetary embryos (e.g. Close et al., 2014). Another prediction is that protoplanets could be detectable via their circumplanetary disc (e.g. Zhu, 2015). On the other hand, it is possible to indirectly probe (or at least infer) the presence of a planet by looking at the dynamical effects that it causes onto the disc. As an example, Garufi et al. (2013) have recently suggested the presence of a planet in HD135344B by analysing the spiral structure and radial distribution of different grain sizes in the disc (see Benisty et al., 2015, for a

beautiful spiral structure detected in scattered light in MWC 78). Another effect that planets can have on discs are azimuthal asymmetries in the gas and dust profiles (e.g. Isella et al., 2013; van der Marel & et al., 2013, in the discs surrounding the young stars LkHα 330 and Oph IRS 48, respectively). Finally, possible obvious tracers of embedded planets are azimuthally symmetric gaps, as the ones detected in HL Tau (ALMA Partnership et al., 2015).

These examples are all referred to transition discs, i.e. discs that present either a gap or a cleared central cavity in the dust component (see Section 1.1.1). This is due to two main reasons. A first one is that these discs are thought to be at the end of their lifetime, therefore they are more likely to have already formed planets. The second reason is that transition discs are thought to be a transient phase of the disc life, just before the final dispersal (see Section 1.1.1). Note that some candidate protoplanets have already been directly observed in the cavity of transition discs (e.g. Huélamo et al., 2011; Kraus & Ireland, 2012, in T Cha and LkCa 15, respectively).

One dynamical effect that has been theoretically addressed recently is disc warping due to the presence of misaligned planets (e.g. Xiang-Gruess & Papaloizou, 2013; Bitsch et al., 2013), i.e. planets orbiting on a plane that is misaligned with respect to the outer regions of the disc. Misaligned planets seem likely to occur. A few resonant mechanisms are known to be responsible for this effect. For example, planet-planet scattering, in the case of multi-planetary systems, appears to be effective even when planets are still embedded in the disc (Lega, Morbidelli & Nesvorný, 2013). Secondly, resonant interactions during migration can excite planets outside the coplanar orbit. Finally, a misaligned planet could simply be tracing a past inclined structure of the disc itself (e.g. Bate, Lodato & Pringle, 2010). Mutual inclinations of planets with respect to the disc plane can then be maintained by the Kozai mechanism (e.g. Teyssandier, Terquem & Papaloizou, 2013). The dynamical response of the disc to the secular torque produced by misaligned (proto)planets (and vice-versa) has been analysed mainly by numerical simulations for the case in which the planet is embedded in the disc (though Terquem, 2013, used an analytical approach). Note that we refer to 'embedded' planet as opposed to a planet that is in the central cavity of the disc. In chapter 2 we have developed a simple 1D model obtaining the steady-state solution for the warped structure of circumbinary discs. The model was developed to deal with stellar binaries, but it is applicable to planetary systems where a massive planet is orbiting a star within a central cavity of the disc.

Rosenfeld et al. (2012) have recently shown that it is becoming possible to potentially measure warps with high precision by looking at the emission line profiles of the gaseous component (see Section 1.2.2 for a comprehensive summary of observed warped discs). They

have applied this method to the closest transition disc ever detected, TW Hydrae. We will thoroughly describe the system and its observations in Section 3.3.1. Rosenfeld et al. (2012) observed the disc with the ALMA in the ^{12}CO $J = 2-1$ and ^{12}CO $J = 3-2$ emission lines at 1.3 and 0.87 mm, respectively. In both bands, they detect an enhanced emission in the inner regions of the disc. In this paper, they propose three theoretical models to explain such observation: a hotter inner disc, a non-Keplerian velocity field due to possible magnetic pressure effects (Shu, Galli & et al., 2007), and a warp, where the disc has Keplerian motions ($v_\phi = v_\mathrm{K}$), but the variation of the inclination i with radius might be enhancing the projected radial velocity. Note that Rosenfeld, Chiang & Andrews (2014) just showed that the same effect could be due to fast radial inflows. In this study we do not want to compare all the possible models. We consider the warp to be the most plausible, since other measurements in scattered light have enlightened an azimuthal asymmetry which is compatible with being caused by a warp (Roberge, Weinberger & Malumuth, 2005; Debes et al., 2013). We use this system as a template, in order to show the applicability of our models (see below), which relate the amount of warping in the disc with the dynamical properties of a possible misaligned central planet.

To summarise: in this chapter we address two main issues. Firstly, we provide a simple prescription to relate the amount of warping of a circumbinary disc to the properties of the two central objects. The binary can be composed by two stars (stars or brown dwarfs) or by a star and a massive planet. In this way, we will have a simple observational feature to infer the presence of a planet in protoplanetary and transition discs. We will be very general on this first problem, by exploring a parameter space that is suitable for a secondary companion with a mass ranging from a stellar to a planetary one. The central object can be either a star or a brown dwarf (since recent observations have started to focus on discs around brown dwarfs, see e.g. Ricci et al., 2012a, 2013). Secondly, we apply this simple model to the case of TW Hya, and see whether the observations by Rosenfeld et al. (2012) are compatible with a massive planet in the disc's cavity. This will be an example of how this technique could be used, since measurements of spatially resolved line profiles in similar discs are going to become more and more accessible, due to ALMA reaching its full potential in the next few years. We also predict the amount of warping in LkCa 15 and T Cha, in case the observed companion were misaligned with respect to the disc.

3.2 Results

As described above, in this Section we use the 1D code described in chapter 2 to obtain a simple analytical prescription for the amount of warping of a circumbinary disc and its

dependence on the physical parameters of the disc and of the central binary. The mass ratio of the two central objects can reach extreme values, therefore in principle this same model can be used to describe a binary formed by a central star and an orbiting massive planet. We follow the same procedure as in chapter 2. We consider two stars M_1 and M_2 co-orbiting on circular orbits. The binary system can be described via the standard two body variables $M = M_1 + M_2$, $\eta = M_1 M_2 / M^2$ and a, where a is the distance between the two central objects. The gravitational potential is computed by considering the prominent secular term only, i.e. the time independent term (Nixon, King & Pringle, 2011; Foucart & Lai, 2013). We use a prescription for the disc where both the surface density and the sound speed depend on the radial coordinate via a simple power law; respectively, $\Sigma \propto R^{-p}$ and $c_s \propto R^{-q}$. The radial extent of the disc is limited by an inner and an outer edge, $R_{\rm in}$ and $R_{\rm out}$. From now on the subscript *in* refers to quantities evaluated at the inner edge of the disc.

By using these analytical prescriptions for the gravitational potential and for the disc, we can follow the warp evolution of circumbinary discs by using Eq 2.15-2.17. We look for the steady-state profiles of the tilt angle by solving the time dependent equations until the solution relax onto a quasi steady-state. The warped structure will be expressed in terms of the angle $\beta(R)$. The parameter β_∞ will indicate the angle between the outer disc's plane and the binary. We recall that we are focusing on the linear regime only, since it is the only regime for which an analytic theory has been developed. In chapter 2 we have shown that for $\beta_\infty \gtrsim 40^\circ$ the evolution becomes non-linear, and the disc can break. In this work we do not consider this regime.

The steady-state solution will depend on four parameters. The two exponents p and q from the disc model, and two dimensionless parameters: $\hat{\alpha} = \alpha / (H_{\rm in}/R_{\rm in})$ and χ (cfr. equations (33)-(36) in Facchini, Lodato & Price, 2013), where the parameter χ is defined by equation 2.28. Physically, these two ratios indicate that the dynamics of the disc is regulated by two physical ingredients: the relative importance of viscous over pressure forces, and the relative importance of the external gravitational torque over internal pressure stresses.

We have performed 1D simulations using the model described in chapter 2. My aim is to explore the 2D $\hat{\alpha}$-χ parameter space for some typical values of p and q, in order to find a simple prescription for the dependence of the amount of warping in a disc with respect to these two parameters. Foucart & Lai (2013) have already found this kind of prescription, but focusing on the case where q is a function of p only. In this section we will compare our results with theirs. Moreover, our method allows us to explore a region of parameter space

p	q	K	C
0.50	0.50	4.1045	0.00991
1.00	0.50	23.891	0.02380
0.93	0.26	2.5072	0.12766
0.72	0.15	0.7256	0.37397
0.72	0.30	1.8249	0.18128
1.00	0.40	9.7410	0.04472

Table 3.1 Obtained values for K and C for different choices of density and sound speed power-law indexes p and q. The parameters were deduced by fitting the fractional amplitude of the warping $\Delta\beta/\beta_\infty$ obtained via 1D simulations. These simulations explore a wide parameter space in χ and $\hat{\alpha}$. The fitting function is given by equation (3.2). The last four choices of p and q represent physical systems (TW Hya, LkCa 15 and T Cha, respectively) that are discussed in Section 3.3. Comparisons between outputs of the simulations and fitting curves are displayed in Figs. 3.3-3.4.

that was not considered by Foucart & Lai (2013). They focus on cases where $R_{\rm in} > R_{\rm warp}$, where $R_{\rm warp}$ can be defined by the following relation:

$$R_{\rm warp} \approx a\left(\frac{3\alpha\eta}{2(H_{\rm in}/R_{\rm in})^2}\right)^{1/2} = R_{\rm in}(2\hat{\alpha}\chi)^{1/2}, \tag{3.1}$$

and it indicates the scale radius where the warp becomes prominent. In terms of limits, it means that for $R \ll R_{\rm warp}$ the disc is aligned with the binary plane, whereas for $R \gg R_{\rm warp}$ the disc is inclined by a same angle β_∞. In this chapter, we explore regions of parameter space where $R_{\rm in} \approx R_{\rm warp}$, e.g. by exploring regions at very high viscosities or a regime where the binary torques are stronger. Note that $R_{\rm in} \approx R_{\rm warp}$ when $\hat{\alpha}\chi \approx 1$.

The simulations are performed for different combinations of the parameters p and q. Firstly we have considered typical density and sound speed profiles. We have used: $(p,q) = (1.00, 0.50)$ and $(0.50, 0.50)$. We have then chosen parameters that were deduced in best fits of observed systems. We focus on the three systems we discuss in Section 3.3: TW Hya, LkCa15 and T Cha. The respective values for (p,q) are: $(0.93, 0.26)$, $(0.72, 0.15-0.30)$ and $(1.00, 0.40)$. The references for these values are summarised in Table 3.2. For every couple of p and q values, we run simulations for $\hat{\alpha} = [0.00, 3.00]$, sampled at every $\Delta\hat{\alpha} = 0.1$, and $a/R_{\rm in} = [0.05, 1.00]$, sampled at every $\Delta(a/R_{\rm in}) = 0.05$ for $\eta = 0.25$. This is equivalent to sampling χ between $4.69 \cdot 10^{-3}$ and 1.875. Note again that the two ranges allow us to explore extreme conditions, such as two equally massive stars orbiting at the very inner edge of a disc. Obviously this kind of conditions will never be observed in relaxed environments, but it could be observed in short transients in dynamically interactive regions.

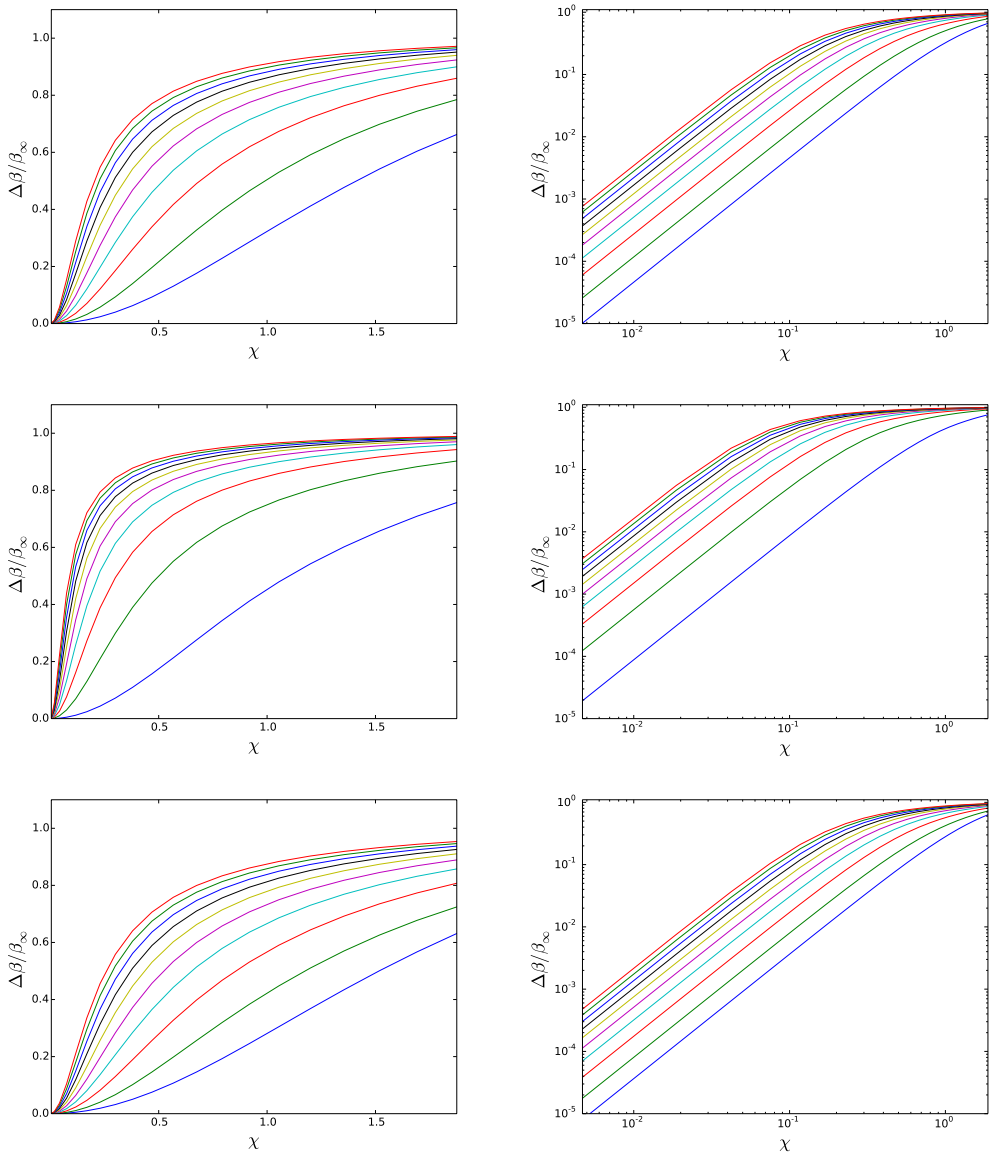

Fig. 3.1 Warping of the steady-state solution of a circumbinary disc as a function of χ for three different values of the couple $(p,q) = (0.50,0.50)$, $(1.00,0.50)$ and $(0.93,0.26)$, from top to bottom respectively. The right panels are the log-log scaled versions of the left panels. Each line represents a simulation at a different value of viscosity: from $\hat{\alpha} = 0.1$ (blue line at the bottom of each plot) to $\hat{\alpha} = 2.8$, sampled every $\Delta\hat{\alpha} = 0.03$. The amount of warping depends on χ as a power law when the warping is small. In particular, $\Delta\beta/\beta_\infty \propto \chi^2$. These results confirm relations (16), (20) and (21) by Foucart & Lai (2013). As the warp grows the dependence on χ deviates from a simple power law, as it flattens so that $\Delta\beta/\beta_\infty$ saturates to 1 when χ is large. The simple quadratic dependence on χ is only valid as long as $\Delta\beta/\beta_\infty \lesssim 0.1$.

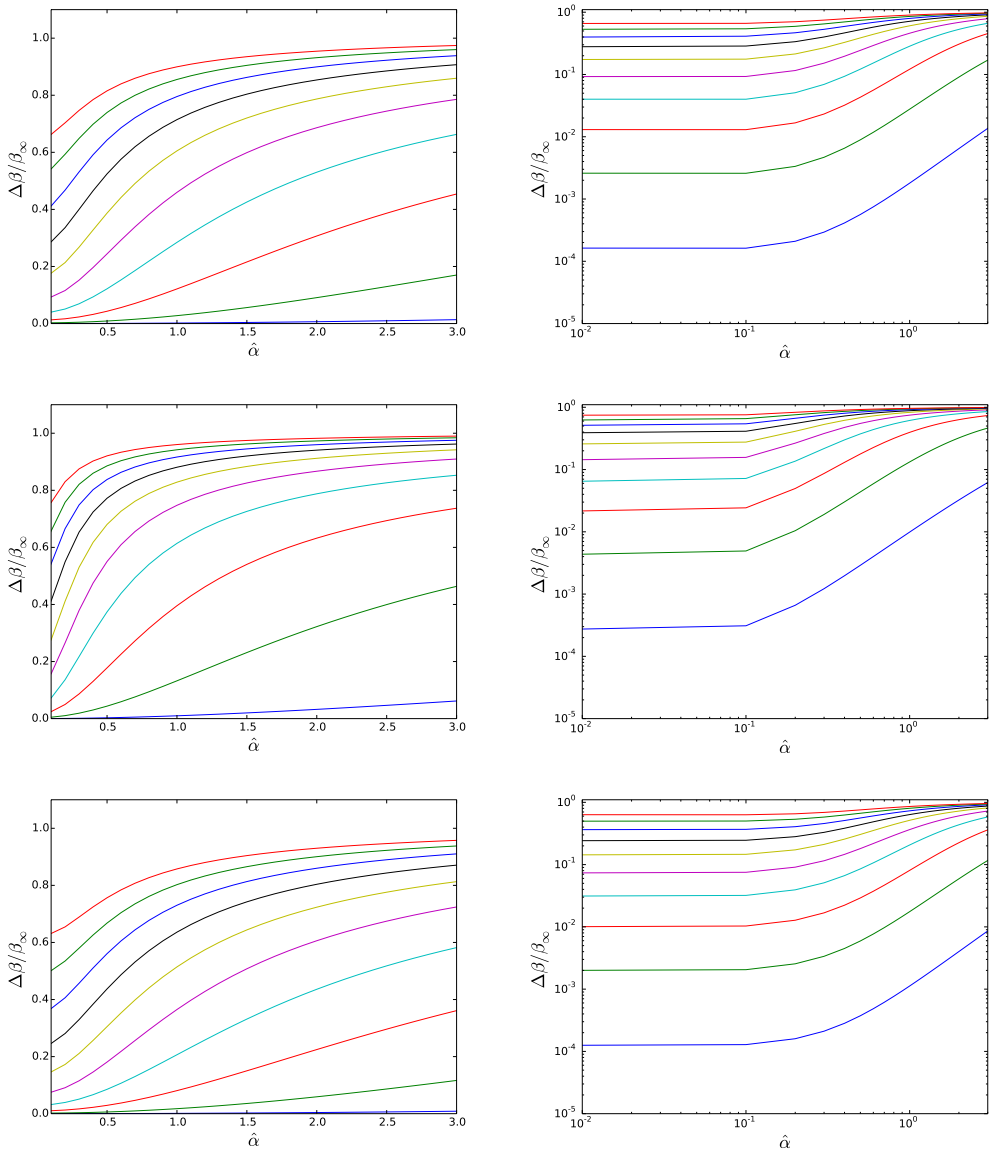

Fig. 3.2 Warping of the steady-state solution of a circumbinary disc as a function of $\hat{\alpha} = \alpha/(H_{\rm in}/H_{\rm in})$ for three different values of the couple $(p,q) = (0.50,0.50)$, $(1.00,0.50)$ and $(0.93,0.26)$, from top to bottom respectively. Each line represents a simulation at a different value of $a/R_{\rm in}$: from $a/R_{\rm in} = 0.1$ (blue line at the bottom of each plot) to $a/R_{\rm in} = 1.0$, sampled every $\Delta(a/R_{\rm in}) = 0.1$, for $\eta = 0.25$. This corresponds to sampling χ from $\chi_1 = 0.01875$ to $\chi_{10} = 1.875$, where $\chi_i = 1.875 * (a_i/R_{\rm in})^2$ and $a_i/R_{\rm in} = i * \Delta(a/R_{\rm in})$. We can observe three different regimes. At low $\hat{\alpha}$ the amount of warping reaches a horizontal asymptote. It then shows a power law trend in an intermediate regime ($\Delta\beta/\beta_\infty \propto \hat{\alpha}^2$). Roughly above the threshold $\Delta\beta/\beta_\infty = 0.1$ we obtain a non analytic relation again, as found for the parameter χ.

The simulations are performed with $N = 2001$ logarithmically distributed grid points. The simulations end when the perturbation coming from the inner edge of the disc reaches the outer edge $R_{\rm out} = 500R_{\rm in}$. At this point, in the inner regions ($R < 250R_{\rm in}$) the discs have already relaxed to their steady-state configuration even in the more viscous cases. The amount of warping in the disc is quantified by the quantity $\Delta\beta/\beta_\infty = (\beta_\infty - \beta_{\rm in})/\beta_\infty$. In these estimates, $\beta_\infty = \beta(R = 120R_{\rm in})$. We consider an unwarped, misaligned initial condition, where $\beta(R) = \beta_\infty$ for every R. Facchini, Lodato & Price (2013) have shown that the solution does not depend on the initial condition. Note that β_∞ is computed far from $R_{\rm out}$ since we do not want to have any spurious effect due to the outer edge boundary condition. Since the warp develops in the inner regions only, $\mathbf{l}$ computed at $R = 120R_{\rm in}$ is a very good approximation for $\mathbf{l}_{\rm out}$. We have used a zero-torque boundary condition both at the inner and at the outer edge of the disc ($\partial_R \mathbf{l}_{\rm in} = \partial_R \mathbf{l}_{\rm out} = 0$).

The results our reported in Figs. 3.1-3.2. All the figures illustrate the dependence of $\Delta\beta/\beta_\infty$, respectively as a function of χ and $\hat{\alpha}$. The plots are general, in the sense that they do not depend on the specific choice of $H_{\rm in}/R_{\rm in}$ and of M_1 and M_2, made in the simulations.

Let us start by looking at Fig. 3.1. It shows that the amount of warping depends on χ as a power law when the warping is small. In particular, $\Delta\beta/\beta_\infty \propto \chi^2$. These results confirm relations (16), (20) and (21) by Foucart & Lai (2013) when $\sin\beta \sim \beta$. However, as the warp grows the dependence on χ deviates from a simple power law, as it flattens so that $\Delta\beta/\beta_\infty$ saturates to 1 when χ is large, a result not predicted by the analytical model by Foucart & Lai (2013). The simple quadratic dependence on χ is only valid as long as $\Delta\beta/\beta_\infty < 0.1$.

From Fig. 3.2 we obtain very similar results. From the plots we can observe three different regimes. At low $\hat{\alpha}$ the amount of warping reaches a horizontal asymptote. It then shows a power law trend in a intermediate regime. By fitting the curves in this regime we obtain $\Delta\beta/\beta_\infty \propto \hat{\alpha}^2$, as predicted by Foucart & Lai (2013) by their equations (16) and (20). Roughly above the threshold $\Delta\beta/\beta_\infty = 0.1$ we obtain a non immediate relation again, as found for the parameter χ. The horizontal asymptote was predicted by Foucart & Lai (2013) again.

We can summarise these results by writing a simple prescription for $\Delta\beta/\beta_\infty$, whenever $R_{\rm warp} < R_{\rm in}$, i.e. in the same regime that Foucart & Lai (2013) analysed:

$$\frac{\Delta\beta}{\beta_\infty} \approx K\chi^2\left(\hat{\alpha}^2 + C\right). \tag{3.2}$$

We fitted the results of the 1D simulations with this analytic prescription on the parameter space that has an associated degree of warping $\Delta\beta/\beta_\infty < 0.1$. The obtained values for K and C in the explored set of (p,q) is reported in Table 3.1. When $R_{\rm warp} \sim R_{\rm in}$, this simple prescription breaks. Typical values for this regime can be easily obtained from Figs. 3.1-3.2.

In Figs. 3.3-3.4 we show the comparison of the results obtained from numerical simulations and the analytic prescription in some specific cases, that are described in Section 3.3. The agreement between the curves is remarkable when $\Delta\beta/\beta_\infty < 0.1$. This result confirms that the power-law dependencies are valid for small warps only.

This simple prescription tells us that by measuring $\Delta\beta/\beta_\infty$ we can obtain significant information on χ and $\hat{\alpha}$. If other parameters are known, such as the orbital parameters of the two stars (for stellar binaries), the degeneracy between χ and $\hat{\alpha}$ can be broken. Therefore, by measuring the warping of a circumbinary disc, it is possible to estimate the disc viscosity, parametrised by α. This topic is better discussed in Section 3.4.

3.3 Application to observed systems

In this section we apply the model to some observed circumbinary and transition discs. We do it for two reasons. Firstly, we want to show how the model described in Section 3.2 can be applied to a physical system. Secondly, we want to verify whether the warp that was observed in one of these systems can be explained by invoking a perturbing planet that is simultaneously clearing out the inner region of the disc. We consider three cases: TW Hya, for which a warp has been inferred based on ALMA observations of the velocity field (Rosenfeld et al., 2012), LkCa 15, and T Cha. These last two objects are transition discs for which a potential protoplanet has been imaged within the central cavity.

3.3.1 TW Hya

TW Hya is a protoplanetary disc 54 ± 6 pc away from Earth (cfr. Hipparcos catalogue, van Leeuwen, 2007a), first detected by Rucinski & Krautter (1983) at infrared wavelengths. Due to its high emission at many wavelengths, it is one of the most studied protoplanetary discs. The disc is nearly face-on ($i \approx 6^\circ - 7^\circ$, where $i = 0^\circ$ is face-on; Qi & et al., 2004). Note that this particular feature helped Rosenfeld et al. (2012) to spatially resolve the projected velocity of the gas in the disc, and to look for any departure from the expected Keplerian velocity.

By modelling the SED (Spectral Energy Distribution) of TW Hya, Calvet et al. (2002) claimed that the disc has a dust central cavity of 4 AU in radius, confirmed by Andrews et al. (2012) again by looking at the SED. This result was then confirmed by interferometric measurements, both in the near-infrared band (Eisner, Chiang & Hillenbrand, 2006) and in the millimetric band (Hughes et al., 2007). Note however that Ratzka et al. (2007) derived a cavity of 0.7 AU in radius by modelling their mid-infrared interferometric data.

A few papers have tried to reconcile these two results by inferring a central cavity of 4 AU, with an inner source of continuum emission coming from within the cavity (Akeson et al., 2011; Arnold et al., 2012). Substantial amounts of gas are observed at smaller radii (this inside the dust cavity) via CO vibrational lines (e.g. Pontoppidan et al., 2008), O I 6300 and 5577 Å forbidden lines (e.g. Alencar & Batalha, 2002), OH mid-infrared lines (e.g. Najita et al., 2010), and Ne II emission at 12.8 μm (e.g. Pascucci & et al., 2011), and are indirectly probed by several accretion signatures ($\dot{M} \simeq 7 \times 10^{-10} M_{\odot}$/yr, see Curran et al., 2011, and references therein). Gorti et al. (2011) modelled the line properties of TW Hya with a gas surface density dropping by $\sim 1-2$ orders of magnitude inside the 4 AU dust cavity, similarly to what has been recently observed in transition discs with spatially resolved dust cavities (e.g. van der Marel et al., 2015). Since the paper by Calvet et al. (2002), many observers proposed a giant planet to be the cause of such an optically thin regime in the inner regions. Recently, Evans et al. (2012) set an observational upper limit of $14 M_{\rm J}$ for the purported planet/companion from a near-infrared aperture masking interferometry survey. However, other hypotheses have been proposed: interested readers are referred to Gorti et al. (2011), Pascucci & et al. (2011) and Alexander et al. (2014) for a discussion on the physical origin of the central hole, where internal photoevaporation and a giant planet hypotheses are considered and compared. The presence of a central planet is anyway highly plausible. It is very interesting that a natural explanation of the warping of the disc is therefore a misaligned planet, which induces a warp in the inner region of the disc, and simultaneously clears out the dust inner cavity. In this section we verify whether this picture is compatible with observations.

From Rosenfeld et al. (2012) we know that the best agreement between the observations and the warped model indicates $H_{\rm in}/R_{\rm in} = 0.1$, $p = 0.93$ and $q = 0.26$. We consider a disc with inner radius $R_{\rm in} = 4$ AU in gas, which appears to be the most plausible case. Rosenfeld et al. (2012) used a central star with mass $M_* = 0.8 M_{\odot}$ in their modelling. However, there has been a long debate on the mass of the central star. We do not give the details here, we just report that mass estimates for the star from spectral diagnostics range between $0.5 - 0.8 M_{\odot}$ (e.g. Alencar & Batalha, 2002; Vacca & Sandell, 2011). Debes et al. (2013) propose a mass estimate of $0.55 \pm 0.15 M_{\odot}$ by using spectral signatures and the light scattered by the dust-laden protoplanetary disc. We have run simulations between the two extremes, by considering $M_* = 0.8 M_{\odot}$ and $0.55 M_{\odot}$. A dynamic mass from gas kinematics still has large uncertainties, since the disc is almost face-on, and thus the projected gas velocities at large distances from the central star are very low.

We estimate the semi-major axis of the planet's orbit by requiring $R_{\rm in}$ to be the tidal truncation radius and M_* to be fixed in the centre of the planetary orbit. We can use this

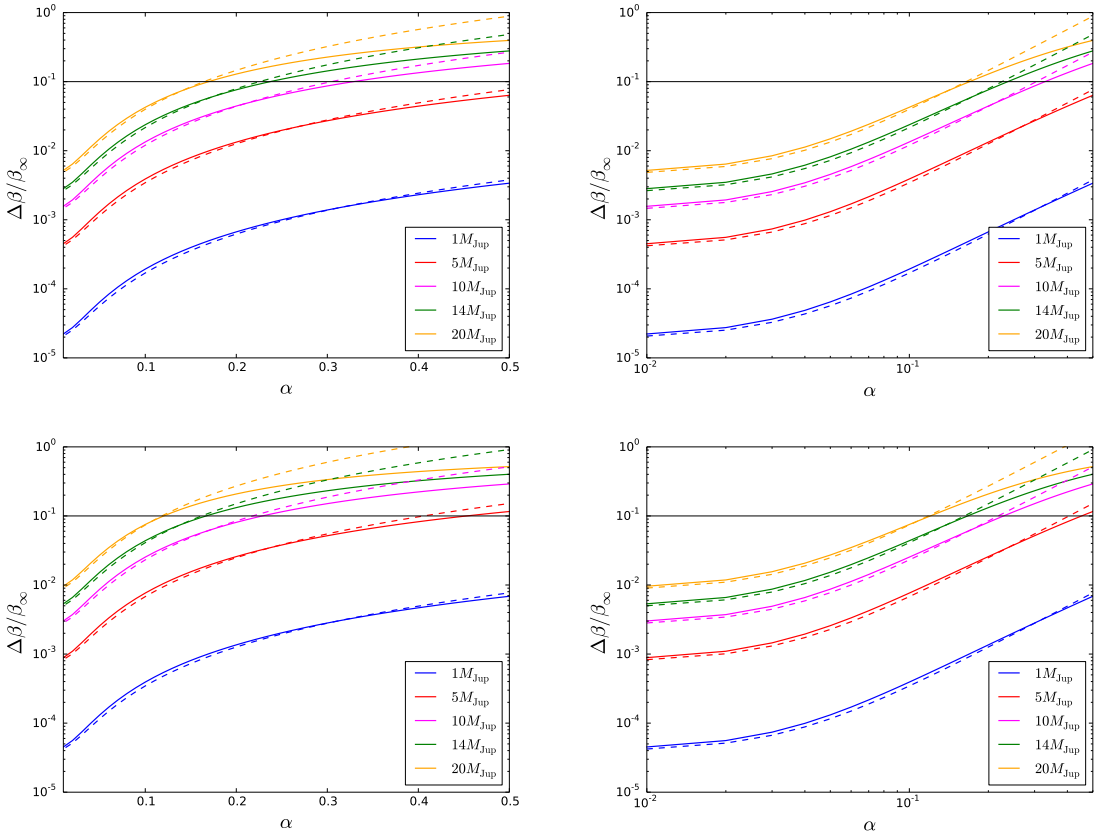

Fig. 3.3 Top two panels: $\Delta\beta/\beta_\infty$ as a function of viscosity for different planets masses and $M_* = 0.8M_\odot$. Bottom two panels: same results with $M_* = 0.55M_\odot$. The simulations are performed using the parameters reported in Rosenfeld et al. (2012): $p = 0.93$, $q = 0.26$ and $H_{\rm in}/R_{\rm in} = 0.1$. In the most extreme case, with the highest possible mass for the planet and the lowest possible mass for the star, the system would need a viscosity of $\alpha \approx 0.15$ to explain the hypothesised warp in this framework. In this specific case the model requires the fractional amplitude of the warp to be greater than 0.1, as shown by the horizontal black line. The dashed lines represent the degree of warping estimated using the analytic prescription from Eq. (3.2). For small warps ($\Delta\beta/\beta_\infty < 0.1$) the agreement between simulations and analytic prescription is remarkable.

approximation since $M_* \gg M_\mathrm{p}$, where M_p is the mass of the planet. We can approximate the inner disc radius to be related to the planetary semi-major axis by the equation:

$$R_\mathrm{in} = a + R_\mathrm{H}, \tag{3.3}$$

where the Hill's radius of the planet, R_H is:

$$R_\mathrm{H} = \left(\frac{M_\mathrm{p}}{3M_*}\right)^{1/3} a \approx 0.18a \left(\frac{M_\mathrm{p}}{14M_\mathrm{J}}\right)^{1/3} \left(\frac{M_*}{0.8M_\odot}\right)^{-1/3}. \tag{3.4}$$

We have made the simple assumption that the tidal and viscous torque are balanced at the Hill's radius of the planet, thus neglecting secondary effects dependent on the disc viscosity. We fix $R_\mathrm{in} = 4$ AU, as observed in the dust component. Thus, for any choice of M_p and M_*, we obtain R_in/a. In this way, we have reduced our model to a two dimensional parameter space, where the tilt of the disc $\Delta\beta/\beta_\infty$ depends on M_p and α only, where the stellar mass has been fixed to either $0.55M_\odot$ or $0.8M_\odot$. We recall that the steady-state solution of a circular circumbinary disc depends on χ and $\hat{\alpha}$, where χ is a function of both η and a. Since we know p, q, M_*, $H_\mathrm{in}/R_\mathrm{in}$ and $a(M_\mathrm{p})$, the only two free variables are M_p and α.

Rosenfeld et al. (2012) obtain a good agreement in the line profiles and in the channel map for the ^{12}CO $J = 2-1$ and ^{12}CO $J = 3-2$ emission lines with an outer disc inclination $i_\infty \approx 4^\circ$ and an inner disc inclination $i_\mathrm{in} \approx 8^\circ$. Therefore, we model a disc with a warping factor of $\Delta\beta \approx 4^\circ$. These observations, however, do not fully determine the warp fractional amplitude, since we do not know what is the orientation of the planetary orbit with respect to the plane of the sky. Note that, since in this case $R_\mathrm{warp} < R_\mathrm{in}$, we do not expect the inner disc to be aligned with the planetary orbit. One additional unknown is thus the misalignment between the outer disc and the planetary orbit, β_∞. However, SPH simulations by Facchini, Lodato & Price (2013) have shown that if the misalignment of the outer disc is larger than $\approx 40^\circ$, the evolution of the warp becomes non-linear. Even though the evolution of the system in the strongly non-linear case is not fully understood yet, Facchini, Lodato & Price (2013) indicate that in these conditions the disc might break into two separate planes and we would thus not expect a smooth warp. Since Rosenfeld et al. (2012) find a good agreement between the observed channel maps and a warped model with an inclination of the disc being a smooth function of R, we conservatively require that $\beta_\infty \lesssim 40^\circ$ (i.e. in the linear regime), so that $\Delta\beta/\beta_\infty \gtrsim 0.1$.

In Fig. 3.3 we show $\Delta\beta/\beta_\infty$ as a function of α for the two estimates of the star mass ($M_* = 0.8M_\odot$ and $0.55M_\odot$, respectively), where different lines depict different planet masses (from $1M_\mathrm{J}$ to $20M_\mathrm{J}$). The horizontal black line indicates the threshold $\Delta\beta/\beta_\infty = 0.1$. The

green line shows the $M_{\rm p} = 14 M_{\rm J}$ case, which is the observational upper limit for the mass of the planet. The dashed lines represent the analytic prescription given the used disc's parameters. The agreement between the analytic fitted prescription and the simulations for $\Delta\beta/\beta_\infty < 0.1$ is good. Note that these results do not depend on the estimate of $R_{\rm in}$. The amount of warping depends on $a/R_{\rm in}$, which is set by the tidal truncation radius condition (it is not a function of $R_{\rm in}$ itself, see Eqs. (3.3)-(3.4)).

Both plots at different stellar masses show that in order to reach the minimum value of $\Delta\beta/\beta_\infty \approx 0.1$, as discussed above, the planet needs to be relatively massive, at least $5 M_{\rm J}$, in the range of explored viscosities. Additionally, it is also apparent that the disc viscosity needs to be high. Even when $M_* = 0.55 M_\odot$ and $M_{\rm p} = 14 M_{\rm J}$, $\Delta\beta/\beta_\infty \gtrsim 0.1$ for $\alpha \gtrsim 0.15$. Therefore in the most extreme case, with the highest possible mass for the planet and the lowest possible mass for the star, the system would still need a viscosity of $\alpha \approx 0.15$ to explain the observed warp with this model. However, note that $\Delta\beta/\beta_\infty$ scales approximately with the inverse fourth power of $H_{\rm in}/R_{\rm in}$ (Eq. (3.2)). Thus, even a slightly smaller value for the disc aspect ratio would require a much smaller value of α in order to reach the same degree of warping, thus requiring a disc viscosity in better agreement with typical values estimated from mass accretion rates (Hartmann et al., 1998).

In our model, the planet is simultaneously inducing the warp and tidally clearing out the central cavity in the dust component. Since we requested α to be very large in order to model the observations by Rosenfeld et al. (2012), we need to check whether the inferred planet would still be able to open up a gap into the gaseous disc, and this generating a dust trap at slightly larger radii (e.g. Pinilla, Benisty & Birnstiel, 2012). In order a gap to be opened, the mass ratio between the planet and the star has to be larger than a critical value $q_{\rm crit}$, expressed by a simple combination of pressure and viscous terms (Armitage, 2010):

$$\frac{M_{\rm p}}{M_*} > q_{\rm crit} = \left(\frac{27\pi}{8}\right)^{1/2} \left(\frac{H}{R}\right)^{5/2} \alpha^{1/2}. \tag{3.5}$$

This criterion is verified by the values we use in our model ($\alpha = 0.15$ and $H/R = 0.1$) for all planet masses, except for the case $M_{\rm p} = 1 M_{\rm J}$. By assuming $M_* = 0.55 M_\odot$, we can express Eq. (3.5) as $M_{\rm p}/M_{\rm J} > 2.29$. Even with such large values of viscosity, the planet is still able to clear out a gap, since the planet itself needs to be very massive in order to induce a detectable warp.

Another critical point is whether the planet is able to maintain its inclination for long timescales. Terquem (2013) has recently shown that planets that orbit within a central cavity can maintain a high inclination with respect to the disc for timescales longer than the disc lifetime (> 10 Myr). Since the planet is well inside the cavity, there is no frictional force

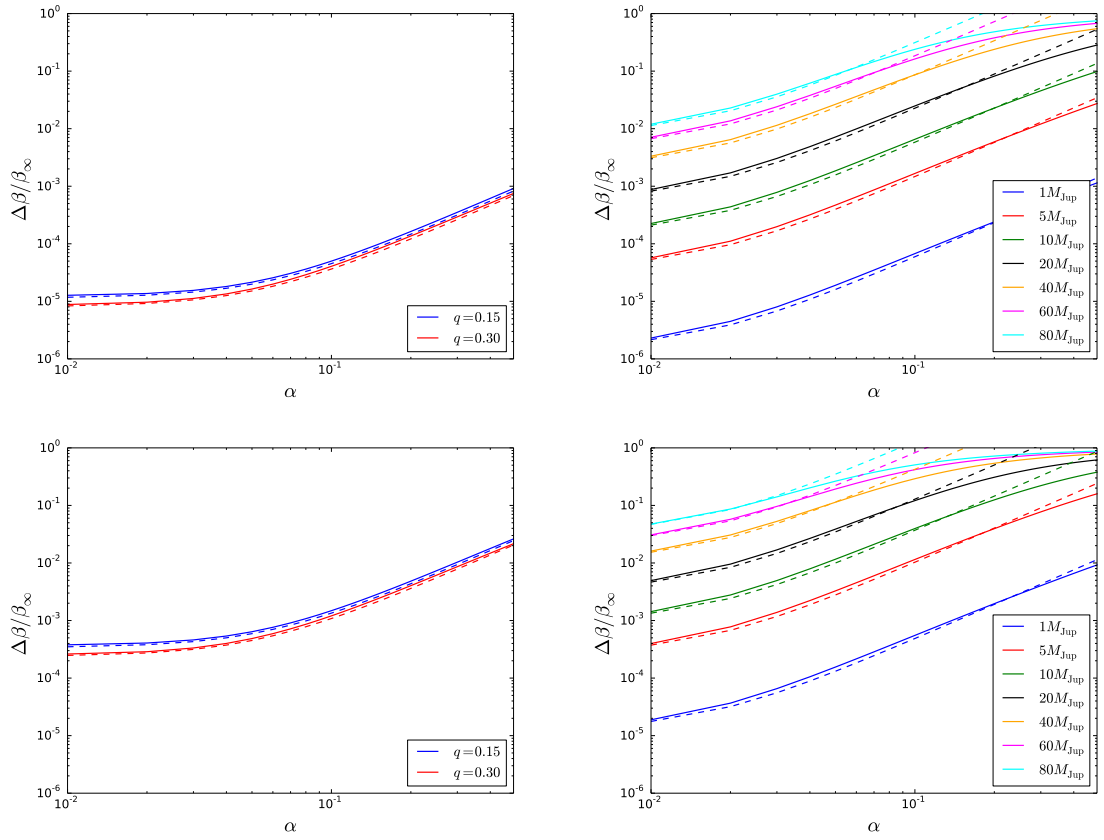

Fig. 3.4 Top left: $\Delta\beta/\beta_\infty$ as a function of viscosity for different values of q in the case of LkCa 15. Top right: $\Delta\beta/\beta_\infty$ as a function of viscosity for different values of $M_{\rm p}$ in the case of T Cha. The two bottom panels show the results of simulations equivalent to the ones of the top panels, but where $R_{\rm in}$ is estimated via Eq. (3.3), given the observed value of a. For LkCa 15 the expected warp is negligible in both cases. In the case of T Cha, if the companion has a mass of at least $20M_{\rm J}$ and sits on an inclined orbit with respect to the disc, an observable warp would be expected for reasonable values of the viscosity. As in Fig. 3.3, the dashed lines represent the degree of warping estimated using the analytic prescription from Eq. (3.2). For small warps ($\Delta\beta/\beta_\infty < 0.1$) the agreement between simulations and analytic prescription is good again.

	TW Hya	LkCa 15	T Cha
M_* ($M_\odot$)	0.55-0.8	1.0	1.5
p	0.93	0.72	1
q	0.26	-	0.4
$H_{\rm in}/R_{\rm in}$	0.1	$0.18\cdot(0.65)^{-q}$	0.078
$M_{\rm p}$ ($M_{\rm J}$)	$<$14	6	$<$80
a (AU)	-	16	6.7
$R_{\rm in}$ (AU)	4	42	12
$a+R_{\rm H}$ (AU)	-	18.0	7.1-8.4
References	1,2,3,4	5,6,7,8	9,10,11

Table 3.2 Parameters used in the simulations shown in Figs. 3.3-3.4 for TW Hya, LkCa 15 and T Cha, respectively. We list all the parameters that are constrained by observations, expect for $a+R_{\rm H}$, which is evaluated from the mass and the orbital radius of the substellar companion. To estimate $a+R_{\rm H}$ for T Cha, where only an upper limit on the mass of the companion is available, we have used masses between $1M_{\rm J}-80M_{\rm J}$. *References*: (1) Rosenfeld et al. (2012); (2) Andrews et al. (2012); (3) Evans et al. (2012); (4) Debes et al. (2013); (5) Piétu, Dutrey & Guilloteau (2007); (6) Andrews et al. (2011); (7) Isella, Pérez & Carpenter (2012); (8) Kraus & Ireland (2012); (9) Huélamo et al. (2011); (10) Cieza et al. (2011); (11) Olofsson et al. (2013).

that damps the orbit towards the disc plane (e.g. Teyssandier, Terquem & Papaloizou, 2013; Xiang-Gruess & Papaloizou, 2013). Therefore, if the planet reaches an inclined orbit within a central cavity of a disc via gravitational interaction or via secular perturbations, it can maintain such an inclination long enough to be statistically observable.

3.3.2 LkCa 15

LkCa 15 is a transition disc in the Taurus-Auriga star forming region (at a distance of $\sim$ 145 pc, Torres et al., 2009) with an inner cavity of roughly 45 AU (Espaillat et al., 2007; Andrews et al., 2011; Isella, Pérez & Carpenter, 2012). Recently, Kraus & Ireland (2012) have observed through aperture masking interferometry a protoplanet located at a distance of $\sim$ 16 AU from the star (for a circular orbit coplanar with the disc), that is, well within the cavity. The mass estimate for the planet is $6M_{\rm J}$, with an upper limit of $12M_{\rm J}$. The stellar mass is $\sim 1M_\odot$ (Simon, Dutrey & Guilloteau, 2000). The inclination of the disc is 49° (Andrews et al., 2011). No warp has been observed in the disc from gas kinematics. However, recent SPHERE observations by Thalmann et al. (2015) suggest that the system is bearing an inner disc, which is slightly misaligned (by $\sim 1^\circ$) to the outer disc.

Here, we estimate the expected $\Delta\beta/\beta_\infty$ that would occur (for a linear warp) if the planetary orbit were inclined with respect to the disc. The assumed parameters for the disc

are summarised in Table 3.2. The resulting fractional warp amplitudes are shown in Fig. 3.4 (top left panel) as a function of α for the extreme values of the power-law index for the sound speed q in the range predicted by Piétu, Dutrey & Guilloteau (2007) ($q = 0.15$ and $q = 0.30$). For any reasonable choice of parameters the expected warp amplitude is extremely low ($\lesssim 10^{-3}$) and we thus do not expect to observe a warp in the outer disc even if the misalignment of the orbit is large. Note however that the inner edge of the disc is much larger than the expected tidal radius of the planet. This could be due to the fact that the estimates of the inner radius of the disc come from millimetric observations, therefore tracking dust grains with a size of ≈ 1 mm. Gas (and small dust) could extend well within the millimetric dust cavity (e.g. Pinilla, Benisty & Birnstiel, 2012), as observed in some systems (e.g. Garufi et al., 2013), where the gaseous inner radius is estimated via SED modelling in the IR or via scattered light measurements (therefore tracking micron-size dust, which is dynamically well coupled with the gas). We have therefore re-run the simulations by assuming a gaseous inner radius given by Eq. (3.3). The results are shown in the bottom left panel of Fig. 3.4. The expected fractional warp increases by a factor of ~ 15. but for this system, it remains under the detectability threshold. Besides, an inclined planet might be at the origin of the misaligned inner disc, if future observations confirm such geometry. Modelling the interaction between the planet and the inner disc would require a different form of the torque, and we thus not analyse this possibility here.

3.3.3 T Cha

T Cha is a transition disc at a distance of ~ 108 pc (Torres et al., 2008) with an inner cavity of ~ 12 AU (Olofsson et al., 2013). A companion candidate has been observed at a separation of 6.7 AU (Huélamo et al., 2011). In this case there is no mass estimate for the companion. The stellar mass is $\sim 1.5 M_{\odot}$ (Alcala et al., 1993). Also in this case, no warp has been observed in the disc in the gas kinematics probed by ALMA Band 7 observations of CO isotopologues $J = 3-2$ rotation line, with a velocity resolution of 0.1 km/s, and an angular resolution of 0.5" (Huélamo et al., 2015). The inclination of the disc is 60° (e.g. Cieza et al., 2011). The assumed parameters for the disc are summarised in Table 3.2.

The resulting fractional warp amplitudes are shown in Fig. 3.4 (right panels) as a function of α for different values of the companion mass ranging from a gaseous giant up to a brown dwarf mass. The top panel shows simulations where $R_{\rm in}$ is equal to the observed value, whereas in the bottom panel $R_{\rm in}$ is estimated with Eq. (3.3). In this second case a sizable warp is expected if the companion mass is larger than $40 M_{\rm J}$ for $\alpha \sim 0.06$. For a less viscous disc, the warp amplitude is expected to be lower and thus only companions with high mass (in the brown dwarf regime) can be expected to produce an observable warp.

3.4 Conclusions

In this chapter we have shown how warped circumbinary discs can be used to study some key physical properties of protoplanetary discs. We have reported a simple prescription that can be used to relate the amount of warping of these discs with the dynamical properties of the two central objects. This relation generalises previous results (Foucart & Lai, 2013) to a wider parameter range and to cases where either the binary torque or the disc viscosity are large enough to lead to the alignment of the inner disc, a situation that has been neglected before. These results are general, and they can be applied both to stellar binaries, to a star and a brown dwarf, and to a central star and a planet.

Observing a misaligned protostellar circumbinary disc would give new constraints on the magnitude of the disc's viscosity (King et al., 2013). As reported in Section 3.1, existing facilities have the capability to measure warps in protostellar discs by looking at the kinematics of the gas. Once the system's dynamical parameters are known (for example, the masses and orbit of the central binary) the other parameter that determines the warp amplitude is the disc viscosity, so that by measuring the amount of warping in a disc it is possible to have an indirect measure of the disc's viscosity itself. Note that a similar approach has been recently attempted (e.g. King et al., 2013; Lodato & Facchini, 2013), by studying the alignment timescale for either a circumbinary or a circumprimary disc.

We then applied such 1D model to TW Hya. In this system, Rosenfeld et al. (2012) have measured a velocity pattern that is not consistent with a flat Keplerian disc and have hypothesised that a warp is present in the disc, whose inclination changes by 4 degrees between the inner and outer radius. TW Hya is also a transition disc, with a large inner hole that can be caused by the tidal interaction with a massive planet $M_{\rm p} \lesssim 14 M_{\rm J}$. Here, we investigate the possibility that the same planet is also responsible for the warp in the disc. A major piece of information that is missing from observations is the orientation of the orbit of the purported planet. Here, we have assumed that the warp is linear and thus that the misalignment of the outer disc cannot be too large (we conservatively require $\beta_\infty \lesssim 40^\circ$), which then implies that $\Delta\beta/\beta_\infty \gtrsim 0.1$. Note that in the linear assumption, the warped structure is smooth in its radial dependence, as required by Rosenfeld et al. (2012) to obtain a good agreement between the observations and a simple warped disc model. We then investigated what disc and orbital parameters are required to reproduce such degree of warping. We conclude that the planet needs to be relatively massive and the disc needs to be relatively viscous. For $M_{\rm p} = 10 - 14 M_{\rm J}$, we require $\alpha \approx 0.15 - 0.25$. These results depend sensitively on the assumed aspect ratio of the disc ($H_{\rm in}/R_{\rm in} = 0.1$) and our constraints would be lessened if the disc was thinner.

We expect that with the new ALMA observations, this kind of warped structures in protoplanetary discs will be observed more frequently and we thus expect our method to be applied to a much wider sample in the future. This method will favour systems with some characteristic features. Using the gas emission lines profile to measure the warp, as described by Rosenfeld et al. (2012), will favour closely face-on discs. In this condition $\sin i \sim i$, therefore the projected radial velocity will be linearly sensitive to the inclination angle. Secondly, independently from the used technique, at a given mass ratio between the central star and the companion, the warping will be more pronounced for low values of the scale-height H, i.e. for thinner and colder discs. Finally, the warp will be more prominent for a larger mass ratio (where the mass ratio is defined as M_p/M_*). Therefore, for a given planet mass, low mass stars (as M dwarfs) will be favoured.

Chapter 4

A tidal encounter caught in the act: modelling a star-disc fly-by in the young RW Aurigae system

In this chapter and in the following one we move forward from the effects of multiplicity on the evolution of discs, and we focus on observations and modelling of the only known system that has recently undergone a star disc - encounter: RW Aur. This object represents a unique possibility of comparing the theoretical expectations described in Section 1.3.1 with a real system. This chapter is based on the published paper by Dai et al. (2015). Most of the SPH simulations have been run by Fei Dai, a M.Sc. student I have mentored during the second year of my PhD, and all the radiative transfer has been performed by Thomas J. Haworth, a PDRA working in my group. Along with Prof. Clarke I have led the project, understanding the geometry of the system, performing most of the analysis of the SPH simulations and writing most of the paper.

4.1 Introduction

RW Aurigae is a young stellar system comprising two roughly solar mass stars at a projected separation of 1.5", i.e. 200 AU at a distance $d \simeq 140$ pc (cfr. Hipparcos catalogue, van Leeuwen, 2007b). The primary is a Classical T Tauri Star which is characterized by an unusually high ratio of accretion rate ($2 - 10 \times 10^{-7} M_{\odot}$ yr^{-1}, Basri & Bertout, 1989; Hartigan, Edwards & Ghandour, 1995) to disc mass ($\sim 10^{-4} M_{\odot}$ as derived from mm continuum dust emission, Osterloh & Beckwith, 1995).

The most notable feature of the RW Aurigae system is the 600 AU long arm structure trailing from the disc of RW Aur A which was imaged by Cabrit et al. (2006) in ^{12}CO($J = 2-1$) and ^{12}CO($J = 1-0$) with the IRAM (Institut de Radioastronomie Millimétrique) Plateau de Bure Interferometer. Cabrit et al. (2006) noted the resemblance between this structure and the tidal arm stripped from the primary star in the simulations of star-disc encounters by Clarke & Pringle (1993). Although these simulations were not designed to fit a particular observation, the superficial resemblance between the morphology of RW Aur and the prograde encounter of Clarke & Pringle (1993) was striking. It is however unclear without detailed modelling whether simulations can fit all the parameters of the system, particularly the gas kinematics and the available radial velocity and proper motion data for the two stars. Moreover Bisikalo et al. (2012) presented evidence from proper motion data that the encounter might in fact be retrograde in which case the Clarke & Pringle (1993) models would predict a morphology unlike that observed in RW Aur. Bisikalo et al. (2012) have on this basis proposed an alternative model involving circumbinary disc accretion. In the detailed modelling that we present below we shall attempt to fit all the available kinematic constraints through a star-disc encounter (i.e we assume that the system is either highly eccentric or marginally unbound. For justification of this assumption, see Section 4.3.3), but note that, since the errors on the proper motion data in Bisikalo et al. (2012) are large, we shall place more emphasis in fitting the radial component of the stars' relative space motions on the plane of the sky.

Interest in the RW Aurigae system has recently been revived by the photometric observations of Rodriguez et al. (2013). Their optical monitoring detected a 2 mag dimming event lasting 180 d which the authors intriguingly interpreted in terms of occultation of RW Aur A by a portion of the tidal arm. We shall investigate whether our best model for the encounter involves a geometry that would permit such an event.

In this chapter we use new hydrodynamical models and synthetic observations to fit many of the parameters of RW Aur. We aim to understand the geometry of the binary system, the mechanism/geometry responsible for its morphological appearance, other observed properties (such as molecular line profiles) and the recent dimming event found by Rodriguez et al. (2013). The rest of this chapter proceeds as follows. In Section 4.2 we describe the range of observational constraints of the RW Aur system which we shall use to constrain our models. In Section 4.3 we outline the codes used in our investigation (the PHANTOM SPH code which is used for the hydrodynamical simulations and the TORUS[1] Monte Carlo radiation transport code which is used to produce synthetic observations from the results of the hydrodynamic models) and also the initial conditions and parameter space surveyed. In Section 4.4 we

[1]http://www.astro.ex.ac.uk/people/th2/torus_html/homepage.html

present and discuss our best-fitting model solution and the degree to which various system parameters are constrained by the observations. In Section 4.5 we present the detailed line profiles and continuum emission map for our best-fitting model. Section 4.6 discusses a possible origin of the 'dimming event' in the light curve of RW Aur, and whether it could be associated with occultation by the tidal arm. Section 4.7 summarizes our conclusions.

4.2 Observations of RW Aur

4.2.1 The disc around star A

The ^{12}CO$(J = 2-1)$ emission from close proximity to RW Aur A shows a perfect point symmetry between its redshifted and blueshifted lobes. Furthermore, the radial velocity gradient is perpendicular to the optical jet. Both of these features suggest an axisymmetric geometry, i.e. RW Aur A most likely has a rotating disc (Cabrit et al., 2006). The sky inclination of the disc was constrained using the ratio of the radial and tangential velocities of emission knots in its jet (López-Martín, Cabrit & Dougados, 2003). Alternatively, the inclination was also constrained by the radial velocity of the jet itself. Combining these, the sky inclination was estimated to be in the range of $45-60^\circ$ (Woitas et al., 2002).

The observed flux densities in ^{12}CO$(J = 2-1)$ and ^{12}CO$(J = 1-0)$ has a ratio of about 4 (see fig. 4 by Cabrit et al., 2006). The ratio of 4 is the square of the frequency ratio between these two lines. This suggests that the disc is optically thick in which case the Rayleigh-Jeans limit predicts that $B_\nu = 2kT\nu^2/c^2$. Beckwith & Sargent (1993, hereafter BS93) predicted that for an optically thick, Keplerian, vertically isothermal disc of radial temperature profile $T \propto R^{-q}$, the molecular line profile scales as ν^{3q-5} towards the wings of the line profile. The disc line profile observed by Cabrit et al. (2006) suggests that $q \sim 0.73$. The same parameter q was also independently estimated as ~ 0.57 from the infrared spectral energy distribution (Osterloh & Beckwith, 1995). The BS93 model also predicted that the peak flux density of disc line profiles occurs at the velocity of the disc's outer radius: $V_{\rm peak} = \sin(i)(GM/R_{\rm out})^{0.5}$. The observed peak for A's disc (~ 3.5 km/s) then constrains $R_{\rm out}$ to be in the range of $50-77$ AU respectively for an inclination of $45-60^\circ$. Cabrit et al. (2006) noted that stellar mass and outer disc radius are degenerate when considering the observed peak velocity. Therefore they argued that the better approach is to compare the shape (rather than absolute peak velocity) of observed and theoretical line profiles in BS93; they claimed $R_{\rm out}$ to be $40-57$ AU.

Cabrit et al. (2006) estimated the temperature of the disc at its outer radius with two methods:

1) Measuring the peak flux density of the disc line profile and using the BS93 model which predicted that the peak flux density scales as $F(\lambda) \sim \lambda^{-2} R_{\rm out}^{5/2} T_{\rm out}^{3/2} M_{\rm star}^{-0.5} d^{-2}$;

2) Using the brightness temperature since the disc is optically thick and in the Rayleigh-Jeans regime.

The two methods consistently gave a temperature of $60-107$ K (the range corresponding to different sky inclination) at the outer radius of the disc.

Cabrit et al. (2006) further estimated the column density of the disc. The fact that the disc is optically thick in ^{12}CO and undetected in ^{13}CO placed lower and upper limits on the column density respectively. These CO column density limits were converted to total column densites using standard ^{12}CO and ^{13}CO abundances in the local interstellar medium. Assuming that the disc surface density scales as $1/R$, Cabrit et al. (2006) derived an estimate of the total mass of the disc of $10^{-5}-10^{-4} M_{\odot}$. This is consistent with the mass estimate by Osterloh & Beckwith (1995) ($3\times10^{-4} M_{\odot}$), but not with the higher estimate by Andrews & Williams (2005) ($4\times10^{-3} M_{\odot}$).

4.2.2 The tidal arm

^{12}CO molecular emission from the tidal arm is entirely redshifted (with the peak velocity at $3.2-3.8$ km/s with respect to star A, Cabrit et al., 2006). The observed radial velocity is larger than the escape velocity at the corresponding distance, indicating that the motion of the tidal arm is unbound. The tidal arm is also optically thick as the observed ^{12}CO$(J=2-1)$/ ^{12}CO$(J=1-0)$ flux density ratio is ~ 4. The tidal arm extends about $4^{"}(\sim 600)$ AU at the distance of 140 pc.

4.2.3 The molecular complex around star B

^{12}CO molecular emission around star B has a broad and asymmetric peak blueshifted by $3-6$ km/s with respect to star A. The asymmetric peak cannot be attributed to an undisturbed rotating disc. Given that the tidal interaction hypothesis is favoured, the molecular complex around B most likely consists of material captured during the tidal encounter. The ^{12}CO$(J=2-1)$/ ^{12}CO$(J=1-0)$ ratio was observed to be ~ 5.7 suggesting that the molecular complex around B is marginally optically thick (Cabrit et al., 2006). Note, however, that the signal to noise of the ^{12}CO$(J=1-0)$ emission line is very low, we therefore do not use this line as a constraint to discuss our model.

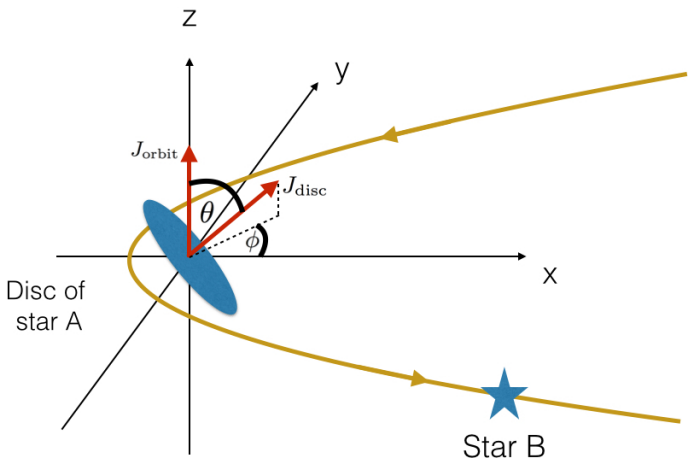

Fig. 4.1 A schematic illustrating the polar and azimuthal angle used to define the mutual inclination between the angular momenta of the disc and the orbit of the secondary.

4.2.4 Proper motion of the system

Bisikalo et al. (2012) compiled the position angles of star B and the angular separations between star A and B over the past 70 yr. Linear regression analysis showed that the projected AB separation was increasing at $0.002''$/ yr. 70 yr is short compared to the Keplerian orbital period ($\sim$ 2000 yr) at the observed separation ($\sim 1.5''$, or 200 AU for 140 pc away), thus justifying a linear approximation for the velocity. They similarly claimed that the position angle of star B was *increasing* at a mean rate of 0.02°/yr, which would imply that the orbital motion of the pair was *anti-clockwise* as projected on to the plane of the sky. This conclusion is however not firm given that the claimed increase is based on a fit involving data from the 1940s whose radial component was discrepant with the recently observed trend of increasing separation. Moreover this fit to the tangential data is in the opposite sense to the apparent trend observed during the 1990s (although the uncertainties during this period were large). We therefore only constrain our model such that the sky-projected separation of star A and B is increasing at the current epoch. Future proper motion observations are needed to decide whether the motion of the two stars projected into the plane of the sky is clockwise or anti-clockwise.

4.2.5 The dimming event

Rodriguez et al. (2013) reported a long ($\sim$ 180 d) and deep (2 mag) dimming of RW Aur from 2010 September until 2011 March. Typical photometric variations of CTTS (Classical T Tauri Stars) only last for days and weeks with a depth $<$ 1 mag. This is usually associated

with circumstellar extinction or hotspots on the accretion disc that rotate into and out of the observer's view. Rodriguez et al. (2013) noted that there was no similar dimming event[2] for the system in the past 50 yr and proposed that the dimming may be due to the occultation of star A by the leading edge of the tidal arm. They further estimated that the occulting body was moving with a transverse velocity of $0.86-2.58$ km/s (dividing the stellar radius of star A by the ingress time of the dimming). The size of the occulting body was estimated to be $\sim 0.09-0.27$ AU using the product between the duration of the dimming and the derived velocity. The large range in the estimates of transverse velocity and size are due to the large uncertainties on the ingress time-scale, approximately between 10 and 30 d.

More recently, Antipin et al. (2015) have again detected RW Aurigae in the 'low state' (i.e. 3-4 mag less than what observed by HST in the mid-90's, White & Ghez, 2001).

4.2.6 Summary of observational constraints

Among the various observations, we identified the following key criteria to gauge how closely our simulations describe the observations. These features were more reliably constrained by observations; they are also easily quantifiable in simulations:

1) The size of the system: Cabrit et al. (2006) reported that the tidal arm extended about $4^{"}$(~ 600 AU at a distance of 140pc); the projected AB separation was $\sim 1.5^{"}$ (~ 200 AU). We aim to reproduce the size of the system as observed. However we argue that it is more important to fit the relative ratio between the dimensions of various structures of the system. This is because the relative ratio is independent of the error in the distance measurement (a parallax of 7.08 ± 0.71 mas corresponding to a distance of 140 ± 14 AU Basri & Bertout, 1989).

2) The relative orientation of the A disc and star B. We gauged the relative orientation using position angles (PA). For the disc, its position angle is defined as the angle between its radial velocity gradient and north. For star B, PA is defined as the angle between the vector joining star A and B and North. According to Cabrit et al. (2006), the PA of the disc is $\sim 40^{\circ}$; the PA for B is $\sim 105^{\circ}$ (or 255° if using the convention of Bisikalo et al., 2012).

3) Sky inclination of the disc: the sky inclination of the disc was estimated to be in the range of $45-60^{\circ}$ (Woitas et al., 2002; López-Martín, Cabrit & Dougados, 2003).

[2]Note that the long term light curve does show a number individual photometric data points at the 'low' level recorded in the 2011 event but a well resolved eclipse light curve has not been detected hitherto.

4) Proper motion: as reported by Bisikalo et al. (2012) the angular separation between star A and star B was increasing at a rate of 0.002”/ yr.

5) The line profiles: the radial velocity of the peak, the peak flux density and the optical depth.

4.3 Numerical Method

4.3.1 Hydrodynamics models

We model the stellar fly-by using the SPH code PHANTOM, the same code we used to model warped discs in chapter 2. We assume that self-gravity in the disc is negligible and that the gravitational potential is dominated by the stars. We employ a locally isothermal equation of state and adopt standard artificial viscosity parameters ($\alpha = 0.1; \beta = 2; \sigma = 0.1$) according to the presciption of Morris & Monaghan (1997). As we will specify in Section 4.3.4, we use 10^5 SPH particles for the parameter space study, and 10^6 particles for the most representative model.

4.3.2 Synthetic observations

We use the radiation transport and hydrodynamics code TORUS to compute synthetic observations in this chapter. TORUS is predominantly a Monte Carlo radiation transport code used for calculating line and continuum transport (e.g. Harries, 2000; Kurosawa, Harries & Symington, 2006) but also features photoionization (Haworth, Harries & Acreman, 2012), non-LTE molecular line transfer (Rundle et al., 2010) and hydrodynamics (Haworth & Harries, 2012).

We map the result of the SPH simulation on to the TORUS grid using the technique described in Acreman, Harries & Rundle (2010). We do not explicitly derive the temperature using radiative transfer, but rather assume that the temperature distribution in the model is a function of cylindrical distance from the primary (see below; equation 4.1), as in Cabrit et al. (2006). For molecular line transfer calculations we solve the equations of non-LTE statistical equilibrium and produce synthetic data cubes in the manner described in detail by Rundle et al. (2010).

Since we are comparing with the observations from Cabrit et al. (2006) we consider the ^{12}CO($J = 2-1$) and ($J = 1-0$) lines and assume the same parameters, i.e. the ^{12}CO abundance relative to hydrogen is 8×10^{-5} and the system is at a distance of 140 pc from the observer. We assume a small micro turbulence value of 0.03 km/s. The data cubes comprise 401×401 pixels and 36 velocity channels spanning -7.19 to 7.63 km/s. This velocity range

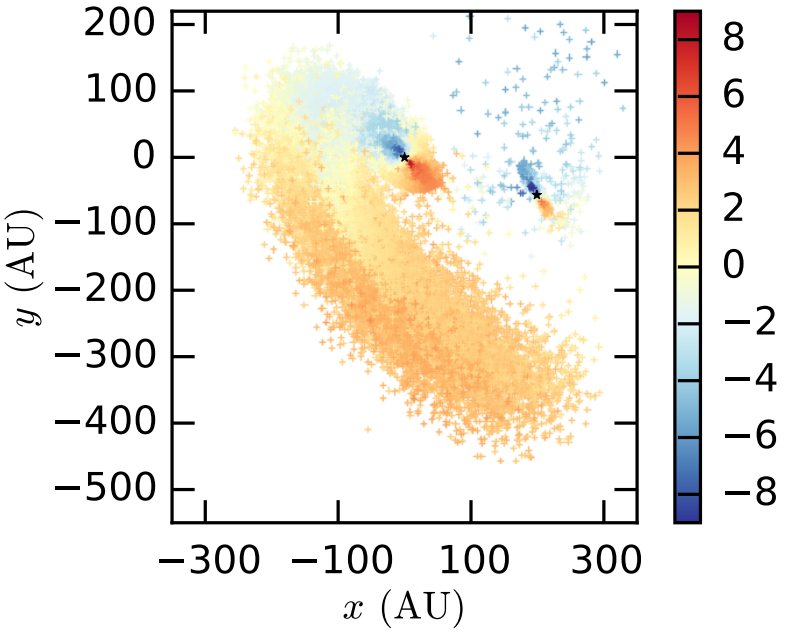

Fig. 4.2 The gas morphology of the best-fitting model in the frame of reference comoving with star A. The *x*-*y* plane indicates the plane of the sky. Crosses indicate SPH particles, which were selected randomly every other 10 particles. The black stars show the position of Star A and B. Colour coding is linear in radial velocity (km/s). Note, for direct comparison with Fig 4.3(c), the heliocentric velocity (15.87 ± 0.55 km/s, Cabrit et al., 2006) of the star A should be added.

and number of channels is chosen to match the IRAM Plateau de Bure Interferometer, the instrument used for the observations in Cabrit et al. (2006) against which we compare our models. The beam size is chosen to match that of the IRAM Plateau de Bure Interferometer (2.42" $\times$ 1.55" and 0.89" $\times$ 0.58" for the $J = 1-0$ and $J = 2-1$ transitions respectively). We convolve the resulting data cubes with a 2-D Gaussian with a width corresponding to the semiminor axis of the two beams using ACONVOLVE from CIAO v 4.5 (Fruscione et al., 2006). Finally, the line profiles of the synthetic observations are obtained by integrating over ellipses that match the ones used by Cabrit et al. (2006).

We also compute a 1.3 mm continuum image using Monte Carlo radiative transfer, algorithmic details of which are given in e.g. Harries (2000) and Harries et al. (2004). We discuss the assumed dust distribution in Section 4.5.2.

4.3.3 Initial conditions

We model the encounter geometry shown in Fig 4.1. in which a spherical polar system (with the z-axis along the normal to the plane of the secondary's orbit, and the x-axis pointing towards the apocentre) is used to define the coordinates (θ, ϕ) of the disc normal (where the separation vector of the two stars at pericentre is located at $\phi = \pi$). We populate particles in a Keplerian disc around the primary according to a prescribed surface density law (see below) and with a Gaussian distribution normal to the disc plane which is the hydrostatic equilibrium solution set by the imposed local temperature (see below). For reasons of computational economy we set an inner radius of 5.9 AU and do not continue to integrate particles that stray within this radius.

We argue that the presence of a single well-defined tidal feature in the observations suggests that the disc of RW Aur A has been subject to either a one-off encounter or to an encounter that is well separated in time from any previous interactions. Thus we consider it likely that the orbit is either of high eccentricity or unbound. It is unlikely that the encounter is *highly* hyperbolic since this would imply a relative velocity at infinity that exceeds typical stellar velocity dispersions in star forming regions. We thus expect that the orbit - whether mildly bound or mildly unbound - is likely to be close to parabolic and hence model this situation here.This is consistent with the low relative radial velocity between the two stars reported by White & Hillenbrand (2004). The masses of RW Aur A and B are set to $1.4 M_{\odot}$ and $0.9 M_{\odot}$ respectively (Ghez, White & Simon, 1997; Woitas, Leinert & Köhler, 2001).

We set the surface density profile to $\Sigma \propto 1/R$ and adopt a power law temperature profile as a function of cylindrical distance from the primary parametrized according to

$$T = T_0 (R/R_0)^{-q} \tag{4.1}$$

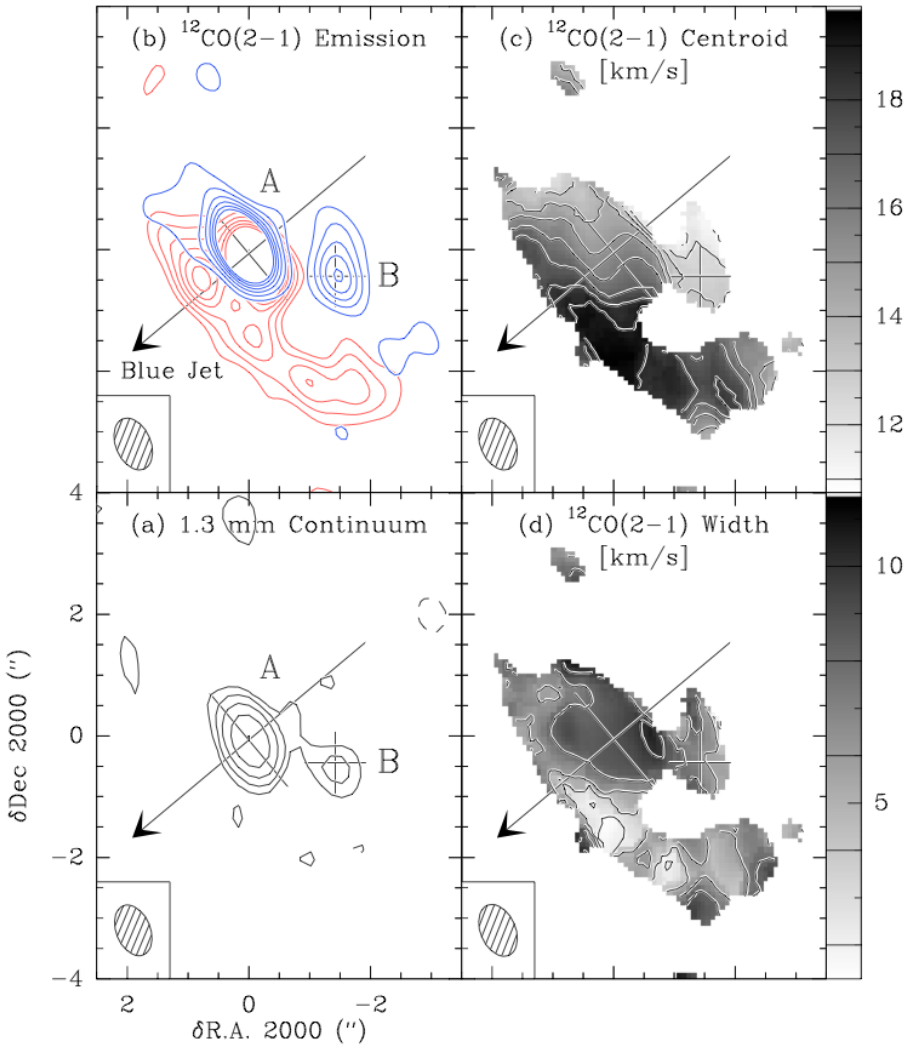

Fig. 4.3 Fig. 1 from Cabrit et al. (2006), showing the interferometric data of PdBI. From their caption: "**a)** 1.3 mm continuum map of the RW Aur system. Contour levels are 3, 6, 12, 24, 48σ ($1\sigma = 0.47$ mJy/beam). Crosses indicate the peak positions, which closely correspond to RW Aur A and B. The large arrow shows the direction of the blueshifted jet. **b)** ^{12}CO$(J = 2-1)$ emission blueshifted and redshifted with respect to the RW Aur A systemic velocity. Contour spacing is 3σ (0.12 Jy km s^{-1}), truncated to 18σ for clarity. **c) and d)** Heliocentric centroid velocity and line width (i.e. first and second order moments) of the ^{12}CO$(J = 2-1)$ line."

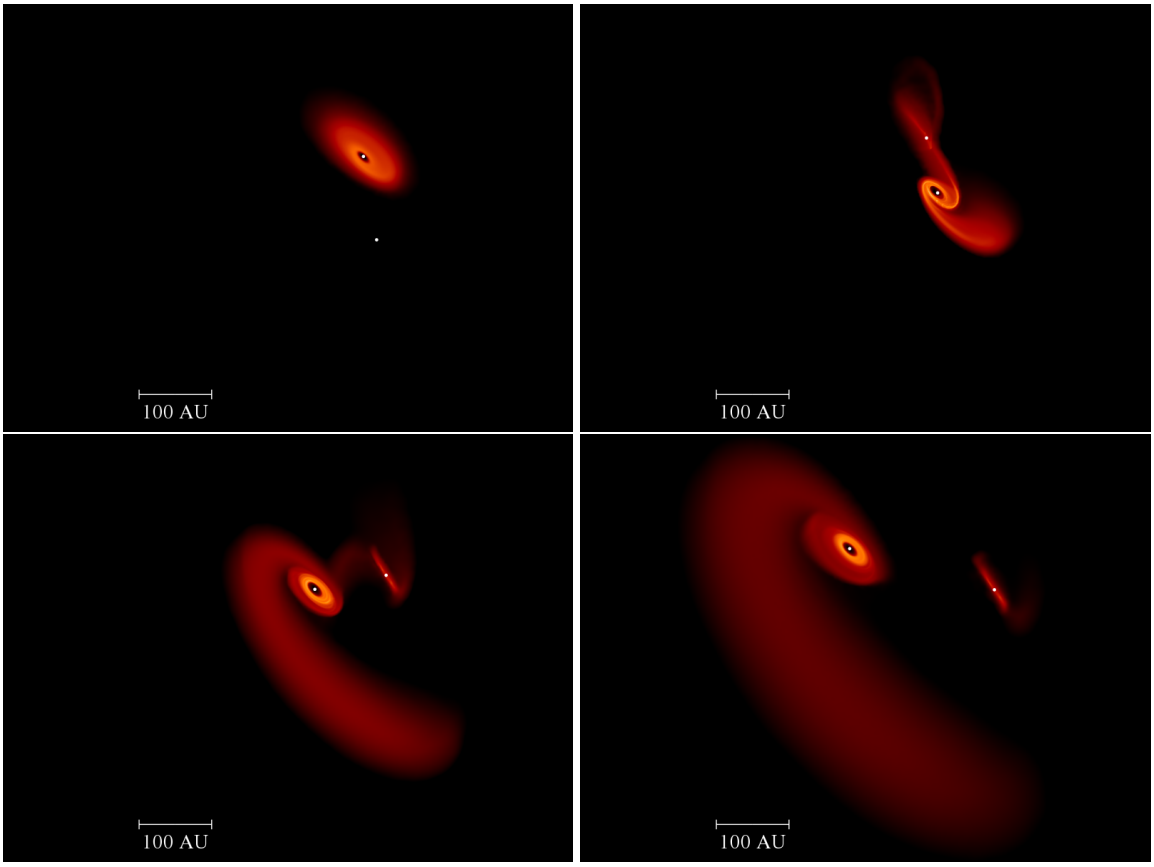

Fig. 4.4 Evolution of the tidal encounter in the plane of the sky, shown with four different snapshots. The bottom right panel shows the structure as seen today. From top left to right bottom the snapshots are taken at -589, -398, -207 and 0 yr from today, respectively. The surface density is logarithmically scaled, and was chosen such that the final snapshot resembles the observations by Cabrit et al. (2006). Note that a stream of material linking star A and star B is present, even though it does not appear in the bottom right panel, due to the choice of surface density threshold (compare this final snapshot with the right-hand panels of Fig. 4.11).

The radial index, q has been estimated to be in the range $0.5 - 0.73$ by various authors ($q = 0.57$ and $q = 0.73$ Osterloh & Beckwith, 1995; Cabrit et al., 2006, respectively). We adopt a temperature around 60 K at $R = 57$ AU in line with the estimate of Cabrit et al. (2006) for an inclination of the disc $i = 60^\circ$, and vary the value of q (which affects the pressure scale length of the outer disc and has a modest effect on the morphology of the tidal tails produced).

The simulation is initiated when the stellar separation is ≥ 10 pericentre radii in order to ensure that the disc is not violently perturbed by the sudden introduction of the companion in its vicinity.

4.3.4 Constraining other parameters

After setting up our model with the plausible initial conditions discussed in the previous section, in principle one could constrain the various other orbital parameters by running the hydrodynamic simulation and synthetic observations in conjunction with a parameter study tool (e.g. Markov chain Monte Carlo). However, such a parameter study is unfeasible in our case: conventionally, 10^6 particles are needed for sufficient resolution in such a hydrodynamic simulation. In conjunction with the simulated observations, this would take several days of computation per model. Moreover there are at least 10 remaining parameters in the model and so the time required for such an approach would be prohibitive.

Instead we adopted the following strategy. We initially ran our hydrodynamic code with 10^5 test particles on a coarse grid in the 10-D parameter space. We then focused on the region that is most consistent with various observational constraints. Parameters were then tuned until simulated values converged to observed values within respective uncertainties. Finally we repeated the same model with 10^6 SPH particles and appropriate scalings (e.g. viscosity scales with number of particles) to reveal small-scale details of the system.

We remind the reader that although we refer to this final model as the best-fitting one, in reality this is only the best-fitting model among the few dozen models we tested. Given the uncertainties in the observations (Section 4.2) and the various shortcomings of our simulations, the statistical errors introduced from our sampling strategy are likely to be outweighed by other factors (see discussion in Section 5). We nevertheless argue that the good level of agreement between simulations and observations in the models performed is already sufficient to demonstrate that the tidal encounter hypothesis is indeed consistent with the existing observations.

Table 4.1 Quantitative comparison of best-fitting model outputs and observed values. [a] From Cabrit et al. (2006) assuming $d = 140$ pc where necessary. [b] López-Martín, Cabrit & Dougados (2003), Woitas et al. (2002). [c] Bisikalo et al. (2012).

Observed features	Observed values	Best fit simulation values
Length of tidal arm	600 AU (4")[a]	650 AU
AB separation on sky	200 AU (1.5")[a]	200 AU
PA of disc (°)	40[a]	47.2
PA of AB (°)	105[a]	105.9
Inclination of disc (°)	45 – 60[b]	64.0
Rate of change of	0.002"yr^{-1}[c]	0.003"yr^{-1}

4.4 Results of hydrodynamics models

In this section, we first consider the parameters of the encounter that affect the gross properties of the flow (i.e. the morphology and kinematics of the tidal tail and disc). It is sufficient for such an analysis to be conducted with the hydrodynamic code alone in the limit of optically thin emission. We fix the stellar masses and eccentricity of the orbit for all simulations and for each simulation we adopt given values of θ and ϕ, of pericentre distance, disc outer radius, surface density and temperature normalization, and temperature power-law index. In Section 5, we consider whether a plausible initial disc model can then reproduce line fluxes and line profiles by using synthetic observations for a range of output times and viewing angles (constrained so as to give the correct projected separation of the two stars on the sky). The viewing angle is parameterised in terms of the direction of the line-of-sight vector identified by the polar coordinates $\theta_{\rm obs}$ and $\phi_{\rm obs}$ in the coordinate frame shown in Fig. 4.1.

4.4.1 Sensitivity of results to parameter choice

To determine which model is most consistent with observations, we vary each parameter around the initial estimates obtained from the pilot simulations. We then identify the system observables that are most dependent on each parameter in order to constrain that parameter.

The choice of periastron separation (70 AU) was mainly decided by fitting observed length and width of the tidal tail both of which increase with pericentre separation (see Fig. 4.5a). The length and width of the tidal tail is also dependent on time of observation. However this degeneracy can be broken, since the choice of periastron separation must also give a consistent radial velocity of material in the tidal tail which is similar to the escape velocity at periastron (see Fig. 4.7). Moreover, since the disruptiveness of the encounter

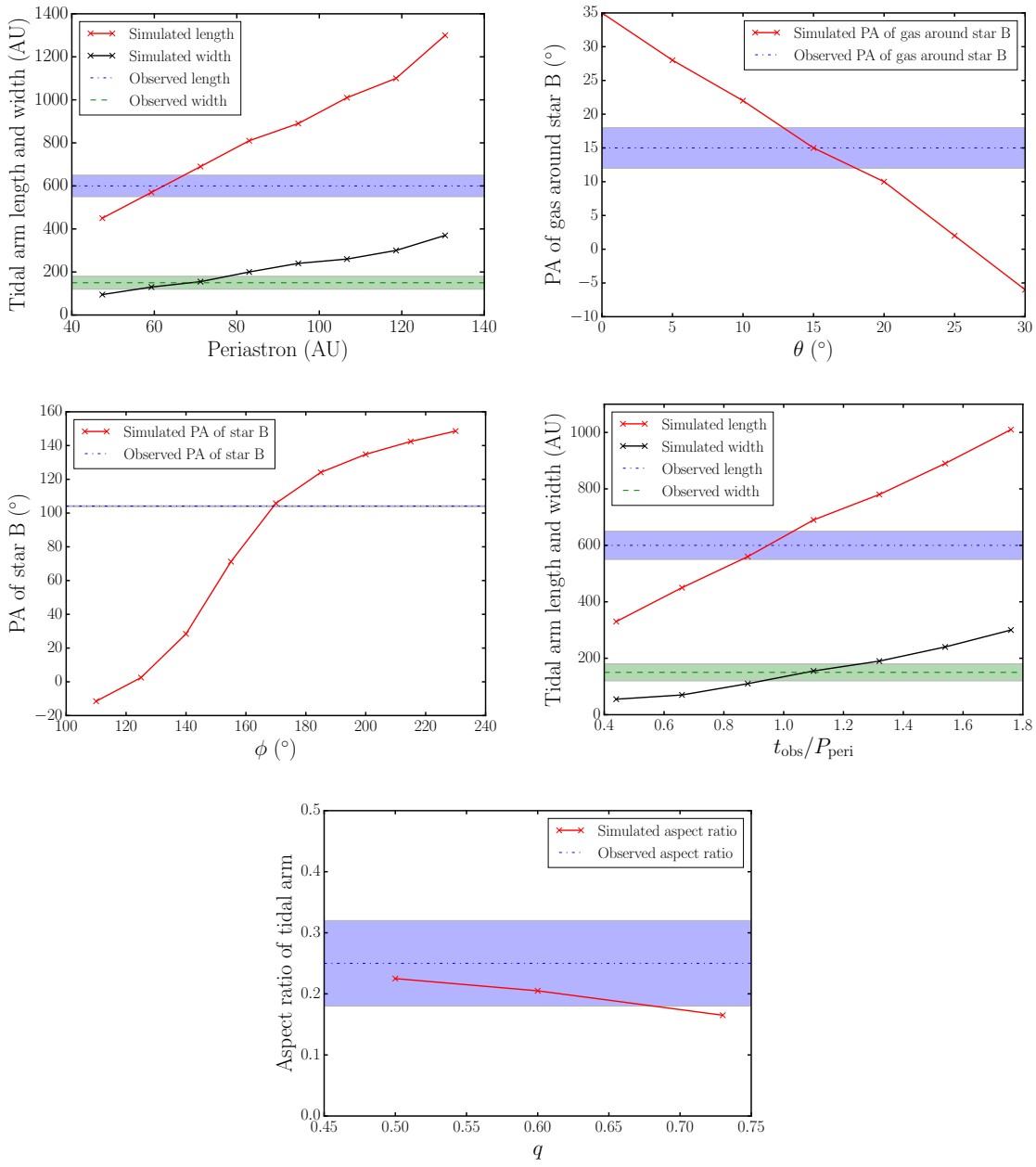

Fig. 4.5 In each of the diagrams, one parameter of the model is varied at a time and plotted against the observational feature that is most dependent on it. Shaded areas show observed values within 1σ. Comparison with observed values helps to constrain the parameter being varied (see Table 4.2 for the best-fitting model). Top left: the pericentre against the length and width of tidal tail; top right: the polar angle θ between the orbital and disc angular momenta against the positional angle of the captured material on star B; centre left: the azimuthal angle ϕ between the orbital and disc angular momenta against the positional angle of star B; centre right: the time of observation against the length and width of tidal tail; bottom: the power index q of radial temperature profile against the aspect ratio (width/length) of the tidal tail.

Table 4.2 Parameter choices that best fit the observations and the effect of parameter variation on system properties.

Parameter varied	Best fit value	Effect
Initial disc radius	60 AU	Post-encounter disc size and tidal tail morphology
Periastron separation	70 AU	Morphology and kinematics of tidal tail
Mutual inclination of disc and binary planes	$\theta = 18°$, $\phi = 170°$	θ: orientation of tidal tail and the captured material on star B; ϕ: velocity and positional angle of star B
Viewing angle	$\theta_{\rm obs} = 76°, \phi_{\rm obs} = 114°$	Morphology in plane of sky
Time of observation	$1.1\,P_{\rm peri}$ after pericentre	Kinematic signatures and ratio of AB separation to extent of tidal arm
Radial Temperature profile	$T = 230\,{\rm K}\left(\frac{R}{\rm AU}\right)^{-0.5}$	Power law index determines aspect ratio of tidal tail
Initial Disc Mass	$0.00167 M_\odot$	Optical depth of different regions of the system

depends on the ratio of the periastron separation to the outer disc radius, the observed scale of the residual disc constrains the initial disc radius (60 AU).

Another important quantity that could be used to constrain the orbital parameters of the flyby is the disc outer radius, after truncation. Since Clarke & Pringle (1993) other groups have worked on the angular momentum and energy transfer mechanisms occurring with a star-disc encounter (e.g. Kobayashi & Ida, 2001; Muñoz et al., 2015). Recently, Breslau et al. (2014) focused on the sizes of protoplanetary discs after such encounters using numerical simulations, where the discs are described by test particles (hydro effects are neglected). They model the encounter via prograde coplanar parabolic orbits. They obtain the following prescription for the outer radius of the truncated disc: $R_{\rm out} = 0.28 R_{\rm peri} m_{12}^{-0.32}$, where $m_{12} = M_2/M_1$. However, note that they did not explore the effects of the misalignment between the disc and the plane of the parabola. Recent results by Lubow, Martin & Nixon (2014) analysed how the tidal truncation radius estimates are affected by the misalignment between a disc and an external binary (Artymowicz & Lubow, 1994). Their results indicate that the external torque decreases quite rapidly with inclination, leading to a larger circumstellar disc. Similarly, we expect the same kind of behaviour for a flyby interaction, even though in this case resonances do not come into play. Finally, the analytic prescription by Breslau et al. (2014) strongly depends on the definition of the outer radius. They define it as the point where the surface density profile presents a maximum in its radial gradient. However nothing prevents an observer from detecting regions of the disc outside this radius, where the material will be less bound and in more elliptical orbits (see again Breslau et al., 2014). To conclude, the outer radius is not the best parameter to be used to constrain *a priori* the orbit of the flyby. We will check *a posteriori* that what we obtain is in reasonable agreement with the observations (see Section 4.5).

The mutual inclination of the disc and the binary orbit (θ) is the main determinant of the morphology of the system. While the azimuthal angle ϕ determines the relative position and separation between star A and star B, the polar angle θ determines the size and orientation of the tidal arm. The tidal arm is most prominent and most massive for a prograde coplanar tidal encounter. As θ increases, the tidal arm decreases in size and mass; it also becomes warped with respect to the original disc plane. If θ is larger than 90°, no extensive tidal arm is produced.

We therefore *require* a prograde encounter. We can obtain a clue about the likely orientation of the disc of A on the sky from the observation of its jet which is directed to the SE. Since the jet must be visible on the observer's side of the disc, it suggests that the NW side of the disc is nearer to the observer. The fact that the NE lobe of A's disc is blueshifted then suggests that the rotation of the disc is clock-wise as seen from the earth. In the successful (rather close to coplanar prograde) model, we have found a viewing angle that well reproduces the observed blueshift of the material centred on B. However, the predicted proper motion in the plane of the sky is then *clock-wise* in contrast to that claimed by Bisikalo et al. (2012). We have discussed above how it is desirable to better constrain the motion in the plane of the sky through future proper motion observations.

The power index q of the adopted radial temperature profile determines the rate at which temperature falls as a function of radius. A smaller value of q results in a hotter and thus thicker outer region of the undisrupted disc. Subsequently, a thicker outer disc produces a thicker tidal tail after the tidal interaction. Therefore, the value of q is constrained via the observed ratio between the width and length of the tidal arm.

4.4.2 The best fitting model

Fig. 4.2 shows the gas morphology of the best-fitting model, the parameters of which are listed in Table 4.2 (compare Fig. 4.2 with Fig. 4.3, where we portray Fig. 1 by Cabrit et al., 2006). The gas is rendered as individual SPH particles which are colour coded according to line of sight velocity. Fig. 4.4 shows the evolution of the fly-by with rendered plots.

This model successfully reproduced the following observed features of the system:

- The northeast lobe of the disc is blueshifted with radial velocity of $\sim -3\,\mathrm{km/s}$ with respect to Star A while the southwest lobe of the disc is redshifted with radial velocity of $\sim 3\,\mathrm{km/s}$.

- The tidal arm has the observed spiral shape with the correct handedness. It is entirely redshifted with a radial velocity of $\sim 3\,\mathrm{km/s}$ which is larger than the escape velocity at the corresponding distance. The tidal arm is thus unbound, as observed.

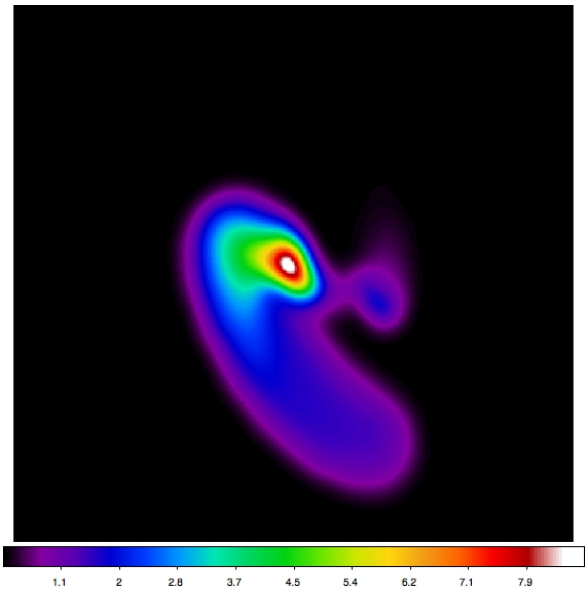

Fig. 4.6 The integrated ^{12}CO($J = 2-1$) emission map of RW Aur after correcting for beam dilution. Colour coding is linear in Jy beam^{-1} km/s.

- The molecular complex on B is blueshifted with respect to star A. The shape of the captured material around B is similar to that observed with its major axis being tilted slightly to the east of north. This good agreement suggests that the gas observed around B may indeed be material captured from A's disc (even if B also originally possessed a small scale disc of its own).

Comparing the observation and simulation more quantitatively, Table 2 lists the various quantifiable morphological features. Our simulations matches the observations in nearly all respects. The strikingly good agreement demonstrates that the system's morphology is most likely associated with a tidal interaction.

4.5 Results of synthetic observations

4.5.1 Line profiles

We took snapshots from our hydrodynamic models at ~ 570 yr ($t_{\rm obs} \sim 1.1 P_{\rm peri}$, where $P_{\rm peri}$ is the Keplerian period at the pericentre) after pericentre and post processed them with TORUS to produce synthetic ^{12}CO data cubes (c.f. section 4.3.2). Fig. 4.7 shows line profiles from subsets of these data cubes after applying convolution accounting for the IRAM beam size, for the best-fitting model.

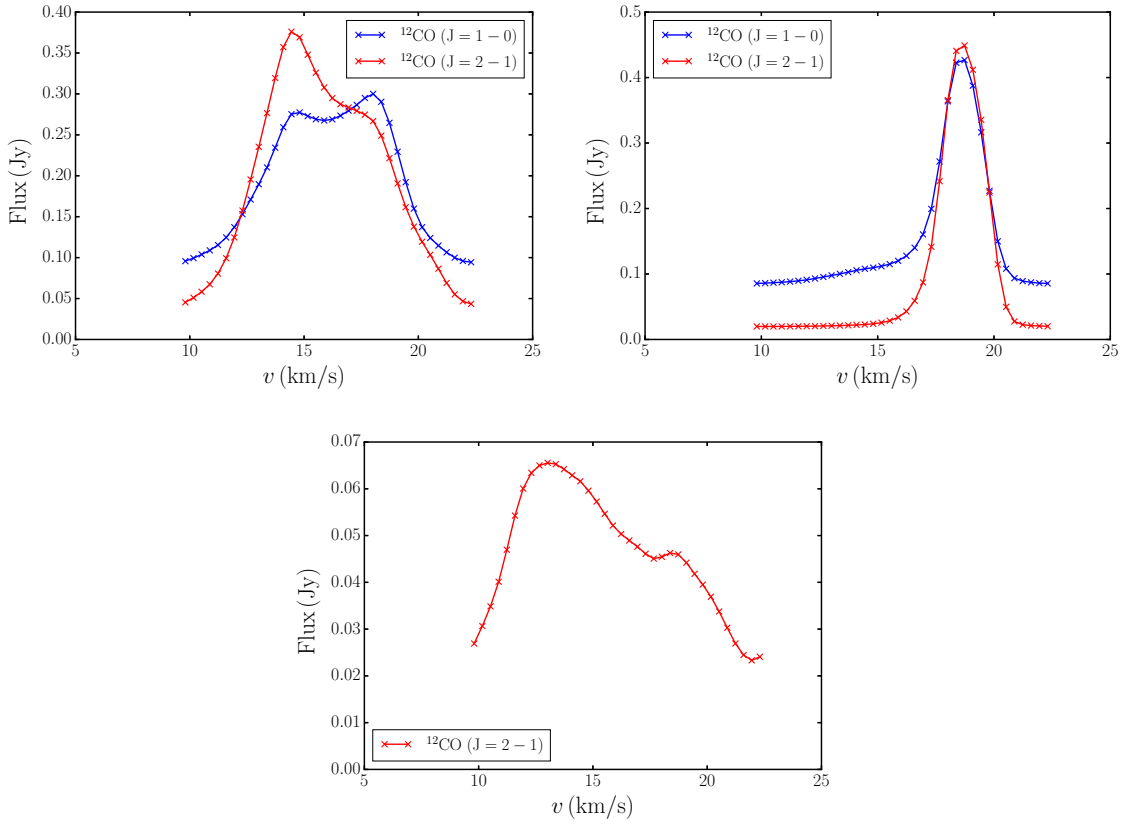

Fig. 4.7 Line profiles of the synthetic observations of the best fit model for the disc around star A (top left panel), the tidal arm (top right panel) and molecular gas around star B (bottom panel). The red curve shows the ^{12}CO$(J = 2-1)$ profile, and the blue curve the ^{12}CO$(J = 1-0)$ one. The latter has been multiplied by a factor 4. The temperature profile is given by $T(R) = 230\,K\,(R/\mathrm{AU})^{-0.5}$, and the mass of the disc is $M_\mathrm{d} = 1.67 \times 10^{-3} M_\odot$. The synthetic profiles recover most of the features of the profiles derived by Cabrit et al. (2006), in particular flux intensities and kinematic signatures. The synthetic profile of the gas around star B is lower than the observed one by a factor of 2. This is due to the simple prescription we have used for the temperature radial profile, which fails to reproduce the emission properties of the gas close to star B, where the heating due to radiation from star B is certainly important.

The synthetic observations allow us to constrain the temperature normalization and the initial mass of the disc $M_{\rm d}$, since these two quantities regulate the flux density normalization and the optical depth of the emission lines. In the case that the line is optically thick, the ratio ^{12}CO$(J=2-1)$/ ^{12}CO$(J=1-0)$ should be ~ 4 in Rayleigh-Jeans limit. We have therefore multiplied the ^{12}CO$(J=1-0)$ by 4 for the regions of the tidal arm and the primary disc, to demonstrate whether these components of the system are optically thick. we do not consider the ^{12}CO$(J=1-0)$ line for the gas around star B, since this line has been marginally detected by Cabrit et al. (2006), as discussed above. The radial velocities were corrected to heliocentric frame by adding the mean heliocentric velocity of star A (15.87 ± 0.55 km/s, Cabrit et al., 2006).

We now consider the impact of temperature normalisation. By using the temperature profile as estimated by Cabrit et al. (2006) ($T(R) = 450\,{\rm K} \times (R/{\rm AU})^{-0.5}$), the most outstanding discrepancy is that the simulated flux densities are $3-5$ times higher than the observed flux densities. We argue that the most likely cause is that the limitation of BS93 model led to Cabrit et al. (2006) overestimating the temperature of the disc. Although BS93 assumed local thermal equilibrium (LTE), this assumption may not be appropriate for RW Aur. TORUS is capable of treating both LTE and non-LTE, allowing us to test this. The comparison in Fig. 4.8 demonstrates that the resultant flux densities are indeed about $2-3$ times lower in the LTE case.

This indicates that in order to explain the observed flux, Cabrit et al. (2006) would have overestimated the temperature by assuming an LTE model. Furthermore, if we use a lower temperature, more consistent with theoretical expectation from stellar irradiation and accretion, ($T = 30$ K at 40 AU, Chiang & Goldreich, 1997), the resultant theoretical emission is more compatible with the observed integrated flux densities. Note that lower temperatures are also indicated by Infrared SED fitting by Osterloh & Beckwith (1995)($T = 25$ K at 40 AU).

We try to constrain the disc mass by requiring the tidal arm and the disc orbiting star A to be optically thick. This requires an initial disc mass of $1.67 \times 10^{-3} M_{\odot}$ and a current disc mass of $1.05 \times 10^{-3} M_{\odot}$. In order to estimate the latter, we have considered an outer disc radius of 57 AU, as estimated by Cabrit et al. (2006). This estimate is higher than that estimated by both Cabrit et al. (2006) and Osterloh & Beckwith (1995) ($10^{-4} M_{\odot}$ and $3 \times 10^{-4} M_{\odot}$, respectively), but lower than the ones estimated by Andrews & Williams (2005) ($4 \times 10^{-3} M_{\odot}$). Note however that mass estimates from dust and CO isotopologues are always affected by very large uncertainties, and that our prescription for the temperature dependence is so simple that we do not expect to recover the observed mass with high precision.

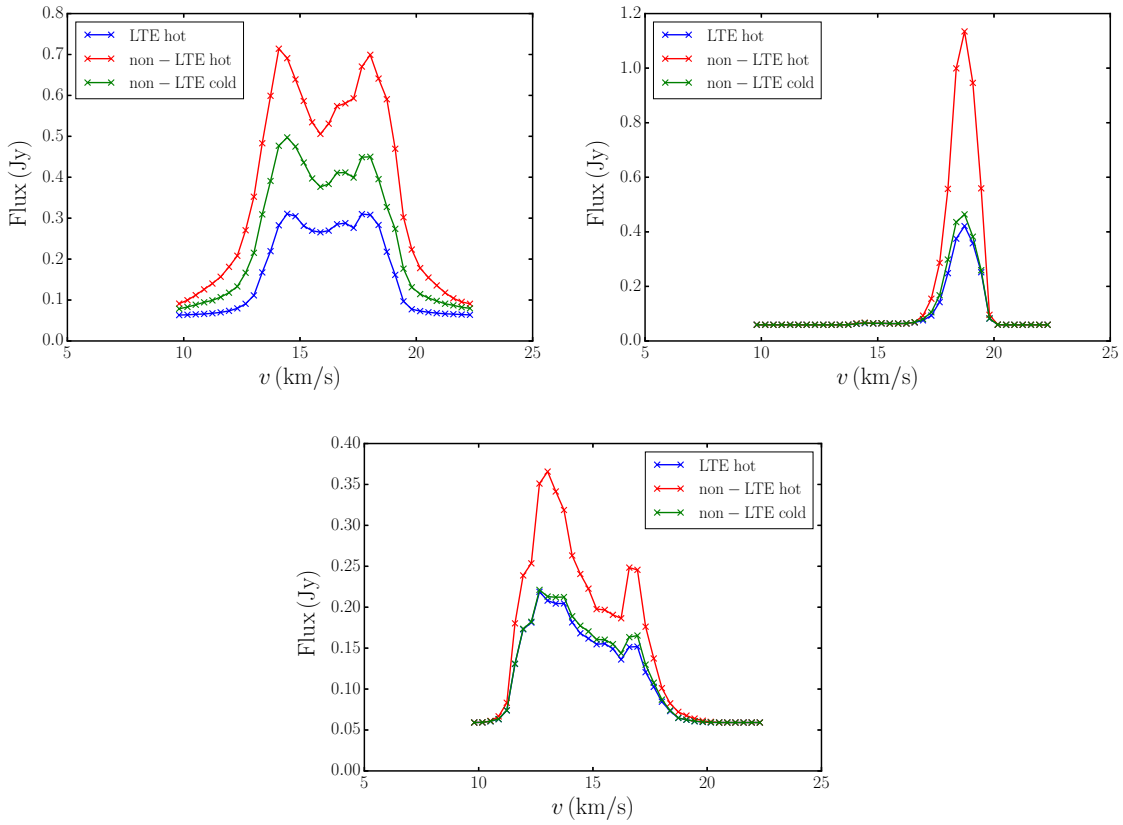

Fig. 4.8 The integrated line profiles of the ^{12}CO($J = 1 - 0$) emission line of the A disc (top left panel), tidal arm (top right panel) and molecular complex (bottom panel). The flux has been multiplied by a factor 4, in order to compare these synthetic profiles with the observed ones in Cabrit et al. (2006). In each panel the lines represent local thermal equilibrium (LTE) (blue), non-LTE with temperature profile estimated by Cabrit et al. (2006) (red) and non-LTE with temperature profile Infrared SED fitting by Osterloh & Beckwith (1995) ($T = 25$ K at 40 AU, green line). Given that the three models are identical in all other respects, the LTE assumption indeed results in a lower integrated flux densities.

After adopting the temperature normalisation and initial disc mass as described above, the resultant line profiles show better agreement with the observations. In particular, both the A disc and the tidal arm are optically thick as observed, and their peak flux is in broad agreement with the observations by Cabrit et al. (2006), together with the moderate asymmetry of the double-horned line profile of the disc. The disc has in fact gained a small eccentricity, as apparent from the right bottom panel of Fig. 4.4. The ^{12}CO($J = 2-1$) line profile of the gas around star B recovers the main features of the observed profile, besides the peak flux, which is lower than the observed one by a factor of 2. This may result from incorrect assumptions about the temperature profile around star B (temperature has a simple dependence on the distance from star A), but may also simply reflect that star B also possessed a disc prior to the encounter (in contrast to what we assume here, where the final disc is composed of material entirely captured from the disc of star A).

Cabrit et al. (2006) obtained an indirect measure of the size of the disc around star A by using the position of the peaks of the typical double-horned profile of the emission lines (see Section 4.2.1). They observed a line profile with peaks at ~ 3.5 km/s from the centre, whereas in our synthetic observation we obtain the two peaks at ~ 2.5 km/s from the centre of the line. This seems to suggest that the disc in our simulations is larger than the one observed by a factor ~ 2. However, if we look at the hydrodynamical simulation of our best model (see Fig. 4.9), or if we look at the synthetic continuum emission shown in Fig. 4.10, the disc size is in good agreement with the observations (~ 50 AU). After convolution we are obtaining contamination from low velocity gas in the inner part of the tidal arm and the elliptical outer region of the disc. The difference in our synthetic line profiles implies that we are over-estimating emission from these outer regions. Detailed thermal modelling is however beyond the scope of this project; the agreement with the size derived from the thermal continuum reassures us that the dynamical effects of the encounter are well reproduced.

4.5.2 Dust emission

We used TORUS (c.f. section 4.3.2) to produce a synthetic observation of the continuum emission at 1.3 mm of the same snapshot showed in Fig. 4.6. We consider standard assumptions on the dust properties. First of all we assume that spatial distribution of the dust follows exactly the gas distribution. This is likely to be the case in our framework, since the dynamics of the gas itself is mainly ballistic during the encounter. The dust component is dynamically driven by the same gravitational potential. At the moment we neglect secondary effects, that might be due to hydro terms in the dynamics of the gas. We assume a gas to dust ratio equal to 100, and a grain size distribution ranging between 50 Å and 1 cm. We use a typical grain size distribution, where $dn/ds \propto s^{-w}$, where n is the numerical density

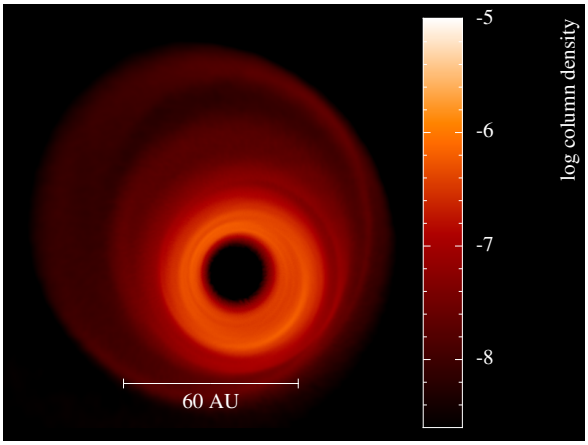

Fig. 4.9 Circumstellar disc around star A as seen at $t = 0$ (today) from the SPH simulation on the *xy*-plane. Column density is in code units. The outer radius of the disc is in agreement with values estimated by Cabrit et al. (2006) ($40 - 57$ AU). The disc has clearly gained an eccentricity after the encounter with star B.

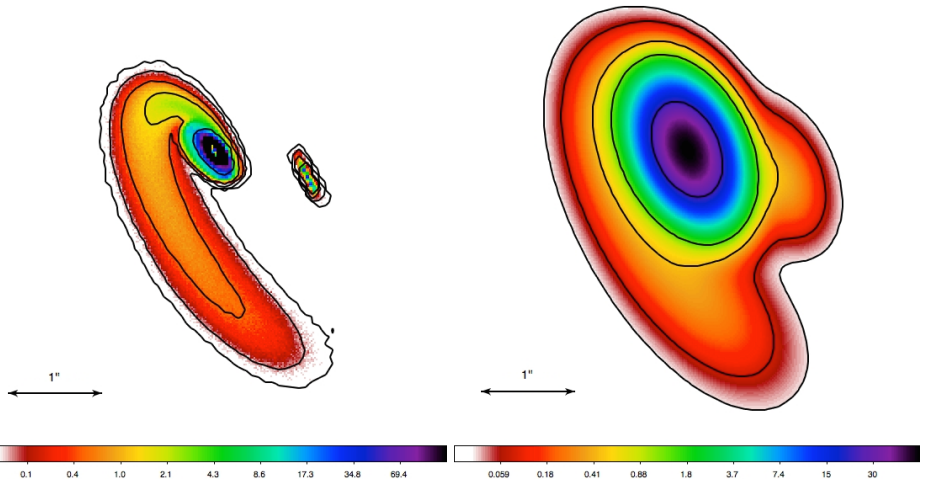

Fig. 4.10 Left panel: synthetic observation of our best-fit model in the continuum at 1.3 mm. Right panel: same emission map, convolved with the beam size used by Cabrit et al. (2006) (FWHM: 0.87" $\times$ 0.54"; PA $= 20^{\circ}$). The colour code shows emission in mJy/beam. Contour levels are at (1/24, 1/6, 1, 3 and 48)σ, where $\sigma = 0.47$ mJy/beam (see Table 1 by Cabrit et al., 2006).

of dust particles, and s is the grain size. It is well known that in the interstellar medium w assumes a typical value $w \sim 3.5$ (Mathis, Rumpl & Nordsieck, 1977). More recently, interferometric observations have suggested a shallower distribution in the outer regions of protoplanetary discs, where $w \sim 3$ (e.g. Ricci et al., 2010a,b, 2012b; Testi et al., 2014). Following these recent results, for our synthetic observation we use $w = 3.3$. We assume that the dust is comprised of amorphous silicate grains (Draine, 2003a,b), obtaining an opacity $\kappa_\nu = 0.131\,\mathrm{cm}^2/\mathrm{g}$ at 1.3 mm (assuming a gas to dust ratio equal to 100). Fig. 4.10 shows the emission we obtain in mJy/beam, where the beam size is the one used by Cabrit et al. (2006) (0.87" $\times$ 0.56", see their Table 1). Contour levels are submultiples and multiples of the noise level $\sigma = 0.47$ mJy/beam in the same observation by Cabrit et al. (2006): (1/24, 1/6, 1, 3, 48)σ. From disc A we obtain emission levels that are compatible with the one observed (given the large uncertainties on the opacity), and a disc size that is in agreement with the one estimated by Cabrit et al. (2006) from the line profiles (~ 50 AU from the unconvolved emission map). We underestimate the dust emission around star B, and this is again suggesting that our simple temperature treatment is underestimating the temperature of the material around the secondary star. By comparing the convolved emission map with the one shown by Cabrit et al. (2006) where the primary disc is located, it seems that we are overestimating the total emission by a very small factor ~ 1.5 (compare the size of the 3σ contours), which is very small when compared to the uncertainties of the problem. Note that the normalization of the emission of our synthetic observation does depend on our assumptions, mostly the dust opacity (e.g. in discs is often assumed a lower opacity at 1.3 mm, as motivated by Beckwith et al., 1990), but also the uniform dust-to-gas ratio, the maximum grain size, and the grain size distribution index. With the assumptions we have made, the emission from the tidal tail is below the noise level (~ 0.3 mJy/beam).

4.6 The dimming event

Rodriguez et al. (2013) argued that the leading edge of the tidal arm may wrap around the A disc and obscure the line of sight between Earth and RW Aur A, thereby producing the observed dimming of RW Aur. In our simulations, there is indeed a stream of gas linking star A and B after the tidal encounter (however, it is not part of the primary tidal arm as Rodriguez et al., 2013, suspected, see the bottom left panel of Fig. 4.4). A portion of this stream of gas might provide the occulting body that caused the observed dimming event, as the integrated line-of-sight column density ($\sim 10^{-2}\,\mathrm{g\,cm^{-2}}$) exceeds the threshold column density ($\sim 7 \times 10^{-4}\,\mathrm{g\,cm^{-2}}$) required to produce the dimming - assuming a flux decrease

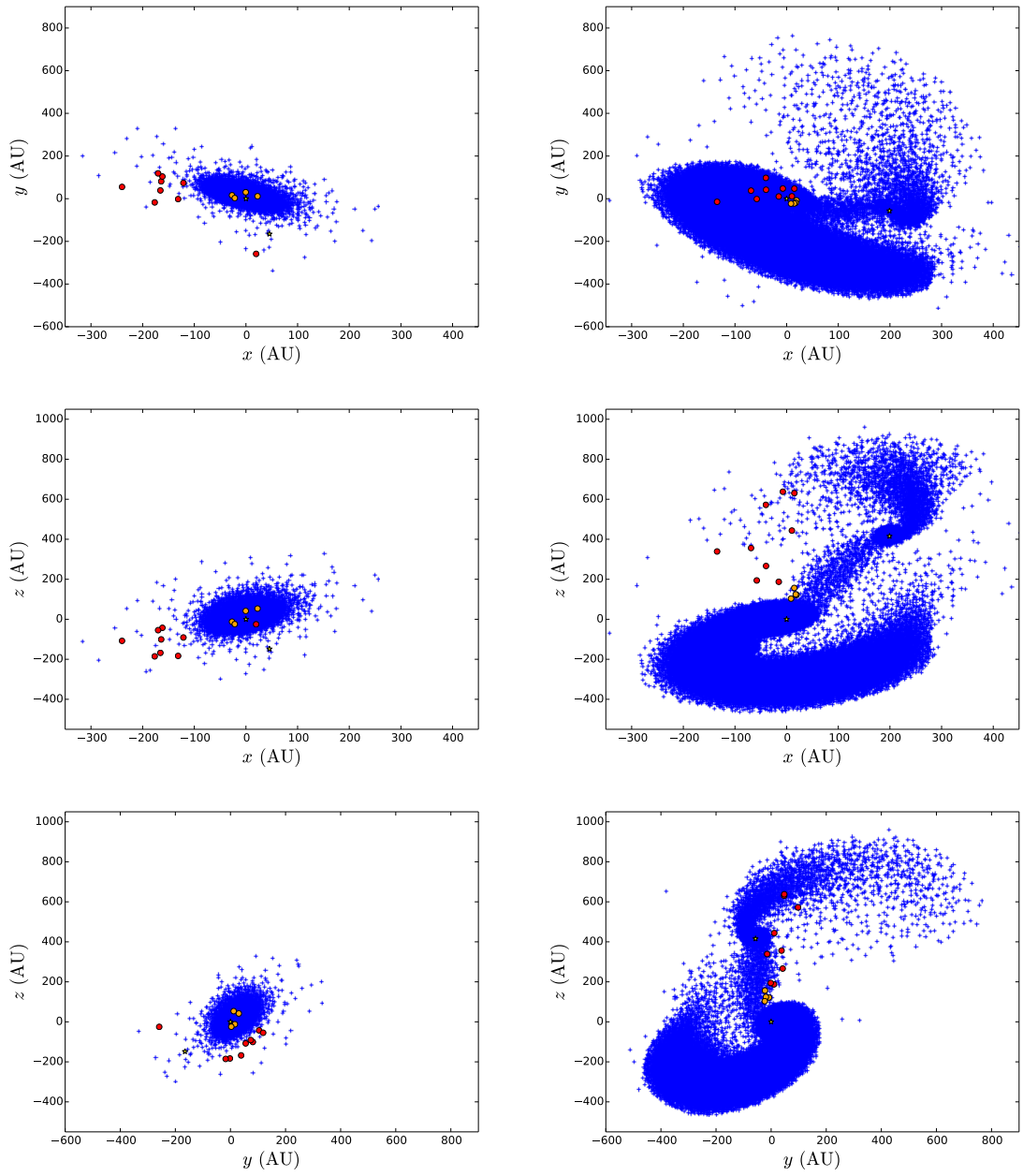

Fig. 4.11 3D structure of RW Aur before (left panels, at -636 yr from today) and after (right panels, at 0 yr from today) the encounter for the best-fitting model. As in the other figures, the x-y plane represents the plane of the sky. The observer is located at $z = +\infty$. The origin of the axes is defined as the position of star A. Blue crosses represent all the SPH particles that have not been accreted on either of the two stars, which are shown in yellow. Filled dots indicate the particles that are partially occulting star A at present time. The red ones are scattered particles that do not show a credible dynamical history. The orange ones evolve in a coherent fluid structure. They are initially orbiting within the disc, are then stripped by the tidal interaction, and end up in the low density periphery of the stream connecting stars A and B. The dimming event observed by Rodriguez et al. (2013) can be explained by a clumpy inhomogeneity at the edge of such stream. Transverse velocities of the particles and column density are in broad agreement with the estimates by Rodriguez et al. (2013).

of the A star of 91% (Rodriguez et al., 2013) and a dust opacity at optical wavelengths $\kappa = 3000\,\mathrm{cm}^2/\mathrm{g}$ (Men'shchikov & Henning, 1997).

In order to verify this hypothesis, we have analysed the SPH simulation of the best-fitting model. We select all the foreground particles that are partially occulting star A at the present time by requiring $h/D > 1$, where h is the smoothing length associated with a single SPH single particle and D is the distance between the particle and star A in the plane of the sky. we then trace back their trajectories, in order to see whether the selected particles have a credible dynamical history. In Fig. 4.11 we plot all the SPH particles of the simulation with blue crosses, the two stars with yellow star symbols, and the occulting particles with filled dots. The orange dots represent the particles that show a credible dynamical history. They start orbiting together within the circumstellar disc (see left-hand panels), and they then get incorporated in the well resolved bridge linking star A and B. At the present time they are located at the low density periphery of the bridge (see right-hand panels). The occulting particles represented by the red dots are individually scattered particles that originate from the very poorly resolved outer regions of the initial disc and are not associated with any coherent fluid structure. Since the orange particles are very few (only 4 for the particular choice of viewing angle), we cannot determine the structure of the low density margins of the bridge, and even less the size of the occulting body ($0.09 - 0.27$ AU, as estimated by Rodriguez et al., 2013). An accurate determination of the density structure of the low density periphery of this bridge would require an unfeasibly high resolution. However, the presence of particles in this region indeed indicates that possible $\sim$ AU scale inhomogeneities at the edge of the stream linking A and B could cause the dimming event observed by Rodriguez et al. (2013). The velocity in the plane of the sky of these particles ranges between $0.97 - 1.09\,\mathrm{km/s}$ and is thus consistent with the estimates from Rodriguez et al. (2013) ($0.86 - 2.58\,\mathrm{km/s}$).

Finally, we have computed the evolution with time of the average column density lying between star A and the observer. In Fig. 4.12 we show that in the past the star has been completely occulted (at optical wavelengths) by the density structure linking stars A and B. This bridge has then evolved, until the line of sight only grazes it nowadays ($t = 0$). In the future, the average column density stays well below the value required to observe a dimming of star A as observed by Rodriguez et al. (2013). Moreover, for $t \gtrsim 0$, the column density in the simulation starts to be dominated by particle noise. However, inhomogeneities in the bridge structure might entail new events in the next years.

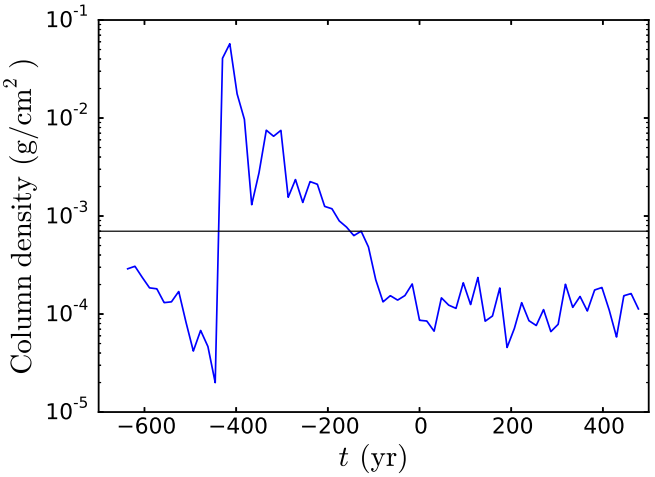

Fig. 4.12 Average column density between the observer and star A as a function of time. The horizontal black line represents the column density that would cause a dimming of $\sim 90\%$, as observed by Rodriguez et al. (2013). In the past the bridge connecting stars A and B has been perfectly on the line of sight of star A, therefore completely occulting the star at optical wavelengths. Nowadays such structure grazes the line of sight. Future dimming events cause by inhomogeneities in the density structure can not be ruled out by this model.

4.7 Summary and conclusions

We have used hydrodynamic models and synthetic observations to constrain the observed morphology, kinematics and line fluxes of the binary system RW Aur which was first proposed as a candidate star-disc encounter by Cabrit et al. (2006). We draw the following conclusions.

With a suitable set of orbital parameters and viewing angle (See Table 1), we can reproduce almost all morphological and dynamical features of the system:

- RW Aur A has a circumstellar disc with an outer radius of ~ 50 AU which is within the observed range of $40-57$ AU. The disc is optically thick in ^{12}CO emission, as the $^{12}\mathrm{CO}(J=2-1)/\,^{12}\mathrm{CO}(J=1-0)$ ratio is ~ 4.

- RW Aur B is separated from star A by ~ 200 AU (~ 1.5” for 140 pc). The projected AB separation is increasing at rate of ~ 0.002”/yr. The molecular complex on B is blueshifted with respect to star A with a broad distribution of radial velocity of $3-6$ km/s. The line profile from the star B is asymmetric and thus most likely due to

material captured during tidal encounter instead of a circumstellar disc. The molecular emission is marginally optically thick with a $^{12}\mathrm{CO}(J=2-1)/\,^{12}\mathrm{CO}(J=1-0) > 4$.

- The expanding, spiral-shaped structure connected to RW Aur A disc is most likely a tidal arm produced in a fly-by of star B. The tidal arm extends about 600 AU (~ 4" for 140 pc). The arm is entirely redshifted with a radial velocity ~ 3 km/s with respect to star A. This is faster than the escape velocity at corresponding distance, indicating the arm is indeed gravitational unbound.

The synthetic molecular line data cubes obtained from a purely radial temperature estimated by Cabrit et al. (2006) have flux densities $3-5$ times higher than observations. Nonetheless, by lowering the temperature to typical disc temperature for CTTS, we can reduce the flux densities to the observed values.

The agreement between observations and simulations thus lends strong support to the hypothesis that the morphology of the RW Aur system is consistent with a tidal encounter scenario. Although the observational evidence for tidal encounters on Galactic scales is well established, this is the only system that is a good candidate for such encounters on the scale of protoplanetary discs (note that a tidal encounter scenario has also been proposed as a possible model to explain the recent ALMA observations of AS 205 S, see Salyk et al., 2014). Note that such gravitational disturbance might be the cause of the high accretion rate of RW Aur A, since tidal encounters can remove angular momentum from the inner regions of the disc (e.g. Ostriker, 1994)

Finally we note that our simulations provide support for the hypothesis of Rodriguez et al. (2013) regarding the origin of observed dimming of star A in 2010/2011. We find that it is plausible that this was caused by inhomogeneities in the outskirts of a 'bridge' structure linking star A and B which may graze the line of sight at current epochs. Our simulations do not have the resolution to trace the structure of the low density periphery of the optically thick bridge, nor to model the $\sim$ AU scale inhomogeneities that would be required to explain such an event. Nevertheless our simulations predict a good agreement between the velocity in the plane of the sky of material in this region with that required by the observed ingress time of the dimming event. However, in the next chapter, we will show that very recent observations indicate that the dimming event is likely not due to the tidal stream lying between the two stars.

Chapter 5

X-Shooter spectrum of the 2014-2015 dim state of RW Aur A: new constraints on the occulting mechanism[1]

This chapter is based on a letter submitted to MNRAS (Facchini et al., 2015). I led the whole collaboration, firstly by being PI of the DDT proposal. Carlo F. Manara conducted the reduction of the raw spectral data, and extracted the estimates of the equivalent widths of the absorption and emission lines. I have performed all the rest of the analysis.

5.1 Introduction

After the submission of the paper on the hydrodynamical model by Dai et al. (2015, whose results are reported in chapter 4), RW Aur A has undergone a second major dimming event (Petrov et al., 2015; Antipin et al., 2015). Petrov et al. (2015) have proposed a new model as the origin of the extinction, which can be due to an outburst of a stellar wind entrapping dust grains of the inner region of the disc. This possibility has lately been supported by the photometric observations by Shenavrin, Petrov & Grankin (2015), who showed that during the last dimming event the RW Aur system shows an excess in the Near-IR (in L and M bands). This emission can be related to an increased emission from hot dust (~ 1000 K) at ~ 0.1 AU, suggesting that the occulting material is likely to be associated with the inner regions of the disc. Finally, Schneider et al. (2015) have revealed the presence of a high gas column density along the line of sight to star A during the second dimming event, and have

[1]This work is based on observations made with the ESO telescopes at the Paranal Observatory under programmes ID 294.C-5047 and 382.C-0711

speculated that RW Aur A might be undergoing a mechanism similar to the one proposed for AA Tau (e.g. Bouvier et al., 2013).

An insight into the kinematic properties of the occulting material is essential if we are to determine the physical origin of the dimming event and to discriminate between the different interpretations discussed above (i.e. the tidal stream, the dust laden wind and the AA Tau scenarios). In this chapter, in Section 5.2 we present new spectral data obtained with the X-Shooter spectrograph mounted on the Very Large Telescope (VLT) during the second dimming event, and we show that we detect signatures of cold gas absorption at significantly blue-shifted velocities. In Section 5.3 we show the accretion luminosities deduced from several emission lines. In Section 5.4 we present the synthetic photometry of RW Aur A from our observation, and discuss the photometric history of the whole system. In Section 5.5 we discuss possible models and draw our conclusions.

5.2 Absorption signatures

We have obtained new spectra of RW Aur A using the VLT/X-Shooter instrument (Vernet et al., 2011) during the night of March, 19th 2015 (DDT Pr.Id. 294.C-5047, PI Facchini). At the time of observation the seeing conditions were very good (0.6" at zenith, $\sim$0.86" at the airmass of the target). The spectra were obtained both with large slits (1.6x11"-1.5x11"-1.2x11" in the UVB, VIS, and NIR arms) and with narrow slits (0.5x11" in the UVB arm, 0.4x11" in the VIS and NIR arms), oriented at parallactic angle. The spectra obtained with the large slits allow us to flux calibrate the spectrum, while those with narrow slits lead to the highest spectral resolution (R$\sim$18000 at $\lambda\sim$600 nm). The observing strategy we adopted consisted of a short exposure in stare with the large slit, followed by a complete ABBA nodding cycle with the narrow slits, and finally a last short stare exposure with the large slit again. This procedure was repeated two times. The spectra were reduced using the standard ESO pipeline for X-Shooter (Modigliani et al., 2010) version 2.5.2 with the same procedure as in e.g. Manara et al. (2013). The final spectrum used in the analysis is obtained by co-adding the two narrow slit spectra taken successively after reduction, telluric correction, and flux calibration. The 1D extracted spectra were corrected for telluric absorption using a standard telluric spectrum obtained at similar airmass conditions as the target. Finally, the narrow slit spectra were rescaled to the large slit ones to account for slit losses, which are not wavelength dependent. The final spectra thus cover the wavelength region from $\lambda\sim$320 nm to $\lambda\sim$2500 nm with resolution R$\sim$10000 up to $\lambda\sim$550 nm and from $\lambda\sim$ 1000 nm, and R$\sim$18200 in between.

We clearly detect a narrow absorption component in the resonant Na I D (at $\lambda \sim 590$ nm) and K I D (at $\lambda \sim 765$ and 770 nm) lines (see Fig. 5.1, top panel), which probe gaseous material along the line of sight. For the Na doublet, we estimate the equivalent width (EW) of such absorption feature by assuming a Gaussian absorption for the broad hot component. We obtain an EW of $\sim 0.3-0.6$ Å for both Na lines (depending on the modelling of the emission line), and of ~ 0.2 Å for both K lines. Petrov et al. (2015) looked for narrow absorption signatures in the same Na lines, but they did not detect them, due to either a too low spectral resolution, or to intrinsic time variability of the physical phenomenon.

We obtain the same EW for both Na I D lines (see Fig. 5.1). However, the absorption oscillation strength f of the two hyperfine transitions differs by a factor of 2 (e.g. Morton & Smith, 1973). This indicates that the lines are saturated, even though the flux does not drop to 0 since the lines are not spectrally resolved by X-Shooter. By using the Na I D_1 line at 589.75 nm (where the absorption oscillation strength is half the one of the Na I D_2 line) we obtain a lower limit on the column density of atomic neutral sodium of $\sim 3-6\times10^{12}$ cm^{-2}. This value is a typical column density where the line saturates in interstellar medium (ISM) measurements (e.g. Crutcher, 1975). The same procedure can be applied to the K I D_1 line, where we obtain $\sim 1\times10^{12}$ cm^{-2} as a lower limit on the column density of atomic neutral potassium. For the K doublet, the moderate spectral resolution cannot discern whether the lines are saturated. We looked for absorption lines at the sodium and potassium ultraviolet doublets at 3300 and 4045 Å. Such doublets are often used to determine the column density in the ISM when the Na I D lines are saturated (e.g. Crutcher, 1975), since the absorption oscillation strengths are lower by a factor of $\sim 10-100$ (e.g. Morton & Smith, 1973). With the gas column density estimated by Schneider et al. (2015) we would expect to detect them. However, due to both the strong accretion signatures and the poorer spectral resolution in the UVB arm we can neither rule our nor confirm the presence of such lines.

Gahm et al. (1999) estimated the radial velocity of star A $v_0 = 15.87$ km/s. The radial velocity of the absorbing gas relatively to the star proper motion is -60 ± 10 km/s for the Na lines, and -51 ± 10 for the K lines (see Fig. 5.1), where the uncertainties are dominated by the spectral resolution. Such velocities are not consistent with the radial velocity of the occulting particles from the SPH simulation of chapter 4, which we estimate to be between 0 and -8 km/s. The tidal stream between the two stars is then very unlikely to be responsible for the dimming events, if these are correlated with the high gas column density detected by Schneider et al. (2015) (see Section 5.5).

We have then looked at the Na I D line profiles of eight high resolution UVES spectra of RW Aur A obtained between 2008 and 2010 (Pr.Id. 382.C-0711, PI Whelan, see central panel of Fig. 5.1). They are broader and significantly different from the line profile obtained with

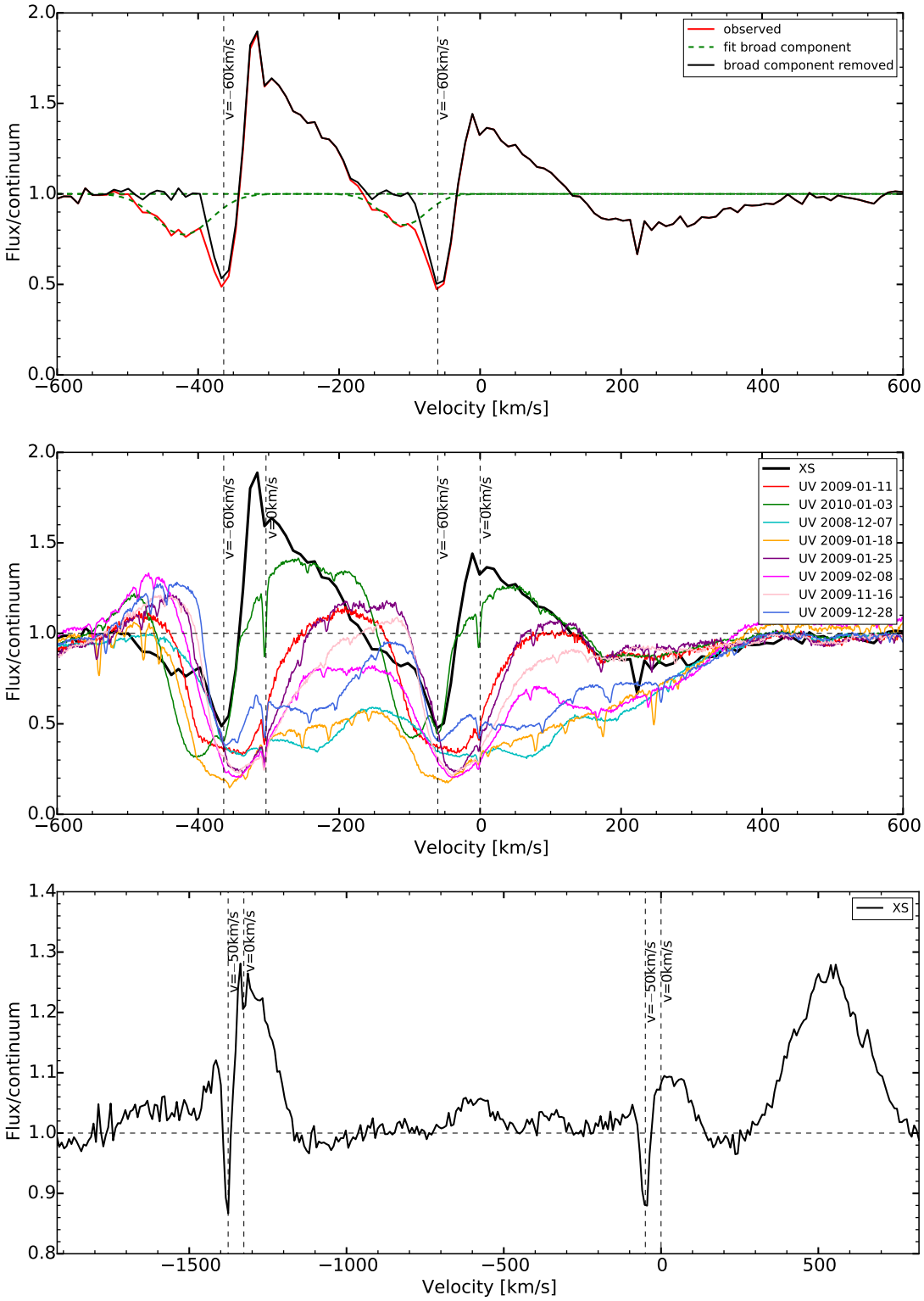

Fig. 5.1 Top panel: Na I D lines from X-Shooter. Central panel: Na I D lines from X-Shooter and UVES prior to the dimming events. Bottom panel: K I D lines from X-Shooter. All the velocities are in the reference frame of star A.

X-Shooter. In particular, there is much less redshifted absorption (from 0 to +200 km/s) in the latter than in (most of) the former, which suggests either that the mass accretion rate has decreased or that the accretion region is now partly occulted. Another major difference is the high velocity blueshifted absorption (from about −100 km/s to about −200 km/s) seen in the X-Shooter spectrum that is not seen earlier, which suggests the development of a fast wind. The 2010 UVES spectrum is the most similar to the X-Shooter one, with a typical P Cyg profile. Only this UVES spectrum shows a clear absorption component at ~ -60 km/s (see Fig. 5.1, central panel). In this case, these components are not saturated. A similar feature was also observed in some older spectra, as the ones shown in fig. 2 by Alencar et al. (2005). The same velocities (~ -60 km/s) in absorption have also been observed in Ca II lines at the beginning of the first dimming event in 2010 by Chou et al. (2013). If the dimming events are correlated with the gaseous material probed by these blueshifted absorption lines, the dimming might just be an extreme state of a more frequent phenomenon.

Finally, in all the UVES spectra of the Na I D lines we observe a much narrower unsaturated absorption component (barely detected by X-Shooter) at ~ -2 km/s relatively to star A proper motion (see central panel of Fig. 5.1). This absorbing material is consistent with moving coherently with star A (within the uncertainty on the estimate of the velocity of the star). These lines are unlikely to be photospheric, since they are very narrow. They present an EW of ~ 0.017 Å and ~ 0.030 Å in the red and blue component, respectively, indicating a neutral sodium column density of $\sim 1.7 \times 10^{11}$ cm^{-2}.

5.3 Accretion luminosities

In the X-Shooter spectral range we have many emission lines tracing accretion onto the primary star. In particular, we consider Hα, Hβ, Hγ, Hδ, Paβ, Paγ, Paδ, Brγ, Ca II K, the Ca II IR triplet, and He I at 587 and 667 μm. We derive the observed luminosity of each line $L_{\rm line}$, and we convert it to an apparent accretion luminosity $\tilde{L}_{\rm acc}$ using the relations by Alcalá et al. (2014). By correcting for extinction we can obtain the actual accretion luminosity $L_{\rm acc}$. We show $\tilde{L}_{\rm acc}$ for each line in Fig. 5.2. The apparent accretion luminosity as derived from the Balmer lines is much lower than the one obtained from the Paschen lines. This indicates that the accretion region is likely being occulted, since the Balmer lines would suffer a higher level of obscuration. Note that reddening cannot explain the large scatter in $\tilde{L}_{\rm acc}$, since Antipin et al. (2015) and Schneider et al. (2015) have shown that the extinction is consistent with being grey up to the K-band. We now consider a grey extinction of $A_V = 3$ mag, and the following stellar parameters: $M_* = 1.4 M_\odot$, $R_* = 1.6 R_\odot$ and $\log T_{\rm eff} = 3.67$ (Rodriguez et al., 2013, and references therein). If we do not take into account the Balmer lines and

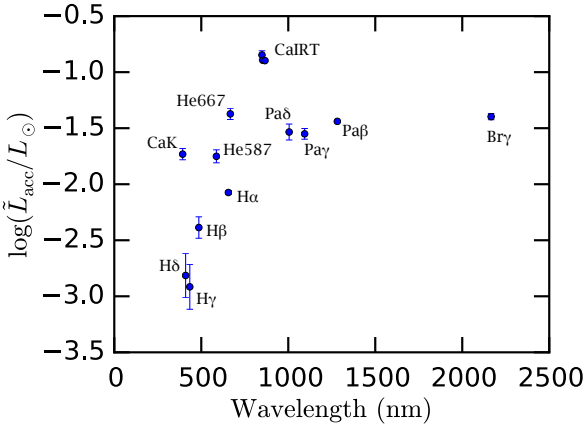

Fig. 5.2 Apparent accretion luminosities (accretion luminosities not corrected for extinction) from various emission lines labelled on the plot. The relations between $\tilde{L}_{\rm acc}$ and $L_{\rm line}$ are taken from Alcalá et al. (2014).

we average across all the other lines, we obtain a mass accretion rate $\dot{M} \approx 4 \times 10^{-8} M_\odot/\mathrm{yr}$. The accretion rate is much lower than the one obtained by Hartigan, Edwards & Ghandour (1995) ($\sim 10^{-6} M_\odot/\mathrm{yr}$), but note that they used different stellar parameters (a larger and less massive star), which would yield an accretion rate of $\sim 2 \times 10^{-7} M_\odot/\mathrm{yr}$ from our accretion luminosity. However we cannot conclude that the accretion rate has decreased since the 90's, since we see probes of occultation of the accretion region which might cause gas absorption on the emission lines.

5.4 Corrected photometry

We now consider the photometric evolution of the RW Aur system, before and during the dimming events. We show here that the flux from star B dominates the photometry during the second dimming event, whereas it does not contribute much to the whole system when star A is bright. We use data from Grankin et al. (2007) (from 1986 to 2005) and from Petrov et al. (2015) (from November 8, 2011). As specified in the latter paper, in the two datasets the two components of the RW Aur system are not resolved. In the literature, we have very few photometric points resolving both components in the optical (for resolved near-IR photometry see Schneider et al., 2015). In particular, optical photometry of star B has been reported only by White & Ghez (2001) and by Antipin et al. (2015). Antipin et al. (2015) have also measured the photometry of star A during the second dimming event, and they showed that star B was brighter during that night. In Table 5.1 we report the photometry

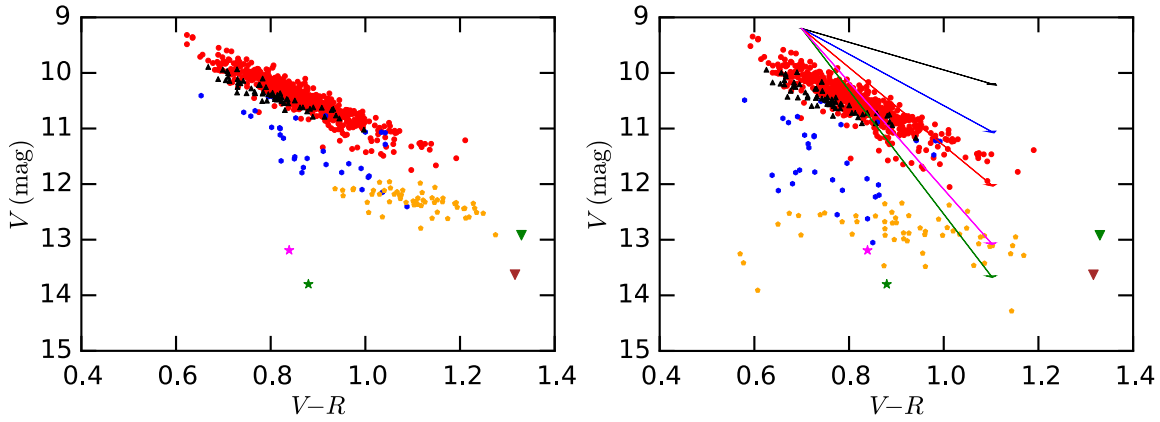

Fig. 5.3 Top panel: photometry of star A + B as in fig. 2 by Petrov et al. (2015). Bottom panel: photometry of star A, after subtraction of the averaged flux from star B as measured by White & Ghez (2001) and Antipin et al. (2015). Legend: red dots are historical data from 1986 to 2005. Blue hexagons: first dimming. Black triangles: between the two dimming events. Orange pentagons: second dimming. Green star and green triangle: photometry of star A and B, respectively, from Antipin et al. (2015). Brown triangle: star B from White & Ghez (2001). Magenta star: star A from our X-Shooter spectrum. All points are in Johnson system. The four arrows portray the reddening vectors for different grain size distributions, defined by the tuple $(q, a_{\max})$, where $a_{\max}$ is expressed in μm. Respectively, black: (3.5, 1); blue: (3.5, 80); red: (3.1, 30); green: (2.5, 17); magenta: (1.5, 8).

by Antipin et al. (2015) and White & Ghez (2001) and the synthetic photometry obtained from our X-Shooter spectra.

In order to reconstruct the photometric evolution of star A, we consider all the photometric points of the unresolved system, and we subtract the flux of star B from them, assuming that it is stable with time. In Fig. 5.3 we show the photometry of the whole system (top panel), and the photometry of star A after subtraction of the flux of star B, which was calculated as the average of the estimates by White & Ghez (2001) and Antipin et al. (2015) (bottom panel). When star A is bright the photometry does not change substantially, since star A dominates the flux of the system in the optical bands. The unresolved photometric points of the two dimming events move substantially in the VR colour-magnitude diagram when we subtract the contribution from star B, and they become statistically similar to the two resolved photometric points of star A. The large scatter in the corrected photometry traces the uncertainty on the unresolved photometry.

Such corrected photometry indicates two main results. The first one is that the A component, while being about 3 mag fainter, retains the same color range, i.e. the extinction law is roughly grey in the optical bands, as suggested by Antipin et al. (2015) and confirmed

Star	Reference	*U*	*B*	*V*	*R*	*I*
A	This work	14.00	13.96	13.19	12.35	11.55
A	Antipin et al. (2015)	14.26	14.50	13.80	12.92	12.10
B	Antipin et al. (2015)	14.97	14.26	12.92	11.59	10.49

Table 5.1 Resolved *UBVRI* photometry of RW Aur A and B during the second dimming event from our X-Shooter spectrum and Antipin et al. (2015). Values are in Johnson system. The errors on our photometry are evaluated to be at the 2% level.

by Schneider et al. (2015) in the NIR bands. The second result descends from a comparison with new X-Ray observations by Schneider et al. (2015). By observing star A during the second dimming event, they estimated a hydrogen column density $N_{\rm H} \sim 2 \times 10^{22}\,{\rm cm}^{-2}$. Let us assume here that the optical dimming is caused by dust entrained in the gas detected by the X-rays, and that scattering is negligible. We consider a dust-to-gas ratio of 0.01 in the absorbing material, and we adopt a dust grain size distribution $dn/da \propto a^{-q}$ with $q = 3.5$ (where a is the size of the dust grain), with a minimum grain size $a_{\rm min} = 50\,$Å (see Section 1.1.2). We compute the opacities κ in the V-band as a function of the maximum grain size by using the code by Wyatt & Dent (2002). We normalise them such that $N_{\rm H} = 2.21 \times 10^{21}\,{\rm cm}^{-2}$ gives an $A_V = 1$ mag for a maximum grain size $a_{\rm max} = 1\,\mu$m ($\kappa \sim 250\,{\rm cm}^2/{\rm g}$), as measured for galactic ISM (e.g. Güver & Özel, 2009). Combining the resolved photometry in both this work and Antipin et al. (2015), we estimate an average dimming of star A of $A_V \sim 3$ mag. Schneider et al. (2015) used the mean brightness of star A during the dimmed state, after subtraction of star B from the unresolved photometry, to find $A_V = 2.2\,$mag - a value consistent within the uncertainties. $N_{\rm H} \sim 2 \times 10^{22}\,{\rm cm}^{-2}$ and $A_V \sim 3\,$mag implies a required opacity κ at 500 nm of $\sim 82\,{\rm cm}^2/{\rm g}$. This can be achieved for a variety of assumptions about the grain size distribution and the dust-to-gas ratio.

In Fig. 5.3 we illustrate the reddening vectors produced by 4 grain size distributions that produce the above optical opacity assuming a dust-to-gas ratio of 0.01; these are characterised by the following pairs of $(q, a_{\rm max})$ values: (3.5, 80); (3.1, 30); (2.5, 17); (1.5, 8). We also show the reddening vector assuming an ISM-like grain size distribution and opacity (i.e. $q = 3.5$ and $a_{\rm max} = 1\,\mu$m). Only the most extreme cases ($q \leq 2.5$) are marginally consistent with the data, even though the reddening contribution from the small grains is significant even for these distributions. This might indicate that the dust-to-gas ratio is higher than 0.01, and there is a considerable amount of dust mass in large grains ($a \gtrsim 20\,\mu$m).

5.5 Discussion and Conclusions

The high column density derived from the X-rays observation by Schneider et al. (2015) would lead to saturated absorption lines both in Na and in K resonant transitions, for standard ionisation fraction and metal abundances. Indeed we clearly detect the Na saturated line, which did not look saturated prior to the dimming event. We can therefore conclude that the gas detected in such absorption lines is the one probed by Schneider et al. (2015). The blueshifted velocity (-60 km/s) of these lines with respect to star A rules out that this dense material has been displaced by the tidal encounter, and suggests it originates from the inner region of the accretion disc, where such high velocities are easily present, e.g. via winds (Petrov et al., 2015). The fact that this line is seen in spectra obtained during the bright state (as in Alencar et al., 2005) indicates that the gas column density has some variability that may not be correlated to the dimming.

The lower apparent accretion luminosities derived for the Balmer lines compared to other lines tracing accretion indicate that the gas material is obscuring the accretion regions. Petrov et al. (2015) suggested that O I and S II forbidden lines do not seem to change substantially in total flux between the bright and dim state, indicating that winds and jets on larger scales are not significantly affected by the obscuration, therefore limiting the spatial extent of the occulting material.

The IR excess observed by Shenavrin, Petrov & Grankin (2015) suggests that the occulting dust material is in proximity of star A (~ 0.1 AU). At least two possible scenarios can explain all these observations in a coherent picture. A first explanation that models the two events in the same framework is an enhanced stellar wind that is able to entrain quite large grains formed in the inner disc, as proposed by Petrov et al. (2015). This mechanism would simultaneously explain the optical and NIR dimming, the high gas column density, the high gas velocities and the IR emission excess. If we assume that the wind is spherical, with a velocity $v = 60$ km/s, a mass density $\rho = N_{\rm H}\mu m_{\rm H}/R$, and $R = 0.1$ AU, we obtain a mass loss rate $\dot{M}_{\rm wind} \approx 2 \times 10^{-8} M_{\odot}/{\rm yr}$, where $\dot{M}_{\rm wind} = 4\pi R^2 \rho v$ from the continuity equation. This seems to indicate that the ratio of mass loss rate over mass accretion rate is ~ 0.5, higher than typical values of 10^{-1} (Hartigan, Edwards & Ghandour, 1995; Calvet & Gullbring, 1998; Hartmann, 2008). However, the wind might not be spherical, and we are probably underestimating the mass accretion rate (see Section 5.3), due to the high gas column density in front of star A absorbing part of the emission lines. The obtained $\dot{M}_{\rm wind}$ implies a maximum grain size for the purported entrained dust of $\sim 8\,\mu$m, where we have considered Epstein dragging and a gas temperature $T = 10^4$ K for the spherical wind (see Section 6.5.2 for the derivation

of the equation):

$$a_{\max} = \frac{1}{4\pi\bar{\rho}} \frac{v_{\rm th}\dot{M}_{\rm wind}}{GM_*}, \text{ where } v_{\rm th} = \sqrt{\frac{8k_{\rm B}T}{\pi m_{\rm H}}}, \tag{5.1}$$

and $\bar{\rho} = 1$ g/cm^3 is the density of the dust grains. The dust laden wind could reproduce the grey extinction with a power law grain size distribution if $a_{\max} \gtrsim 8 - 15\,\mu$m (see Fig. 5.3), in broad agreement with the maximum grain size obtained here. However, the apparent grey extinction can be explained both by effective grain growth occurred in the occulting body (and possibly a high dust-to-gas ratio), or by a significant scattering process (or by a combination of both, see Schneider et al., 2015).

A second, less likely, possibility is that the high gas column density along the line of sight and the dust leading to optical and NIR extinction are not directly correlated. The inner disc could have suffered a sudden geometric variation (as as puffed up inner rim) due to the interaction with a strong stellar wind (probed by the saturated absorption lines). If the inner disc is warped, such structure could lie along the line of sight and occult the primary star (the outer disc is inclined by $45 - 60^\circ$; Cabrit et al., 2006). Moreover, the puffed up ring would intercept more stellar photons and re-radiate them at the local temperature, thus explaining the IR excess observed by Shenavrin, Petrov & Grankin (2015). A magnetically driven warp, as in the case of AA Tau (e.g. Cox et al., 2013), is unlikely to happen for a $1.4M_\odot$ star, since the magnetic dipole moment is expected to decrease steeply with mass in PMS stars (e.g. Gregory et al., 2012). A warped structure could be produced by a close spectroscopic binary misaligned to the outer disc (e.g. Facchini, Lodato & Price, 2013). Such a binary has been proposed by Petrov, Pelt & Tuominen (2001) to model a 2.7 days variability observed in some emission line profiles (even though such hypothesis has been contested by other authors, e.g. Dodin, Lamzin & Chuntonov, 2012).

Finally, in all the high resolution UVES spectra we have detected a very narrow absorption feature in the Na I D lines, that for a standard ionisation fraction and metal abundances indicates a low column density material co-moving with star A. This is in agreement with the models reported in chapter 4 (see Fig. 4.11), where we predicted that a stream of material has been displaced between stars A and B along the line of sight with the correct velocity by the tidal interaction. However, at this stage we cannot rule out that these narrow components are simply tracing atomic gas of the local cloud.

Chapter 6

External photoevaporation of protoplanetary discs in mild environments: the impact of dust

This chapter is based on a paper submitted to MNRAS (Facchini, Clarke & Bisbas, 2015), and represents the most important project included in this thesis. I have conducted all the analysis reported here. The only calculations that I have not performed myself are the temperature estimates obtained with the PDR code, which were conducted by Thomas G. Bisbas at UCL.

6.1 Introduction

Lada & Lada (2003), Porras et al. (2003) and others have shown that the probability density function for cluster membership number N for clusters in the Solar Neighbourhood scales with $1/N^2$. Therefore the cumulative probability for a star to be born in a cluster of size $\leq N$ is inversely proportional to N (e.g. Adams, 2010). Within 2 kpc of the Sun, the median value of this distribution (also taking into account isolated stars) is ~ 300 (Adams et al., 2006; Allen et al., 2007). The majority of close-by protoplanetary discs are then very likely to evolve embedded in relatively 'mild' (low N) environments. Clusters and groups with $N \leq 500$ have typical FUV ($6 \leq h\nu < 13.6\,eV$) fields $G_{FUV} \leq 3000\,G_0$ (e.g. Fatuzzo & Adams, 2008), where G_0 is the local FUV interstellar field (1.6×10^{-3} erg s^{-1} cm^{-2}, Habing, 1968). Fatuzzo & Adams (2008) have also shown that the FUV flux depends strongly on the most massive star in the cluster, and on the intra-cluster column density of absorbing material. Stars in small groups ($N \sim 50-100$) are likely to be impinged by an environmental FUV field of $\sim 30-300\,G_0$, i.e. slightly larger than the local field. Note that at such low values

the external radiation becomes comparable to the radiation from the central star even at large ($R \lesssim 100$ AU) radii (e.g. Bergin et al., 2003). The majority of protoplanetary discs are then very likely to lie in the subcritical regime of external photoevaporation (see Section 1.4 for an introduction on the different regimes of external photoevaporation), at least in the Solar Neighbourhood.

The subcritical regime is the most difficult to probe observationally. However, there are some observed signatures that might be indicating that such a mechanism is occurring even in quite isolated systems (i.e. very low external UV fluxes). A potential example of this is the disc around IM Lup. Panić et al. (2009) have shown that outside the mm-bright disc ($R_{\rm out,dust} = 400$ AU; Pinte et al., 2008), the gas structure as probed by CO emission lines indicates a steep decrease in the surface density profile, which resembles the profiles obtained by Adams et al. (2004) in their flow models. Öberg et al. (2015) have also detected a DCO^+ double ringed structure, which could be tracing a radially increasing temperature gradient in the outer regions of the disc (even though they propose non thermal desorption of CO ices as the best explanation of the observed feature), in agreement with the predictions from external photoevaporative models. Note that similar features are also predicted by photoevaporation models where the winds are driven by the FUV field emitted by the central star and by the accreting material (Gorti & Hollenbach, 2009; Gorti, Hollenbach & Dullemond, 2015). From simple calculations of external photoevaporation models the gas flow in the outer regions of this disc would be highly dust depleted, since the drag force is very weak for the large grains probed by submm observations, and such an effect is compatible with the dust depleted outer regions of the disc. There are other systems where this second effect (a radially decreasing dust-to-gas ratio, as probed by line/continuum size discrepancies) is observed (e.g. Piétu, Dutrey & Guilloteau, 2007; Andrews et al., 2012; Rosenfeld et al., 2013; de Gregorio-Monsalvo et al., 2013). Note however that Birnstiel & Andrews (2014) have shown that such discrepancies can also be explained by the size-dependent radial drift of dust particles, without appealing to an outer disc wind. We will suggest alternative observational diagnostics that can discriminate between the two scenarios.

In this chapter, we firstly aim to compute the mass loss rates of discs affected by external photoevaporation in the subcritical regime, by extending the parameter space investigated by Adams et al. (2004) to larger (but still subcritical) discs, and milder ambient fields. Our method of solution broadly follows that of Adams et al. (2004) but with some important differences relating to the effect of non-isothermality in correctly locating the critical point of the flow. We also iterate towards a self-consistent solution which takes into account the fact that only small grains are entrained in the flow. Note that the effect of partial entrainment of dust grains upon the thermal structure of the flow has been recently applied

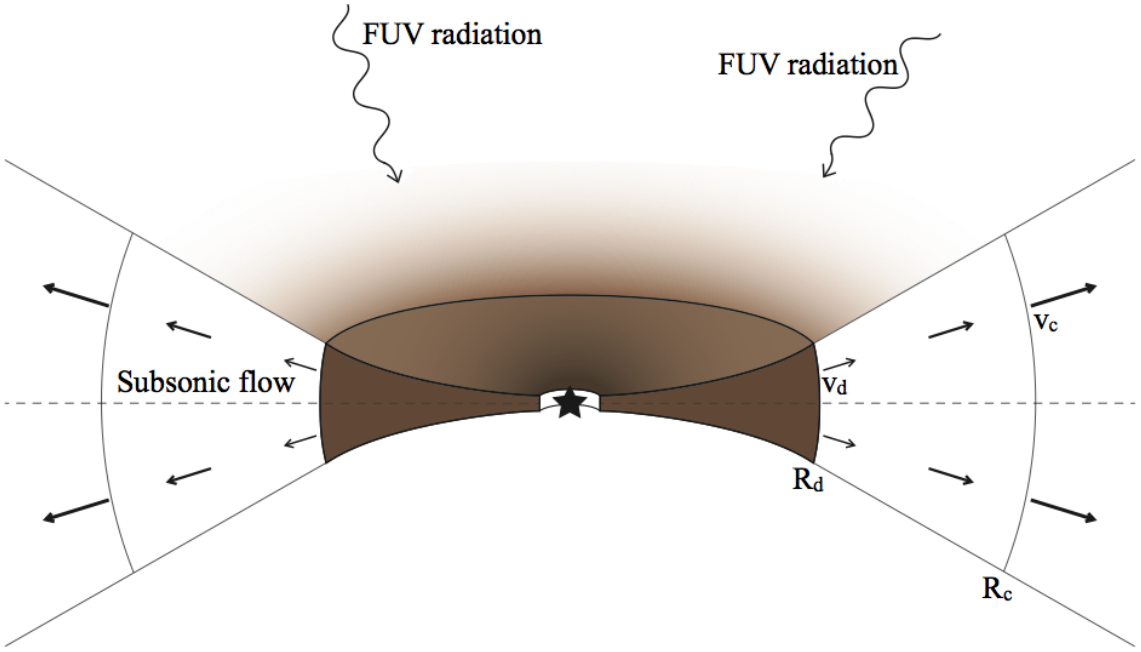

Fig. 6.1 Schematic illustrating a photoevaporating disc impinged by an ambient FUV radiation, in the subcritical regime ($R_d < R_g$). The radiation can be directional or more isotropic, depending on the source of irradiation. From the outer edge of the disc, a subsonic radial flow develops, until it reaches the critical radius R_c, where the flow velocity is close to the sound speed. From this point outwards the velocity of the wind is approximately uniform. The mass loss from the disc's outer rim is more significant than the mass loss from the disc surface in the subcritical regime.

to the internal photoevaporation scenario by Gorti, Hollenbach & Dullemond (2015). We finally present typical radial profiles of the main hydrodynamical quantities, and propose potential observational signatures of ongoing photoevaporation in this subcritical regime.

The chapter is structured as follows. In Section 6.2 we briefly summarise the photoevaporative model by Adams et al. (2004), and explain how our description differs from theirs. In Sections 6.3 - 6.6 we detail the main ingredients of our model; respectively the thermal properties, gas hydrodynamics, dust hydrodynamics, and the iteration procedure to obtain the final solutions. In Section 6.7 we present our results, which are then discussed in Section 6.8. In Section 6.9 we summarise our conclusions.

6.2 Comparison with previous work

We consider the subcritical regime ($R_d < R_g$) previously investigated by Adams et al. (2004) and assume that the disc is irradiated by an isotropic FUV ambient radiation. Adams et al.

(2004) have shown that the ratio between the mass loss rate from the disc surface $\dot{M}_{\rm sur}$ and the mass loss from the disc edge $\dot{M}$ scales as $\dot{M}_{\rm sur}/\dot{M} \sim (R_{\rm d}/R_{\rm g})^{1/2}$. Since they focus on the subcritical regime, where $R_{\rm d} < R_{\rm g}$, the mass loss rate is dominated by the radial flow emerging from the outer rim of the disc, and not by the material flowing from its surface. Thus the subsonic wind can be described with a 1D radial model (see Fig. 6.1 for a schematic of the model). Adams et al. (2004) computed the temperature as a function of local gas density n and FUV (from the ambient radiation) optical depth τ by using the photo-dissociation region (PDR) code by Kaufman et al. (1999). They then coupled this temperature dependence with the steady state momentum/continuity equations in order to iteratively find a self-consistent steady state solution of the gaseous flow. The model we present in this chapter is very similar to the one proposed by Adams et al. (2004), but contains some key differences, that will be described in more detail between Sections 6.3 - 6.5. In particular:

1. We take deviations from isothermality into account in locating the critical point of the flow, in contrast to Adams et al. (2004) who impose the condition that the flow is transonic at the location corresponding to the sonic point for *isothermal* gas. This self-consistent location of the critical point results in a different location and local flow velocity at this point compared with the isothermal solution. Our results will probe that this difference is the most important one, since it will modify the mass loss rates by a significant amount. Having located the critical point of the flow we are able to integrate inwards to the disc edge (in contrast to Adams et al. (2004) who adopt an iterative scheme in integrating outwards from the disc edge).

2. The self-consistent location of the critical point allows us to obtain solutions over a larger range of parameter space than Adams et al. (2004). Specifically we are able to find solutions for lower values of the interstellar field $G_{\rm FUV}$ (i.e. down to $30\,G_0$) and for a wider range of outer disc radii (out to $R_{\rm d} = 250$ AU).

3. Having determined a flow solution at fixed dust to gas ratio we then take account of the fact that only the small grains are entrained in the flow and re-compute the flow solution implementing the reduced dust to gas ratio in the flow.

4. Our code computing the temperature structure is different from Adams et al. (2004) (see Section 6.3 below).

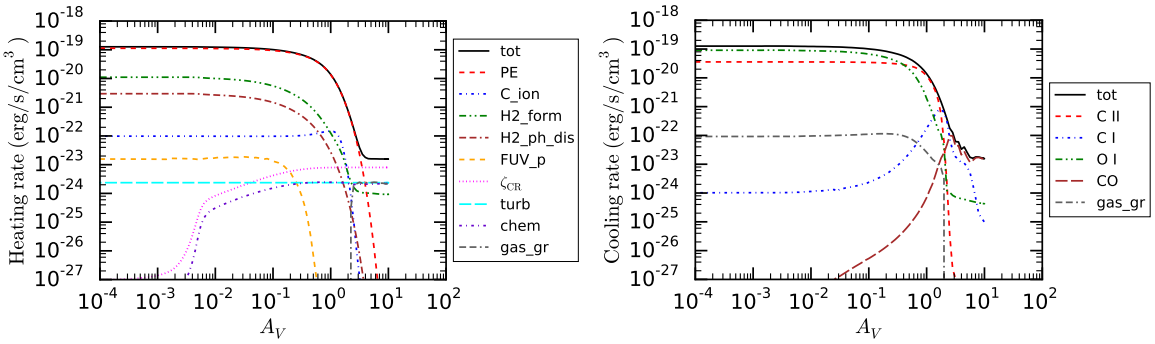

Fig. 6.2 Heating and cooling rates per unit volume for a slab of material of density $n = 10^4\,\mathrm{cm}^{-3}$ impinged by a FUV field of $G_{\mathrm{FUV}} = 300\,G_0$, after it has reached thermo-chemical equilibrium computed with the reduced chemical network. The dust-to-gas ratio is 10^{-2} and the PAH-to-dust ratio is 2.6×10^{-2}. The heating functions (labelled in the legend) are respectively: total heating rate (tot); photoelectric heating (PE); C ionisation (C_ion); H_2 formation (H2_form); H_2 photodissociation (H2_ph_dis); FUV pumping (FUV_p); cosmic rays (ζ_{CR}); turbulent heating (turb); chemical heating (chem); gas-grain collisions (gas_gr). More details can be found in Bisbas et al. (2012).

6.3 Temperature estimates - PDR

FUV radiation ($6 \leq \mathrm{h}\nu < 13.6\,\mathrm{eV}$) plays a crucial role in determining the thermal structure and corresponding chemistry in so-called photodissociation regions (PDRs) where gas undergoes a transition between ionised and molecular state. If a disc is interacting with an ionising radiation field impinging externally, then between the ionisation front (if present) and its dense gas, the region is optically thin to FUV radiation but optically thick to EUV radiation ($\mathrm{h}\nu \geq 13.6\,\mathrm{eV}$). This causes the gas to be in a state of partial dissociation where the temperature is set by the FUV radiation field. Under these conditions, determination of the gas temperature requires modelling of various heating and cooling processes in terms of a complex and non-linear set of differential equations describing a network of chemical reactions. In the last two decades, many groups have managed to develop numerical codes that are able to solve such problems (see Rollig et al., 2007, for a paper detailing inter-comparison between such codes). Below we describe the 3D-PDR code (Bisbas et al., 2012) that we use to obtain the gas temperature as a function of column density, grain opacity, local gas density and FUV field.

Table 6.1 Abundances of species used in the present work, from Asplund et al. (2009).

H	4×10^{-1}	Mg^+	3.981×10^{-5}
H_2	3×10^{-1}	C^+	2.69×10^{-4}
He	8.5×10^{-2}	O	4.898×10^{-4}

6.3.1 3D-PDR

The 3D-PDR code (Bisbas et al., 2012) is a three-dimensional time-dependent code treating photodissociation regions of arbitrary density distribution. Using an iteration scheme it solves the chemistry at every element consisting of the gaseous structure until thermal balance has been reached. 3D-PDR uses a set of various heating and cooling functions fully described in Bisbas et al. (2012), and showed in Fig. 6.2 for a specific case. The code has been used in various one-dimensional (Bisbas et al., 2014; Bisbas, Papadopoulos & Viti, 2015) and three-dimensional (Offner et al., 2013, 2014; Gaches et al., 2015) applications. The 1D version of the code UCL-PDR has been benchmarked with many other PDR codes (Rollig et al., 2007).

In this chapter, we have adopted the code modifications described in Bisbas et al. (2014). We use a reduced version of the UMIST 2012 network (McElroy et al., 2013) which contains 33 species (including e^-) and 330 reactions. Table 6.1 shows the initial abundances used by the 3D-PDR code at the beginning of the calculations (taken from Asplund et al., 2009). Using the full chemical network of 215 species corrects the temperature by a factor of $\sim 10-15\%$. Since other unknown parameters (as polyclicic aromatic hydrocarbon abundances, see below) lead to even larger uncertainties, we opted for the reduced network to save computational time. We consider one-dimensional uniform density profiles with $10^2 < n < 10^8\,\mathrm{cm}^{-3}$ interacting with radiation fields of 30, 300 and $3000\,G_0$. The spatial extent of each density profile is chosen so that the visual extinction, A_V, is in the range $10^{-7} \leq A_V \leq 10$. Density is sampled every 0.1 dex, and A_V every 0.05 dex. The results are then interpolated with cubic-spline functions to a much finer grid. The cosmic ray ionisation rate, ζ_{CR}, is taken to be $\zeta_{\mathrm{CR}} = 5 \times 10^{-17}\,\mathrm{s}^{-1}$. The treatment of PAHs is discussed in the next Section. We evolve the chemistry in each simulation for 10 Myr. We have checked that the temperature balance is reached on shorter timescales, ~ 10 kyr. *A posteriori*, we have verified that the flow timescale is always longer than 10 kyr, thus temperature balance within the flow is a reasonable assumption.

6.3.2 Dust and PAHs

Dust plays a key role in the determination of the gas temperature. For example, the main heating mechanism of the gas is photoelectric heating from the atomic layers of PAHs (e.g. Weingartner & Draine, 2001; Croxall et al., 2012), but it can also affect the temperature with other mechanisms such as H_2 formation and gas-grain collisions. Secondly, dust can have a significant impact on the chemistry, which eventually sets the abundances of the main coolants, e.g. by controlling the amount of ices. Note that all these mechanisms depend on the total surface area of dust grains. Finally, dust sets the attenuation factor of the FUV radiation via the penetrating depth τ, where we set $\tau = 1.8 A_V = N_{\rm H} \sigma_{\rm FUV}$ and $N_{\rm H}$ is the hydrogen column density. A detailed description of this last effect will be described in Section 6.5.

Typical interstellar dust can be modelled with a simple distribution $d\tilde{n}/ds \propto s^{-q}$, where $\tilde{n}$ is the numerical density of dust particles, and s is the grain size. It is well known that in the interstellar medium q assumes a typical value $q \sim 3.5$ (historically labelled as MRN distribution, from Mathis, Rumpl & Nordsieck, 1977). More recently, interferometric observations have suggested a shallower distribution in the optically thin regions of protoplanetary discs at submm - mm wavelengths, where $q \sim 2.5 - 3$ (e.g. Ricci et al., 2010a,b, 2012b), and dust evolution models have suggested the same qualitative result (e.g. Birnstiel, Ormel & Dullemond, 2011). Moreover, the maximum grain size does increase substantially in the midplane of protoplanetary discs (see the recent review by Testi et al., 2014, and references therein), to sizes $\gtrsim 1$ mm. Grain growth can alter the heating and cooling processes mentioned above.

The only observation indirectly constraining the grain size distribution within the photoevaporative winds is by Störzer & Hollenbach (1999), who estimated the cross section of supercritical winds at FUV wavelengths from the location of the ionisation front around proplyds in Orion. Their best estimate is $\sigma_{\rm FUV} = 8 \times 10^{-22}\,{\rm cm}^2$, where the error bars are assumed to be very large, since the used sample is very small (~ 10 objects) and the estimate is model dependent. Störzer & Hollenbach (1999) and later Adams et al. (2004) noticed that such cross section is ~ 0.3 the typical ISM one, thus indicating moderate grain growth of the dust entrained in the wind.

We compute the cross section at FUV wavelengths ($\lambda = 0.1\,\mu$m) for an ISM-like dust distribution ($q = 3.5$ and $s_{\rm max} = 0.25\,\mu$m, see e.g. Draine, 2011) using the code described in Wyatt & Dent (2002) (see their section 4.1). We use the optical constants from Li & Greenberg (1997), for iceless silicate grains with a porosity of 0.3. The absorption coefficients of the grains $Q_{\rm abs}(\lambda, s)$ are computed using Mie theory (Bohren & Huffman, 1983), Rayleigh-Gans theory or geometric optics in the appropriate limits (Laor & Draine, 1993). Assuming a dust-to-gas ratio to 10^{-2} we obtain a cross section $\sigma_{\rm FUV} \approx 2.6 \times 10^{-21}\,{\rm cm}^2$, as expected. We

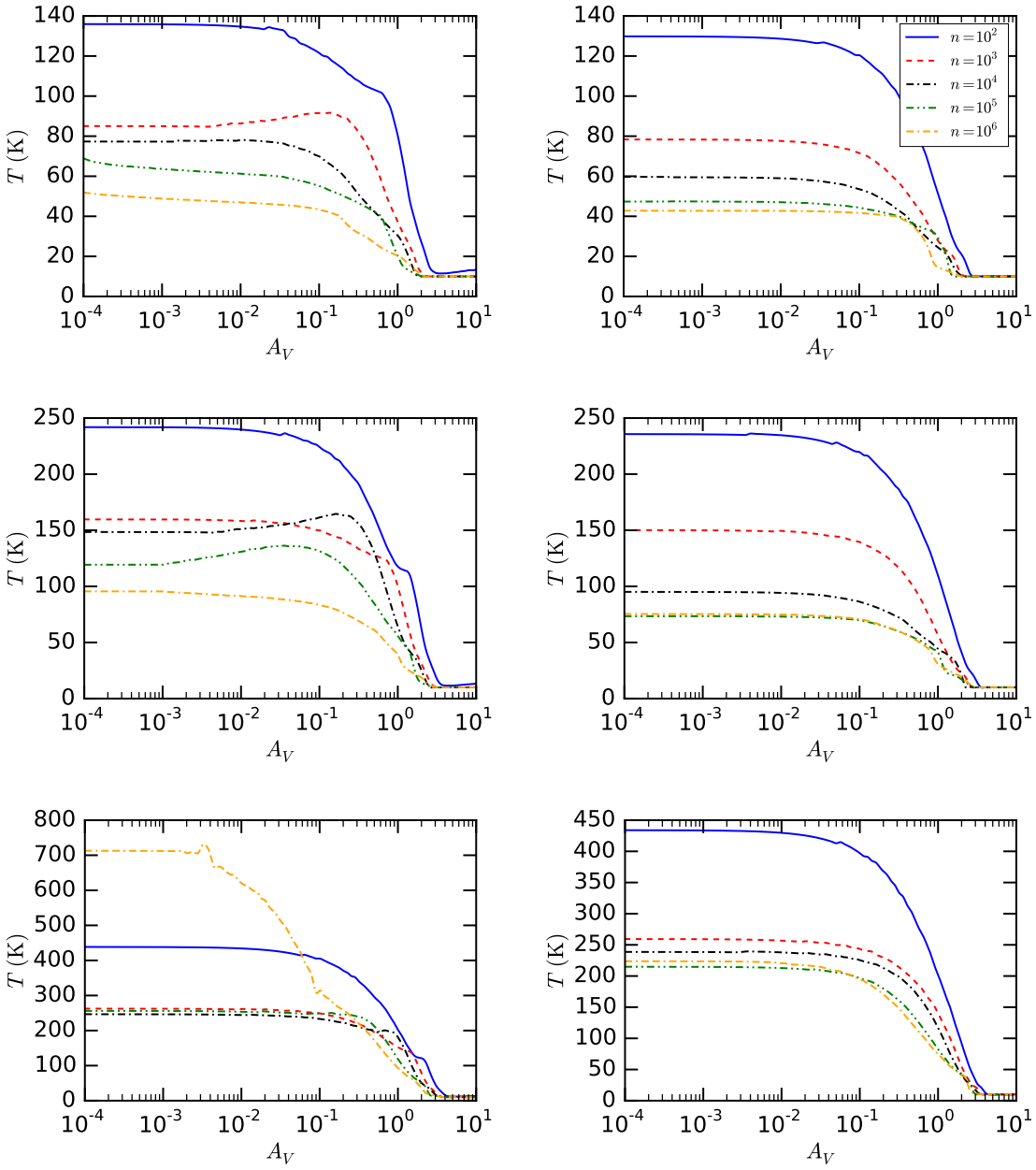

Fig. 6.3 Gas temperature as a function of visual extinction A_V for three different values of the ambient FUV field: 30, 300 and 3000 G_0, from top to bottom. The left panels are associated to a grain size distribution with maximum grain size $s_{\max} = 3.5\,\mu$m, the right panels to a distribution with $s_{\max} = 1$ mm. Line colours indicate different gas numerical densities n, ranging between $10^2 - 10^6$ cm^{-3} (the legend is reported in the right top panel).

then determine the maximum grain size of a distribution with $q = 3.5$ that has an associated cross section 0.3 times smaller than the ISM-like one. The best fit gives $s_{\max} = 3.5\,\mu$m. This result confirms that the estimates by Störzer & Hollenbach (1999) are probing moderate grain growth.

In the PDR code (and throughout the whole chapter), we consider two MRN distributions ($q = 3.5$) with maximum grain sizes $s_{\max} = 3.5\,\mu$m and $s_{\max} = 1$ mm. We fix the dust-to-gas ratio to 10^{-2}. The first distribution is chosen as to give the same cross section used by Adams et al. (2004) in their models, in order to have a direct comparison with their results. The second distribution represents a disc where substantial grain growth has occurred, and the population of small grains, which contribute the most to the dust surface area when $q > 3$, is reduced by a factor $\sim 10^2$.

Polycyclic Aromatic Hydrocarbons (PAHs) are the dominant heating source, since photons are very efficient in removing electrons from such mono-layered molecules. However, the amount of PAHs in protoplanetary discs is not well constrained by observations. Infra-Red observations from Spitzer and from the ground have revealed strong PAH emission features in some Herbig Ae/Be stars, whereas very few T Tauri stars have shown them at a detectable level (Geers et al., 2006, and references therein). This difference is probably due to the more intense UV field emitted by the Ae/Be stars (e.g. Visser et al., 2007) exciting the PAHs. For the same reason, PAH emission is spatially concentrated in the inner region of the discs, where the UV flux from the central star is higher (Geers et al., 2007; Maaskant et al., 2014). PAH abundance in discs is still being debated. Observations (e.g. Geers et al., 2006; Oliveira et al., 2010) tend to indicate that PAH-to-dust mass ratio in discs is $\sim 10\%$ of the PAH-to-dust mass ratio in the galactic ISM, which is $\approx 4 \times 10^{-2}$ (Draine & Li, 2007; Tielens, 2008), but the estimate is poorly constrained. In thermo-chemical disc models, people have used different values of PAH-to-dust mass ratio, e.g. 0.5×10^{-2} (Bruderer et al., 2012), or 1.3×10^{-2} (Woitke et al., 2015). Because of the level of the uncertainties on this value, we simply fix the PAH-to-gas mass ratio to 2.6×10^{-4}, as in Wolfire et al. (2003), since we use their prescription to compute the photoelectric heating. For the dust-to-gas ratio of 10^{-2} used in this chapter, this value yields to a PAH-to-dust mass ratio of 2.6×10^{-2}.

Another debated topic is whether grain growth affects the amount of PAHs, i.e. whether they should scale accordingly to the amount of small grains. This is still largely unconstrained. As an example, one of the strongest PAH emission features is observed in Oph IRS 48 (Geers et al., 2007), where grain growth has certainly occurred (e.g. van der Marel & et al., 2013). Even though some recent models (e.g. Gorti, Hollenbach & Dullemond, 2015) assume a reduced PAH abundance when small grains are depleted by effective grain growth, in this

chapter we prefer keeping the PAH abundance fixed, since there is no clear observational indication that PAHs would follow the small grains.

In order to compute the photoelectric heating due to PAHs, we adopt the treatment by Bakes & Tielens (1994), with the additional modifications suggested by Wolfire et al. (2003) (with the $\phi_{\rm PAH}$ factor defined in their equation 21 equal to 0.4).

6.3.3 Results

Fig. 6.3 shows the results of the 3D-PDR code for FUV fields of 30, 300 and 3000 G_0 for the two grain size distributions. We present the gas temperature as a function of visual extinction A_V, for logarithmically sampled values of gas density n. As expected, the gas temperature increases with intensity of the external radiation. At a given $G_{\rm FUV}$, for the parameters we have chosen, temperature is usually a decreasing function of visual extinction A_V. For $s_{\rm max} = 3.5\,\mu$m temperature does also increase with A_V in the marginally optically thick regime, when $n \sim 10^3 - 10^4\,{\rm cm}^{-3}$. Similarly, temperature is not a monotonically decreasing function of density n. This non-monotonic behaviour is a well known result in PDR codes (Kaufman et al., 1999).

These results are strongly dependent on the metallicity and on the dust-to-gas ratio, since they both regulate the heating and cooling functions. In particular, reducing the amount of small grains has the net effect of slightly decreasing the temperatures, as we can see comparing the temperatures obtained with the two different dust distributions. The smaller dust total surface area reduces some heating mechanisms, such as photoelectric heating, H_2 formation rate and H_2 photodissociation. However, the total heating is still dominated by the photoelectric effect on PAHs. Cooling is not affected significantly, since the main coolants are C II and O I in the optically thin regime (see Fig. 6.2). The net effect is that temperature is not affected significantly by the total dust-to-gas ratio, provided that PAH abundance is kept fixed. For the cases considered here and displayed in Fig. 6.3, at fixed density the temperature always shows a plateau at low optical depths, and then decreases steeply with visual extinction, until it approaches unity and the gas becomes optically thick to the external radiation. These two characteristics will shape the final profiles of the subsonic winds. Finally, the temperatures are lower than the ones computed by Adams et al. (2004) (e.g. by a factor ~ 2 when $G_{\rm FUV} = 300\,G_0$), in the regions of parameter space that overlap, even in the hottest case when $s_{\rm max} = 3.5\,\mu$m. For the same dust distribution, we obtain temperatures similar to the ones by Kaufman et al. (1999) (and therefore by Adams et al. (2004), who use the same PDR code) by using the prescription by Bakes & Tielens (1994) (without the correction by Wolfire et al., 2003) for the PAH photoelectric heating. In particular, we reproduce the same trend observed by Kaufman et al. (1999) in their fig. 1.

6.4 Hydrodynamics

In the last section we have shown how to derive the temperature of the gas in the PDR region as a function of local density n and visual extinction A_V. We now want to couple these results to the hydrodynamical equations describing the flow departing from the edge of a protoplanetary disc.

6.4.1 Equations for the wind structure

We develop a 1D description of the problem in a quasi spherical geometry, where we self-consistently solve for the radial steady-state structure of the wind launched from the disc outer edge. The equations shown in this section are based on the similar model by Adams et al. (2004).

The time independent version of the continuity equation is:

$$\dot{M} = 4\pi R^2 \mathscr{F} \mu m_{\rm H} n v, \tag{6.1}$$

where $m_{\rm H}$ is the hydrogen atom mass and v is the velocity of the gas. $\mathscr{F}$ is the fraction of the solid angle subtended by the disc outer edge (see equation 14 by Adams et al., 2004). The flow might be not perfectly spherical, since the wind might not be pressure confined at the boundaries of the wedge defined by the solid angle $4\pi\mathscr{F}$. We could model the flow with a hyper-spherical continuity equation, where $\dot{M} \propto R^{\alpha}$ and $\alpha > 2$ ($\alpha = 2$ defines the spherical case, see equation 6.1). For simplicity, we consider the spherical case only in this work.

Similarly, the time indipendent momentum equation is:

$$v\frac{dv}{dR} + \frac{1}{\rho}\frac{dP}{dR} + \frac{GM_*}{R^2} - \frac{j^2}{R^3} = 0, \tag{6.2}$$

where $j^2 = GM_* R_{\rm d}$. We are considering a flow with uniform specific angular momentum, given by the Keplerian angular momentum at the outer radius of the disc. We assume an ideal gas law for the pressure $P = nk_{\rm B}T$, where T is a function of density and optical depth (as shown in Section 6.3).

Following Adams et al. (2004), we can express the above equations in a dimensionless form, where our parametrisation choice is slightly different. We define $\xi \equiv R/R_{\rm d}$, $f \equiv T/T_{\rm c}$, $g \equiv n/n_{\rm c}$ and $u \equiv v/c_{\rm s,c}$, where $c_{\rm s}$ is the sound speed of the gas. With the subscript c we indicate quantities evaluated at a critical radius $R_{\rm c} > R_{\rm d}$, which is defined in Section 6.4.2. Note that with these dimensionless units the local sound speed $u_{\rm s}^2$ is coincident with the

temperature f. We also define the parameters β:

$$\beta = \frac{GM_*\mu m_{\rm H}}{R_{\rm d}k_{\rm B}T_{\rm c}} = \frac{GM_*}{R_{\rm d}c_{\rm s,c}^2}, \tag{6.3}$$

and the optical depth $\tau \equiv N_{\rm H}\sigma_{\rm FUV}$, where

$$N_{\rm H} = \int_R^\infty n(R')dR' \tag{6.4}$$

is the column density between R and infinity. We thus obtain:

$$\frac{d\tau}{d\xi} = -\sigma_{\rm FUV}R_{\rm d}n_{\rm c}g = -\tau_{\rm d}g, \tag{6.5}$$

where $\tau_{\rm d} = \sigma_{\rm FUV}R_{\rm d}n_{\rm c}$. Combining the continuity and the momentum equation, we obtain a single differential equation for the dimensionless velocity u:

$$\frac{d\ln u}{d\xi}(u^2 - f - g\frac{\partial f}{\partial g}) = \frac{2}{\xi}(f + g\frac{\partial f}{\partial g}) - \beta\frac{\xi - 1}{\xi^3} + \tau_{\rm d}g\frac{\partial f}{\partial \tau}. \tag{6.6}$$

This last equation reduces to the standard Parker wind equation (Parker, 1958), in the limit of isothermality and in the absence of the centrifugal term. By solving this equation, we can obtain the velocity structure of the flow, from which we can obtain the density structure of the gas via the continuity equation. In order to find a solution, we integrate the equation inwards. In order to do so, we need to define the aforementioned critical radius $R_{\rm c}$, and we need to use reasonable initial conditions.

6.4.2 The critical radius

The structure of equation 6.6 shows a natural definition of a critical point: when the r.h.s. of the equation equals 0. When this happens, the l.h.s. of the same equation has to equal 0 as well. This can happen when u has a null gradient, or when the second multiplicand is 0. We require this second case to be the one, since we are looking for the analogue of the transonic solution in the typical Parker wind problem (Clarke & Carswell, 2007). In the isothermal case, this same procedure defines the sonic radius $R_{\rm s}$, where $u^2 = f$. We expect the critical radius to be of the same order of magnitude as the sonic radius. By requiring that the l.h.s. of the equation is 0, but $du/d\xi \neq 0$, we implicitly define a critical velocity:

$$u_{\rm c}^2 = f + g\frac{\partial f}{\partial g}, \tag{6.7}$$

which is related to the sound speed $u_{\rm s}$ via an additional term taking into account possible departures from isothermality. The equation for the dimensionless critical radius $\xi_{\rm c} = R_{\rm c}/R_{\rm d}$ is then:

$$g\tau_d \frac{\partial f}{\partial \tau}\xi_c^3 + 2u_{\rm c}^2\xi_{\rm c}^2 - \beta\xi_{\rm c} + \beta = 0, \tag{6.8}$$

where all the quantities are evaluated at the critical radius. This problem has to be solved implicitly, since all the quantities depend on where the critical radius is located, and on the initial conditions of the problem. Locating the critical radius self-consistently is a key ingredient of our approach in order to be able to integrate the flow structure inwards from this point to the disc outer edge. Note that this is a key difference between our model and the one proposed by Adams et al. (2004). In Section 6.7 we will show that taking into account this non-isothermal term affects significantly the final mass loss rates.

For every set of parameters M_*, $R_{\rm d}$ and $G_{\rm FUV}$ there is a family of solutions each of which has a different value of $T_{\rm c}$, mass loss rate and pressure at $R_{\rm d}$. We require that our flow is in pressure equilibrium with the disc at $R_{\rm d}$; therefore in principle we could use the pressure at the disc edge as a further independent variable which would define the mass loss rate and flow structure for a given disc in a given environment (cf. Adams et al., 2004). This however requires iterative solutions for various guessed flow velocities at $R_{\rm d}$ and is not a preferred method in the case where the critical point conditions are themselves a function of the flow solution. Since we start each flow solution from the self-consistently determined critical point of the flow, it is operationally convenient to use $T_{\rm c}$ as the independent variable. Each solution can then be mapped onto the corresponding value of the pressure at the disc outer edge.

In order to evaluate the critical radius for a given value of $T_{\rm c}$ we proceed as follows. We first guess the value of the critical radius (i.e. as parametrised by $\xi_{\rm c}$); for an initial guess we take the re-scaled sonic radius $\xi_{\rm s}$, using the isothermal limit of equation 6.8:

$$\xi_{\rm s} = \frac{\beta}{4}\left[1 + \left(1 - \frac{8}{\beta}\right)^{1/2}\right], \tag{6.9}$$

and noting that β is fixed for given $T_{\rm c}$ by equation 6.3.

Once we have an initial guess for the critical radius, for every iteration on the value of $\xi_{\rm c}$ we calculate the pair of values for the number density and optical depth at this point for which the PDR models predict that $T = T_{\rm c}$ locally. This step requires an assumption about the density structure of the flow *outside* the critical radius. Here we follow Johnstone, Hollenbach &

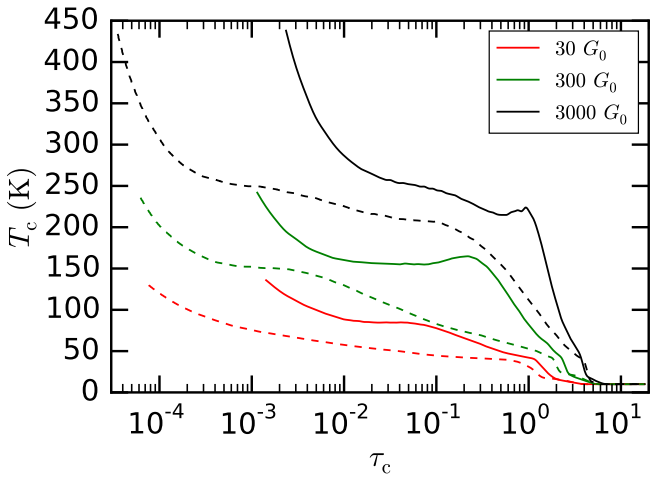

Fig. 6.4 The critical temperature, i.e. the input parameter to obtain a solution to the thermo - hydrodynamical equations, as a function of the optical depth evaluated at the critical radius R_c, for $G_{FUV} = 30$, 300 and $3000\,G_0$ for solution with $R_d = 120$. This implicit relation defines the boundary conditions at $R = R_c$. Solid lines refer to $s_{max} = 3.5\,\mu$m, dashed lines to $s_{max} = 1$ mm. Every curve is for one specific solution only, since it depends on the value of σ_{FUV}, which varies for different flow solutions (see Section 6.5.1).

Bally (1998) and Adams et al. (2004) in assuming that the velocity is approximately constant in this region so that from the continuity equation we then obtain:

$$n(R) = n_c \left(\frac{R_c}{R}\right)^2, \quad \text{for } R > R_c, \tag{6.10}$$

and consequently

$$\tau_c = \sigma_{FUV} \int_{R_c}^{\infty} n_c \left(\frac{R_c}{R'}\right)^2 dR' = \sigma_{FUV} R_c n_c. \tag{6.11}$$

Figure 6.4 gives an example of T_c as a function of τ_c for an initial guess $R_c \sim 500$ AU and for a range of FUV fluxes. For low FUV fluxes, the are no solutions in the low optical depth range ($\tau < 10^{-3}$). This constraint is set by the lower limit we have implicitly imposed on the density, when we have not dealt with anything less dense than 10^2 cm^{-3} in Section 6.3.

We are now able to determine τ_c and n_c by solving the equation:

$$T_c - T(\tau_c) = 0. \tag{6.12}$$

We can evaluate the partial derivatives of T with respect to density and optical depth (at fixed R_c) and use these in equations 6.7 and 6.8. We then solve for the next value of R_c by solving equation 6.8 using a bisector method. We then iterate the whole process, until we

reach convergence on the value of ξ_c. By doing so, we have obtained the critical radius, and we have the initial conditions for T (given by the input parameter T_c), v, n and τ. The critical radius is always larger than the sonic radius (as defined by equation 6.9), but at the most by a factor of a few tenths of a dex (see an example in Fig. 6.5). On the other hand, the critical velocity is usually smaller than the sound speed at the critical radius, by $\sim 20\%$ at the most (see an example in Fig. 6.6). Finally, we can estimate the mass-loss rate $\dot{M}$ from equation 6.1. We are ready to start integrating equation 6.6 in order to deduce the velocity profile of the subsonic flow between R_d and R_c.

Extending the solutions

In the definition of the sonic radius (see equation 6.9), by construction we are requiring that $\beta > 8$. Thus we are implicitly setting an upper limit to the T_c we can set at a given R_d:

$$T_c < \frac{GM_*\mu m_H}{8k_B R_d} \simeq 873\left(\frac{M_*}{M_\odot}\right)\left(\frac{20\,\mathrm{AU}}{R_d}\right)\mathrm{K}. \tag{6.13}$$

This strongly limits the explorable region of parameter space, when R_d is large and the FUV flux (and therefore temperature) is high. In order to enlarge the parameter space, when $\beta < 8$, as a first guess for R_c we choose the critical radius of the solution with the same T_c and the closest value of R_d showing a iteratively converged solution for the critical radius. In Fig. 6.5 we show R_c versus T_c when $G_{FUV} = 30\,G_0$, for a range of disc radii R_d between 20 and 250 AU, sampled every 10 AU. The critical radius does not show a strong dependence on R_d, at fixed T_c. In this way we are able to obtain more solutions, even though in some regions of parameter space we do not manage to obtain one.

6.4.3 Method of solution

Once we have located the critical radius and determined the boundary condition for flow density, optical depth and velocity for a given T_c, a disc radius and a FUV flux G_{FUV}, we can integrate equation 6.6 from R_c to R_d (in rescaled units, from ξ_c to 1). We use a simple Euler code. At every step we compute u_{i+1} from equation 6.6. Then, we calculate dimensionless density g_{i+1} from the dimensionless form of equation 6.1, and τ_{i+1} from equation 6.5. At given g_{i+1} and τ_{i+1} we can compute the new temperature partial derivatives $\partial f/\partial g_{i+1}$ and $\partial f/\partial \tau_{i+1}$ from the PDR output, and therefore obtain the next value of the temperature f_{i+1}. With this set of equations we can self-consistently solve for the flow steady-state. We use an initially logarithmically spaced grid, since the absolute value of the gradient of most of the quantities increases as the solution approaches R_d. This happens mostly in the transition between the optically thin and the optically thick regime, when the temperature drops steeply

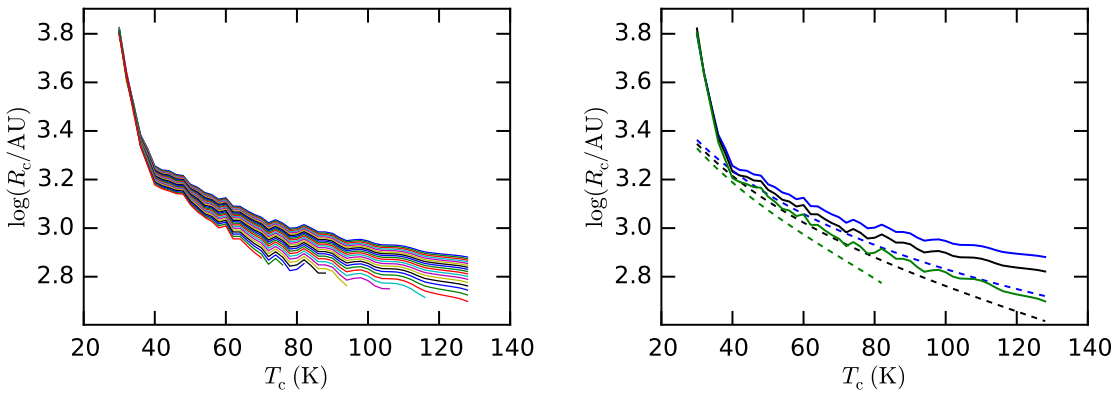

Fig. 6.5 Left panel: critical radius dependence on critical temperature for $G_{\rm FUV} = 30\,G_0$ and $s_{\rm max} = 1$ mm, for a set of disc radii ranging from 20 AU (top line) to 250 AU (bottom line), sampled every 10 AU. Every line illustrates a different disc radius $R_{\rm d}$. Right panel: solid lines are the same as in the top panel, for $R_{\rm d} = 20$, 100 and 180 AU (blue, black and green lines, respectively). Dashed lines indicate the sonic radius, as defined by equation 6.9.

(as shown in Fig. 6.3). In order to better resolve this region we also apply an adaptive mesh algorithm, i.e. we require that $\delta\xi$ is mall enough to ensure that the relative change in velocity between two steps is less than 1% ($|u_{i+1} - u_i|/u_i < 0.01$).

However, we need to apply slight modifications to the algorithm at the two boundaries of the integration, in the proximity of both the critical radius $R_{\rm c}$ and the disc outer radius $R_{\rm d}$.

The critical point

In Section 6.4.2 we have defined the critical radius as the radius at which the r.h.s. of equation 6.6 vanishes. Moreover, at this same radius the second multiplicand of the l.h.s. of the same equation is 0. Since we are starting integrating the same equation from $R_{\rm c}$, we have a null value both at the numerator and at the denominator. This leads to the possibility of having multiple *transcritical* solutions (the analogue version of the transonic solutions in the standard isothermal case). More specifically, we will have a solution that will be supersonic between $R_{\rm d}$ and $R_{\rm c}$, and one solution that will be subsonic. We are looking for the second one. Therefore we need to enforce the solution to relax onto the subsonic branch. We do so by following a procedure that is similar to the one used by Murray-Clay, Chiang & Murray (2009) for an analogous problem.

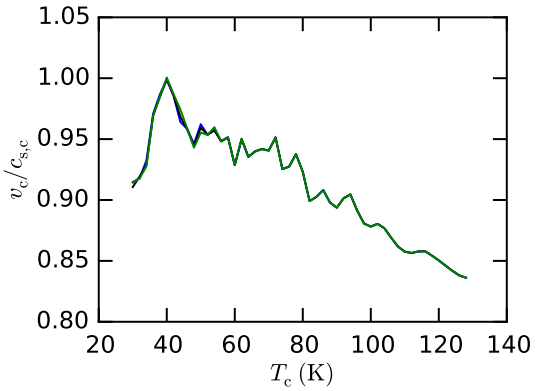

Fig. 6.6 Ratio of critical velocity to the sound speed at R_c for solutions with $G_{FUV} = 30\,G_0$ and $s_{max} = 1\,mm$, and $R_d = 20$, 100 and 180 AU (blue, black and green lines, respectively).

We expand equation 6.6 around the critical point to first order in both radius and velocity: $\xi = \xi_c + \delta\xi$, and $u = u_c + \delta u$. We obtain the following relation:

$$\left.\frac{\delta u}{\delta \xi}\right|_{\xi_c} = \frac{-B + \sqrt{B^2 - 4AD}}{2A}, \tag{6.14}$$

where:

$$A = 2u_c + \frac{2g}{u_c}\frac{\partial f}{\partial g} + \frac{g^2}{u_c}\frac{\partial^2 f}{\partial g^2}; \tag{6.15}$$

$$B = 2\tau_d g \frac{\partial f}{\partial \tau} + \frac{8g}{\xi}\frac{\partial f}{\partial g} + \frac{4g^2}{\xi}\frac{\partial^2 f}{\partial g^2} + 2\tau_{\rm d} g^2 \frac{\partial^2 f}{\partial \tau \partial g}; \tag{6.16}$$

$$\begin{aligned} D = u_c \times \quad & \Big(\frac{2u_c^2}{\xi^2} - \beta\frac{2\xi - 3}{\xi^4} + \frac{8g}{\xi^2}\frac{\partial f}{\partial g} + \frac{4\tau_{\rm d} g}{\xi}\frac{\partial f}{\partial \tau} \\ & + \frac{4g^2}{\xi^2}\frac{\partial^2 f}{\partial g^2} + \frac{4\tau_{\rm d} g^2}{\xi}\frac{\partial^2 f}{\partial \tau \partial g} + \tau_{\rm d}^2 g^2 \frac{\partial^2 f}{\partial \tau^2}\Big), \end{aligned} \tag{6.17}$$

where all the quantities are evaluated at $\xi = \xi_c$. In equation 6.14 we chose the positive root, in order to pick the subsonic solution at $\xi < \xi_c$.

Similarly to Murray-Clay, Chiang & Murray (2009), we calculate the velocity by using:

$$\frac{du}{d\xi} = F_{\rm exact}\left.\frac{du}{d\xi}\right|_{\rm exact} + (1 - F_{\rm exact})\left.\frac{\delta u}{\delta \xi}\right|_{\xi_c}, \tag{6.18}$$

where $du/d\xi|_{\rm exact}$ is evaluated from equation 6.6, and

$$F_{\rm exact} = -{\rm erf}\Big[h\Big(1-\frac{f}{u^2}-\frac{g}{u^2}\frac{\partial f}{\partial g}\Big)\Big], \tag{6.19}$$

where erf is the error function. The parameter $h = 20$ gives the smoothing length of the transition between $du/d\xi|_{\rm exact}$ and $\delta u/\delta\xi|_{\xi_{\rm c}}$ when computing $u(\xi)$. We use this modified version of equation 6.6 until $F_{\rm exact} = 1$ to the level of machine precision.

Temperature corrections near $R_{\rm d}$

Some solutions become completely optically thick before reaching the disc outer radius (i.e. $R > R_{\rm d}$). In the PDR calculations, we have set a minimum temperature equal to 10 K. However, the temperature of the flow could be higher than that, due to the impinging radiation from the central star. When we compute the temperature of the flow, we therefore include heating from the central star, by using the following simple prescription:

$$T = \max\left(T_{\rm PDR}, T_{\rm rad}\right), \tag{6.20}$$

where $T_{\rm PDR}$ is the temperature evaluated via the PDR code (i.e. the one used so far in the chapter), and $T_{\rm rad}$ is given by:

$$T_{\rm rad} = 100\,{\rm K}\left(\frac{R}{1\,{\rm AU}}\right)^{-1/2}, \tag{6.21}$$

i.e. a temperature profile found to fit the spectral energy distributions of passive discs (e.g. Andrews & Williams, 2005, 2007).

6.5 Dust component

In Section 6.4, we have reported the equations and the procedure to obtain a solution for the gas quantities between the critical radius and the disc's outer edge. However, this solution depends on the dust properties within the flow. In particular, as mentioned in Section 6.3.2, the attenuation factor strongly depends on the grain size distribution and on the maximum grain size $s_{\rm entr}$ entrained in the wind. Such dependence can be summarised in how $\sigma_{\rm FUV}$ is related to these two properties of the dust material. In this section, we also describe the hydrodynamic equations for the dust particles, which will be used to determine the maximum grain size entrained in the flow, and thus the cross section.

6.5.1 Cross section

It is well known that protoplanetary discs witness substantial grain growth in the discs' midplane (see Section 6.3.2). Such grain growth can be schematised in two effects: producing a shallower distribution, i.e. a lower q, and leading to a larger maximum grain size $s_{\max}$. As introduced in Section 6.3.2, in this chapter we focus on two distributions with the same power law index $q = 3.5$ but different maximum grain sizes ($s_{\max} = 3.5\,\mu$m and 1 mm). The same distributions have been used to compute the dependence of the temperature on n and A_V. As mentioned above, we consider a dust-to-gas ratio of 0.01 for both the distributions.

We compute the cross section at FUV wavelengths ($\lambda = 0.1\,\mu$m) using the code of Wyatt & Dent (2002) as briefly described in Section 6.3.2. In the equations reported below, we describe a general treatment where q can assume different values. We take into account that there is a maximum grain size entrained in the photoevaporative wind, and we compute the cross sections for the truncated distribution:

$$\sigma_{\rm FUV} = \mu m_{\rm H} \frac{q_{\rm s}}{m_{\rm entr}\delta_{\rm gd}}, \tag{6.22}$$

where

$$q_{\rm s} = \int_{s_{\min}}^{s_{\rm entr}} \pi s^2 Q_{\rm abs}(\lambda, s) s^{-q} ds, \tag{6.23}$$

$$m_{\rm entr} = \frac{4}{3}\frac{\pi\bar{\rho}}{4-q}(s_{\rm entr}^{(4-q)} - s_{\min}^{(4-q)}), \tag{6.24}$$

and

$$\delta_{\rm gd} = 100\left(\frac{s_{\max}^{(4-q)} - s_{\min}^{(4-q)}}{s_{\rm entr}^{(4-q)} - s_{\min}^{(4-q)}}\right). \tag{6.25}$$

In these equations, $\delta_{\rm gd}$ is the effective gas-to-dust ratio within the flow, and $\bar{\rho}$ is the mean mass density of a dust grain (in this chapter 1 g/cm^3). The minimum grain size of the distribution has been set to $s_{\min} = 5 \times 10^{-7}$ cm in the whole chapter.

The cross sections are reported in Fig. 6.7, as a function of the maximum grain size entrained in the flow, for $s_{\max} = 3.5\,\mu$m (red line) and $s_{\max} = 1$ mm (black line). The cross section does not vary by much when the distribution is truncated to $s_{\rm entr} \gtrsim \lambda$, because the largest contribution to the cross section in the geometric limit comes from the smallest grains when $q > 3$. We do not recompute the temperature $T(n)$ with the PDR code for the new truncated distributions, since it depends weakly on the maximum grain size. As discussed in Section 6.3, this is due to the fact that heating is mostly generated by the photoelectric effect on PAHs and on small grains, since the total surface area per unit mass is dominated by the

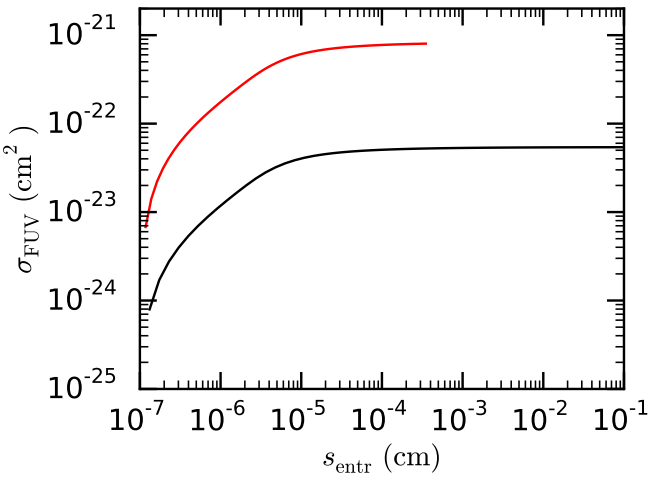

Fig. 6.7 Cross section at $\lambda = 0.1\,\mu$m as a function of the maximum grain size entrained in the flow, for $s_{\rm max} = 1$ mm (black line) and $s_{\rm max} = 3.5\,\mu$m (red line). The initial distribution assumes a dust-to-gas ratio of 0.01. The cross section does not vary by much when the distribution is truncated to $s_{\rm entr} \gtrsim \lambda$, since the largest contribution to the cross section in the geometric limit comes from the smallest grains when $q > 3$.

small grains of the distribution when $q > 3$. Cooling is not significantly affected the absence of the largest grains, since O I and C II emission lines dominate the radiative cooling.

6.5.2 Fluid equations for dust particles

In order to obtain the maximum grain size entrained in a gaseous solution, we need to solve the hydrodynamical equations of dust particles. We discretise the grain size distribution in $N_{\rm bin} = 50$ bins, where the grain size is sampled logarithmically between $s_{\rm min}$ and $s_{\rm max}$. The dust mass density can be written as:

$$\rho_j \simeq \tilde{n}_j \frac{4}{3} \pi \bar{\rho} s_{{\rm max},j}^3, \tag{6.26}$$

where the subscript j refers to the j-th bin of dust particles. Here ρ_j is the mass density of the j-th bin, and $s_{{\rm max},j}$ is the maximum grain size of the j-th bin.

The steady version of the momentum equation for dust particles is:

$$v_j \frac{dv_j}{dR} + \frac{GM_*}{R^2} - \frac{j^2}{R^3} + \frac{F_{\rm D}}{m_j} = 0, \tag{6.27}$$

where we have assumed that dust is pressureless, and that the buoyancy term related to the gas pressure gradient is negligible (which is typically the case for astrophysical systems,

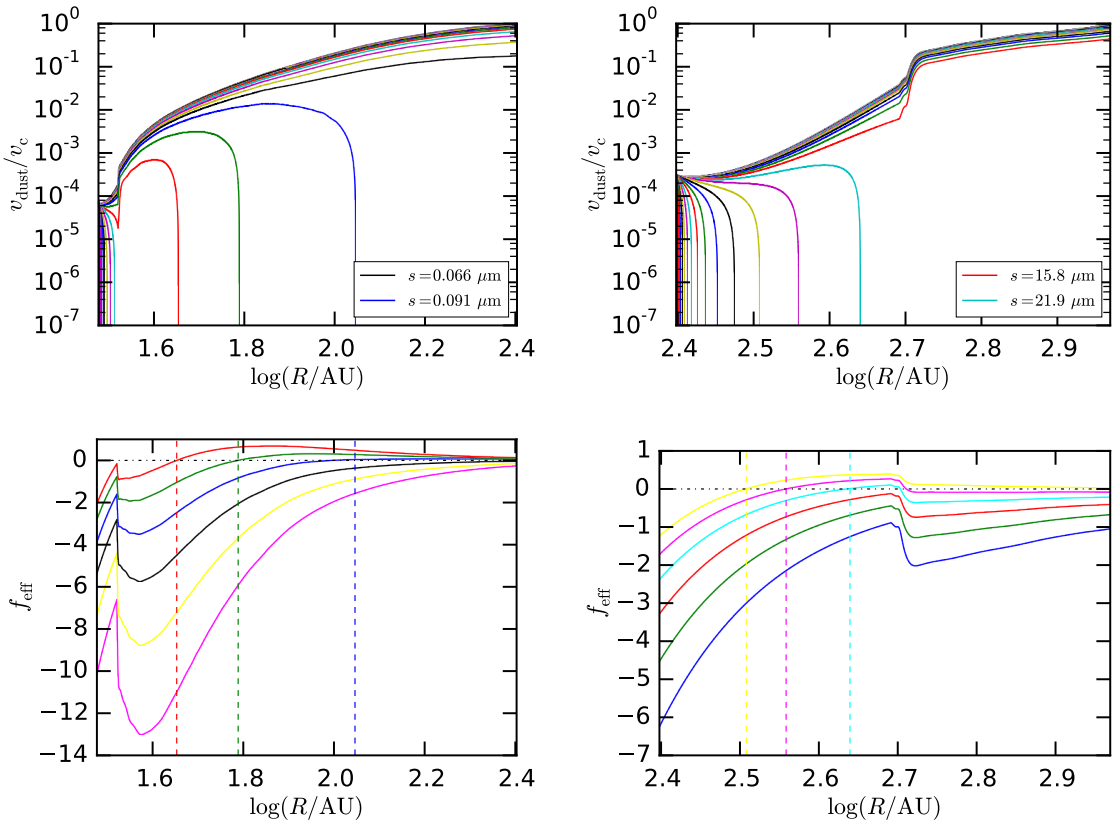

Fig. 6.8 Top panels: velocity profiles of the 50 dust bins between $R_{\rm d}$ and $R_{\rm c}$, for $s_{\rm max} = 1\,{\rm mm}$, $G_{\rm FUV} = 3000\,G_0$, $P_{\rm d} \sim 10^{-5}$ in cgs units, and $R_{\rm d} = 30$ (left panel) and 200 AU (right panel). The largest grain dragged out to the critical radius and the smallest grain stalling at a finite location within the flow are highlighted in the legend. Bottom panels: $f_{\rm eff}$ computed via equation 6.32 for six grain sizes. The six bins are selected in order to be the three largest sizes that are dragged all the way through the flow, and the three smallest sizes that stall at a finite radius, close to the disc edge. Note the perfect coincidence between the location where the grain velocity drops to 0, and the stalling radius (i.e. where $f_{\rm eff} = 0$). The stalling radii are indicated by the vertical dashed line.

see e.g. Rice et al., 2006; Laibe & Price, 2012). The fluid quantities that do not show any subscript refer to gas properties, as in Section 6.4. The quantity m_j is the mass of the j-th dust particle. The last term $F_{\rm D}$ represents the aerodynamic force experienced by the dust particle. This force can assume different expressions, depending on the physical regime. If the size of the dust particle $s \lesssim \lambda_{\rm mfp}$, the mean-free path of gas molecules within the flow, the drag force reduces to the so-called Epstein (1924) drag. If the size of the particle is larger than the mean-free path, drag is a classical fluid Stokes (1851) drag. Within the winds addressed in this chapter, $\lambda_{\rm mfp} > 10^5$ cm (using $\lambda_{\rm mfp} \approx (\sigma_{\rm gas} n)^{-1}$, where $\sigma_{\rm gas} \sim 10^{-16}$ cm^2 is the geometrical cross-section of the gas molecules and $n < 10^{11}$ cm^{-3}). For the dust particles considered here, $s \ll \lambda_{\rm mfp}$, and we can therefore use the Epstein limit to estimate the drag term (e.g. Armitage, 2010):

$$F_{\rm D} = \frac{4\pi}{3} \rho s^2 v_{\rm th} (v_j - v), \tag{6.28}$$

where $\rho = \mu m n$ is the gas mass density, and

$$v_{\rm th} = \sqrt{\frac{8 k_{\rm B} T}{\pi \mu m_{\rm H}}} \tag{6.29}$$

is the mean thermal speed of the gas molecules.

If we rewrite equation 6.27 in the usual dimensionless form, and in the Epstein regime, we obtain:

$$u_j \frac{du_j}{d\xi} = -\left[\beta \frac{\xi - 1}{\xi^3} + \tilde{J}_j g \sqrt{f} (u_j - u)\right], \tag{6.30}$$

where:

$$\tilde{J}_j = \sqrt{\frac{8}{\pi}} \frac{\mu m_{\rm H} n_{\rm c}}{\bar{\rho}} \frac{R_{\rm d}}{s_j}, \tag{6.31}$$

and $u_j = v_j / c_{\rm s,c}$. For a given gaseous solution, we can obtain the velocity profile of the j-th bin of dust particles by integrating equation 6.30. We assume that dust particles are launched from the disc at the same speed of gas molecules, i.e. $u_{j,{\rm d}} = u_{\rm d}$. Moreover, we require that the gas-to-dust ratio at the disc outer radius is 100, and this automatically sets the normalisation of the grain size distribution.

In order to obtain the maximum grain size entrained in the flow, we do not need to integrate equation 6.30 for every gaseous solution and every dust bin. If we consider the highly subsonic regime ($u_j \sim 0$) equation 6.30 becomes:

$$\frac{du_j}{dt} = -\beta \frac{\xi - 1}{\xi^3} + \tilde{J}_j g \sqrt{f} u \equiv f_{\rm eff}, \tag{6.32}$$

where $f_{\rm eff}$ is the effective acceleration that a dust particle would feel if it were stationary. We define the stalling radius as the point at which a stationary dust grain would be in equilibrium, i.e. $f_{\rm eff} = 0$, which is different for each grain size. We have demonstrated by integration of equation 6.30 that dust particles within the flow indeed collect at their respective stalling radii (i.e. where $f_{\rm eff} = 0$) where these exist (see Fig. 6.8). This can be explained by the fact that equation 6.30 resembles the equation of motion of an overdamped harmonic oscillator, where the system returns to equilibrium without oscillating and in an exponentially decaying fashion. As expected, the results show that the smaller grains are tightly coupled to the gas flow, and are easily dragged out to the critical radius. The largest grains are dragged to the stalling radius as defined above. Note that the stalling radius does not depend on the initial velocity, i.e. this result does not depend on the initial condition we have chosen for the velocity of the dust grains at $R_{\rm d}$.

This result confirms that in order to obtain the maximum grain size entrained in the flow $s_{\rm entr}$ we just need to solve equation $f_{\rm eff} = 0$, without obtaining the exact velocity profiles of every dust bin.

6.6 Iteration procedure and final solutions

In this section we summarise the iteration procedure we use to obtain the wind solutions by using all the ingredients reported in Sections 6.4-6.5. All the results depend on the temperature estimates obtained with the PDR code in Section 6.3.

We initially set the main parameters of the system: the external FUV field ($G_{\rm FUV}$), the disc's outer radius ($R_{\rm d}$), and the stellar mass (M_*). All the results showed in this chapter have $M_* = M_\odot$. We then set a critical temperature $T_{\rm c}$, which will be uniquely related to the pressure at the outer edge of the disc $P_{\rm d}$ of the final solutions. We then start the iteration procedure by assuming an initial $\sigma_{\rm FUV} = 8 \times 10^{-22}\,{\rm cm}^2$ for the $s_{\rm max} = 3.5\,\mu{\rm m}$ case and $\sigma_{\rm FUV} = 6 \times 10^{-23}\,{\rm cm}^2$ when $s_{\rm max} = 1\,{\rm mm}$. We now list the following steps:

1. we calculate the critical radius by using equations 6.11-6.12;

2. we obtain all the boundary conditions of the gaseous flow at the critical radius, as explained in Section 6.4.2;

3. we integrate the hydrodynamic equations from $R_{\rm c}$ inwards to the disc's outer radius, with the method detailed in Section 6.4.3;

4. we compute the maximum grain size $s_{\rm entr}$ entrained in the flow, by using equation 6.32;

5. we obtain the new cross section $\sigma_{\rm FUV}$;

6. we go back to step (i), and we iterate the same procedure until we reach convergence on the cross section $\sigma_{\rm FUV}$.

As mentioned above, every solution selected via the input parameter $T_{\rm c}$ can be uniquely indicated by the gas pressure at the outer edge of the disc, which is a final output of our procedure. The boundary between the actual disc and the slow wind needs to be in pressure equilibrium (in principle there could be a contact discontinuity in both temperature and gas density). The pressure at the outer edge of the disc can be modelled by assuming simple prescriptions for the surface density and temperature profiles. For the latter, we use expression 6.21. For the former, we use the simple relation:

$$\Sigma(R) = \frac{M_{\rm d}(2-p)}{2\pi R_{\rm d}^2}\left(\frac{R}{R_{\rm d}}\right)^{-p}, \tag{6.33}$$

where $M_{\rm d}$ is the mass of the disc, and we set $p = 1$ for the whole chapter. A final pressure-balanced solution is thus selected by the mass of the disc.

The parameter space we explore is the following. We range over the disc outer radius between 20 and 250 AU, sampled every 10 AU. We explore three different values of external FUV field: 30, 300 and $3000\,G_0$, and for each of these we explore a set of initial conditions specified by the parameter $T_{\rm c}$. The critical temperature is sampled every 2 K, and the explored range is shown in Fig. 6.4 for the different field values. Not all these initial conditions lead to a final solution, in particular there are cases where the equation defining the critical radius does not have a real solution. As already explained in the chapter, we focus on two grain size distributions with $q = 3.5$, where the maximum grain sizes are respectively $3.5\,\mu$m and 1 mm. The former leads to the same cross section used in the models by Adams et al. (2004) when $s_{\rm entr} > 0.1\,\mu$m, and this will allow us to compare our results with theirs in more detail.

6.7 Results

We report here the global properties of the final solutions we have obtained. By construction, we obtain a class of *transcritical* solutions with a critical point in the heated flow. This implies that the velocity at the outer edge of the disc is subsonic, and thus all the solutions we obtain lie in the subcritical regime.

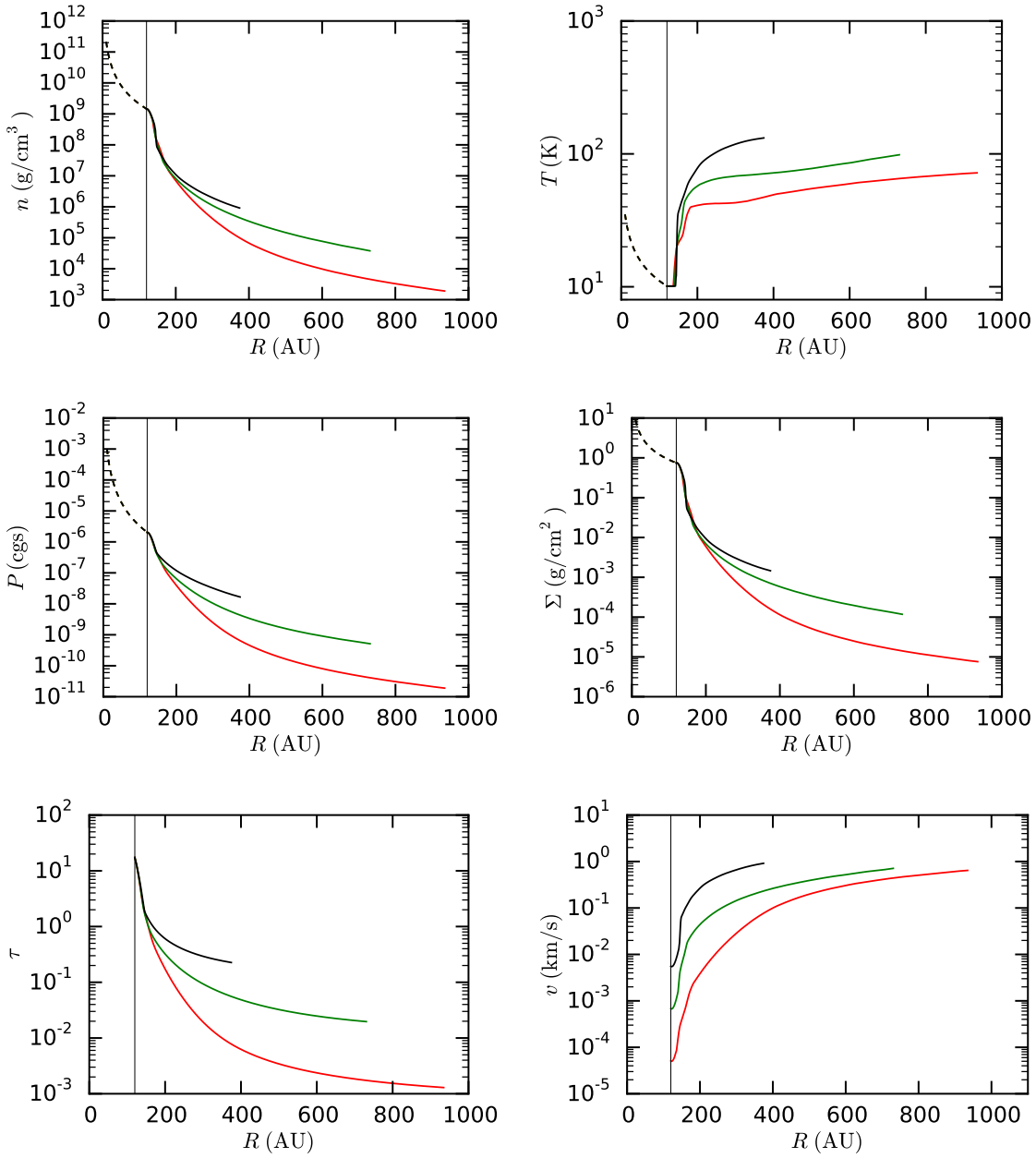

Fig. 6.9 Profiles of the main thermo-hydrodynamical gaseous quantities for wind solutions between $R_\mathrm{d} = 120$ (highlighted by the black vertical line) and R_c, with $s_\mathrm{max} = 1\,\mathrm{mm}$. Colours indicate the three ambient field intensities analysed in the chapter (red: $30\,G_0$; green: $300\,G_0$; black: $3000\,G_0$). The solutions were chosen as to have $P_\mathrm{d} \sim 10^{-6}$ in cgs units. The dashed lines represent the fluid quantities in the discs.

6.7.1 Profiles

The radial profiles of the gaseous quantities have characteristic features. Three examples are reported in Fig. 6.9, where we show the steady-state solutions for discs with $R_{\rm d} = 120\,{\rm AU}$, $s_{\rm max} = 1\,{\rm mm}$, and $G_{\rm FUV} = 30$, 300 and $3000\,G_0$ (red, green and black lines). The solutions have been chosen such to have $P_{\rm d} \sim 10^{-6}$ in cgs units. The dashed lines indicate the fluid quantities in the disc, parametrised by the temperature and surface density profiles given by relations 6.21 and 6.33. The wind solutions are shown out to the critical radius, which varies with the intensity of the external FUV field.

In the outer regions of the photoevaporative wind, the temperature increases with radius, as the flow becomes optically thinner to the external FUV radiation. Approaching the disc outer rim, the temperature drops drastically, as the gas becomes optically thick. In this radially narrow region, the gas is close to an isothermal hydrostatic solution, where the gas density n grows exponentially, and the velocity drops accordingly. As we go inwards in the radial direction, very close to the disc outer edge, the velocity has a null gradient, which is expected for an isothermal Parker wind with the addition of the centrifugal term. Note that in all the solutions shown the optical depth at the critical point is less than unity (though only marginally so in the case $G_{\rm FUV} = 3000\,G_0$). This justifies a posteriori our assumption that the flow is roughly isothermal and at constant velocity outward of the critical point.

Other solutions have profiles that are optically thin to the FUV radiation along the whole flow. These solutions are characterised by a contact discontinuity in both temperature and density at the base of the flow (but the wind at $R_{\rm d}$ is still in pressure equilibrium with the disc). An example is shown in Fig. 6.10. The density structure is close to being a power law profile (as in fig. 3 by Adams et al., 2004), apart from the regions close to the disc edge, where the centrifugal term in the momentum equation becomes dominant. As we see in the next section, these solutions are characterised by a low disc mass and a tenuous mass loss.

Caveat

The profiles (and thus the mass loss rates) have been computed using the 1D model presented in this chapter. However, the realistic geometry of the mechanism is fully 3-dimensional, in particular whenever the ambient radiation is dominated by a single energetic source (an early spectral type star). For the FUV intensities analysed in this paper, the problem can be reduced to a 2D one, since the cluster membership size associated to such FUV fields are low enough to yield a very low probability of having a massive star in the cluster. Thus the ambient field can be considered as resulting from the integrated contributions of all the stars in the proto-cluster, and thus the radiation can be described as isotropic. By exploiting

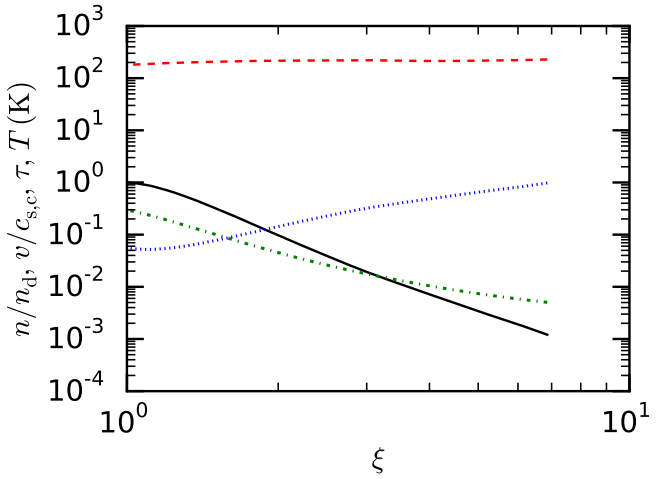

Fig. 6.10 Profiles between $R_{\rm d}$ and $R_{\rm c}$ of some relevant quantities for a disc with size $R_{\rm d} = 40\,{\rm AU}$, $G_{\rm FUV} = 3000\,G_0$, $s_{\rm max} = 1\,{\rm mm}$ and $T_{\rm c} = 228\,{\rm K}$. This solution is associated with $\dot{M} = 4.52 \times 10^{-9}\,M_\odot/{\rm yr}$, $P_{\rm d} = 4.93 \times 10^{-7}$ in cgs units, $n_{\rm d} = 1.98 \times 10^{-7}$ particles per cc, and $s_{\rm entr} \approx 1.7\,\mu{\rm m}$. Different lines indicate: black solid line: $n/n_{\rm d}$; red dashed line: T (K); blue dotted line: $v/c_{\rm s,c}$; green dashed-dotted line: τ.

the cylindrical symmetry of the disc, we can reduce the problem to the vertical and radial direction only.

In this study, we have assumed that the temperature within the wind is set by the FUV photons penetrating in the radial direction. However, the wind itself is impinged by FUV radiation in the vertical direction. We can assume that the vertical structure of the disc is set by hydrostatic equilibrium at the disc outer radius, i.e. that:

$$n(z,R) = n(R)e^{-z^2/(2H^2)}, \tag{6.34}$$

where $H = H_{\rm d} \times (R/R_{\rm d})$ and $H_{\rm d} = c_{\rm s,d}/\Omega_{\rm d}$. We set $n(R)$ equal to the radial density profile obtained with the 1D radial model. Given this vertical structure, we can compute the optical depth in the midplane of the disc along the vertical direction $\tau_{\rm z}(R) = \sigma_{\rm FUV} \int_0^\infty n(z,R)dz$, and compare it to the radial optical depth $\tau(R) = \sigma_{\rm FUV} \int_R^\infty n(R')dR'$. Examples of this comparison are shown in Fig. 6.11, where we show the ratio of the two optical depths for the profiles of Figs. 6.9-6.10.

Interestingly, the optical depth along the vertical direction is lower than the radial one in the optically thin regions, for all the profiles. This can be easily derived analytically at

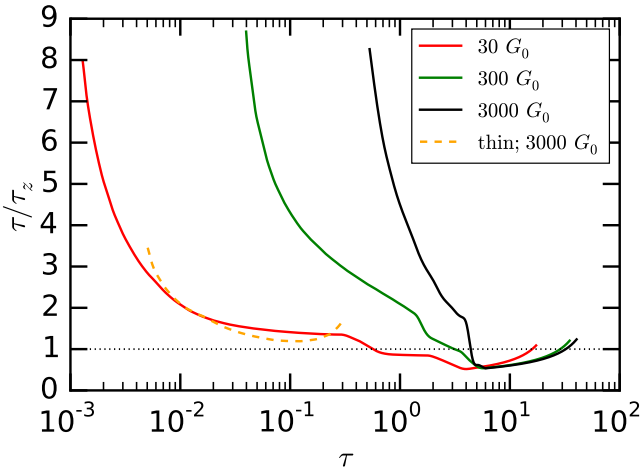

Fig. 6.11 Ratio of vertical to radial optical depth versus radial optical depth for the three profiles shown in Fig. 6.9 and the profile shown in Fig. 6.10.

$R = R_c$. From equation 6.11 we know that $\tau(R_c) = \sigma_{FUV} n_c R_c$. Therefore, we obtain:

$$\frac{\tau_z(R_c)}{\tau(R_c)} = \frac{R_d}{H_d}\sqrt{\frac{2}{\pi}}. \tag{6.35}$$

This is confirmed by the plot shown in Fig. 6.11, where this ratio is ≈ 10 at the lowest value of τ (i.e. at $R = R_c$). In the mildly optically thick regime, the local FUV intensity in the midplane of the disc is about the same from the two directions (see Fig. 6.11). Thus, a 2D model would probably yield to higher temperatures in the optically thin regions within the flow, thus increasingly slightly the mass loss rates. However, this effect would also modify the density structure of the flow in the vertical direction, leading to a hyperspherical wind. It is therefore not obvious what the final effect would be. A follow-up work to this project is constructing a 2D model of the flow, where the wind solutions need to be obtained with time-dependent hydro, since the steady-state problem is numerically prohibitive. A final note is that at $R = R_c$ the flow is usually very optically thin in the radial direction. In this regime, the temperature does not vary with optical depth (see Fig. 6.3), and we thus not expect the final mass loss rate to be heavily affected by the 2D nature of the problem.

6.7.2 Mass loss rates

For any given set of initial parameters G_{FUV}, R_d and T_c for which we obtain a solution, we can easily determine the mass loss rate from equation 6.1: this quantity is the most significant outcome of our model, since it determines whether the external photoevaporation mechanism

is relevant for the global evolution of a protoplanetary disc, even when the environmental conditions are mild (e.g. $G_{\rm FUV} = 30\,G_0$). Note that all the mass loss rate estimates presented in this chapter scale linearly with the assumed value of $\mathscr{F}$ (see equation 6.1), i.e. depend on the scale height of the disc at its outer boundary $H_{\rm d}$.

As an example, we condense most of the mass loss rates we obtain for both grain size distributions in Fig. 6.12. We show them with their dependence on the pressure at the outer disc edge, as determined from the integration of the hydrodynamic equations. In the plots we focus on the range of pressure values that typify protoplanetary discs (which generally have midplane values of between $10^{-8} - 10^{-3}$ in cgs units depending on the disc mass, for $R > 20\,{\rm AU}$). The $\times$-symbols indicate the actual outputs of the integration. Every line is associated with a disc outer radius, ranging from 70 to 250 AU. For the smallest disc sizes ($R_{\rm d} < 70\,{\rm AU}$), the class of solutions is truncated at high $P_{\rm d}$ values, and they do not appear on this plot. Finally, we struggle to obtain solutions in a physical range for the $s_{\rm max} = 3.5\,\mu{\rm m}$ case, when $G_{\rm FUV} = 3000\,G_0$ and the discs are larger than $\sim 60\,{\rm AU}$. This limit is caused by our method of solution, since in these cases equation 6.8 for the critical radius does not have a real root.

Mass loss rates increase with disc outer radius, as one would intuitively expect, since the material at the outer rim is less embedded in the gravitational potential well of the central star. Moreover, the mass loss rates also increase with external FUV intensity, since higher fluxes heat the gas up to higher temperatures. In most of the parameter space shown in Fig. 6.12, there is a very weak dependence of the mass loss rates on the pressure in the outer disc (which is related, for canonical parameters, to the total disc mass). The only exception is in the case of low values of $P_{\rm d}$. The reason is the following: a lower $\dot{M}$ corresponds to a roughly optically thin (and thus isothermal) flow (see e.g. Fig. 6.10). The flow solution is then just a centrifugally modified Parker wind solution. In this case the velocity structure is independent of the density normalisation. For a disc lying in this regime, with fixed $R_{\rm d}$, the density normalisation at the base of the wind (and hence the mass loss rate) just scales linearly with the density in the disc. Hence (for a given disc temperature at $R_{\rm d}$), $\dot{M}$ is linear with pressure.

Fig. 6.13 shows the same results reported in Fig. 6.12 for the three values of $G_{\rm FUV} = 30,\ 300$ and $3000\,G_0$, where the mass loss rates are shown as a function of the disc outer radius, for different disc masses. The masses have been chosen such that $M_{\rm d} = M_{\rm d,0}(R_{\rm d}/250\,{\rm AU})^2$ in order to maintain the same surface density normalisation in the disc, where $M_{\rm d,0}/M_\odot = 1$, 10^{-2} and 10^{-4} (solid, dashed and dashed-dotted lines, respectively). It is again apparent that the mass loss rates increase both with disc outer radius, and with the intensity of the impinging FUV radiation. As before we see a weak dependence on disc mass

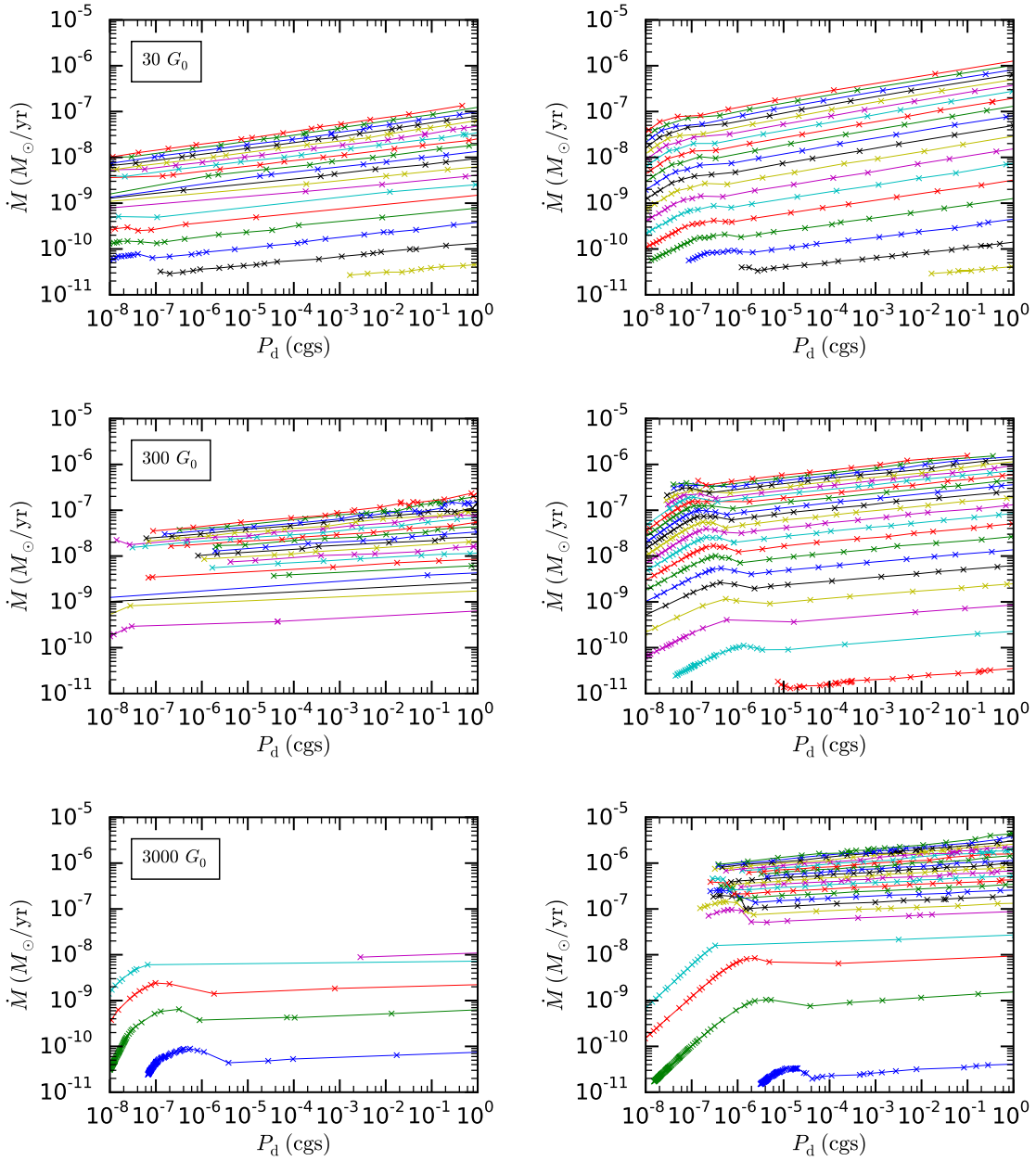

Fig. 6.12 Mass loss rates vs pressure at the edge of the disc for models with $s_{\max} = 3.5\,\mu$m (left panels) and $s_{\max} = 1$ mm (right panels). Every line represents a different outer radius R_d, sample every 10 AU. The top line of every panel describes a disc with $R_\mathrm{d} = 250$ AU. The bottom left panel shows the solutions for R_d ranging between 20 and 60 AU. The markers on the top of the lines indicate the output of the actual integrations. Typical values of pressure at the outer edge of protoplanetary discs range between $10^{-8} - 10^{-3}$, in cgs units.

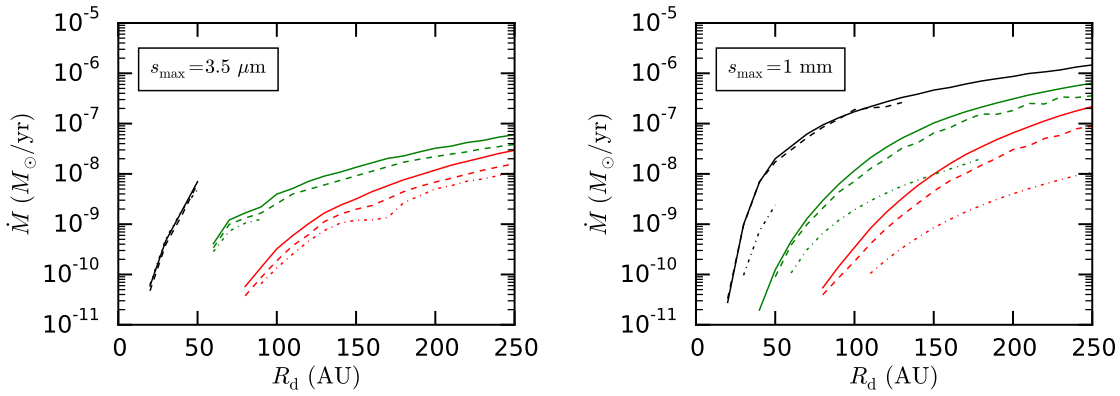

Fig. 6.13 Mass loss rates dependence on the disc outer radius, for the two different grain size distributions with $s_{\max} = 3.5\,\mu$m (left panel) and 1 mm (right panel). Different colours (red, green and black) indicate different external FUV field intensities, respectively $G_{\rm FUV} = 30$, 300 and $3000\,G_0$. We show mass loss rates for disc masses $M_{\rm d} = M_{\rm d,0}(R_{\rm d}/250\,{\rm AU})^2$, where $M_{\rm d,0}/M_\odot = 1$, 10^{-2} and 10^{-4} (solid, dashed and dashed-dotted lines, respectively).

apart from where this is low, where the mass loss rate is nearly linear with disc mass at given $R_{\rm d}$.

Another important feature is that the mass loss rates are very sensitive to the grain size distribution for large discs. When there is substantial grain growth, the cross section $\sigma_{\rm FUV}$ decreases significantly (see Fig. 6.7), allowing a larger penetrating depth in the photoevaporative wind, and therefore a more significant mass loss rate. This is clearly shown in Fig. 6.13, where the mass loss rates from large discs are higher for the grain size distribution with larger maximum grain size, by roughly the ratio of the cross sections, as expected. However, the mass loss rates associated with the two grain size distributions are comparable when the discs are small ($R_{\rm d} \lesssim 100$ when $G_{\rm FUV} = 30\,G_0$, $R_{\rm d} \lesssim 70$ when $G_{\rm FUV} = 300\,G_0$).

The fact that the gaseous flow is depleted of the larger grains has a relevant impact for the lowest mass loss rates, where $s_{\rm entr} \lesssim \lambda = 0.1\,\mu$m. There is in fact a strong correlation between the maximum grain size entrained in the flow, and the mass loss rate due to the photoevaporative wind. The top panels of Fig. 6.14 report such correlation for all the obtained solutions. As usual, every line represents a different disc size. The empirical understanding is straightforward: the more vigorous is the wind, the larger are the grains that are dragged out with the gaseous flow. Obviously the maximum grain size entrained in the flow cannot be larger the the maximum grain size of the whole distribution, as well represented by the upper

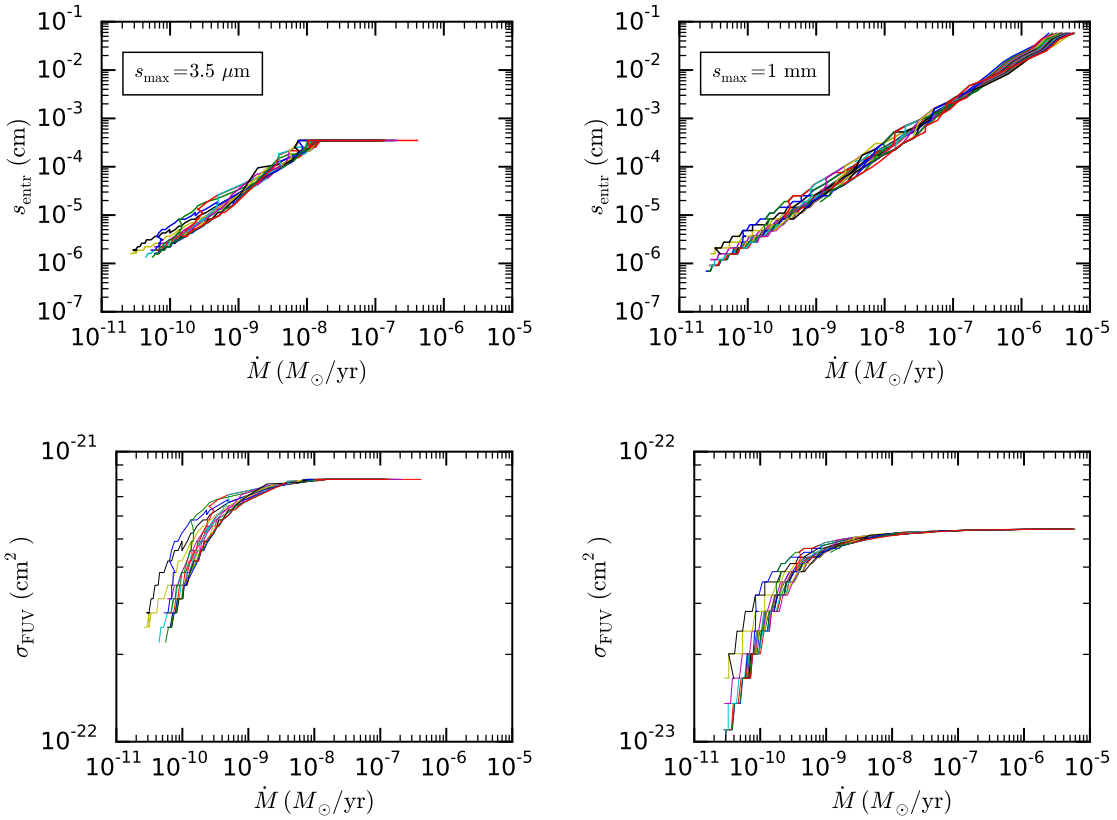

Fig. 6.14 Top panels: maximum grain size entrained in the photoevaporative wind, in the case of $G_{\rm FUV} = 30\,G_0$. As usual, every line represents a different disc size. There is a strong correlation between $s_{\rm entr}$ and the mass loss rates: the more vigorous is the flow, the larger the entrained maximum grains are. Bottom panels: cross sections of the same solutions reported in the top panels. Note the different range on the y-axis. As expected, the cross sections become very sensitive to $s_{\rm entr}$ when $s_{\rm entr} \lesssim \lambda = 0.1\,\mu$m, as shown in Fig. 6.7.

limit of $3.5\,\mu$m in the left panel of Fig. 6.14. If we neglect the centrifugal term in equation 6.27 (or in equation 6.32), and we set $f_{\rm eff} = 0$ to determine $s_{\rm entr}$, we obtain:

$$s_{\rm entr} \approx \frac{v_{\rm th}}{GM_*} \frac{1}{4\pi \mathscr{F} \bar{\rho}} \dot{M}, \tag{6.36}$$

where we have used the continuity equation 6.1 to extract $\dot{M}$. Since $v_{\rm th}$ weakly depends on temperature only, which does not vary substantially among different solutions, the relation between $s_{\rm entr}$ and $\dot{M}$ is roughly linear, as apparent in Fig. 6.14. The cross sections are significantly affected only at the low end of the mass loss rates (see bottom panel of Fig. 6.14), where the wind is so tenuous that $s_{\rm entr} \lesssim \lambda = 0.1\,\mu$m, and the cross section drops significantly.

For the $s_{\rm max} = 3.5\,\mu$m case, the mass loss rates we obtain are generally lower (by a factor of ~ 10) than the ones derived by Adams et al. (2004) (see their fig. 3), in the regions of parameter space that overlap, i.e. for small discs ($R_{\rm d} \lesssim 60$ AU). Since we have used a very similar cross section in this case, the difference cannot be due to a different penetrating depth. The factors that could be at the origin of such difference are at least two. The first one is the lower temperature in our models (see Section 6.3). In order to check whether the temperature has a significant effect in determining the mass loss rates, we have obtained other solutions with higher temperatures, of the same order as the ones presented in fig. 3 by Adams et al. (2004) by using the prescription by Bakes & Tielens (1994) for the PAH photoelectric heating. The mass loss rates are not affected significantly, thus we can rule out that the lower mass loss rates in our study are due to the lower temperatures. The second factor, which is the most important one, is that in our non-isothermal treatment, the critical radius is always larger than the sonic radius by a factor of a few. Since the density scales very steeply with radius (more steeply than R^{-2}), a larger outer radius as boundary condition implies a much lower density $n_{\rm c}$, in order to have a final pressure-balanced solution at $R_{\rm d}$. This implies a lower mass loss rate (see equation 6.1).

6.8 Discussion

The mass loss rates shown in Fig. 6.13 indicate that external photoevaporation can have a significant impact in the global evolution of protoplanetary discs. In particular, large discs ($R_{\rm d} > 150$ AU) show vigorous mass losses even for very low ambient fields ($G_{\rm FUV} = 30\,G_0$). Depending on the grain size distribution of the dusty material entrained in the flow, these discs can have mass loss rates as high as $\sim 10^{-7} M_\odot/{\rm yr}$, if grain growth has been effective

even at these outer regions of the disc. Thus, this effect needs to be considered when we model the evolution of protoplanetary discs.

Clarke (2007), and later Anderson, Adams & Calvet (2013) (see also Mitchell & Stewart, 2010), have shown that these photoevaporative winds affect disc evolution not on account of the mass lost in the flow, but by limiting the viscous spreading of the disc, and thus accelerating disc clearing. When the discs are large, the photoevaporative wind removes mass from the outer edge on a timescale shorter than the timescale with which the disc is able to replenish the mass in these regions. Thus the disc shrinks, until it reaches a radius where these two timescales are equal (see also Adams et al., 2004, for a similar discussion). Another way of looking at the same mechanism is that when the mass flux at the base of the flow is higher than the one within the disc due to viscous spreading, the disc shrinks, whereas it expands as a standard viscous disc when the opposite happens. Anderson, Adams & Calvet (2013) already noticed that FUV external photoevaporation can have a significant impact in reducing the lifetime of protoplanetary discs for moderate external field intensities ($G_{\rm FUV} = 300\,G_0$). Both Clarke (2007) and Anderson, Adams & Calvet (2013) used the mass loss rates derived by Adams et al. (2004). It will be worth investigating how the disc evolution will be affected by the lower mass loss rates we derived for compact discs, and the much higher ones when grain growth has occurred. The high mass loss rates we obtain in the latter case suggest that external photoevaporation might be a dominant mechanism in determining the outer radius of protoplanetary discs even in very mild environments, once large dust grains have formed in the discs' outer regions.

In principle, in order to test this model in the low ambient field regime, we could follow two paths. The first one is statistical. For example, we could sample the outer radii of protoplanetary discs in different star forming regions, where the external FUV field can be considered quite uniform within the whole star forming region. Since Clarke (2007) showed that present disc sizes are very insensitive to the initial disc sizes when external photoevaporation is effective, in principle there should be a correlation between the present average disc size, and the external FUV flux. Note however it is very challenging to obtain good estimates of disc sizes (although ALMA is now overcoming the problem), and even more it is very difficult to measure the FUV field in these regions. A prediction for the FUV intensity within the cluster can be estimated by integrating the contribution from all the known radiation sources, even though the 3D structure of these regions is still not known. Another theoretical uncertainty is that the expected outer radii strongly depend on the assumed viscosity in the disc, and on its initial mass. Note that Anderson, Adams & Calvet (2013) have already conducted a similar exploratory study for the ONC, where the

FUV radiation within the cluster can be estimated well, since it is dominated by the radiation of the massive θ^1C star.

A second approach is to observe this photoevaporative flow directly in discs where we know that the external radiation is mild, since there are no close energetic sources. Examination of Fig. 6.9 suggests that the surface densities in the flow can be high enough ($\sim 10^{-3} - 10^{-2}$ g/cm^2) to be detectable in molecular line emission (e.g. ^{12}CO) with reasonable sensitivities. The outer regions are typified by a steep cliff in surface density surrounded by a gently sloping plateau of low density gas. The same regions would also be highly depleted in large grains ($s_{\rm entr} \lesssim 1\,\mu$m), and thus the disc outer radius estimated from dust continuum emission will be smaller than the one traced by molecular line emission. A good example of this feature is the huge 114-426 protoplanetary disc observed in silhouette by HST in Orion (Ricci, Robberto & Soderblom, 2008), where the outer regions associated with a photoevaporative flow (e.g. Miotello et al., 2012) are not observed in dust continuum emission at submm wavelengths (Mann et al., 2014; Bally et al., 2015), and present hints of radial gradient in the maximum grain size entrained in the flow (Miotello et al., 2012). Note however the in this case the disc is so large ($R_{\rm d} \sim 1000$ AU) that it is expected to lie in the supercritical regime of FUV photoevaporation.

The presence of these dust depleted structures in the outskirts of protoplanetary discs can be interpreted as the outcome of other physical processes, such as the radial drift of dust particles in the absence of a wind (Birnstiel & Andrews, 2014). However, discs affected by external photoevaporation will present other two features that are not compatible with the pure radial drift scenario. The first one is a positive temperature gradient in the regions associated with the flow. The second signature is kinematic: since the specific angular momentum in the flow equals the specific angular momentum at $R_{\rm d}$, the angular velocity of the flow will scale as R^{-2}, instead of the typical Keplerian $R^{-3/2}$. The observability of this feature favours small discs, where the absolute deviation from a Keplerian velocity in the flow will be more significant. The radial motions of the photoevaporative flow will however be hardly detectable, since the wind reaches velocities of ~ 1 km/s at the critical radius where molecular gas is likely to be highly photodissociated.

6.9 Conclusions

In this chapter we present new mass loss rates of externally photoevaporated discs covering a large parameter space. In particular, we are able to self-consistently solve the hydrodynamical equations of the photoevaporative winds for large discs (up to $R_{\rm d} = 250$ AU) and low FUV fluxes (down to $G_{\rm FUV} = 30\,G_0$), where previous studies have been unable to obtain numerical

solutions. We have shown that the method of solution can significantly affect the final estimates of the mass loss rates. More specifically, by properly treating the non-isothermal nature of the flow, we obtain lower mass loss rates than had been previously determined for an ISM-like dust component of the disc.

We have shown that the grain size distribution of the dust component of the disc has a significant effect on the mass loss rate. When grain growth has occurred in the midplane of the disc, out to its outer radius, the mass loss is remarkably more vigorous, mostly because of the consequent reduction of the cross section of dust particles at FUV wavelengths. For a moderate maximum size of the dust grain size distribution ($s_{\max} = 1\,\mathrm{mm}$), and a standard dust to gas ratio of 0.01, the mass loss rate is $\dot{M} > 10^{-8} M_{\odot}/\mathrm{yr}$ when $R_{\mathrm{d}} > 150\,\mathrm{AU}$ and $G_{\mathrm{FUV}} = 30\,G_0$, and $M_{\mathrm{d}} \gtrsim 10^{-3} M_{\odot}$. For the same parameters the mass loss rate can be as high as $10^{-7} M_{\odot}/\mathrm{yr}$ when $R_{\mathrm{d}} \sim 250\,\mathrm{AU}$. These high mass loss rates are expected to significantly affect the global evolution of protoplanetary discs. Our results indicate that even very mild environments can lead to significant truncation of the disc outer radius, especially when grain growth is effective. Such truncation is also expected to yield an acceleration of disc clearing. *We thus predict* that external photoevaporation is a more significant mechanism leading to disc clearing than previously considered. For such low values of the external field, future disc evolution models should include photoevaporation caused by both the external FUV field and the FUV flux from the central star (Gorti & Hollenbach, 2009; Gorti, Hollenbach & Dullemond, 2015), as suggested by Anderson, Adams & Calvet (2013).

We have suggested observable characteristic features that can probe a currently photoevaporating disc. In particular, our results show that photoevaporative winds are highly dust depleted, and that their surface densities can be observed in molecular line emission with present facilities (ALMA in particular). Strong evidence of ongoing external photoevaporation in this mild regime is a positive thermal radial gradient in the flow region, which can be probed by spatially resolved line ratios of different rovibrational transitions, and a non-Keplerian rotation curve that can be obtained via line kinematics.

Finally we emphasise that the present work is restricted to solar mass stars. As noted by Adams et al. (2004), we expect the effect of external photoevaporation to be yet more significant in the case of lower mass stars since the gravitational well is shallower.

Chapter 7

Conclusions and future prospects

In this thesis, I have addressed different aspects of the impact of environment on the evolution of protoplanetary discs. The approach has been very heterogeneous, and the covered topics have ranged over a wide spectrum of physical phenomena: from numerical simulations to spectral observations, from warps to external photoevaporation. In this final chapter, I summarise the main results presented in this document, and propose possible future prospects.

7.1 Warps

In chapters 2-3 we have focused on warp propagation in the specific case of circumbinary discs. In particular, we have shown that warp propagation in the linear regime is well described by simple 1D wave equations, by obtaining a good agreement between 1D full 3D SPH simulations, for a wide range of viscosities. These results are valid on timescales shorter than the viscous timescale, since we assume that the surface density of the discs does not vary in time. In chapter 3 we have used the 1D modelling of the warped discs to show that in some extreme cases warped structures could be used to detect planets within transition discs cavities. However, the detectability of such structures via line kinematics seems very challenging for standard disc parameters. Hot Jupiters could be detectable only if the gaseous material in inner regions of the transition discs is highly viscous.

Whereas new observations are probing possible signatures of disc warping (see Section 1.2.2), and the theoretical basis of such mechanism is well established (at least for α-discs, see chapters 2-3), the connection between the two has been poorly addressed in the literature. In particular, not much attention has been drawn to observational diagnostics of warped protoplanetary discs, in order to extract quantitative information when such structures are observed. Nixon & Pringle (2010) estimated the asymmetric illumination of a disc warped by a tidal interaction with a stellar fly-by, and noticed that such effect induces significant changes

in the spectral energy distribution (SED) at wavelengths $\lambda > 100\,\mu$m. Similarly, Flaherty & Muzerolle (2010) provided a prediction for the SEDs of warped discs, where the warping was not computed via hydrodynamical simulations, but was simply parametrised in a razor-thin model. Rosenfeld, Chiang & Andrews (2014) (see also Casassus et al., 2015) predicted that warps would cause typical twisted first moment maps in molecular line emission. Finally, Ruge et al. (2015) post-processed 3D hydrodynamical simulations of both coplanar and warped circumbinary discs, showing how the latter cause an asymmetric illumination that can be traced in total intensities maps by ALMA. More quantitative studies are needed to better interpret recent (and future) observations. In particular, the results shown in chapter 3 indicate that there is a nice correlation between the properties of circumbinary discs, the masses and inclination of the two central perturbers, and the amount of warping. In this work, we have confirmed the results by Foucart & Lai (2013), who obtained analytical expressions for the amount of tilting and twisting of circumbinary discs. Such expressions have also been confirmed by both Lodato & Facchini (2013) and Foucart & Lai (2014) in the case of radially finite discs. Measuring the degree of twisting of a warped disc can thus lead to an indirect determination of disc's viscosity in protoplanetary discs, but again to do so needs a better development of synthetic observations of warped discs. Note that similar analyses on warped discs orbiting X-ray binaries have started constraining some features of accretion disc viscosity (as its anisotropy, see King et al., 2013; Nixon, 2015).

Following this idea, we are currently producing synthetic observations of 3D warped circumbinary discs, where the hydrodynamics is simulated via PHANTOM, and radiative transfer is performed with RADMC-3D. We aim to obtain synthetic images for sub-mm continuum, line profiles, and scattered light (Juhász & Facchini, in prep.), ranging over different parameters (e.g. viscosity, binary inclination, disc inclination in the plane of the sky, etc...). The initial results are promising, and they show that twisting can be used to estimate disc viscosity when $\alpha \gtrsim 0.01$. Moreover, two-armed spirals can be observed in scattered light, as in the HD 100543 system (Wagner et al., 2015). Further analysis is however required at this stage.

7.2 RW Aur

In chapter 4 we used a series of hydrodynamic (SPH) simulations to investigate the possibility that the unusual morphology of RW Aur might be explained by a tidal encounter in the form of a star-disc fly-by. We identified orbital parameters best able to reproduce all the features of RW Aur inferred in the PdBI observations by Cabrit et al. (2006), such as: the length of the tidal arm, separation between RW Aur A and B, disc position angles, and relative

stars proper motions. Furthermore, we post-processed the hydrodynamic simulations with the non-LTE radiative transfer code TORUS to compute synthetic molecular line and dust continuum observations to compare with the observations from Cabrit et al. (2006), finding excellent agreement with the CO optical thickness of the different components, kinematic signatures in the line profiles, and observed continuum and CO fluxes, although CO emission around B is slightly underestimated. The model also predicts that the line of sight to RW Aur A currently intersects a bridge of stripped off material between the two stars. Another important prediction is that the tidal interaction was strong and recent, with a prograde encounter reaching periastron of 70 AU only ~ 570 yrs ago. If this interpretation is correct, RW Aur would be the only CTTS system known to date to have undergone strong tidal interactions so recently in the past, proving a unique opportunity to gain insight into the effect that this type of interaction can have on future planet formation and disc evolution in binary systems.

Although of low column density ($N_{\rm H} \leq 10^{-4}\,{\rm g/cm^2}$, i.e. $A_V \leq 0.1\,{\rm mag}$), the bridge structure between the two stars may have small clumps of denser material able to occasionally dim the central star, and explaining the observed repeated dimming events. We have proposed this model at the end of chapter 4. However, more recent observations during the last dimming event, including the X-Shooter observations presented in chapter 5, indicate that this is not the most likely possibility. In particular, the IR excess simultaneous to the optical dimming (Shenavrin, Petrov & Grankin, 2015) and the high gas velocities probed by our observations suggest that the dimming events are related to a sudden change of geometry of the inner disc. Interestingly, this phenomenon is likely related to a burst of stellar wind, which can be triggered by the high accretion rate caused by the tidal encounter.

Further observations are needed to identify the mechanism at the origin of the dimming event. Some authors (and we) have speculated that the grey extinction observed photometrically from optical to NIR bands might be due to efficient scattering, as in the famous case of AA Tau (Bouvier et al., 2013). In order to validate or rule out this possibility, we have obtained new time on the VLT with a ToO proposal (Pr.Id. 096.C-0384, PI Facchini, priority A) to observe a new X-Shooter spectrum of RW Aur A during its bright state. The wide spectral range of the spectrograph ($0.3 - 2.5\,\mu$m) and proper flux calibration will allow us to compare the spectrum of RW Aur A during and after the dimming events. Such comparison will lead to a precise estimate of the extinction curve, which can determine whether scattering gives significant contribution in the optical flux. Furthermore, a thorough comparison of both emission and absorption line profiles before and after the dimming will help understanding the nature of these recurrent dim state.

Finally, we have obtained time with ALMA Cycle 3 (Pr.Id. 2015.1.01506.S, PI Rodriguez, priority B) to observe both RW Aur A and B in band 6 and 7. We will be able to resolve the circumprimary disc for the first time, and possibly look for asymmetric structures (spirals) caused by the purported tidal interaction. Moreover, we should be able to determine whether the material around star B has been tidally captured by the secondary star, or presents signatures of keplerian rotation, i.e. suggesting the star B was already bearing a disc before the encounter occurred. We will also look for SO emission, a chemical tracer of spirals/accretion shocks in discs (e.g. Sakai et al., 2014). In summary, the ALMA observations will shed a better light on the effects of a star-disc encounter in the dynamical, thermal and chemical evolution of protoplanetary discs.

7.3 External photoevaporation

From the multiple effects of a star-disc encounter on a protoplanetary disc, we have then moved to arguably the most significant environmental effect on discs' evolution: external photoevaporation. In chapter 6 we have coupled thermo- and hydrodynamical equations of a radial flow launched from the disc's outer radius in a self-consistent model to determine the mass loss rates of material orbiting at the outer regions of protoplanetary discs when they are impinged by an external radiation. In particular we have focused on the so-called subcritical regime, where the disc outer rim is not heated to high enough temperatures that material is launched in free space supersonically. In this study, we have improved similar models available in the literature, and we have taken into account the effect that grain growth within the disc can have onto the mass loss rates driven by the ambient FUV field. Grain growth to mm sizes has a huge impact on large discs, where mass loss rates can be as high as $2 \times 10^{-7} M_{\odot}$/yr when $R_{\rm d} = 250\,$AU even for very mild external irradiation ($G_{\rm FUV} = 30\,G_0$). On the other side, the mass loss rates for compact discs are found to be very low even for moderate fields ($G_{\rm FUV} = 3000\,G_0$). This result suggests that external photoevaporation could play a key role in truncating disc sizes on a wide range of environmental conditions, much more significantly that has been appreciated hitherto.

Clarke (2007) and Anderson, Adams & Calvet (2013) have shown that disc truncation due to external photoevaporation accelerates disc clearing by inhibiting the viscous spreading of the disc. A natural follow-up of the study presented in this document is to re-run similar calculations of 1D viscous evolution of the discs' surface density, coupling the viscous evolution equations to the new mass loss rates reported here. Another interesting prospect is to derive a quantitative estimate of disc truncation due to stellar fly-bys and external photoevaporation as a function of cluster size N. This project should determine which

mechanism is more efficient in setting disc sizes in young stellar clusters. The result might give an important contribution in understanding how protoplanetary discs evolve in these young associations, where the majority of stars is born, and thus in estimating how environmental effects can affect the formation and evolution of young planetary systems.

References

Acreman D. M., Harries T. J., Rundle D. A., 2010, MNRAS, 403, 1143

Adams F. C., 2010, ARA&A, 48, 47

Adams F. C., Hollenbach D., Laughlin G., Gorti U., 2004, ApJ, 611, 360

Adams F. C., Proszkow E. M., Fatuzzo M., Myers P. C., 2006, ApJ, 641, 504

Akeson R. L. et al., 2011, ApJ, 728, 96

Albrecht S. et al., 2012, ApJ, 757, 18

Alcala J. M., Covino E., Franchini M., Krautter J., Terranegra L., Wichmann R., 1993, A&A, 272, 225

Alcalá J. M. et al., 2014, A&A, 561, A2

Alencar S. H. P., Basri G., Hartmann L., Calvet N., 2005, A&A, 440, 595

Alencar S. H. P., Batalha C., 2002, ApJ, 571, 378

Alexander R., 2012, ApJL, 757, L29

Alexander R., Pascucci I., Andrews S., Armitage P., Cieza L., 2014, Protostars and Planets VI, 475

Alexander R. D., Clarke C. J., Pringle J. E., 2006, MNRAS, 369, 229

Allen L. et al., 2007, Protostars and Planets V, 361

ALMA Partnership et al., 2015, ApJL, 808, L3

Anderson K. R., Adams F. C., Calvet N., 2013, ApJ, 774, 9

Andre P., Montmerle T., 1994, ApJ, 420, 837

Andre P., Ward-Thompson D., Barsony M., 1993, ApJ, 406, 122

Andrews S. M. et al., 2014, ApJ, 787, 148

Andrews S. M., Rosenfeld K. A., Wilner D. J., Bremer M., 2011, ApJL, 742, L5

Andrews S. M., Williams J. P., 2005, ApJ, 631, 1134

Andrews S. M., Williams J. P., 2007, ApJ, 671, 1800

Andrews S. M. et al., 2012, ApJ, 744, 162

Antipin S. et al., 2015, Information Bulletin on Variable Stars, 6126, 1

Armitage P. J., 2010, Astrophysics of Planet Formation

Armitage P. J., 2011, ARA&A, 49, 195

Arnold T. J., Eisner J. A., Monnier J. D., Tuthill P., 2012, ApJ, 750, 119

Artymowicz P., Lubow S. H., 1994, ApJ, 421, 651

Asplund M., Grevesse N., Sauval A. J., Scott P., 2009, ARA&A, 47, 481

Bakes E. L. O., Tielens A. G. G. M., 1994, ApJ, 427, 822

Bally J. et al., 2015, ApJ, 808, 69

Bally J., O'Dell C. R., McCaughrean M. J., 2000, AJ, 119, 2919

Basri G., Bertout C., 1989, ApJ, 341, 340

Bastian N., Lamers H. J. G. L. M., de Mink S. E., Longmore S. N., Goodwin S. P., Gieles M., 2013, MNRAS, 436, 2398

Bate M. R., 2009, MNRAS, 392, 590

Bate M. R., 2012, MNRAS, 419, 3115

Bate M. R., Bonnell I. A., Clarke C. J., Lubow S. H., Ogilvie G. I., Pringle J. E., Tout C. A., 2000, MNRAS, 317, 773

Bate M. R., Bonnell I. A., Price N. M., 1995, MNRAS, 277, 362

Bate M. R., Lodato G., Pringle J. E., 2010, MNRAS, 401, 1505

Beckwith S. V. W., Henning T., Nakagawa Y., 2000, Protostars and Planets IV, 533

Beckwith S. V. W., Sargent A. I., 1993, ApJ, 402, 280

Beckwith S. V. W., Sargent A. I., Chini R. S., Guesten R., 1990, AJ, 99, 924

Benisty M. et al., 2015, A&A, 578, L6

Bergin E., Calvet N., D'Alessio P., Herczeg G. J., 2003, ApJL, 591, L159

Beuermann K. et al., 2010, A&A, 521, L60

Beust H., Dutrey A., 2005, A&A, 439, 585

Biller B. et al., 2012, ApJL, 753, L38

Biller B. A. et al., 2014, ApJL, 792, L22

Birnstiel T., Andrews S. M., 2014, ApJ, 780, 153

Birnstiel T., Dullemond C. P., Brauer F., 2010, A&A, 513, A79

Birnstiel T., Klahr H., Ercolano B., 2012, A&A, 539, A148

Birnstiel T., Ormel C. W., Dullemond C. P., 2011, A&A, 525, A11

Bisbas T. G., Bell T. A., Viti S., Barlow M. J., Yates J., Vasta M., 2014, MNRAS, 443, 111

Bisbas T. G., Bell T. A., Viti S., Yates J., Barlow M. J., 2012, MNRAS, 427, 2100

Bisbas T. G., Papadopoulos P. P., Viti S., 2015, ApJ, 803, 37

Bisikalo D. V., Dodin A. V., Kaigorodov P. V., Lamzin S. A., Malogolovets E. V., Fateeva A. M., 2012, Astronomy Reports, 56, 686

Bitsch B., Crida A., Libert A.-S., Lega E., 2013, A&A, 555, A124

Bohren C. F., Huffman D. R., 1983, Absorption and scattering of light by small particles

Bonnell I., Arcoragi J.-P., Martel H., Bastien P., 1992, ApJ, 400, 579

Bouvier J., Grankin K., Ellerbroek L. E., Bouy H., Barrado D., 2013, A&A, 557, A77

Breslau A., Steinhausen M., Vincke K., Pfalzner S., 2014, A&A, 565, A130

Bruderer S., van Dishoeck E. F., Doty S. D., Herczeg G. J., 2012, A&A, 541, A91

Cabrit S., Pety J., Pesenti N., Dougados C., 2006, A&A, 452, 897

Calvet N., D'Alessio P., Hartmann L., Wilner D., Walsh A., Sitko M., 2002, ApJ, 568, 1008

Calvet N., Gullbring E., 1998, ApJ, 509, 802

Casassus S. et al., 2015, ArXiv e-prints

Casassus S. et al., 2013, Nature, 493, 191

Chen X. et al., 2013, ApJ, 768, 110

Chiang E. I., Goldreich P., 1997, ApJ, 490, 368

Chiang E. I., Murray-Clay R. A., 2004, ApJ, 607, 913

Chou M.-Y. et al., 2013, AJ, 145, 108

Cieza L. A. et al., 2011, ApJL, 741, L25

Cieza L. A. et al., 2009, ApJL, 696, L84

Clarke C., 2011, The Dispersal of Disks around Young Stars, Garcia P. J. V., ed., pp. 355–418

Clarke C., Carswell B., 2007, Principles of Astrophysical Fluid Dynamics

Clarke C. J., 2007, MNRAS, 376, 1350

Clarke C. J., Pringle J. E., 1993, MNRAS, 261, 190

Close L. M. et al., 2014, ApJL, 781, L30

Connelley M. S., Reipurth B., Tokunaga A. T., 2008a, AJ, 135, 2496

Connelley M. S., Reipurth B., Tokunaga A. T., 2008b, AJ, 135, 2526

Connelly J. N., Bizzarro M., Krot A. N., Nordlund Å., Wielandt D., Ivanova M. A., 2012, Science, 338, 651

Cox A. W., Grady C. A., Hammel H. B., Hornbeck J., Russell R. W., Sitko M. L., Woodgate B. E., 2013, ApJ, 762, 40

Croxall K. V. et al., 2012, ApJ, 747, 81

Crutcher R. M., 1975, ApJ, 202, 634

Curran R. L., Argiroffi C., Sacco G. G., Orlando S., Peres G., Reale F., Maggio A., 2011, A&A, 526, A104

Dai F., Facchini S., Clarke C. J., Haworth T. J., 2015, MNRAS, 449, 1996

Dale J. E., Ercolano B., Bonnell I. A., 2013, MNRAS, 431, 1062

D'Alessio P., Cantö J., Calvet N., Lizano S., 1998, ApJ, 500, 411

de Gregorio-Monsalvo I. et al., 2013, A&A, 557, A133

de Juan Ovelar M., Kruijssen J. M. D., Bressert E., Testi L., Bastian N., Cánovas H., 2012, A&A, 546, L1

Debes J. H., Jang-Condell H., Weinberger A. J., Roberge A., Schneider G., 2013, ApJ, 771, 45

Deeg H. J., Ocaña B., Kozhevnikov V. P., Charbonneau D., O'Donovan F. T., Doyle L. R., 2008, A&A, 480, 563

Demianski M., Ivanov P. B., 1997, A&A, 324, 829

Dodin A. V., Lamzin S. A., Chuntonov G. A., 2012, Astronomy Letters, 38, 167

Doyle L. R. et al., 2011, Science, 333, 1602

Draine B. T., 2003a, ApJ, 598, 1017

Draine B. T., 2003b, ApJ, 598, 1026

Draine B. T., 2006, ApJ, 636, 1114

Draine B. T., 2011, Physics of the Interstellar and Intergalactic Medium

Draine B. T., Li A., 2007, ApJ, 657, 810

Duchêne G., Bontemps S., Bouvier J., André P., Djupvik A. A., Ghez A. M., 2007, A&A, 476, 229

Duquennoy A., Mayor M., 1991, A&A, 248, 485

Dutrey A., Guilloteau S., Simon M., 1994, A&A, 286, 149

Dutrey A. et al., 2014, Protostars and Planets VI, 317

Eisner J. A., Chiang E. I., Hillenbrand L. A., 2006, ApJL, 637, L133

Epstein P. S., 1924, Physical Review, 23, 710

Español P., Revenga M., 2003, Phys. Rev. E, 67, 026705

Espaillat C., Calvet N., D'Alessio P., Hernández J., Qi C., Hartmann L., Furlan E., Watson D. M., 2007, ApJL, 670, L135

Espaillat C. et al., 2014, Protostars and Planets VI, 497

Evans T. M. et al., 2012, ApJ, 744, 120

Facchini S., Clarke C. J., Bisbas T., 2015, MNRAS submitted

Facchini S., Lodato G., Price D. J., 2013, MNRAS, 433, 2142

Facchini S. et al., 2015, MNRAS submitted

Facchini S., Ricci L., Lodato G., 2014, MNRAS, 442, 3700

Fatuzzo M., Adams F. C., 2008, ApJ, 675, 1361

Fedele D., van den Ancker M. E., Henning T., Jayawardhana R., Oliveira J. M., 2010, A&A, 510, A72

Flaherty K. M., Muzerolle J., 2010, ApJ, 719, 1733

Flebbe O., Muenzel S., et al., 1994, ApJ, 431, 754

Foucart F., Lai D., 2013, ApJ, 764, 106

Foucart F., Lai D., 2014, MNRAS, 445, 1731

Fragner M. M., Nelson R. P., 2010, A&A, 511, A77

Fruscione A. et al., 2006, in Society of Photo-Optical Instrumentation Engineers (SPIE) Conference Series, Vol. 6270, Society of Photo-Optical Instrumentation Engineers (SPIE) Conference Series

Gaches B. A. L., Offner S. S. R., Rosolowsky E. W., Bisbas T. G., 2015, ApJ, 799, 235

Gahm G. F., Petrov P. P., Duemmler R., Gameiro J. F., Lago M. T. V. T., 1999, A&A, 352, L95

Gammie C. F., Goodman J., Ogilvie G. I., 2000, MNRAS, 318, 1005

Garufi A. et al., 2013, A&A, 560, A105

Geers V. C. et al., 2006, A&A, 459, 545

Geers V. C., van Dishoeck E. F., Visser R., Pontoppidan K. M., Augereau J.-C., Habart E., Lagrange A. M., 2007, A&A, 476, 279

Ghez A. M., White R. J., Simon M., 1997, ApJ, 490, 353

Gorti U., Hollenbach D., 2009, ApJ, 690, 1539

Gorti U., Hollenbach D., Dullemond C. P., 2015, ApJ, 804, 29

Gorti U., Hollenbach D., Najita J., Pascucci I., 2011, ApJ, 735, 90

Grankin K. N., Melnikov S. Y., Bouvier J., Herbst W., Shevchenko V. S., 2007, A&A, 461, 183

Gregory S. G., Donati J.-F., Morin J., Hussain G. A. J., Mayne N. J., Hillenbrand L. A., Jardine M., 2012, ApJ, 755, 97

Guilloteau S., Dutrey A., Piétu V., Boehler Y., 2011, A&A, 529, A105

Güver T., Özel F., 2009, MNRAS, 400, 2050

Habing H. J., 1968, Bulletin Astronomical Inst. Netherlands, 19, 421

Hall S. M., 1997, MNRAS, 287, 148

Hardy A., Caceres C., Schreiber M. R., Cieza L., Alexander R. D., Canovas H., Williams J. P., Wahhaj Z., 2015, ArXiv e-prints

Harries T. J., 2000, MNRAS, 315, 722

Harries T. J., Monnier J. D., Symington N. H., Kurosawa R., 2004, MNRAS, 350, 565

Hartigan P., Edwards S., Ghandour L., 1995, ApJ, 452, 736

Hartmann L., 2008, Accretion Processes in Star Formation

Hartmann L., Calvet N., Gullbring E., D'Alessio P., 1998, ApJ, 495, 385

Haworth T. J., Harries T. J., 2012, MNRAS, 420, 562

Haworth T. J., Harries T. J., Acreman D. M., 2012, MNRAS, 426, 203

Helled R. et al., 2014, Protostars and Planets VI, 643

Herbst W., LeDuc K., et al., 2010, AJ, 140, 2025

Hollenbach D., Johnstone D., Lizano S., Shu F., 1994, ApJ, 428, 654

Huélamo N., de Gregorio-Monsalvo I., Macias E., Pinte C., Ireland M., Tuthill P., Lacour S., 2015, A&A, 575, L5

Huélamo N., Lacour S., Tuthill P., Ireland M., Kraus A., Chauvin G., 2011, A&A, 528, L7

Hughes A. M., Wilner D. J., Calvet N., D'Alessio P., Claussen M. J., Hogerheijde M. R., 2007, ApJ, 664, 536

Ingleby L. et al., 2009, ApJL, 703, L137

Isella A., Carpenter J. M., Sargent A. I., 2009, ApJ, 701, 260

Isella A., Pérez L. M., Carpenter J. M., 2012, ApJ, 747, 136

Isella A., Pérez L. M., Carpenter J. M., Ricci L., Andrews S., Rosenfeld K., 2013, ApJ, 775, 30

Ivanov P. B., Papaloizou J. C. B., Polnarev A. G., 1999, MNRAS, 307, 79

Jenkins J. M. et al., 2015, AJ, 150, 56

Jensen E. L. N., Akeson R., 2014, Nature, 511, 567

Jensen E. L. N., Mathieu R. D., Fuller G. A., 1996, ApJ, 458, 312

Johansen A., Blum J., Tanaka H., Ormel C., Bizzarro M., Rickman H., 2014, Protostars and Planets VI, 547

Johansen A., Oishi J. S., Mac Low M.-M., Klahr H., Henning T., Youdin A., 2007, Nature, 448, 1022

Johnstone D., Hollenbach D., Bally J., 1998, ApJ, 499, 758

Kaufman M. J., Wolfire M. G., Hollenbach D. J., Luhman M. L., 1999, ApJ, 527, 795

Keto E., Caselli P., 2008, ApJ, 683, 238

King A. R., Livio M., Lubow S. H., Pringle J. E., 2013, MNRAS, 431, 2655

Kobayashi H., Ida S., 2001, Icarus, 153, 416

Koepferl C. M., Ercolano B., Dale J., Teixeira P. S., Ratzka T., Spezzi L., 2013, MNRAS, 428, 3327

Kostov V. B. et al., 2014, ApJ, 784, 14

Kotze M. M., Charles P. A., 2012, MNRAS, 420, 1575

Kraus A. L., Ireland M. J., 2012, ApJ, 745, 5

Kraus A. L., Ireland M. J., Hillenbrand L. A., Martinache F., 2012, ApJ, 745, 19

Kurosawa R., Harries T. J., Symington N. H., 2006, MNRAS, 370, 580

Lada C. J., 1987, in IAU Symposium, Vol. 115, Star Forming Regions, Peimbert M., Jugaku J., eds., pp. 1–17

Lada C. J., Lada E. A., 2003, ARA&A, 41, 57

Laibe G., Price D. J., 2012, MNRAS, 420, 2345

Laor A., Draine B. T., 1993, ApJ, 402, 441

Larwood J. D., Papaloizou J. C. B., 1997, MNRAS, 285, 288

Lee J. W., Kim S.-L., Kim C.-H., Koch R. H., Lee C.-U., Kim H.-I., Park J.-H., 2009, AJ, 137, 3181

Lega E., Morbidelli A., Nesvorný D., 2013, MNRAS, 431, 3494

Li A., Greenberg J. M., 1997, A&A, 323, 566

Lodato G., Facchini S., 2013, MNRAS, 433, 2157

Lodato G., Price D. J., 2010, MNRAS, 405, 1212

Lodato G., Pringle J. E., 2006, MNRAS, 368, 1196

Lodato G., Pringle J. E., 2007, MNRAS, 381, 1287

Longmore S. N. et al., 2014, Protostars and Planets VI, 291

López-Martín L., Cabrit S., Dougados C., 2003, A&A, 405, L1

Lubow S. H., Martin R. G., Nixon C., 2014, ArXiv e-prints

Lubow S. H., Ogilvie G. I., 2000, ApJ, 538, 326

Lubow S. H., Ogilvie G. I., 2001, ApJ, 560, 997

Lubow S. H., Ogilvie G. I., Pringle J. E., 2002, MNRAS, 337, 706

Lynden-Bell D., Pringle J. E., 1974, MNRAS, 168, 603

Maaskant K. M., Min M., Waters L. B. F. M., Tielens A. G. G. M., 2014, A&A, 563, A78

MacFadyen A. I., Milosavljević M., 2008, ApJ, 672, 83

Madhusudhan N., Lee K. K. M., Mousis O., 2012, ApJL, 759, L40

Malmberg D., Davies M. B., Heggie D. C., 2011, MNRAS, 411, 859

Malmberg D., de Angeli F., Davies M. B., Church R. P., Mackey D., Wilkinson M. I., 2007, MNRAS, 378, 1207

Mamajek E. E., 2009, in American Institute of Physics Conference Series, Vol. 1158, American Institute of Physics Conference Series, Usuda T., Tamura M., Ishii M., eds., pp. 3–10

Manara C. F., Beccari G., Da Rio N., De Marchi G., Natta A., Ricci L., Robberto M., Testi L., 2013, A&A, 558, A114

Mann R. K., Andrews S. M., Eisner J. A., Williams J. P., Meyer M. R., Di Francesco J., Carpenter J. M., Johnstone D., 2015, ApJ, 802, 77

Mann R. K. et al., 2014, ApJ, 784, 82

Mann R. K., Williams J. P., 2010, ApJ, 725, 430

Marino S., Perez S., Casassus S., 2015, ApJL, 798, L44

Mathieu R. D., Stassun K., Basri G., Jensen E. L. N., Johns-Krull C. M., Valenti J. A., Hartmann L. W., 1997, AJ, 113, 1841

Mathis J. S., Rumpl W., Nordsieck K. H., 1977, ApJ, 217, 425

Matthews B. C., Krivov A. V., Wyatt M. C., Bryden G., Eiroa C., 2014, Protostars and Planets VI, 521

McElroy D., Walsh C., Markwick A. J., Cordiner M. A., Smith K., Millar T. J., 2013, A&A, 550, A36

McKee C. F., Ostriker E. C., 2007, ARA&A, 45, 565

Men'shchikov A. B., Henning T., 1997, A&A, 318, 879

Miotello A., Robberto M., Potenza M. A. C., Ricci L., 2012, ApJ, 757, 78

Miotello A., Testi L., Lodato G., Ricci L., Rosotti G., Brooks K., Maury A., Natta A., 2014, A&A, 567, A32

Mitchell T. R., Stewart G. R., 2010, ApJ, 722, 1115

Modigliani A. et al., 2010, in SPIE Conference Series, Vol. 7737, SPIE Conference Series, p. 28

Morris J. P., Monaghan J. J., 1997, Journal of Computational Physics, 136, 41

Morton D. C., Smith W. H., 1973, ApJS, 26, 333

Movshovitz N., Bodenheimer P., Podolak M., Lissauer J. J., 2010, Icarus, 209, 616

Muñoz D. J., Kratter K., Vogelsberger M., Hernquist L., Springel V., 2015, MNRAS, 446, 2010

Murray J. R., 1996, MNRAS, 279, 402

Murray-Clay R. A., Chiang E. I., Murray N., 2009, ApJ, 693, 23

Najita J. R., Carr J. S., Strom S. E., Watson D. M., Pascucci I., Hollenbach D., Gorti U., Keller L., 2010, ApJ, 712, 274

Nayakshin S., 2005, MNRAS, 359, 545

Nealon R., Price D. J., Nixon C. J., 2015, MNRAS, 448, 1526

Nelson R. P., Papaloizou J. C. B., 1999, MNRAS, 309, 929

Nelson R. P., Papaloizou J. C. B., 2000, MNRAS, 315, 570

Nixon C., 2015, MNRAS, 450, 2459

Nixon C., King A., 2015, ArXiv e-prints

Nixon C., King A., et al., 2012, ApJL, 757, L24

Nixon C. J., King A. R., 2012, MNRAS, 421, 1201

Nixon C. J., King A. R., Pringle J. E., 2011, MNRAS, 417, L66

Nixon C. J., Pringle J. E., 2010, MNRAS, 403, 1887

Öberg K. I., Furuya K., Loomis R., Aikawa Y., Andrews S. M., Qi C., van Dishoeck E. F., Wilner D. J., 2015, ApJ, 810, 112

O'Dell C. R., Wen Z., Hu X., 1993, ApJ, 410, 696

Offner S. S. R., Bisbas T. G., Bell T. A., Viti S., 2014, MNRAS, 440, L81

Offner S. S. R., Bisbas T. G., Viti S., Bell T. A., 2013, ApJ, 770, 49

Offner S. S. R., Klein R. I., McKee C. F., Krumholz M. R., 2009, ApJ, 703, 131

Ogilvie G. I., 1999, MNRAS, 304, 557

Ogilvie G. I., 2006, MNRAS, 365, 977

Olczak C., Kaczmarek T., Harfst S., Pfalzner S., Portegies Zwart S., 2012, ApJ, 756, 123

Olczak C., Pfalzner S., Spurzem R., 2006, ApJ, 642, 1140

Olech A., Rutkowski A., Schwarzenberg-Czerny A., 2009, MNRAS, 399, 465

Oliveira I. et al., 2010, ApJ, 714, 778

Olofsson J. et al., 2013, A&A, 552, A4

Orosz J. A. et al., 2012, Science, 337, 1511

Osterloh M., Beckwith S. V. W., 1995, ApJ, 439, 288

Ostriker E. C., 1994, ApJ, 424, 292

Owen J. E., 2014, ApJ, 789, 59

Owen J. E., Clarke C. J., 2012, MNRAS, 426, L96

Owen J. E., Clarke C. J., Ercolano B., 2012, MNRAS, 422, 1880

Owen J. E., Hudoba de Badyn M., Clarke C. J., Robins L., 2013, MNRAS, 436, 1430

Panić O., Hogerheijde M. R., Wilner D., Qi C., 2009, A&A, 501, 269

Panić O., van Dishoeck E. F., Hogerheijde M. R., Belloche A., Güsten R., Boland W., Baryshev A., 2010, A&A, 519, A110

Papaloizou J. C. B., Lin D. N. C., 1995, ApJ, 438, 841

Papaloizou J. C. B., Pringle J. E., 1983, MNRAS, 202, 1181

Parker E. N., 1958, ApJ, 128, 664

Pascucci I., et al., 2011, ApJ, 736, 13

Pascucci I. et al., 2006, ApJ, 651, 1177

Petrov P. P., Gahm G. F., Djupvik A. A., Babina E. V., Artemenko S. A., Grankin K. N., 2015, A&A, 577, A73

Petrov P. P., Pelt J., Tuominen I., 2001, A&A, 375, 977

Pfalzner S., 2008, A&A, 492, 735

Piétu V., Dutrey A., Guilloteau S., 2007, A&A, 467, 163

Pineda J. E., Quanz S. P., Meru F., Mulders G. D., Meyer M. R., Panić O., Avenhaus H., 2014, ApJL, 788, L34

Pinilla P., Benisty M., Birnstiel T., 2012, A&A, 545, A81

Pinilla P., Birnstiel T., Ricci L., Dullemond C. P., Uribe A. L., Testi L., Natta A., 2012, A&A, 538, A114

Pinte C. et al., 2008, A&A, 489, 633

Pontoppidan K. M., Blake G. A., van Dishoeck E. F., Smette A., Ireland M. J., Brown J., 2008, ApJ, 684, 1323

Porras A., Christopher M., Allen L., Di Francesco J., Megeath S. T., Myers P. C., 2003, AJ, 126, 1916

Price D. J., 2012, Journal of Computational Physics, 231, 759

Price D. J., Federrath C., 2010, MNRAS, 406, 1659

Pringle J. E., 1981, ARA&A, 19, 137

Pringle J. E., 1991, MNRAS, 248, 754

Pringle J. E., 1992, MNRAS, 258, 811

Pringle J. E., 1996, MNRAS, 281, 357

Qi C., et al., 2004, ApJL, 616, L11

Quillen A. C., 2006, ApJ, 640, 1078

Ratzka T., Leinert C., Henning T., Bouwman J., Dullemond C. P., Jaffe W., 2007, A&A, 471, 173

Reggiani M. et al., 2014, ApJL, 792, L23

Reipurth B., Clarke C. J., Boss A. P., Goodwin S. P., Rodríguez L. F., Stassun K. G., Tokovinin A., Zinnecker H., 2014, Protostars and Planets VI, 267

Ricci L., Isella A., Carpenter J. M., Testi L., 2013, ApJL, 764, L27

Ricci L., Robberto M., Soderblom D. R., 2008, AJ, 136, 2136

Ricci L., Testi L., Natta A., Brooks K. J., 2010a, A&A, 521, A66

Ricci L., Testi L., Natta A., Neri R., Cabrit S., Herczeg G. J., 2010b, A&A, 512, A15

Ricci L., Testi L., Natta A., Scholz A., de Gregorio-Monsalvo I., 2012a, ApJL, 761, L20

Ricci L., Trotta F., Testi L., Natta A., Isella A., Wilner D. J., 2012b, A&A, 540, A6

Rice W. K. M., Armitage P. J., Wood K., Lodato G., 2006, MNRAS, 373, 1619

Richert A. J. W., Feigelson E. D., Getman K. V., Kuhn M. A., 2015, ArXiv e-prints

Richling S., Yorke H. W., 2000, ApJ, 539, 258

Roberge A., Weinberger A. J., Malumuth E. M., 2005, ApJ, 622, 1171

Roccatagliata V., Ratzka T., Henning T., Wolf S., Leinert C., Bouwman J., 2011, A&A, 534, A33

Rodriguez J. E., Pepper J., Stassun K. G., Siverd R. J., Cargile P., Beatty T. G., Gaudi B. S., 2013, AJ, 146, 112

Rollig M., Abel N. P., Bell T., et al., 2007, A&A, 467, 187

Rosenfeld K. A., Andrews S. M., Hughes A. M., Wilner D. J., Qi C., 2013, ApJ, 774, 16

Rosenfeld K. A., Chiang E., Andrews S. M., 2014, ApJ, 782, 62

Rosenfeld K. A. et al., 2012, ApJ, 757, 129

Rosotti G. P., Dale J. E., de Juan Ovelar M., Hubber D. A., Kruijssen J. M. D., Ercolano B., Walch S., 2014, MNRAS, 441, 2094

Rucinski S. M., Krautter J., 1983, A&A, 121, 217

Ruge J. P., Wolf S., Demidova T., Grinin V., 2015, A&A, 579, A110

Rundle D., Harries T. J., Acreman D. M., Bate M. R., 2010, MNRAS, 407, 986

Sakai N. et al., 2014, Nature, 507, 78

Salyk C., Pontoppidan K., Corder S., Muñoz D., Zhang K., Blake G. A., 2014, ApJ, 792, 68

Scally A., Clarke C., 2001, MNRAS, 325, 449

Scheuer P. A. G., Feiler R., 1996, MNRAS, 282, 291

Schneider P. C. et al., 2015, A&A submitted

Shakura N. I., Sunyaev R. A., 1973, A&A, 24, 337

Shenavrin V. I., Petrov P. P., Grankin K. N., 2015, Information Bulletin on Variable Stars, 6143, 1

Shu F. H., Galli D., et al., 2007, ApJ, 665, 535

Simon M., Dutrey A., Guilloteau S., 2000, ApJ, 545, 1034

Smith N., Bally J., Morse J. A., 2003, ApJL, 587, L105

Springel V., 2010, MNRAS, 401, 791

Stokes G. G., 1851, Transactions of the Cambridge Philosophical Society, 9, 8

Stolte A. et al., 2010, ApJ, 718, 810

Störzer H., Hollenbach D., 1999, ApJ, 515, 669

Strom K. M., Strom S. E., Edwards S., Cabrit S., Skrutskie M. F., 1989, AJ, 97, 1451

Takeuchi T., Lin D. N. C., 2002, ApJ, 581, 1344

Terquem C., 2013, MNRAS, 435, 798

Testi L. et al., 2014, Protostars and Planets VI, 339

Teyssandier J., Terquem C., Papaloizou J. C. B., 2013, MNRAS, 428, 658

Thalmann C. et al., 2015, ApJL, 808, L41

Tielens A. G. G. M., 2008, ARA&A, 46, 289

Tobin J. J., Hartmann L., Chiang H.-F., Wilner D. J., Looney L. W., Loinard L., Calvet N., D'Alessio P., 2013, ApJ, 771, 48

Torres C. A. O., Quast G. R., Melo C. H. F., Sterzik M. F., 2008, Young Nearby Loose Associations, p. 757

Torres R. M., Loinard L., Mioduszewski A. J., Rodríguez L. F., 2009, ApJ, 698, 242

Triaud A. H. M. J. et al., 2010, A&A, 524, A25

Trilling D. E. et al., 2007, ApJ, 658, 1289

Turner N. J., Fromang S., Gammie C., Klahr H., Lesur G., Wardle M., Bai X.-N., 2014, Protostars and Planets VI, 411

Vacca W. D., Sandell G., 2011, ApJ, 732, 8

van der Marel N., et al., 2013, Science, 340, 1199

van der Marel N., van Dishoeck E. F., Bruderer S., Pérez L., Isella A., 2015, A&A, 579, A106

van Leeuwen F., 2007a, A&A, 474, 653

van Leeuwen F., 2007b, A&A, 474, 653

Vernet J. et al., 2011, A&A, 536, A105

Vicente S. M., Alves J., 2005, A&A, 441, 195

Vincke K., Breslau A., Pfalzner S., 2015, A&A, 577, A115

Visser R., Geers V. C., Dullemond C. P., Augereau J.-C., Pontoppidan K. M., van Dishoeck E. F., 2007, A&A, 466, 229

Vonneumann J., Richtmyer R. D., 1950, J. App. Phys., 21, 232

Wagner K., Apai D., Kasper M., Robberto M., 2015, ApJL, 813, L2

Weidenschilling S. J., 1977, MNRAS, 180, 57

Weingartner J. C., Draine B. T., 2001, ApJS, 134, 263

Welsh W. F. et al., 2012, Nature, 481, 475

White R. J., Ghez A. M., 2001, ApJ, 556, 265

White R. J., Hillenbrand L. A., 2004, ApJ, 616, 998

Williams J. P., Cieza L. A., 2011, ARA&A, 49, 67

Williams J. P. et al., 2014, ApJ, 796, 120

Windemuth D., Herbst W., 2014, AJ, 147, 9

Woitas J., Leinert C., Köhler R., 2001, A&A, 376, 982

Woitas J., Ray T. P., Bacciotti F., Davis C. J., Eislöffel J., 2002, ApJ, 580, 336

Woitke P. et al., 2015, ArXiv e-prints

Wolfire M. G., McKee C. F., Hollenbach D., Tielens A. G. G. M., 2003, ApJ, 587, 278

Wright N. J., Drake J. J., Drew J. E., Guarcello M. G., Gutermuth R. A., Hora J. L., Kraemer K. E., 2012, ApJL, 746, L21

Wyatt M. C., Dent W. R. F., 2002, MNRAS, 334, 589

Wyatt M. C., Panić O., Kennedy G. M., Matrà L., 2015, Ap&SS, 357, 103

Xiang-Gruess M., Papaloizou J. C. B., 2013, MNRAS, 431, 1320

Young M. D., Baird J. T., Clarke C. J., 2015, MNRAS, 447, 2907

Young M. D., Clarke C. J., 2015, MNRAS, 452, 3085

Zhu Z., 2015, ApJ, 799, 16

Zhu Z., Nelson R. P., Hartmann L., Espaillat C., Calvet N., 2011, ApJ, 729, 47

Acknowledgements

First of all I want to thank my supervisor Cathie Clarke. Without you, my PhD would have never started. I am very grateful for all the availability you had with me during these three years, and for how you helped me growing in my skills and in my empirical understanding of physical mechanisms. And finally, thanks for your help and discretion in the last few months. I am also thankful to the Isaac Newton Studentship electors. Without the INS, I would have never been able to come to Cambridge.

Then, I would like to thank all the the DISCSIM group, the discussions with all of you have been extremely valuable. And thanks in particular to Attila and Giovanni for the uncountable number of chats during coffee time. I am also grateful to Giuseppe Lodato, with whom I hope to keep on collaborating. I also thank other collaborators, in particular Carlo Manara, without whom proposing for telescope time (and understanding the results) would have been an absolute utopia, and Chris Nixon, for all the discussions on warps in discs. I am also immensely grateful to my officemates, who made these three years much more fun: Luca, Aimee, Keith, Christina, Nimisha, Tom, Adriano and Maciej. Finally, thanks to Matt, Will and Gabriel for organising football matches! It has been great playing with you guys.

An additional thanks to Grant Kennedy and Richard Alexander, my two examiners. The discussion during the viva has been very interesting, and has helped improving the quality of some chapters of this thesis.

And now, I would like to thanks all the people who have supported me and accompanied me in these years. First of all, my family. Thank you mum and dad, for staying with me all this time, and for being present every time I needed it. The more I grow, the more I realise how grateful I am of you both. Then, all my friends, back in Italy and here in the UK. Thanks for keeping on witnessing that life is beautiful, because it has a meaning, and a path to go towards it. And finally, thank you to Irene, for staying beside me all these years. It is impossible to put into words my gratitude for everything you have done for me. Thank you.